An interference search for new scalar and pseudoscalar states decaying to a top-anti-top quark pair with the ATLAS experiment

Dissertation
zur Erlangung des Doktorgrades
an der Fakultät für Mathematik, Informatik und Naturwissenschaften
Fachbereich Physik
der Universität Hamburg

vorgelegt von
Nicola de Biase

Hamburg
2024

Gutachter/innen der Dissertation:	Prof. Dr. Peter Schleper Dr. Janna Katharina Behr
Zusammensetzung der Prüfungskommission:	Prof. Dr. Peter Schleper Dr. Janna Katharina Behr Prof. Dr. Kerstin Tackmann Prof. Dr. Timo Weigand Prof. Dr. Dieter Horns
Vorsitzende/r der Prüfungskommission:	Prof. Dr. Dieter Horns
Datum der Disputation:	11.10.2024
Vorsitzender des Fach-Promotionsausschusses PHYSIK:	Prof. Dr. Markus Drescher
Leiter des Fachbereichs PHYSIK:	Prof. Dr. Wolfgang J. Parak
Dekan der Fakultät MIN:	Prof. Dr.-Ing. Norbert Ritter

Declaration on oath

I hereby declare and affirm that this doctoral dissertation is my own work and that I have not used any aids and sources other than those indicated.

If electronic resources based on generative artificial intelligence (gAI) were used in the course of writing this dissertation, I confirm that my own work was the main and value-adding contribution and that complete documentation of all resources used is available in accordance with good scientific practice. I am responsible for any erroneous or distorted content, incorrect references, violations of data protection and copyright law or plagiarism that may have been generated by the gAI.

06.06.2024 Nicola ob Bian

Date Signature of doctoral candidate

Acknowledgements

I would like to thank Katharina Behr for supervising my PhD. You always supported me, while giving me the space to express my ideas and pursue my interests. I am grateful for the opportunity to learn from you, for all your help in navigating my PhD, and for being an example to follow. I am also grateful for your support to my participation in many schools, workshops, and conferences.

Thanks to Peter Schleper for reviewing my thesis, and to Dieter Horns, Timo Weigand, and Kerstin Tackmann for agreeing to be part of my doctoral committee.

A special thanks also goes to Trine Poulsen and Eleanor Jones, who have supported me in different phases of my PhD, both professionally and personally.

The search presented in this thesis was conducted in collaboration with many other researchers. I would like to thank Samuel Calvet, Yizhou Cai, Mohammed Faraj and Michele Pinamonti for their contribution to the analysis.

A special thanks goes to Will Buttinger, whose help was crucial for the understanding of the statistical challenges of signal-background interference and for the implementation of the statistical tools to treat them. In this context, I would also like to thank Glen Cowan, Alexander Reid, and the entire ATLAS Statistics Committee.

A PhD is a long journey which is impossible to travel without good friends. I was very lucky in this regard.

Grazie Adri. È difficile esprimere quanto la tua amicizia sia importante per me. In questi anni sei stata la mia roccia e la mia confidente e te ne sarò per sempre grato. Y por cierto gracias por el chisme.

Yahya, vivere con qualcuno non è mai facile, ma io ho avuto la fortuna di farlo con un amico sincero. Sei stato sempre presente, nei momenti di gioia, di festa, di ballo e di cucina *accazzodicane*, ma anche nei momenti difficili.

Gracias Pepe, porque fuiste mi primer amigo en esta ciudad, y sigues siendo una de las personas en que mas confío en mi vida.

Bianca, rimpiango solo di non averti conosciuta prima. Grazie per aver reso la mia vita migliore, e per avermi accompagnato in questo viaggio.

Danke Moritz für die Käsespätzle. Also for being a wonderful friend, but mostly for the Käsespätzle.

Gracias Ana porque me encanta quejarme contigo.

Grazie Silvia per avermi sostenuto nonostante la distanza e per aver sempre trovato il tempo per coltivare la nostra amicizia.

Ai miei amici di sempre, Francesco, Paolo e Stefano. La distanza non conta nulla. Giggi sei un cane ma sempre fedele.

Thank you to all my friends in the DESY volleyball group, present and past. You were a beam of light in a dark day.

Nayla, fuiste la sorpresa màs bella de estos años en Hamburgo. Gracias por ser parte de mi vida.

Infine, vorrei ringraziare la mia famiglia. Grazie Maria Stella perché grazie a te non ho paura di

nulla. In ogni momento difficile che ho attraversato nella mia vita, ci sei sempre stata, e mi hai aiutato ad uscirne fuori. Sei il mio punto fermo.
Grazie ai miei genitori. Ogni traguardo che ho raggiunto nella mia vita ha un'origine ben precisa, e quell'origine siete voi.

Abstract

A search for heavy pseudoscalar (A) and scalar (H) Higgs bosons decaying into a top-quark pair ($t\bar{t}$) is presented. The search has been conducted using 140 fb^{-1} of proton–proton collision data collected by the ATLAS experiment at the Large Hadron Collider (LHC), with a centre-of-mass energy of $\sqrt{s}$ = 13 TeV. The analysis accounts for interference effects between the signal process and Standard Model (SM) $t\bar{t}$ production. Final states with exactly one or two electrons or muons are considered. Specific methods for statistical inference in the presence of signal-background interference are presented in the context of the search.
No significant deviation from the SM prediction is observed. The results of the search are interpreted within the framework of a two-Higgs-doublet model (2HDM) of type II in the alignment limit, in which the pseudoscalar and scalar Higgs bosons are mass-degenerate ($m_A = m_H$), as well as within the hMSSM parameterisation of the minimal supersymmetric extension of the Standard Model. Ratios of the vacuum expectation values of the two Higgs fields, $\tan\beta$, smaller than 3.49 (3.16) are excluded at the 95% confidence level for $m_A = m_H = 400$ GeV in the 2HDM (hMSSM). In the 2HDM interpretation, masses up to 1240 GeV are excluded at 95% confidence level for the lowest tested $\tan\beta$ value of 0.4. In the hMSSM interpretation, masses up to 950 GeV are excluded for $\tan\beta = 1.0$. Additionally, exclusion limits on the (pseudo)scalar-top-quark coupling as a function of the (pseudo)scalar mass are provided in the context of a generic model in which the couplings are varied independently of the decay width of the new particle.

The LHC and its experiments are scheduled for an extensive upgrade, with the goal of accumulating an integrated luminosity of 3 ab^{-1} at the end of the High-Luminosity LHC programme. An important part of the ATLAS upgrade is the replacement of the current Inner Detector (ID) with a new, all silicon, Inner Tracker (ITk). Dense hadronic environments, encountered in the core of high-p_T jets, are particularly challenging for the reconstruction of charged-particle trajectories (tracks), as they are characterised by a high local density of ionising particles. The energy deposits (clusters) left by these particles in the silicon sensors are likely to merge and form clusters with contributions from multiple particles. This negatively affects the track reconstruction efficiency, and the precision in the evaluation of track properties. A study of the expected performance of clustering and tracking in dense hadronic environments with the ITk is presented. The tracking performance is found to be improved with respect to ID tracking, thanks to the fine granularity of the ITk. The study also highlights the potential gain from dedicated algorithms for merged-cluster identification for the mitigation of the negative effects of cluster merging within the ITk.

Zusammenfassung

In dieser Arbeit wird eine Suche nach schweren pseudoskalaren (A) und skalaren (H) Higgs-Bosonen vorgestellt, die in ein Top-Quark-Paar ($t\bar{t}$) zerfallen. Die Suche wurde mit einem Datensatz durchgeführt, der in Proton-Proton-Kollisionen bei einer Schwerpunktsenergie von $\sqrt{s} = 13$ TeV gewonnen wurde und einer integrierten Luminosität von 140 fb^{-1} entspricht. Die Analyse berücksichtigt Interferenzeffekte zwischen dem Signalprozess und der $t\bar{t}$-Produktion des Standardmodells (SM). Es werden Endzustände mit genau einem oder zwei Elektronen oder Myonen betrachtet. Spezifische Methoden für die statistische Inferenz bei Vorhandensein von Signal-Hintergrund-Interferenz werden im Rahmen der Suche vorgestellt.
In der Suche wurde keine signifikante Abweichung von der SM-Vorhersage beobachtet. Die Ergebnisse der Suche werden im Rahmen eines Modells mit zwei Higgs-Feldern (Two-Higgs-Doublet Model, 2HDM) vom Typ II im Alignment Limit interpretiert, in dem die pseudoskalaren und skalaren Higgs-Bosonen die gleiche Masse haben ($m_A = m_H$), sowie im Rahmen der hMSSM-Parametrisierung der minimalen supersymmetrischen Erweiterung im Standardmodell. Verhältnisse der Vakuumerwartungswerte der beiden Higgs-Felder, $\tan\beta$, kleiner als 3,49 (3,16) werden auf dem 95%-Konfidenzniveau für $m_A = m_H = 400\,\text{GeV}$ im 2HDM (hMSSM) ausgeschlossen. In der 2HDM-Interpretation werden Massen bis zu 1240 GeV auf dem 95%-Konfidenzniveau für den niedrigsten getesteten $\tan\beta$-Wert von 0,4 ausgeschlossen. In der hMSSM-Interpretation werden Massen bis zu 950 GeV für $\tan\beta = 1.0$ ausgeschlossen. Zusätzlich werden Ausschlussgrenzen für die Kopplung von (Pseudo)Skalaren an Top Quarks angegeben, separat für die Hypothese des Vorhandenseins eines einzelnen skalaren bzw. pseudoskalaren Teilchens.

Der LHC und seine Experimente sollen umfassend aufgerüstet werden, mit dem Ziel, am Ende des des High-Luminosity LHC-Programms von 3 ab^{-1} zu erreichen. Ein wichtiger Teil des ATLAS-Upgrades ist der Ersatz des derzeitigen Inneren Detektors (ID) durch einen neuen, vollständig aus Silizium bestehenden Inneren Tracker (ITk). Dichte hadronische Umgebungen, wie sie im Zentrum von hochenergetischen Jets anzutreffen sind, stellen eine besondere Herausforderung für die Rekonstruktion der Spuren (Tracks) geladener Teilchen dar, da sie durch eine hohe lokale Dichte ionisierender Teilchen gekennzeichnet sind. Die Energiedeposition (Cluster), die diese Teilchen in den Siliziumsensoren hinterlassen, verschmelzen dabei mit hoher Wahrscheinlichkeit und bilden Cluster mit Beiträgen von mehreren Teilchen. Dies wirkt sich negativ auf die Effizienz der Spurrekonstruktion und die Genauigkeit bei der Bewertung der Spureneigenschaften aus. Im Rahmen dieser Arbeit wurden die Rekonstruktion und Identifikation von Mehrteilchenclustern bei hohen Teilchendichten im ITk untersucht. Dabei wurde festgestellt, dass die Effizienz und Präzision der Spurrekonstruktion dank der feinen Granularität des ITk gegenüber der Spurrekonstruktion im ID verbessert wird. Die Studie unterstreicht auch den potenziellen Nutzen spezieller Algorithmen zur Identifizierung von Mehrteilchenclustern, zur Verbesserung der Spurrekonstruktion bei hohen Teilchendichten.

Contents

1 Introduction **1**

2 Theoretical foundations **5**
2.1 The Standard Model of particle physics . . . 5
2.1.1 Elementary particles . . . 5
2.1.2 Fundamental interactions . . . 6
2.1.3 Quantum Chromodynamics . . . 8
2.1.4 The electroweak sector . . . 9
2.1.5 The Higgs sector . . . 10
2.2 Production and Decay of Top Quarks in the SM . . . 12
2.2.1 Pair production of top quarks at hadron colliders . . . 12
2.2.2 Top quarks decays . . . 13
2.3 Problems and limitations of the Standard Model . . . 14
2.4 Extending the scalar sector . . . 17
2.4.1 Type-II 2HDMs . . . 18
2.4.2 2HDM+a . . . 19
2.4.3 hMSSM . . . 20
2.4.4 Generic (pseudo)scalar model . . . 20
2.4.5 Production and decay of heavy Higgs bosons at hadron colliders . . . 21

3 The ATLAS experiment at the LHC **23**
3.1 The Large Hadron Collider (LHC) . . . 23
3.1.1 LHC Runs . . . 24
3.2 The ATLAS experiment . . . 25
3.2.1 ATLAS coordinate system . . . 26
3.2.2 The magnetic system . . . 27
3.2.3 The Inner Detector . . . 27
3.2.4 The Calorimeters . . . 29
3.2.5 The Muon Spectrometer . . . 31
3.3 The Trigger and Data Acquisition System . . . 32
3.4 Upgrades for Run-4 and High-Luminosity LHC . . . 33

4 Data and simulation of p-p collisions in ATLAS **35**
4.1 Data sample . . . 36
4.2 Simulations . . . 36
4.2.1 SM $t\bar{t}$ production . . . 36

4.2.2 Single-top production . . . 37
4.2.3 $t\bar{t}+V$ and $t\bar{t}+h$ productions . . . 38
4.2.4 W+jets and Z+jets . . . 38
4.2.5 Diboson . . . 39
4.2.6 Signal samples . . . 39

5 Reconstruction and identification of physics objects **41**
5.1 Basic objects . . . 41
5.1.1 Charged-particles track reconstruction . . . 41
5.1.2 Topological clusters . . . 42
5.2 Electrons . . . 43
5.3 Muons . . . 44
5.4 Jets . . . 47
5.4.1 Constructing the jets: the anti-k_T algorithm . . . 47
5.4.2 Building jet inputs: PFlow jets . . . 48
5.4.3 Jet calibration . . . 49
5.4.4 Reclustered jets . . . 51
5.4.5 b-tagging . . . 51
5.4.6 Missing transverse momentum . . . 52
5.4.7 Overlap removal . . . 53
5.5 Baseline object selection . . . 54
5.5.1 Electrons . . . 54
5.5.2 Muons . . . 55
5.5.3 Small-radius jets . . . 55
5.5.4 Reclustered jets . . . 56

6 Analysis strategy **57**
6.1 Final state and event topologies . . . 57
6.2 Event selection in the one-lepton channel . . . 58
6.2.1 Preselection . . . 58
6.2.2 Trigger selection . . . 58
6.2.3 Common selection . . . 59
6.2.4 Merged selection . . . 60
6.2.5 Resolved selection . . . 60
6.3 Event reconstruction in the one-lepton channel . . . 61
6.3.1 Neutrino reconstruction . . . 62
6.3.2 Merged topology . . . 62
6.3.3 Resolved topology . . . 63
6.4 Signal region definition in the one-lepton channel . . . 64
6.5 Event selection and categorisation in the two-lepton channel . . . 66
6.6 Optimisation of the one-lepton signal region definition . . . 67
6.6.1 Reconstruction of moderately boosted hadronic top-quark decays . . . 68
6.6.2 Angular categorisation . . . 72
6.7 Data-driven background estimation and correction . . . 74
6.7.1 W+jets background in the one-lepton channel . . . 74

6.7.2 Multi-jet background estimation in the one-lepton channel . . . 75
6.7.3 Z+jets background in the two-lepton channel . . . 77
6.7.4 Fakes background in the two-lepton channel . . . 77
6.8 Systematic uncertainties . . . 77
6.8.1 Experimental uncertainties . . . 78
6.8.2 Modelling uncertainties . . . 79

7 Statistical methods **85**
7.1 Profile likelihood fits . . . 85
7.2 Profile likelihood parametrisation in the presence of interference . . . 87
7.2.1 Technical implementation via the offset method . . . 87
7.3 Statistical inference . . . 91
7.3.1 Hypothesis tests . . . 91
7.3.2 The CL_s method for quantifying exclusion in the BSM parameter space . . . 94
7.4 p-value variations in the presence of interference . . . 95
7.5 From p-values to exclusion regions . . . 96

8 Statistical inference and results **99**
8.1 Construction of the profile likelihood . . . 99
8.2 Profile likelihood fits under the background-only hypothesis . . . 100
8.3 Impact and ranking of systematic uncertainties . . . 104
8.4 Search stage . . . 106
8.5 Exclusion in the BSM parameter space . . . 109

9 Discussion and outlook **113**
9.1 Comparison with existing constraints . . . 113
9.2 Outlook . . . 117

10 The future of charged particle reconstruction in ATLAS **119**
10.1 Classification of clusters and tracks . . . 120
10.2 Track selection and matching to jets . . . 121
10.3 Simulation . . . 121
10.4 Effect of cluster merging on track parameters . . . 122
10.5 Tracks inside of jets . . . 128
10.5.1 Cluster merging . . . 128
10.5.2 Tracking efficiency . . . 129
10.6 Summary . . . 133

11 Conclusions **135**

A Local p-values for the search stage **141**

B Constraints on the coupling strength modifier in the generic (pseudo)scalar interpretation **147**

Bibliography **151**

List of Figures 167

List of Tables 175

CHAPTER 1

Introduction

Over the past few decades, the Standard Model (SM) of particle physics has been incredibly successful at describing measurements at collider experiments. It has undergone rigorous experimental tests, even successfully predicting the existence of various particles, including the W and Z bosons, discovered at CERN's Super Proton Synchrotron in 1983 [1, 2], as well as the top quark, first observed at the Tevatron collider in 1995 [3, 4]. Between 1989 and 2000, numerous precision measurements of SM parameters and processes were carried out at the experiments of the Large Electron-Positron collider (LEP), with extraordinary agreement with their theoretical predictions [5, 6]. The triumph of the SM culminated in 2012, when its last missing particle, the Higgs Boson, was discovered separately by both the ATLAS and CMS experiments at the Large Hadron Collider (LHC) at CERN [7, 8].

Despite its many successes, the SM still fails to answer many open questions in particle physics. Why is there such a strong prevalence of matter over antimatter in the universe? How can gravity be described at a particle level? Why is the energy scale of electroweak interactions so small compared to the energy scale of gravitational interactions? Strong astrophysical evidence suggests the existence of a type of matter not interacting electromagnetically, responsible for about 85% of the matter content in the universe [9–13]; what is the particle nature of this *dark matter*? Many extensions of the SM, so-called Beyond-Standard-Model (BSM) theories, have been proposed, which predict the existence of new elementary particles.

To this day, the vast majority of searches for new particles carried out at the LHC rely on the assumption that their production and decay do not interfere with SM processes; this means that the BSM production of a new, hypothetical elementary particle would manifest itself as a resonance, i.e. a bump on an otherwise smooth kinematic distribution of a SM background process. Since no new elementary particle has been discovered since the Higgs boson in 2012, it is reasonable to abandon common assumptions, and search for unusual BSM signatures that would manifest themselves as interference patterns on top of a smooth background kinematic distribution. Rather than looking for a bump, one can look for more complex patterns, such as a localised excess followed by a localised deficit of events.

At the LHC, scalar or pseudoscalar particles with a Higgs-like Yukawa coupling to fermions would be predominantly produced via a fusion of two gluons, mediated by a heavy-quark loop, and preferably decay to top-quarks. Their decay process to a top-antitop ($t\bar{t}$) quark pair would interfere with SM $t\bar{t}$ production at LHC, resulting in a characteristic peak-dip structure in the distribution of the reconstructed invariant mass of the $t\bar{t}$ system, whose shape strongly depends on the parameters and

type of the BSM scenario.

In this thesis, a search for heavy scalars and pseudoscalars with the ATLAS experiment is presented, using the whole LHC Run-2 dataset of proton–proton collisions at a centre-of-mass energy $\sqrt{s} = 13$ TeV, collected between 2015 and 2018, and amounting to a 140 fb^{-1} integrated luminosity. The results of the search are interpreted in terms of BSM models predicting an additional Higgs doublet (2HDM [14], hMSSM [15], 2HDM+a [16]) or a generic additional (pseudo)scalar state. The search targets the dominant production mode of (pseudo)scalar states at the LHC and offers access to a fairly unexplored region of the parameter space of the benchmark BSM models, where the heavy states decay predominantly to $t\bar{t}$. Previous ATLAS Run-1 [17] and CMS partial Run-2 [18] searches targeting the same process only constrained the parameter spaces of the benchmark models for values of the (pseudo)scalar mass up to about 700 GeV, while the work presented in this thesis extends the mass reach up to about 1 TeV, providing the strongest constraints to date in parameter regions with dominant decays to $t\bar{t}$.

The search presented in this thesis is part of a diverse programme of searches and measurements carried out by the ATLAS collaboration, which depends critically on the excellent performance of both the detector and the algorithms to reconstruct and identify particles and their decays within it. In 2029, the LHC will enter the new High-Luminosity-LHC (HL-LHC) era, featuring an instantaneous luminosity of up to $7.5 \cdot 10^{34}$ cm^{-2} s^{-1}. This is a significant increase compared to the peak instantaneous luminosity of $3 \cdot 10^{34}$ cm^{-2} s^{-1} of the ongoing operation Run-3 period, which started in 2022 and will last until 2025. The increase in instantaneous luminosity will allow to accumulate more data than ever before, and to search for and measure extremely rare processes in the SM, such as di-Higgs production, and beyond. An integrated luminosity of 3 ab^{-1} is targeted by the end of the HL-LHC programme, compared to the 350 fb^{-1} foreseen at the end of Run-3. The HL-LHC era will also come with significant challenges, given the substantial increase in interactions per time unit. For this reason, the current ATLAS sub-detector for the reconstruction of the trajectories of charged particles will be completely replaced by a new all-silicon *Inner Tracker* (ITk). In this thesis, a study of the expected performance of charged-particle reconstruction with the ITk is presented, with a particular focus on the performance in dense hadronic environments, i.e. environments with a high local density of charged particles. Dense hadronic environments are common in the cores of high-transverse-momentum hadronic jets, where precise and efficient tracking is crucial for the identification of heavy-flavour hadrons and top-quark decays.

This thesis is structured as follows. In Chapter 2, the theoretical foundations of the SM are presented, together with useful information on collider physics. Relevant BSM benchmarks whose scalar sector produces interference effects with the SM are also presented in this chapter. In Chapter 3 the LHC and the ATLAS experiment are described, both in their current configuration and with regard to future upgrades. In Chapter 4, the dataset used for the search for heavy Higgs bosons decaying to $t\bar{t}$ is described, along with the Monte Carlo simulations of background processes and of the benchmark signal processes introduced in Chapter 2. In Chapter 5, the reconstruction of physics objects in the ATLAS experiment is presented, with a focus on the objects used in the search presented in this thesis. In Chapter 6, the analysis strategy for the interference search is described in detail, including event selection, reconstruction and categorisation, data-driven estimation of background processes, and modelling of systematic uncertainties. In Chapter 7, the statistical methods for the interpretation of results are described. This is especially relevant due to the presence of interference between the BSM process and the SM, which calls for the development of dedicated methods for statistical inference, different from the ones commonly used in resonance searches. The statistical methods

developed in this thesis will form the basis for many future interference searches, including those in other final states. In Chapter 8, the results of the interference search are interpreted in the context of the benchmark models of Chapter 2. In Chapter 9, the results are compared to other analyses constraining the parameter space of the same BSM benchmark models considered in this thesis, and possible future developments are described.
In Chapter 10, the expected performance of charged-particle reconstruction with the ITk, for HL-LHC is discussed, with a focus on dense hadronic environments. This is of crucial importance for all future searches performed in the HL-LHC era. Finally, Chapter 11 offers a summary of the projects presented in this thesis.

Author's contributions

Today's largest particle physics experiments are collaborative efforts involving many people working together on various aspects of the project. The ATLAS collaboration consists of about 3000 members who contribute to maintaining and upgrading the detector and the software needed to reconstruct physics observables from the raw data, as well as to analyse the data and interpret the results. This collective effort is essential for the work presented here. Given that the results in this thesis depend on the contributions of many people, the author's specific contributions are summarised here.

The author was one of the main contributors to the interference search for heavy scalar and pseudoscalar particles decaying to $t\bar{t}$. The author contributed to the development and maintenance of the analysis framework. The author developed the event selection and reconstruction in the boosted one-lepton channel and was responsible for the definition and optimisation of the signal regions in this channel. The author was the main responsible for the development and testing of the methods for statistical inference in the presence of signal-background interference effects presented in Chapter 7. The author was also one of the main contributors in studying the robustness of the statistical model, and the impact of many systematic uncertainties.

The author performed all the studies related to clustering and tracking in dense hadronic environments with the ITk.

The search presented in this thesis has been published on arXiv [19], and all plots carry the ***ATLAS*** label. The studies on clustering and tracking in dense hadronic environments with the ITk have been published as an ATLAS PUBNOTE, and carry the ***ATLAS*** Preliminary label. Unless specified in the caption, plots not carrying any labels have been produced by the author.

CHAPTER 2

Theoretical foundations

2.1 The Standard Model of particle physics

The history of particle physics is largely the history of the uncovering of successive layers of substructure in the composition of matter, with the final aim of uncovering its elementary constituents. The study of the structure of matter is also inextricably tied to the description of the fundamental interactions among its constituents. Four fundamental interactions are known to this day: gravity, electromagnetism, the weak interaction, and the strong interaction. Our current knowledge of the elementary particles that make up matter and their interactions is summarised in the *Standard Model* (SM) of particle physics. Despite not being able to describe gravitational interactions, the SM has been very successful in describing phenomena at the smallest scales accessible to experiments to date, also thanks to the fact that, at the smallest scales, the strength of gravity is negligible compared to that of the other interactions.

2.1.1 Elementary particles

The particles in the SM can be divided into two groups based on their spin. Spin-$\frac{1}{2}$ particles are called *fermions* and they behave according to the Fermi-Dirac statistics; particles with integer spin follow the Bose-Einstein statistics and are called *bosons*. Regular matter is made of fermions. Fermions can be grouped into three generations, which have identical quantum numbers but higher masses for higher generations. Moreover, for each fermion in the model, an anti-fermion exists with the same mass and opposite-sign charges. Fermions are also classified based on whether or not they interact strongly. Strongly interacting fermions are called quarks and carry a colour charge, which is responsible for their strong interaction. Up (u), charm (c), and top (t) quarks have a positive $+2/3$ electric charge, while down (d), strange (s), and bottom (b) have a negative $-1/3$ electric charge. All quarks interact weakly but their mass eigenstates do not coincide with their weak eigenstates. The mixing between the mass and weak eigenstates is described via the Cabibbo-Kobayashi-Maskawa (CKM) matrix:

$$\begin{pmatrix} d' \\ s' \\ b' \end{pmatrix} = V_{CKM} \begin{pmatrix} d \\ s \\ b \end{pmatrix}. \tag{2.1}$$

Non-strongly interacting fermions are called leptons. There are three leptons with a negative -1 charge: electrons (e), muons (μ) and taus (τ) and three neutral ones. Also, electrically neutral leptons exist, which only interact weakly: the electron neutrino (ν_e), the muon neutrino (ν_μ), and the tau neutrino (ν_τ).

The Spin-1 bosons of the SM, also known as *vector bosons*, are the carriers of the three interactions described by the theory. The electromagnetic interaction affects all particles with an electric charge and is mediated by the photon. The photon is massless and electrically neutral. The strong interaction is mediated by the gluon, which is massless and electrically neutral, but carries a colour charge. The strong interaction affects all particles with a colour charge, namely the quarks and the gluon itself. Finally, the weak interaction affects all fermions in the SM. It is mediated by two electrically charged bosons, W^+ and W^-, as well as by the neutral Z boson. All three weak bosons are massive, unlike the other force carriers, which are massless. Finally, the SM contains a spin-0 boson, the Higgs boson. It was postulated to introduce vector boson and fermion masses in a way that would preserve the gauge invariance of the theory (Section 2.1.2), via a mechanism called spontaneous symmetry breaking (Section 2.1.5).

2.1.2 Fundamental interactions

The SM can be described mathematically as a *gauge field theory*, which is a special kind of *quantum field theory*, in which the interactions between matter fields are introduced by requiring the invariance of the theory under a transformation group. The gauge group of the theory is

$$\mathrm{SU(3)_C} \times \mathrm{SU(2)_L} \times \mathrm{U(1)_Y}. \tag{2.2}$$

$SU(3)$ is the special unitary group of third degree and describes the strong interaction. The suffix C is introduced to denote that *colour* is the conserved charge under this group. $SU(2)$ is the special unitary group of second degree and $U(1)$ is the unitary group of first degree; together, they describe the electroweak interactions. The L suffix indicates that the $SU(2)$ gauge fields only interact with the left-handed components of the fermion fields, while the Y suffix denotes the conserved charge of the $U(1)$ gauge group, the *weak hypercharge*.

Gauge field theories

In a quantum field theory, the evolution of a system is given by its *Lagrangian density* $\mathcal{L}$ by solving the corresponding Euler-Lagrange equations:

$$\frac{\partial \mathcal{L}}{\partial \phi_j} - \partial_\mu \left(\frac{\partial \mathcal{L}}{\partial \left(\partial_\mu \phi_j \right)} \right), \tag{2.3}$$

where ϕ_j are the quantum fields.

The Lagrangian density of a free fermion is

$$\mathcal{L} = i\bar{\psi}\gamma^\mu \partial_\mu \psi - m\bar{\psi}\psi, \tag{2.4}$$

where ψ is a Dirac spinor describing the fermion, and m is the mass of the fermion. The gamma matrices

γ^μ satisfy the Dirac anti-commutation relations $\left\{\gamma^\mu, \gamma^\nu\right\} = 2g^{\mu\nu}$, where $g^{\mu\nu}$ is the Minkowski metric tensor. To introduce an interaction in a gauge theory, the Lagrangian is required to be invariant under local transformations in a gauge group G:

$$\psi\left(x\right) \rightarrow \psi'\left(x\right) = \exp\left\{ig\theta^a\left(x\right)T^a\right\}\psi\left(x\right), \tag{2.5}$$

where T^a are the generators of the group and the functions of space-time $\theta^a(x)$ are the parameters of the transformation. To obtain invariance it is sufficient to introduce bosonic interaction fields A^a_μ, with the gauge transformation rule

$$A^a_\mu \rightarrow A^a_\mu - \partial_\mu\theta^a\left(x\right) - gf^{abc}\theta^b\left(x\right)A^c_\mu, \tag{2.6}$$

where f^{abc} are the structure constants of the gauge group, and to substitute the derivative operator ∂_μ with the covariant derivative

$$D_\mu = \partial_\mu + igT^aA^a_\mu. \tag{2.7}$$

This introduces a fermion-boson interaction term in the form $-j^{\mu,a}A^a_\mu$ with

$$j^{\mu,a} = \bar{\psi}\left(g\gamma^\mu T^a\right)\psi. \tag{2.8}$$

Due to the gauge symmetry, $j^{\mu,a}$ are conserved currents ($\partial_\mu j^{\mu,a} = 0$), and therefore the corresponding charges are conserved as well. In order to achieve local gauge invariance, it is also necessary to remove the mass term from the Lagrangian, effectively rendering fermion fields massless, although they are observed to be massive. The solution to this problem is solved by the Higgs mechanism (Section 2.1.5). The dynamics of the gauge fields is described by gauge-invariant terms in the Lagrangian formed from the gauge fields A^a_μ and their derivatives, provided they are Lorenz-invariant. The gauge tensors $F^{\mu\nu,a} = \partial^\mu A^{\nu,a} - \partial^\nu A^{\mu,a} - gf^{abc}A^{\mu,b}A^{\nu,c}$ are invariant under 2.1.2, so terms proportional to $F^a_{\mu\nu}F^{\mu\nu,a}$ can be included in the Lagrangian. Mass terms for the gauge bosons would not be gauge-invariant and must be added via the Higgs mechanism (Section 2.1.5). The complete Lagrangian for a gauge field theory is

$$\mathcal{L} = \mathcal{L}_f + \mathcal{L}_{int} + \mathcal{L}_B, \tag{2.9}$$

where:

- $\mathcal{L}_f = i\bar{\psi}\gamma^\mu\partial_\mu\psi$ is the fermion kinetic term;
- $\mathcal{L}_{\text{int}} = j^{\mu,a}A^a_\mu$ is the interaction term between fermions and gauge bosons;
- $\mathcal{L}_B = -\frac{1}{4}F^a_{\mu\nu}F^{\mu\nu,a}$ is the gauge boson term, containing a kinetic part as well as an interaction term between gauge bosons, arising in case of non-commutativity among the group generators;

The gauge boson term contains a kinetic part as well as an interaction term between gauge bosons. The interaction term arises in the case of non-commutativity between the group generators. In principle, the gauge boson term could also include a CP-violating term in the form $\vartheta g^2/(32\pi^2)F^a_{\mu\nu}\tilde{F}^{\mu\nu,a}$, with $\tilde{F}^{\mu\nu,a} = \varepsilon_{\mu\nu\rho\sigma}F^{\rho\sigma,a}$; however, in the SM, such a term leads to no physical effect for all the interactions except the strong interaction, due to the structure of the gauge groups involved. For the

strong interactions, the ϑ parameter is measured to be compatible with 0, and no CP violation is observed in the strong sector of the SM.

A final remark to make about quantum field theories (and gauge ones are no exception), is that the strength of an interaction between two fields is given by the coupling constant g appearing in both the conserved current and the gauge tensors. Predictions of the theory are obtained as transition probabilities between quantum states, which are usually calculated perturbatively, by summing a finite number of terms proportional to increasing powers of g. However, some terms are divergent and need to be fixed by a procedure called *renormalisation* [20, 21]. An effect of this procedure is that some observables of the theory, such as coupling constants or particle masses, cease to be constant and acquire a dependence on the transferred momentum in a given process. The dependence of the coupling constant on the transferred momentum of the process is known as *running of the coupling*.

2.1.3 Quantum Chromodynamics

Quantum Chromodynamics (QCD) is the quantum field theory describing the strong interaction. The only fermions affected by strong interactions are the quarks. The gauge group of the theory is $SU(3)_C$, which can be represented as the group of unitary 3×3 complex matrices with determinant 1. The conserved charge of the group is colour, hence the quark fields are represented as colour triplets

$$q = \begin{pmatrix} q_r \\ q_g \\ q_b \end{pmatrix}. \tag{2.10}$$

The group has eight generators, which can be represented as $T^a = \lambda^a/2$, where λ^a are the Gell-Mann matrices. Consequently, eight gluon fields exist to mediate strong interactions. Due to the non-commutativity of the gauge groups, gluons fields are subject to self-interactions. Figure 2.1 shows the fundamental vertices in QCD.

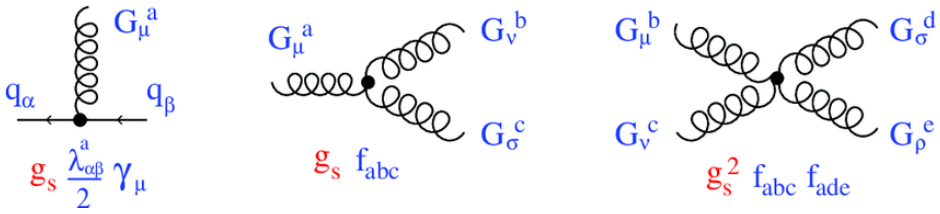

Figure 2.1: Fundamental vertices in QCD.

A notable property of QCD is that the strong interaction is stronger at low energies, to the point that low-energy processes cannot be calculated perturbatively. At low energies, quarks form bound states (hadrons) such as protons and neutrons. Trying to take apart a hadron would require more energy as the distance between its constituent quarks increases, until the energy stored in the field is high enough to produce quark-anti-quark pairs, which would later combine with the original quarks to form colour-neutral hadrons. Thus, it is impossible to observe isolated quarks and gluons; this property of QCD takes the name of *colour confinement*.

Due to colour confinement, a hard scattering process involving quarks or gluons in the final state results in the production of a cascade, a *jet*, of hadrons, in a process called hadronisation. The hadronisation takes place at an energy scale in which QCD cannot be treated perturbatively.

2.1.4 The electroweak sector

The Electromagnetic and weak interactions in the SM are described in a unified manner by the Glashow, Weinberg and Salam model [22]. They affect all fermions in the theory. The gauge group of the theory is

$$\mathrm{SU(2)_L} \times \mathrm{U(1)}_Y, \tag{2.11}$$

where, as mentioned in Section 2.1.2, the subscript L indicates that the $\mathrm{SU(2)_L}$ transformation group only acts on the left-handed components of the fermion fields. The left/right-handed components of fermion fields are defined as

$$\psi_{L/R} = \frac{1 \mp \gamma^5}{2}\psi, \tag{2.12}$$

with $\gamma^5 = i\gamma^0\gamma^1\gamma^2\gamma^3$. The SU(2) group has three generators, which can be written as $\sigma_k/2$, where σ_k are the Pauli matrices. The three conserved charges are the three components $\{I_1, I_2, I_3\}$ of the so-called *weak isospin*. The left-handed components of the fermion fields are represented as weak isospin doublets, with total isospin $I = 1/2$ and $I_3 = (+1/2, -1/2)$. The right-handed components of the fermion fields are isospin singlets with isospin $I = 0$. The fundamental fermion fields in the model are then represented as:

$$\begin{pmatrix}\nu_e \\ e\end{pmatrix}_L, e_R, \qquad \begin{pmatrix}\nu_\mu \\ \mu\end{pmatrix}_L, \mu_R, \qquad \begin{pmatrix}\nu_\tau \\ \tau\end{pmatrix}_L, \tau_R, \tag{2.13}$$

$$\begin{pmatrix}u' \\ d'\end{pmatrix}_L, u'_R,\ d'_R \qquad \begin{pmatrix}c' \\ s'\end{pmatrix}_L, c'_R,\ s'_R \qquad \begin{pmatrix}c' \\ s'\end{pmatrix}_L, c'_R,\ s'_R \tag{2.14}$$

where the apices in the quark sector come from the mixing between weak and mass eigenstates (Section 2.1.1). Right-handed neutrinos are not predicted by the SM. The weak isospin and hypercharge of fermions are related by the equation

$$I_3 + Y = 2Q, \tag{2.15}$$

where Q is the electric charge of the particle. The gauge fields of the theory are a vector triplet coming from the SU(2) group $\mathbf{W}_\mu = \left(W^1_\mu, W^2_\mu, W^3_\mu\right)$ and an isospin singlet B_μ from the U(1) group.
The covariant derivative of the electroweak group is

$$D_\mu = \left(\partial_\mu + ig\frac{\sigma^k}{2}W^k_\mu + i\frac{g'}{2}B_\mu\right), \tag{2.16}$$

where g and g' are the coupling constants of the SU(2) and U(1) groups, respectively.
The experimentally observed charged fields $W^\pm$, which account for the charged current phenomenology of weak interactions, are obtained from the mixing of the first two components of the $\mathbf{W}_\mu$ triplet:

$$W^\pm_\mu = \frac{W^1_\mu \mp iW^2_\mu}{\sqrt{2}}. \tag{2.17}$$

The experimentally observed Z boson and photon fields, accounting for weak neutral currents and electromagnetic interactions, respectively, arise from the mixing of the W^3_μ and B_μ fields, instead. At

leading order in the couplings of the theory, the photon and Z fields can be expressed as:

$$\begin{pmatrix} A_\mu \\ Z_\mu \end{pmatrix} = \begin{pmatrix} \cos\theta_W & \sin\theta_W \\ -\sin\theta_W & \cos\theta_W \end{pmatrix} \begin{pmatrix} B_\mu \\ W^3_\mu \end{pmatrix}, \tag{2.18}$$

where the parameter θ_W is called *Weinberg angle*.

2.1.5 The Higgs sector

The boson fields in the Glashow-Weinberg-Salam model are required to be massless in order to preserve its gauge invariance. However, the experimental evidence shows that the $W^\pm$ and Z bosons are massive, with masses of 80 GeV and 91 GeV, respectively. Moreover, the fermion mass terms would also violate the gauge symmetry and cannot be included in a gauge theory. The Higgs mechanism of *spontaneous symmetry breaking* (SSB) allows to introduce mass terms for bosons and fermions in the SM in a dynamic way, without breaking the gauge symmetry. The fundamental idea is the introduction of a Lagrangian term that is invariant under gauge transformation but results in a vacuum state that does not respect the symmetry of the Lagrangian. The SM Lagrangian is extended to include a complex scalar $\mathrm{SU}(2)_L$ doublet, the Higgs field

$$\phi = \begin{pmatrix} \phi^+ \\ \phi^0 \end{pmatrix}. \tag{2.19}$$

The Lagrangian term for the Higgs field is

$$\mathcal{L} = (D^\mu \phi)^\dagger (D_\mu \phi) - V(\phi), \tag{2.20}$$

with Higgs potential $V(\phi)$ in the form

$$V(\phi) = -\mu^2 \phi^\dagger \phi + \lambda \left(\phi^\dagger \phi\right)^2, \tag{2.21}$$

where μ and λ are real parameters of the model. It is crucial for the mechanism that the potential $V(\phi)$ has a minimum for values of the field different from 0. This is achieved by the condition $\mu^2 > 0$. The minimum of the potential is realised by the condition $\left(\phi^\dagger \phi\right) = \mu^2/\lambda \equiv v^2/2$. The parameter v is the *vacuum expectation value* (VEV) of the Higgs field, and the relation $\langle 0 | \phi^\dagger \phi | 0 \rangle = v^2/2$ holds. Since the Higgs potential depends only on $\left(\phi^\dagger \phi\right)$, infinite vacuum states are possible. The actual realisation of a vacuum state breaks the symmetry of the vacuum without breaking the symmetry of the Lagrangian. Without loss of generality, we can choose the vacuum such that

$$\langle 0 | \phi | 0 \rangle = \frac{1}{\sqrt{2}} \begin{pmatrix} 0 \\ v \end{pmatrix}. \tag{2.22}$$

With this notion, the scalar field can be parametrised as

$$\phi = \frac{1}{\sqrt{2}} \exp\left(i \frac{\sigma^k}{2} \theta^k\right) \begin{pmatrix} 0 \\ v + h \end{pmatrix}, \tag{2.23}$$

where three degrees of freedom of the scalar field are absorbed by the Goldston bosons θ^k and one by the Higgs boson h. In order to retrieve the phenomenology associated to the Higgs Lagrangian term, the unitary gauge can be applied, setting $\theta^k = 0$. The Lagrangian will then lose its manifest invariance under the gauge group. The term giving rise to the gauge boson masses is

$$(D^\mu\phi)^\dagger(D_\mu\phi) = \frac{(v+h)^2}{8}\left[g^2\left(\left(W_\mu^1\right)^2 + \left(W_\mu^2\right)^2\right) + \begin{pmatrix} B_\mu & W_\mu^3 \end{pmatrix}\begin{pmatrix} g'^2 & -gg' \\ -gg' & g^2 \end{pmatrix}\begin{pmatrix} B_\mu \\ W_\mu^3 \end{pmatrix}\right] \tag{2.24}$$

After diagonalising the mass matrix for the W_μ^3 and B_μ bosons and mixing the W_μ^1 and W_μ^2 fields as in equation 2.1.4, we obtain:

$$(D^\mu\phi)^\dagger(D_\mu\phi) = \frac{(v+h)^2}{2}\left[\left(\frac{g}{2}\right)^2\left(\left(W_\mu^+\right)^2 + \left(W_\mu^-\right)^2\right) + \begin{pmatrix} A_\mu & Z_\mu \end{pmatrix}\begin{pmatrix} 0 & 0 \\ 0 & \frac{g^2+g'^2}{4} \end{pmatrix}\begin{pmatrix} A_\mu \\ Z_\mu \end{pmatrix}\right]. \tag{2.25}$$

We then have diagonal mass terms for all gauge bosons

$$m_W = \frac{gv}{2},\ m_Z = \frac{v}{2}\sqrt{g^2+g'^2},\ m_A = 0. \tag{2.26}$$

By comparing equations 2.25 and 2.18 one also obtains a leading order relation between the Weinberg angle and electroweak couplings:

$$\tan\theta_W = \frac{g'}{g} \tag{2.27}$$

The Lagrangian terms in 2.25 containing h and a gauge boson, represent the interactions between the Higgs boson and the gauge fields. The mass term for the Higgs boson comes from the $\mu^2\phi^\dagger\phi$ term in 2.21

$$m_H = \sqrt{2}\mu = \sqrt{2\lambda}v. \tag{2.28}$$

Higgs self-coupling terms arise from the $\lambda\left(\phi^\dagger\phi\right)^2$ part of the Higgs potential. Finally, fermion masses are included in the SM by adding gauge invariant Yukawa terms in the Lagrangian, in the form

$$\mathcal{L}_Y = -c_f\left(\bar\psi_L\phi\psi_R + \bar\psi_R\phi\psi_L\right) = -\frac{1}{\sqrt{2}}(v+h)c_f\left(\bar\psi_L\psi_R + \bar\psi_R\psi_L\right), \tag{2.29}$$

where the coefficients c_f are free parameters of the model. Fermion masses are

$$m_f = c_f\frac{v}{\sqrt{2}} \tag{2.30}$$

and their values are not predicted by the model. The Lagrangian term 2.29 also introduces a Higgs-fermion coupling $-c_f/\sqrt{2}h\bar\psi\psi = m_f/vh\bar\psi\psi$ proportional to the fermion mass. Figure 2.2 shows the fundamental vertices including the Higgs boson, including its coupling with fermions, with vector bosons, and self-couplings.

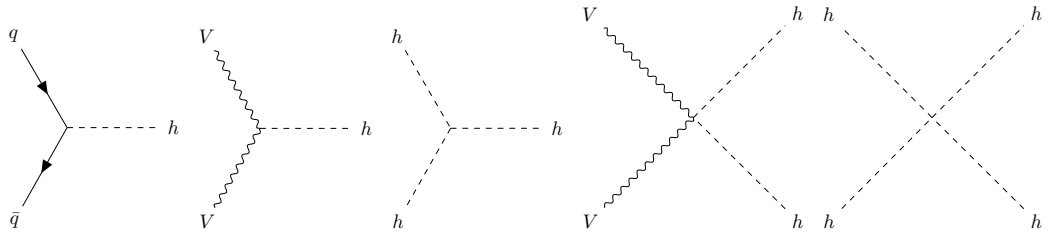

Figure 2.2: Fundamental vertices for Higgs boson interactions, with $V = W^{\pm}, Z$

2.2 Production and Decay of Top Quarks in the SM

Within the SM, top quarks can be produced via the strong and the weak interactions, while only the weak interaction determines their decay into lighter particles, as it is the only one that can change flavour. A comprehensive description of the phenomenology of top quarks can be found in Ref. [23].

2.2.1 Pair production of top quarks at hadron colliders

The dominant production mechanism for top quark pairs at hadron colliders is via the strong interaction. A precise estimation of the SM $t\bar{t}$ production is of the utmost importance for the search presented in this thesis, even more so considering the complexity of the expected signal process, which interferes with the SM expectation instead of just producing an excess of events, like in most searches (section 2.4.5).

The SM production of $t\bar{t}$ pairs from a proton-proton pp interaction is regulated by two components: a hard-scattering process between two partons i and j in the colliding protons, happening at a momentum transfer scale Q high enough that perturbative QCD is applicable; the parton-level composition of protons, probed at the momentum scale Q. The parton-level composition of protons, at a momentum scale Q, is described by means of *parton distribution functions* (PDFs) $f_i(x, Q^2)$, which represent the probability density for a parton i in a proton probed at the scale Q to carry a fraction x of the longitudinal momentum of the proton. It is a fundamental property of QCD that the high-momentum, short-distance component of the interaction, which corresponds to the hard-scattering process, can be *factorised* from the long-distance component, related to the PDFs of the hadrons. The two components can be determined separately, the first perturbatively, the second via dedicated measurements. A comprehensive summary of factorisation theorems in QCD can be found in Ref. [24].

The cross-section for $t\bar{t}$ production in a pp collision at a centre-of-mass energy s is

$$\sigma_{pp\to t\bar{t}X}\left(s, m_{\text{top}}\right) = \sum_{ij} \int_{(2m_{\text{top}})^2}^{s} d\hat{s} \quad L_{ij}\left(\hat{s}, \mu_f\right) \hat{\sigma}_{ij}\left(\hat{s}, m_{\text{top}}, \alpha_S(\mu_r), \mu_f\right) \tag{2.31}$$

where:

- $\hat{s}$ is the squared centre-of-mass energy of the two initial-state partons;
- L_{ij} are parton-parton luminosity factors, which account for the probability of the initial-state partons to have a center-of-mass energy of $\sqrt{\hat{s}}$, and depend on the PDFs as described in[25];
- μ_r and μ_f are renormalisation and factorisation scales, which are arbitrary scales used to remove divergencies in the calculation of physics observables.

The renormalisation scale μ_r is introduced in renormalisation theory to separate ultra-violet divergent terms in the perturbative expansion of scattering amplitudes from the finite terms, in a process called regularisation. The factorisation scale μ_f determines the separation between the short-distance, hard scattering process and the long-distance component in the factorisation of the cross-section in Eq. 2.2.1. Both scales are in principle arbitrary and the values of physics observables, calculated as the full sum of a perturbative series do not depend on them. However, at a finite perturbative order, a residual dependence on the scale remains, and their values are chosen to minimise the dependence of observables on them. A common choice is $\mu_r = \mu_f = Q$. A systematic uncertainty on the cross-section is defined by varying the two scales independently by factors of 0.5 and 2 to account for this arbitrary choice (see Section 6.8).

The PDFs are obtained by parametrising them at a low momentum scale Q_0 and performing a series of measurements to fit the values parameters. Typical datasets to do this come from $e - p$ deep inelastic scattering at the HERA experiment at DESY, but additional measurements from $p - p$ collisions at Tevatron and LHC have extended the reach of the fits to higher values of x. Using DGLAP equations [26–28], the PDFs are evolved to higher momentum scales. Different datasets can be used for this procedure, as well as different parametrisations. Different PDF choices are considered to build systematic uncertainties on the $t\bar{t}$ cross-section.

Once the PDFs are known, the $t\bar{t}$ cross-section can be calculated perturbatively. At leading order (LO), only gg- or $q\bar{q}$-initiated, $2 \to 2$ processes contribute to the cross-section. Figure 2.3 shows the LO Feynman diagrams for SM $t\bar{t}$ production. Due to the behaviour of PDFs at the TeV scale,

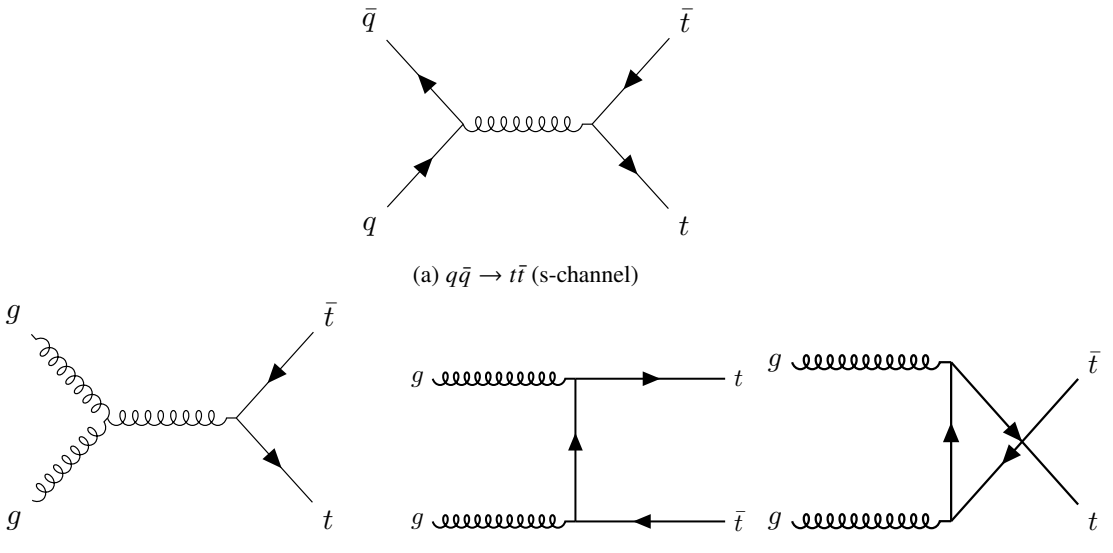

(a) $q\bar{q} \to t\bar{t}$ (s-channel)

(b) $gg \to t\bar{t}$ (s-channel)

(c) $gg \to t\bar{t}$ (t-channel)

(d) $gg \to t\bar{t}$ (u-channel)

Figure 2.3: LO Feynman diagrams for SM $t\bar{t}$ production at hadron colliders.

gg-initiated production of $t\bar{t}$ pairs dominates at the LHC.

2.2.2 Top quarks decays

Top quarks decay via weak interactions only and, thanks to their mass of 172.69 ± 0.30 GeV [23], they can decay into a real W boson and a down-type quark from any of the three generations. The

branching fractions of the decays $t \to Wb$, $t \to Ws$ and $t \to Wd$ are determined by the CKM matrix. Due to the hierarchical structure of the matrix, the $t \to Wb$ is completely dominant, accounting for more than 99% of top decays [23].

Thanks to its high mass, the top quark also has a decay width of 1.42 GeV [23], significantly larger than the hadronisation scale ($\sim 10^2$ MeV), meaning that it decays before top-flavoured bound states are formed.

The W boson from the decay of the top quark can decay into a pair of quarks or into a lepton and its corresponding neutrino. Taking into account that quarks exist in three colours, the branching fraction of the decay $W \to bq'\bar{q}$ is $\sim 67\%$, while the branching fractions of $W \to bl\nu_\ell$ are $\sim 11\%$ for each lepton flavour $l = e, \mu, \tau$ [23].

The decay of a $t\bar{t}$ pair can be classified into three categories, based on the decay of the two W bosons:

- **Fully hadronic** (or full-had): both W bosons decay hadronically, forming jets;
- **Single Lepton** (or one-lep): one W boson decays hadronically, while the other decays leptonically;
- **Dilepton** (or dilep): both W bosons decay leptonically.

The branching fractions for the above-mentioned decay modes, along with the resulting final states are summarised in table 2.1. From an experimental point of view, it is convenient to not consider the

Decay mode	Final state	BR (%)
Fully hadronic	$(q'\bar{q}b)(q'''\bar{q}''\bar{b})$	45.7
One-lepton	$(l^+\nu_l b)(q'''\bar{q}''\bar{b})$ or $(q'\bar{q}b)(l^-\bar{\nu}_l\bar{b})$	43.8
Dilepton	$(l^+\nu_l b)(l^-\bar{\nu}_l\bar{b})$	10.5

Table 2.1: Branching fractions of $t\bar{t}$ decay modes, with their respective final states, as reported in [23]. In the modes including leptons, all flavours $l = e, \mu, \tau$ are included.

decays involving τ leptons as regular members of the one-lep category. This is due to the peculiar challenges of the τ reconstruction, which cannot be measured directly in the detector, due to their short lifetime and decay length. τ leptons can decay into a lighter lepton and two neutrinos, or they can decay hadronically into a neutrino and one or three pions.

In many physics analyses, $t\bar{t}$ decays involving hadronically decaying τ leptons, are not considered as part of the one-lepton category. The analysis presented in this thesis is one of those. It is important to note that $t\bar{t}$ decays involving $\tau \to \nu_\tau \ell \nu_\ell$ decays, with $\ell = e, \mu$ are included in the one-lepton category.

2.3 Problems and limitations of the Standard Model

The SM accurately describes a vast number of subnuclear phenomena, and has been very successful in predicting new particles, such as the top quark and the Higgs boson. However, it is widely considered an incomplete theory, due to a number of observations that are not adequately or completely explained within its context and due to some unsatisfactory features. The following section gives an overview of some of the shortcomings of the SM.

Gravity

Despite accurately describing three of the currently known four fundamental interactions, the SM fails to include the gravitational interactions in a coherent QFT. The quantisation of gravity is a task which has not yet been achieved; instead, the theory of general relativity, which is not a quantum theory, is used to describe the universe at large scales, in a completely separate framework from our description of the universe at subnuclear scales.

Dark Matter

It is a well-established fact since about 90 years, that the amount of electromagnetically interacting matter in the universe is not enough to explain its dynamics at galactic and large scales. In the 1930s, Fritz Zwicky observed that the gravitational masses of the galaxies in the Coma cluster, significantly differ from what can be inferred from their luminosity [9]. In the 1970s, Vera Rubin made a similar observation [10], measuring the rotational velocities of spiral galaxies as a function of the distance from their centre, and concluded that the mass from electromagnetically interacting matter is not enough to account for the observed velocities in the tails of the galaxy. The existence of *non-luminous, non-absorbing* matter, known as *Dark Matter* (DM) was then hypothesised to explain the observations. Numerous other observations have been since made that support the existence of dark matter, such as anisotropies in the Cosmic Microwave Background (CMB) [11] and observations of gravitational lensing [12]. To our current understanding, DM should account for about 85% of the matter content in the universe [13].
Historically, non-luminous particles such as neutrinos were considered as DM candidates, but experimental evidence shows they are not suited to account for the observed effects. Not only they are not massive and abundant enough to explain the observation at the galactic scale, but they are also too light to reproduce the anisotropies in the CMB.
Dark matter searches are performed both at particle accelerators and in astroparticle experiments. The Higgs sector, or possibly an extension of it, is often considered a promising portal to DM, also thanks to the Higgs coupling to particles via their mass.

Matter-Antimatter asymmetry

Based on our current cosmological knowledge, at the Big Bang, there was an equal amount of matter and antimatter in the universe. However, the universe as we know it today is completely dominated by matter. It is also not possible that there are portions of the universe dominated by matter, because the matter-antimatter annihilation at the interface between the areas, would produce visible light. This means that there must have been a process in the early universe that created the asymmetry we see today. The necessary conditions to create the matter-antimatter asymmetry are known as Sakharov conditions [29] and are:

- Baryon number violating processes;
- Charge (C) and Charge-Parity (CP) violation;
- Processes out of thermal equilibrium.

Of the three, the first and third are realised in the Baryogenesis phase of the early universe. CP violation is possible in the SM weak sector, thanks to non-zero phases in the CKM matrix, but the measured amount of CP violation in the CKM sector is not enough to explain the extent of the asymmetry.

The strong CP problem

The QCD Lagrangian can in principle contain as CP-violating term in the form $\vartheta g_S^2/(32\pi^2) G^a_{\mu\nu}\tilde{G}^{\mu\nu,a}$, where $\tilde{G}^{\mu\nu,a}$ are the Hodge duals of the QCD tensors. However, the lack of experimental evidence for CP-violating processes in QCD, suggests that the ϑ parameter is very close to, if not equal, to 0. The fine-tuning of this parameter finds no justification in the SM. A possible way to dynamically produce this effect is the Peccei-Quinn mechanism [30, 31], which would also result in the existence of a pseudoscalar particle beyond the SM, the *axion*. Axion-like particles would also be good candidates for dark matter.

Too many parameters

The SM contains a large number of free parameters, which are not obtained by first principles, but need to be measured experimentally. Among them are the masses of the twelve fermions (and subsequently their Yukawa couplings with the Higgs field), the parameters of the CKM matrix, the Higgs boson mass and the coupling constants of the fundamental interactions. This large number of free parameters suggests that the SM is not a complete theory, but that is rather part of a more complete theory, where the SM can be deducted from fewer postulates.

The hierarchy problem

The experimental observation of the mass of the SM Higgs boson $m_h \approx 126$ GeV creates a challenge in possible extensions of the SM. The mass of the Higgs boson receives radiative corrections due to fermion loops as in the Feynman diagram in Figure 2.4. The loop integral appearing in the calculation

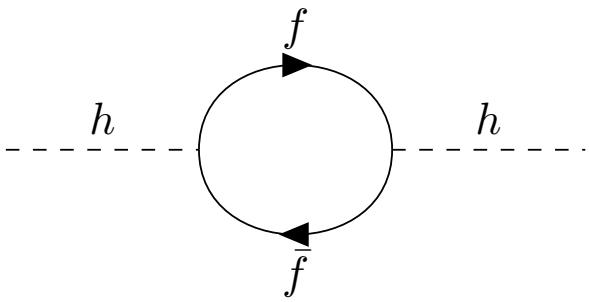

Figure 2.4: Radiative correction to the Higgs boson mass from a fermion loop.

of the correction is divergent, however one can regularise the divergence by integrating up to a cut-off energy scale Λ. The radiative correction to the Higgs-boson mass due to a fermion loop is

$$\delta m_h^2 \sim \lambda_f^2 \Lambda^2 + o\left(\Lambda^2\right), \tag{2.32}$$

where λ_f is the Yukawa coupling of the Higgs boson to the fermion. This is a quadratic dependence on the cut-off scale, which is very strong compared to the logarithmic dependence one obtains for the radiative corrections to fermion masses.
The quadratic divergence of the radiative correction as a function of the cut-off scale is in principle not a problem, as the SM is a renormalisable theory. However, we know that the SM is not successful in describing interactions at the Planck energy scale $\Lambda_P \sim 10^{19}$ GeV, where the quantum behaviour of gravity becomes relevant. If we accept the SM as valid until the Planck scale, we should be able to interpret it as an effective low-energy theory included in a more fundamental high-energy theory. In the context of the fundamental high-energy theory, the physical mass of the Higgs boson is

$$m_h^2 \,(\text{phys}) \approx m_h^2 + C\Lambda_P^2, \tag{2.33}$$

where C is a constant term depending on the coupling of the Higgs to the fermion f. Since m_h (phys) ≈ 126 Gev and $\Lambda_P \sim 10^{19}$ GeV, if we use the high-energy theory to make predictions at the TeV scale, we need extreme fine-tuning between the parameters of the model to obtain the measured mass of the Higgs boson. This result makes the high-energy theory very unsatisfactory in terms of naturalness, and is known as the *hierarchy problem*. The hierarchy problem hints toward the fact that the SM ceases to be valid at lower energy than the Planck scale and gives a guide towards BSM theories that do not present this naturalness problem.

2.4 Extending the scalar sector

There are numerous possible extensions of the SM that address one or several of its open questions; in the following, a few examples are provided in which the scalar sector is extended.
Extensions of the scalar sector are common in many theories beyond the Standard Model (BSM), such as Supersymmetry (SUSY) [32–37] and ALPs [38] dark matter models. Extensions of the scalar sector could also produce additional sources of CP violation, which are needed to explain the matter-antimatter asymmetry. When extending the scalar sector of the SM, one has to be careful not to violate experimental and theoretical constraints.
One such constraint is the observation that the parameter

$$\rho = \frac{m_W^2}{m_Z^2 \cos^2\theta_W}$$

is experimentally measured to be compatible with 1. In a theory with N scalar multiplets ϕ_i with weak isospin I_i, weak hypercharge Y_i and VEV v_i, at tree level

$$\rho = \frac{\sum_{i=1}^{N}\left[I_i(I_i+1) - \frac{1}{4}Y_i^2\right]v_i}{\frac{1}{2}Y_i^2 v_i}. \tag{2.34}$$

One can easily verify that in the SM, which only includes a single Higgs doublet with$I = 1/2$ and $Y = 1$, the equality $\rho = 1$ is trivially verified at tree level. Any SM extension including SU(2) singlets with $Y = 0$or SU(2) doublets with $Y = \pm 1$ also satisfies the constraint at tree level.
Another constraint is given by *Flavour-Changing Neutral Currents* (FCNC). Those are experimentally

extremely suppressed and not allowed at tree level in the SM. With an extended Higgs sector, FCNCs are not automatically suppressed, so conditions on the model need to be applied to reproduce the experimentally observed suppression of such processes.
Finally, the unitarity of the scattering amplitude of longitudinal vector bosons and of fermions into longitudinal vector bosons has to be ensured. This is achieved in the SM via the coupling of the Higgs boson to vector bosons and fermions. In models with an extended Higgs sector, it is not necessary that a single scalar boson satisfies the unitarity constraints, but the sum of the scalar interactions with vector bosons and fermions needs to satisfy this condition.

2.4.1 Type-II 2HDMs

Two Higgs Doublets Models (2HDMs) are one of the simplest extensions of the SM Higgs sector that satisfy the above-mentioned constraints and predict the existence of two instead of one scalar $\mathrm{SU(2)_L} \times \mathrm{U_1}$ doublet. If we impose CP conservation and a softly broken Z_2 symmetry[1] in the form $(\phi_1 \to \phi_1, \phi_2 \to -\phi_2)$, then the most general potential for the two Higgs doublets ϕ_1 and ϕ_2 with Y=1 is:

$$\begin{aligned} V = & m_{11}^2 \phi_1^\dagger \phi_1 + m_{22}^2 \phi_2^\dagger \phi_2 - m_{12}^2 \left(\phi_1^\dagger \phi_2 + \phi_2^\dagger \phi_1 \right) + \frac{\lambda_1}{2} \left(\phi_1^\dagger \phi_1 \right)^2 + \frac{\lambda_2}{2} \left(\phi_2^\dagger \phi_2 \right)^2 + \\ & \lambda_3 \phi_1^\dagger \phi_1 \phi_2^\dagger \phi_2 + \lambda_4 \phi_1^\dagger \phi_2 \phi_2^\dagger \phi_1 + \frac{\lambda_5}{2} \left[\left(\phi_1^\dagger \phi_2 \right)^2 + \left(\phi_2^\dagger \phi_1 \right)^2 \right], \end{aligned} \tag{2.35}$$

where all parameters are real. The VEV of the two fields are, respectively:

$$\langle \phi_1 \rangle = \begin{pmatrix} 0 \\ \frac{v_1}{\sqrt{2}} \end{pmatrix}, \quad \langle \phi_2 \rangle = \begin{pmatrix} 0 \\ \frac{v_2}{\sqrt{2}} \end{pmatrix}, \tag{2.36}$$

where $v_1^2 + v_2^2 = v^2$ to obtain the SM masses of the W and Z bosons. The two complex Higgs doublets have eight degrees of freedom in total. After symmetry breaking, three degrees of freedom are used to generate the longitudinal degrees of freedom of the massive $W^\pm$ and Z bosons, and the remaining five produce Higgs bosons, two charged ones $H^\pm$, two electrically neutral scalars h and H, and one electrically neutral pseudoscalar A. The free parameters of the model are:

- the ratio $\tan\beta = \frac{v_1}{v_2}$ of the VEVs of the Higgs fields;
- the mixing angle α between the two scalar Higgs bosons;
- the four masses of the Higgs bosons (the two charged ones are degenerate in mass);
- the scale of the Z_2 symmetry breaking m_{12}.

Some of these parameters are either determined by the low energy phenomenology of the SM Higgs boson, or constrained by measurements of the SM Higgs production and decays. For the purposes of this thesis, we set $m_h = 125$ GeV, $\cos(\beta - \alpha) = 0$, $m_{12}^2 = \frac{m_A^2 \tan\beta}{1+\tan^2\beta}$; this is known as the SM-like limit of 2HDM and identifies the lighter scalar Higgs h with the SM one. There is strong experimental evidence

[1] The reason for the introduction of this symmetry will become apparent once the Yukawa couplings are introduced.

for requiring $\cos(\beta - \alpha) = 0$, coming from precision measurements of the Higgs boson production and decay [39]. Figure 2.5 shows the regions of the $(\cos(\beta - \alpha), \tan\beta)$ plane excluded by fits to the measured Higgs boson production and decays. Only a narrow region around $\cos(\beta - \alpha) = 0$ is still allowed. The relation between the masses of the heavy scalar and pseudoscalar is also constrained

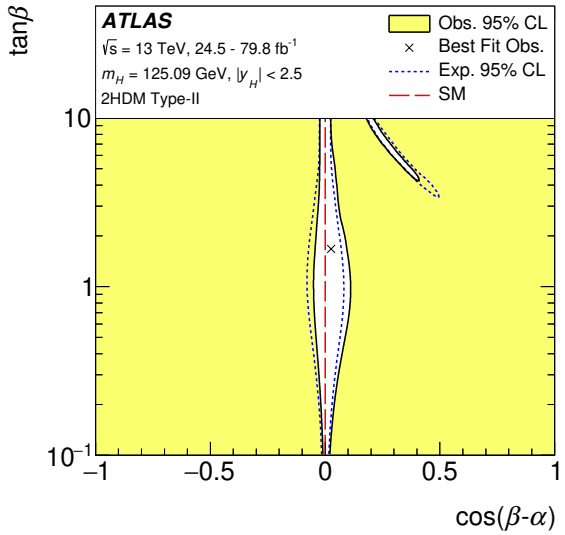

Figure 2.5: Regions of the $(\cos(\beta - \alpha), \tan\beta)$ plane excluded by fits to the measured Higgs boson production and decays.

by electroweak precision measurements, e.g. the measurement of ρ [16]. In order to satisfy this constraint, the choice $m_A = m_H$ is made for the 2HDM benchmark in the search presented in this thesis. The Yukawa-coupling sector of 2HDMs, which couples the Higgs fields to fermions, presents an additional complication compared to the SM. In the SM, the most general realisation of a Yukawa coupling between the Higgs field and the fermions does not allow for FCNCs at tree level, which is a property very well supported by the experimental evidence for the suppression of such currents. However, in 2HDMs, FCNCs are in principle allowed at tree level, if one constructs the most general Lagrangian for the interactions between fermions and the Higgs sector. To achieve the experimentally required suppression of FCNCs in 2HDMs, two possible strategies are:

- Only allow Yukawa couplings between the fermions and a single Higgs doublet (**Type-I**);
- Allow the RH components of up-type quarks to couple to a single Higgs doublet and the RH components of down-type quarks to couple only to the other (**Type-II**).

In this thesis, only Type-II 2HDMs are considered. The Type-II condition is automatically achieved by requiring invariance under the Z_2 symmetry.

2.4.2 2HDM+a

Various DM models postulate a scalar or pseudoscalar mediator between the SM sector and DM. In so-called *simplified models of DM* [40–42], only a (pseudo)scalar mediator and DM are postulated,

in addition to the SM. The 2HDM+a benchmark [16] extends these simplified models to a simple, UV-complete model with a richer phenomenology, by adding a DM mediator in the form of a pseudoscalar singlet field a to a 2HDM. The model predicts a single DM particle χ. In practice, the Lagrangian in equation 2.4.1 is extended to include the term

$$\mathcal{L}_a = \frac{1}{2}m_a^2 a^2 + a(ib_a\phi_1^\dagger\phi_2 + \text{h.c.}) + a^2(\lambda_{a_1}\phi_1^\dagger\phi_1 + \lambda_{a_2}\phi_2^\dagger\phi_2), \tag{2.37}$$

where the parameter b_a is positive to guarantee CP conservation. The Dark Matter mediator a mixes with the 2HDM pseudoscalar A via the mixing angle θ. It couples to the Dark Matter fermion with a simple Yukawa-like coupling.

The 2HDM+a model has fourteen free parameters. However, similarly to the generic 2HDM, the parameter space of the 2HDM+a model is constrained by electroweak precision measurements [43, 44] and by flavour constraints. In order to satisfy electroweak and flavour constraints [16], in this thesis, the requirement $m_A = m_H = m_{H^\pm}$ is imposed. The LHC DM working group provides a set of benchmarks [45] obtained by varying five of the fourteen free parameters of the model (m_a, m_A, m_χ, $\tan\beta$, $\sin\theta$), while the others are fixed by the aforementioned constraints and measurements. In the search presented in this thesis, constraints are derived in the $m_a - \tan\beta$ plane, where the analysis is expected to give the strongest contribution to expand existing constraints.

2.4.3 hMSSM

A special case of type-II 2HDM considered in this thesis is the Higgs sector of the hMSSM [15]. This is a minimal Supersymmetric extension of the SM [46–50] where the lightest Higgs boson is identified with the SM Higgs, with a mass of 125 GeV. In the hMSSM, the Higgs sector only contains two free parameters, i.e. the mass of the pseudoscalar A and $\tan\beta$. The mass of the scalar heavy Higgs H is fixed by the mass of the pseudoscalar. For $m_A \approx 2m_t$, the scalar H is around 40 GeV heavier than the pseudoscalar A, while the mass difference reduces to $\Delta m \sim 10$ GeV at $m_A \approx 1$ TeV.

2.4.4 Generic (pseudo)scalar model

Additional scalars in the SM can be introduced also via effective theories which just specify the coupling of the new (pseudo)scalars with SM particles. In this thesis, results are interpreted also in terms of a benchmark model of this kind, where a BSM (pseudo)scalar couples only to top quarks, via Lagrangian terms in the form:

$$\mathcal{L}_{Y,H} = -g_{Ht\bar{t}}\frac{m_t}{v}\bar{t}tH, \quad \mathcal{L}_{Y,A} = ig_{At\bar{t}}\frac{m_t}{v}\bar{t}\gamma^5 tA. \tag{2.38}$$

This effective model does not predict a relationship between the widths and couplings of the (pseudo)scalars, differently from 2HDM-like models, where the width is a function of the other parameters, and cannot be changed independently. This allows for a more model-agnostic interpretation of the results of the search presented in this thesis compared to 2HDMs.

2.4.5 Production and decay of heavy Higgs bosons at hadron colliders

The main production mechanism of Higgs bosons at hadron colliders is *gluon-gluon fusion* via a heavy quark loop. This accounts for about 88% of SM Higgs bosons production at LHC [23]. In type-II 2HDMs, the gluon-gluon-initiated production of (pseudo)scalars at hadron colliders is also dominant, with different contributions to the heavy-quark loop depending on the value of $\tan\beta$. In addition, since the coupling with top quarks is dominant, the decay into a $t\bar{t}$ pair is favoured. The dominant production/decay chain of a heavy Higgs in this scenario is $gg \to A/H \to t\bar{t}$ and is represented by the diagram in Figure 2.6. Comparing with the LO diagrams for SM production of $t\bar{t}$ pairs at hadron

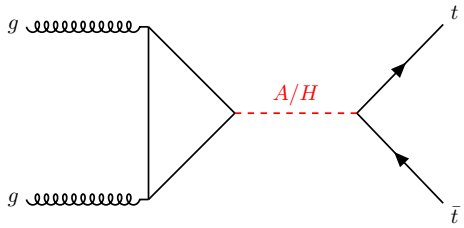

Figure 2.6: Feynman diagram at LO of the main production/decay chain of a heavy Higgs boson in a Type-II 2HDM

colliders in fig 2.3, is is evident that the two processes must interfere, given they share the same initial and final states. In fact, the cross-section for gluon-gluon initiated $t\bar{t}$ production at LHC, including the contribution from heavy BSM (pseudoscalars) would be written as:

$$\sigma(gg \to t\bar{t}) \propto \left|\mathcal{M}_S\right|^2 + 2 \cdot \mathrm{Re}\left(\mathcal{M}_S \mathcal{M}_B^*\right) + \left|\mathcal{M}_B\right|^2, \tag{2.39}$$

where $\mathcal{M}_S$ and $\mathcal{M}_B$ are the BSM signal and SM $t\bar{t}$ background contributions to the scattering amplitude, respectively. The cross-section in Equation 2.4.5 has a contribution due to the signal process only, a contribution from the background process only, and a contribution from the signal-background interference. This results in a characteristic peak-dip structure in the mass spectrum of the $t\bar{t}$ system, as exemplified in Figures 2.7 and 2.8 for the Type-II 2HDM benchmark and generic (pseudo)scalar benchmark, respectively. Here the contribution purely from the SM background is subtracted. It is interesting to notice that, in the generic (pseudo)scalar model, at large values of the coupling $g_{A/Ht\bar{t}}$, the peak-dip structure in the $m_{t\bar{t}}$ spectrum changes into a peak-peak structure, which is resonance-like close to the mass of the BSM (pseudo)scalar state.

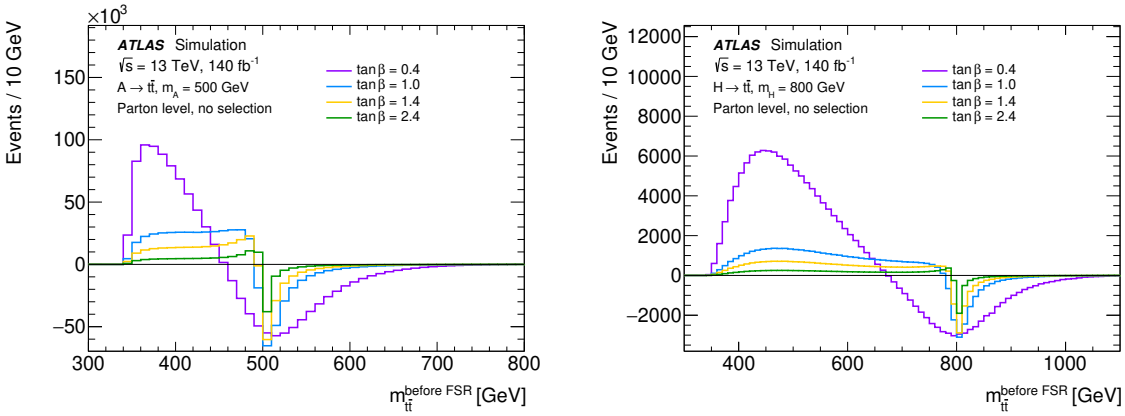

(a) $m_A = 500$ GeV (b) $m_H = 800$ GeV

Figure 2.7: Signal-plus-interference distributions in $m_{t\bar{t}}$ at parton level before final state radiation for (a) a single pseudoscalar A with mass $m_A = 500$ GeV and (b) a single scalar H with mass $m_H = 800$ GeV, for various values of $\tan\beta$ in a type-II 2HDM.

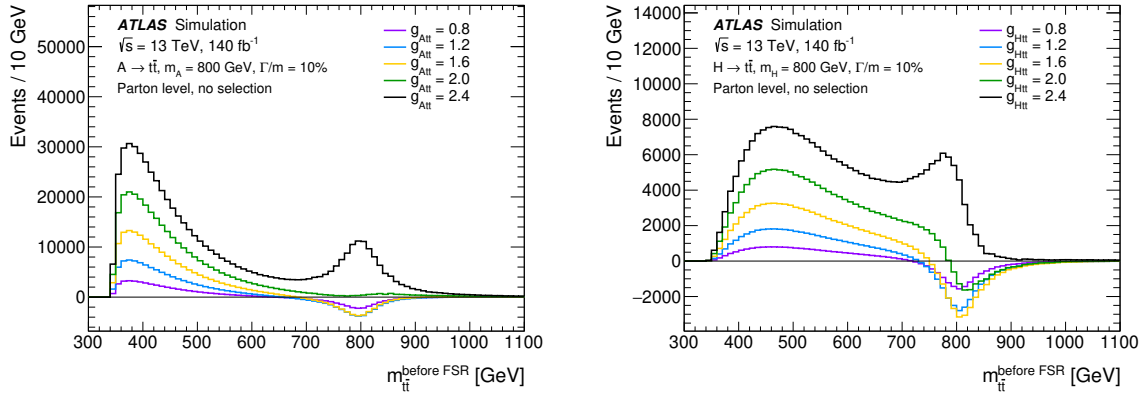

(a) $m_A = 800$ GeV (b) $m_H = 800$ GeV

Figure 2.8: Signal-plus-interference distributions in $m_{t\bar{t}}$ at parton level before final state radiation for (a) a single pseudoscalar A with mass $m_A = 800$ GeV and (b) a single scalar H with mass $m_H = 800$ GeV, for various values of $g_{A/Ht\bar{t}}$ in the generic (pseudo)scalar model.

CHAPTER 3

The ATLAS experiment at the LHC

The data for the analysis presented in this thesis is collected with the ATLAS experiment [51], at CERN. CERN is an international research facility, currently counting 23 states among its members. At the time of its founding, CERN activities were focused on nuclear physics, while today its main area of research is particle physics. CERN is home of the most powerful hadron collider in the world, the Large Hadron Collider (LHC). The data used in this thesis was collected by the ATLAS experiment at LHC [52], during its Run-2 operation period. This chapter is dedicated to the description of the LHC, and ATLAS experiment, as they were during the Run-2 data-taking, with additional information on their upgrades.

3.1 The Large Hadron Collider (LHC)

The LHC is situated at CERN within an underground tunnel with a circumference of approximately 27 km, at depths ranging from 50 to 100 m, and is the biggest and most powerful particle accelerator in the world. Within this collider, during the Run-2 operation period, two proton beams were accelerated to energies around 6.5 TeV through separate vacuum tubes, colliding at four designated points around the ring housing particle detectors. The LHC also accelerates heavy ion beams in dedicated data-taking periods. The beams are segmented into bunches of about 10^{11} protons and maintained within a circular trajectory by radiofrequency cavities and superconducting electromagnets. To achieve superconductivity, the magnets necessitate cooling to 1.85 Kelvin and are thus linked to an extensive liquid helium distribution system. The collider encompasses two types of magnets: dipole magnets, responsible for maintaining the circular path of the beam, and quadrupole magnets, utilised for beam focusing.

The LHC is the final component in a sequence of accelerators that bring protons to increasingly higher energies. Figure 3.1 provides a schematic overview of the CERN accelerator complex along with the associated experiments. The process begins with a source of protons: a container of hydrogen gas. Protons are generated by ionising hydrogen atoms using an electric field. Initially, the protons undergo acceleration to 50 GeV in the first component of the complex, known as *Linac2*, which is a linear accelerator. Subsequently, the beam is introduced into the Proton Synchrotron Booster (PSB), bringing its energy to 1.4 GeV, followed by the Proton Synchrotron (PS), further increasing the energy to 25 GeV. The Super Proton Synchrotron (SPS) then accelerates the protons to 450 GeV before they enter the LHC.

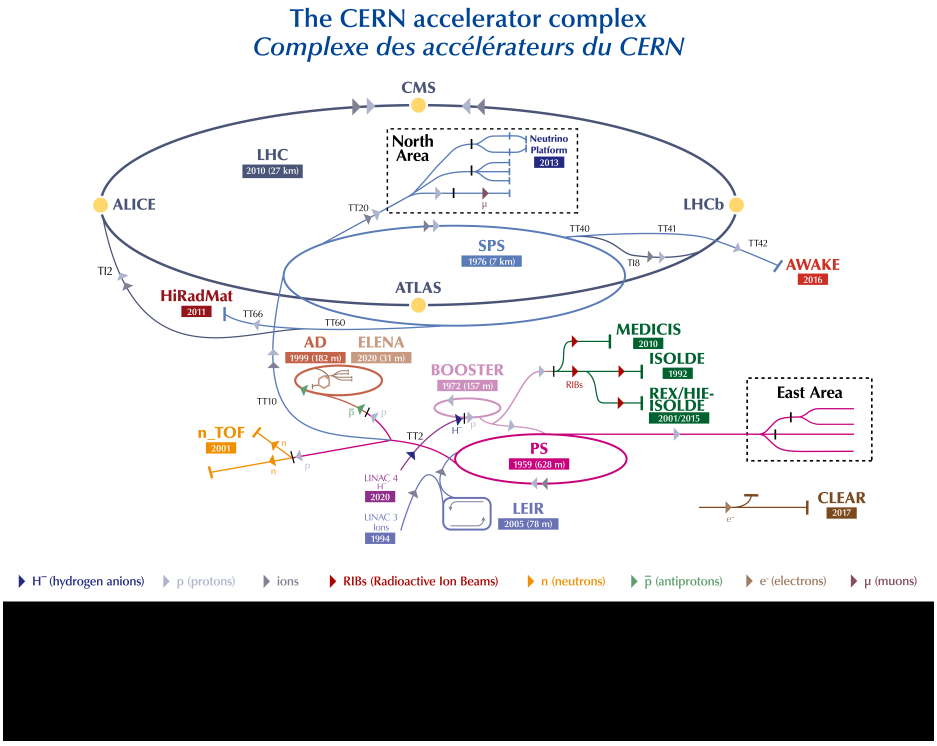

Figure 3.1: A schematic overview of the CERN accelerator complex along with the associated experiments [53].

The four biggest experiments located at the LHC are **ATLAS**, **CMS** [54], **ALICE** [55], and **LHCb** [56]. Of the four, ATLAS and CMS are general purpose experiments, which initially served for the discovery of the Higgs boson, and still have a rich physics programme focused on precision measurements of SM parameters and on the discovery of physics beyond the SM .

3.1.1 LHC Runs

LHC operation periods, and consequently the data collection periods of its experiments, are divided in so-called *Runs*, with extended shutdown periods in between (*Long shutdowns*), for repairs and upgrades.

The first operation period, Run-1, lasted from 2010 to 2012. During Run-1, proton beams were collided at a centre-of-mass energy of $\sqrt{s} = 7$ TeV until 2012, when the collision energy was increased to 8 TeV. The total integrated luminosity delivered by LHC in this period amounted to 22.8 fb^{-1}, of which 21.3 fb^{-1} were recorded by ATLAS. Not all recorded events pass the quality requirements necessary to use them in physics analyses. In order for an event to be classified as *good for physics*, all ATLAS sub-detectors must be functional, and additional conditions on the state of the sub-detectors must be satisfied, so that good data quality can be ensured. The total integrated luminosity recorded by ATLAS and labelled as good for physics in Run-1 is 20.3fb^{-1}.

The second operation period, Run-2, lasted from 2015 to 2018. For Run-2, the LHC was upgraded to provide a centre-of-mass energy of $\sqrt{s} = 13$ TeV. The total integrated luminosity registered by ATLAS and good for physics in Run-2 is 140.1 fb^{-1} [57].

The third operation period, Run-3, started in 2022, is still in progress, and will last until 2025. For Run-3, the collision energy was increased to 13.6 TeV.

The instantaneous luminosity delivered by the LHC increased in each run and with it so increased the *pile-up* in its experiments. The term pile-up is used to refer to the situation in which multiple independent collisions occur within the same or nearby bunch crossings at a particle detector. Pile-up in LHC experiments is made of two components: *in-time* and *out-of-time*. The in-time component is due to multiple collisions in the same bunch-crossing. The out-of-time pile-up component in an event is due to collisions in previous or following bunch crossings, which have an effect on the current event due to the finite time of signal formation and the finite duration of a signal in the detector. Figure 3.2 shows the luminosity-weighted distribution of the number of interactions per bunch crossing in the ATLAS detector, in its three operation periods. The curve relative to Run-3 is partial.

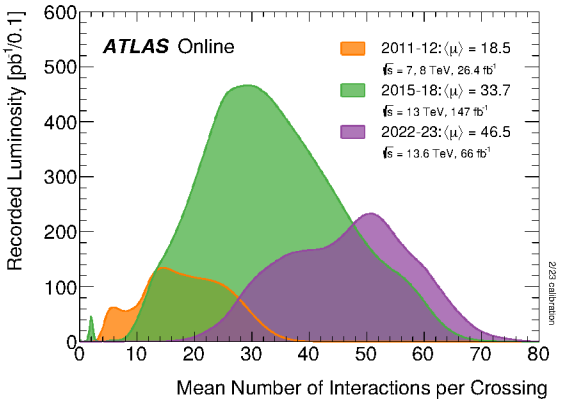

Figure 3.2: Luminosity-weighted distribution of the number of interactions per bunch crossing in the ATLAS detector. Taken from Ref. [58].

3.2 The ATLAS experiment

ATLAS is one of the four principal experiments situated at the LHC. It has a cylindrical symmetry and is the largest detector ever constructed for a particle collider with dimensions of 46 meters in length and a diameter of 25 meters, weighing 7000 tonnes. It is positioned within a cavern approximately 100 meters below ground near the primary CERN site, adjacent to the village of Meyrin in Switzerland.

The structure of the ATLAS experiment, depicted in Figure 3.3, features a cylindrical section called the *barrel*, surrounding the beam axis, flanked by *endcaps* designed to optimise particle detection in the forward region. The detector system encompasses nearly the entire solid angle around the interaction point (IP) through various layers of sub-detectors engineered to measure distinct properties of particles originating from the proton-proton (pp) collisions. Going from the innermost to the outermost components of ATLAS:

- The Inner Detector (ID) is designed to measure the momenta of charged particles and the positions in which a hard-scattering interaction took place or a decay happened (*vertices*).
- A solenoidal superconducting magnet generates a uniform magnetic field of 2 T along the beam

axis to aid the inner tracker. More precisely, it bends the charged-particle trajectories so that their momenta can be measured by reconstructing their curvature in the ID.

- The Electromagnetic (EM) Calorimeter is dedicated to the detection and measurement of the energy of the electromagnetic showers produced by photons and electrons.
- The Hadronic Calorimeter is used to detect and measure the properties of hadronic showers (*jets*) induced by the hadronisation of a single quark or gluon.
- An air-core superconducting toroidal magnet supplies a magnetic field with a strength of up to 4 T to the outermost sub-detector, the Muon Spectrometer.
- The Muon Spectrometer (MS), situated within the magnetic field generated by the toroidal magnet, serves to reconstruct the trajectory of muons.

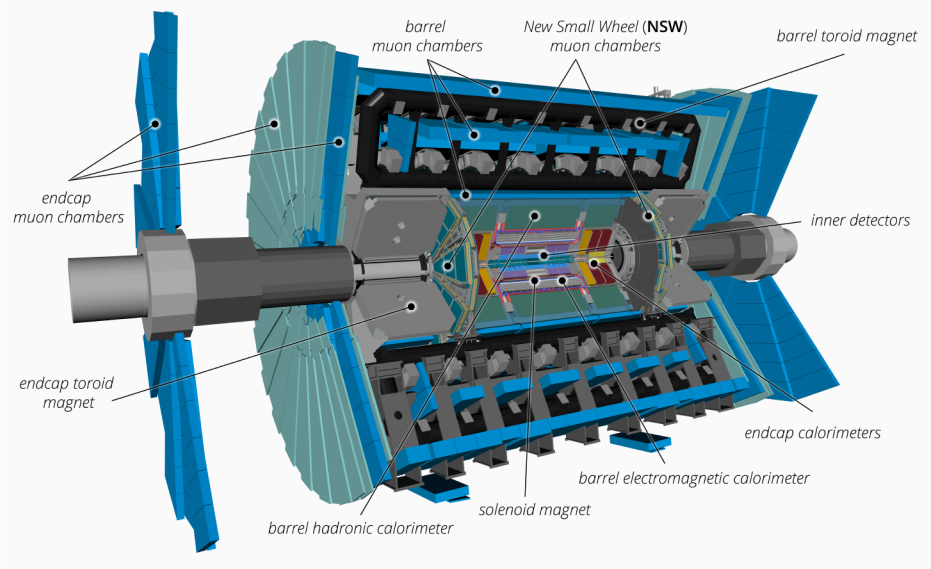

Figure 3.3: A digital rendering of the ATLAS experiment, from Ref. [59]. This rendering refers to the detector configuration used in Run-3, which differs from the Run-2 configuration in the MS, particularly in the Small Wheels (Section 3.2.5).

3.2.1 ATLAS coordinate system

ATLAS employs a Cartesian right-handed coordinate system centred at the nominal collision point. In this system, the z-axis aligns with the beamline, while the x-y plane is perpendicular to it, with the x-axis directed toward the centre of the LHC ring and the y-axis pointing upward. Alternatively, this reference frame can be represented in spherical coordinates by introducing the azimuthal angle $\phi \in [-\pi, \pi]$, which is zero along the x-axis and increases clockwise in the z direction, and the polar angle θ, measured relative to the positive z-axis.

A transformation of the polar angle θ yields the pseudorapidity η , which is typically used instead of θ:

$$\eta = -\ln\left[\tan\left(\frac{\theta}{2}\right)\right]. \tag{3.1}$$

The pseudorapidity is 0 in the $x-y$ plane, and increases in magnitude closer to the beam axis, with $|\eta| \to \infty$ for $\theta \to 0$. Differences in pseudorapidity are invariant under Lorenz boost in the z direction.

In the ultra-relativistic limit ($E \approx p$), commonly observed in high-energy physics experiments, the pseudorapidity approximates well the rapidity of a particle

$$y = \frac{1}{2}\ln\frac{E+p_z}{E-p_z}, \tag{3.2}$$

where E is the energy of the particle and p_z is its momentum component along the beam axis. Differences in rapidity are extensively used in jet algorithms (Section 5.4.1).

In physics analyses, a commonly used variable is the angular separation in the $\eta-\phi$ plane, denoted as ΔR and calculated as:

$$\Delta R = \sqrt{(\Delta\eta)^2 + (\Delta\phi)^2}. \tag{3.3}$$

3.2.2 The magnetic system

The ATLAS superconductive magnet system consists of a central solenoid (CS) and three superconducting toroids, with one centrally located and encompassing the barrel, and two positioned at opposite ends of the detector, in the endcap region. These superconducting toroids adopt an air-cored structure to minimise the impact of multiple scattering on momentum reconstruction.

The CS features an internal diameter of 2.4 meters, generating a magnetic field of approximately 2 T along the z-axis within the inner tracker region, peaking at 2.6 Tesla at the superconductor surface. This solenoidal field deflects particle tracks in the transverse plane, allowing a transverse momentum measurement by the ID.

Comprising two endcap toroids (ECT) and barrel toroids (BT), the toroidal magnetic system achieves peak magnetic field strengths of 3.9 Tesla and 4.1 Tesla for the BT and the ECT, respectively. Each toroid consists of eight rectangular coils, symmetrically arranged around the beam axis. The ECT coil system is rotated by 22.5 degrees relative to the BT system.

The toroidal system aims to provide an extensive lever arm for muon transverse momentum measurement. With ATLAS featuring two distinct magnetic fields, it enables independent measurements of muon momenta - one in the inner detector and another in the muon spectrometer. This dual measurement strategy ensures robust muon momentum resolution ranging from a few GeV to the TeV scale.

3.2.3 The Inner Detector

The ATLAS Inner Detector [60] is positioned closest to the interaction point among the sub-detectors. Given the high number and spatial density of particles produced at each collision at the LHC, and the presence of multiple interaction vertices due to pile-up, precision tracking and vertexing are essential for physical analyses in ATLAS. Thus, tracking detectors with high granularity are imperative to manage the immense track density produced at the LHC.

The ID comprises three distinct detector systems, embedded in the magnetic field generated by the solenoidal magnet. These three sub-detectors are:

- The Pixel Detector, a silicon detector with 80 million pixels occupying a $1.7\,\mathrm{m}^2$ area. The innermost barrel layer (IBL) [61] is made of pixels with a $50 \times 250\ \mu$m pitch, while all other layers have a pitch of $50 \times 400\ \mu$m, offering a spatial resolution of about $10 \times 115\ \mu\mathrm{m}^2$. Its two-dimensional segmentation in the $r - \phi$ plane and along the z direction enables precise position measurements with minimal ambiguity.

- The Semiconductor Tracker (SCT), a semiconducting detector comprising 8 layers of silicon microstrips in the barrel section and 8 disks in the endcap sections, with a $80\,\mu$m pitch. Adjacent layers of strips are oriented with a small stereo angle to provide some sensitivity in the coordinate longitudinal to the strip direction.

- The Transition Radiation Tracker (TRT), constructed with small-diameter straw tubes filled with a non-flammable gas mixture, isolated within individual gas volumes. The TRT employs a gas mixture comprising 70% Xe, 20% CO_2, and 10% CF_4. Each tube, with a 4 mm diameter and containing a 0.03 mm diameter gold-plated tungsten readout wire, detects transition radiation produced by ultra-relativistic charged particles passing through polypropylene foils. Transition radiation photons are emitted at an angle $\theta \simeq \frac{1}{\gamma}$ relative to the direction of the incoming particle, and they ionise the gas via the photoelectric effect. The ionisation is detected at the readout wire. The TRT achieves an overall resolution of at least 50 μm, covering a radial range from 56 cm to 107 cm, with each module containing between 329 and 793 axial tubes.

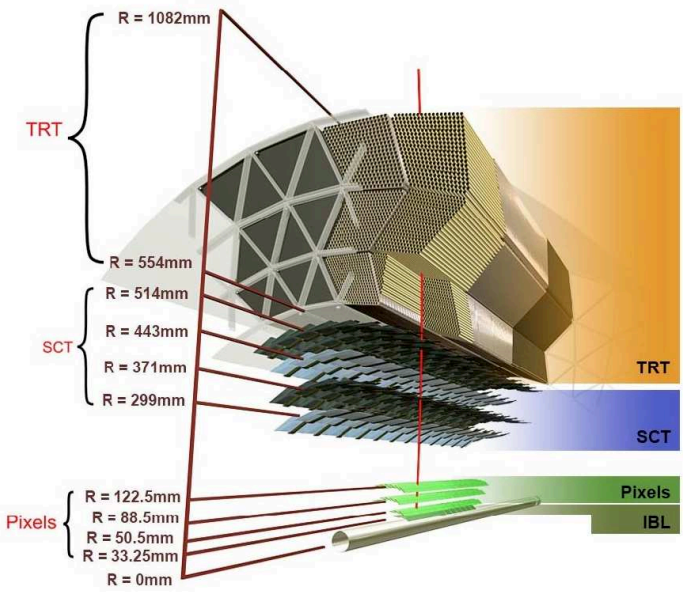

Figure 3.4: Transverse section of the ATLAS ID, from Ref. [59]. Going outward from the beamline the ID components are: the Pixel detector, including the insertable B-layer (IBL), the Semiconductor Tracker (SCT) and the Transition Radiation Tracker (TRT).

3.2.4 The Calorimeters

The calorimeter system [62, 63] in ATLAS surrounds the ID and solenoid magnet and serves the purpose of measuring the energy of electrons, photons and hadronic jets by total absorption of all electromagnetically or strongly interacting particles, with the exception of muons.
All electromagnetically and strongly interacting particles, except muons, produce showers when passing through a calorimeter. Photons and electrons produce purely electromagnetic showers, due to the combination of Bremsstrahlung and electron-positron pair production in the electromagnetic field of atomic nuclei. Hadrons also form showers inside of calorimeters, that are called *hadronic showers*, and are mainly due to inelastic strong interaction with atomic nuclei. Since hadrons can also be electromagnetically charged, or decay to photons (e.g. $\pi^0 \rightarrow \gamma\gamma$), hadronic showers have both an electromagnetic and a hadronic components. Hadronic showers also produce particles which cannot be stopped in the calorimeter, i.e. muons and neutrinos, thus requiring a specific calibration to reconstruct the energy of hadronic jets from the calorimeter response (Section 5.4.3).

ATLAS calorimeters are of the *sampling* type, i.e. they are made of alternating active layers, producing a measurable signal when interacting with particles in the shower, and passive layers, which only serve the purpose of absorbing energy from the shower. Passive layers are typically chosen as heavy metals, so that the calorimeter volume required to stop all particles in the shower is as short as possible.
The ATLAS calorimeter system can be divided in two sections, based on their technology: the Liquid Argon (LAr) calorimeter uses lead (Pb) as passive material, and LAr scintillator as a active material; the Tile calorimeter uses iron as passive material, and plastic scintillator as active material. A better categorisation of the calorimeter sub-detectors, though, is in terms of their function. The electromagnetic calorimeter system is situated closer to the beam, and has the purpose of stopping and measuring the energy of photons and electrons. The hadronic calorimeter system surrounds the electromagnetic one and stops and measures the energy of hadrons. A digital rendering of the ATLAS calorimeter system is shown in Figure 3.5.

The electromagnetic calorimeter The electromagnetic (EM) calorimeter only uses the LAr technology, due to its exceptional radiation hardness, with lead absorbers in both the barrel and endcap regions. It spans the pseudorapidity range $|\eta| < 3.2$, with its barrel segment covering $|\eta| < 1.475$ and the endcaps encompassing $1.375 < |\eta| < 3.2$. It has an accordion-like geometry in the radial direction, depicted in Figure 3.6. This geometry was designed to eliminate azimuthal cracks, as their presence would negatively affect the energy resolution.

In the central region $|\eta| < 2.5$, the EM calorimeter is radially segmented into three longitudinal layers with varying granularities, with the finest granularity in the innermost layer, which experiences the highest particle density.

The forward calorimeter (FCal) is located in proximity of the beamline in the forward and backward directions. The passive material for this section of the detector is copper instead of lead.

The hadronic calorimeter The EM calorimeter is surrounded by the hadronic tile calorimeter, whose barrel section is divided into a proper barrel region, covering $|\eta| < 1.0$, and extended barrel regions ranging from $0.8 < |\eta| < 1.7$. It alternates iron absorbers with radially-oriented plastic scintillating tiles.

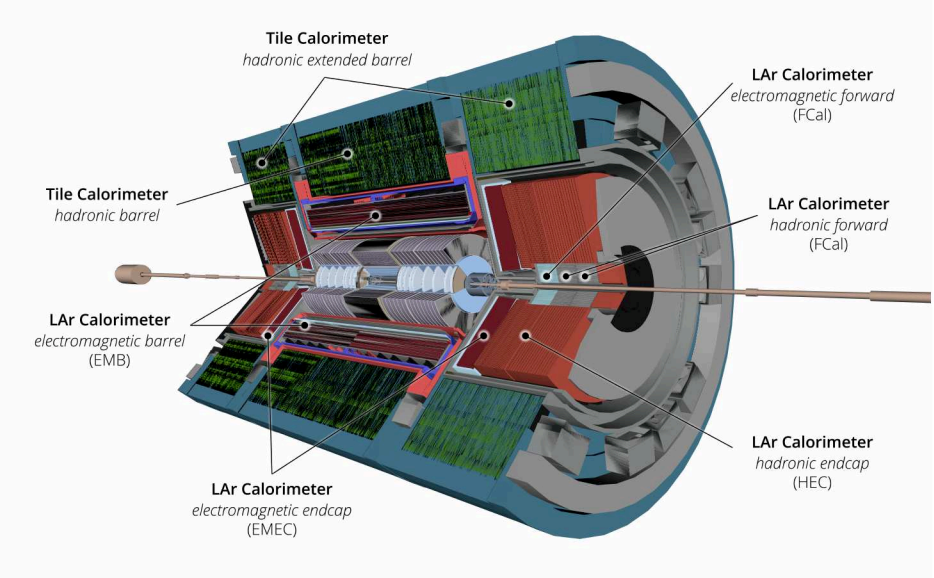

Figure 3.5: Digital rendering of the ATLAS calorimeter system, from Ref. [59]. Both the technology of each subsection and the function are specified in the labels.

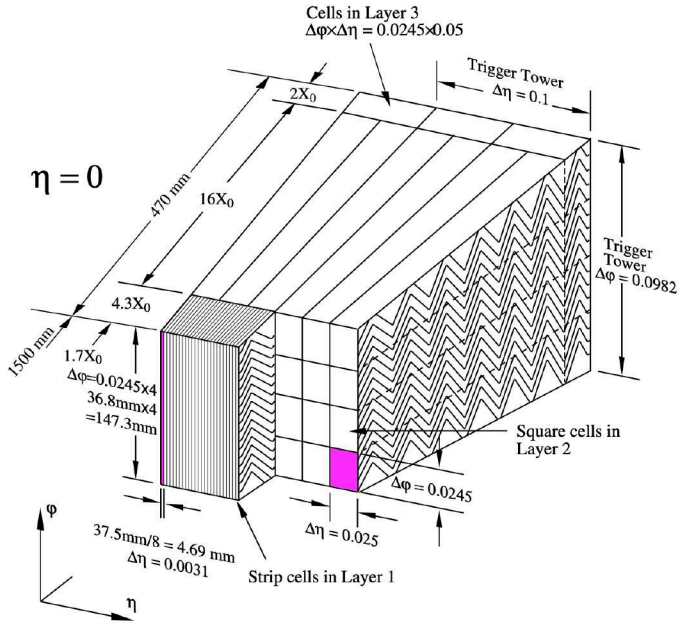

Figure 3.6: Schematic representation of the structure and segmentation of the central barrel section of the ATLAS EM LAr calorimeter [64].

Positioned behind the EM endcap calorimeter, the hadronic endcap calorimeter utilises a similar LAr technology as the EM calorimeter, and features two wheels per endcap. To minimise material gaps between the subsystems, the hadronic endcap calorimeter slightly overlaps with the tile calorimeter, covering ranges up to $|\eta| = 1.5$. Similarly, it overlaps with the forward calorimeter, which covers

regions up to $|\eta| = 3.1$, by extending to $|\eta| = 3.2$. Each wheel is made of 32 wedge-shaped modules, with copper absorber plates interleaved with LAr.

The hadronic section of the FCal is situated right after the EM section, in proximity of the beamline, and uses a LAr scintillator, with tungsten as passive material.

3.2.5 The Muon Spectrometer

Muons traversing the ATLAS detectors typically pass through them entirely. Being leptons, they do not generate hadronic showers in the hadronic calorimeters, and their high mass results in negligible energy loss via Bremsstrahlung, thus they do not produce electromagnetic showers either. Although muons decay into an electron and two neutrinos with a mean lifetime of approximately 2.2 μs, their decay typically occurs outside the detector due to their high energy. Muons lose energy through excitation-ionization of atoms within the detectors and can be treated as minimum-ionizing particles. Consequently, the muon spectrometer constitutes the outermost part of ATLAS.

The ATLAS Muon Spectrometer [59, 65] was designed to autonomously measure muon momenta across a broad range of transverse momentum and pseudorapidity, independent of other detectors. Its angular and transverse momentum resolution is crucial, as high momentum muons represent clear experimental signatures in various physics measurements and searches, including the one presented in this thesis.

The muon system, spanning the pseudorapidity range $|\eta| < 3.0$, comprises various components situated in both the barrel and endcap regions. The barrel region is composed of three concentric, roughly cylindrical stations, while the endcap sections present three wheels per endcap, the innermost one known as *Small Wheel*[1] as it is smaller in size than the other two, and situated inside of the two outermost barrel stations. Figure 3.7 shows a rendering of the ATLAS MS, in its configuration for Run-3.

Different detection techniques are employed in the different subdetectors depending on the pseudorapidity range, due to varying particle rate conditions with η. The Muon Spectrometer components for Run-2 included:

- Monitored Drift Tubes (MDT): aluminium tubes filled with an Argon and CO_2 gas mixture at 3 bar pressure. Each tube contains a 50 μm diameter anodic wire, providing a spatial resolution of 80 μm.
- Cathode Strip Chambers (CSC): multi-wire proportional chambers (MWPC) with cathode plane strips readout to achieve a spatial resolution of approximately 60 μm.
- Resistive Plate Chambers (RPC): positioned in the barrel ($|\eta| < 1.05$) for triggering, offering excellent time resolution (~ns) but poor spatial resolution (~cm).
- Thin Gap Chambers (TGC): for triggering in the endcap region, operating as MWPCs arranged vertically and providing a 25 ns time resolution along with ϕ measurement orthogonal to precision chambers with a typical resolution of $5 - 10$ mm.

For Run-3, New Small Wheels [**ATLAS-TDR-020**] were installed in place of the old ones. The TGCs and CSCs in the old wheels were replaced by small strip TGCs (sTGC) and MicroMegas (MM).

[1] This is the MS configuration used in Run-2. The Run-3 configuration is almost identical, with the New Small Wheels in place of the Small Wheels.

An sTGC is simply a TGC with a smaller strip pitch, to ensure better spatial resolution. MM detectors are gas chambers where the amplification of electron-ion pairs happens close to the anodic plane. This creates a fast response as ions, whose drift time is the bottleneck for time resolution in this kind of detector, only need to travel a short distance before being collected at the anode.

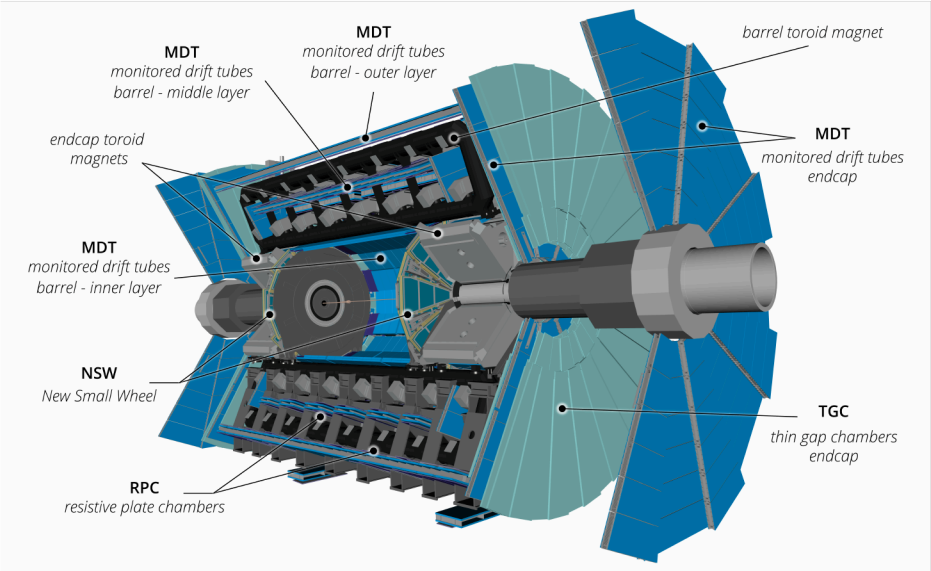

Figure 3.7: Digital rendering of the ATLAS MS system in its Run-3 configuration, from Ref. [59]. The main muon detector components are visible.

3.3 The Trigger and Data Acquisition System

The LHC generates collisions at a rate of approximately 40 MHz. Each collision event occupies roughly 1.5 MB of storage space, implying that ATLAS would need to process data at a rate of around 45 TB/s to record all events. However, current technology limits the data recording speed to approximately 300 MB/s. This limitation is not a significant issue from a physical standpoint since the occurrence of hard inelastic ppscattering events is much lower than the LHC collision rate. To manage the data flow effectively, ATLAS employs a trigger and data acquisition system.

The ATLAS trigger system is engineered to quickly analyse event characteristics and determine whether to record the event based on predefined feature thresholds. It consists of two levels: the first level (Level-1) primarily handles larger data volumes and operates using hardware-based algorithms, applying simpler criteria compared to the second level, known as the High-Level Trigger (HLT), which is software-based.

The Level-1 trigger utilises specialised electronics to identify Regions-of-Interest (RoIs) within the detector, utilising coarse granularity information from the calorimeter and muon detectors as input. An RoI represents a region in the $\eta - \phi$ plane exhibiting physically interesting activity. This trigger mechanism reduces the event rate from the LHC bunch crossing rate of approximately 40 MHz to 100 kHz. The RoIs identified at Level-1 are stored in buffers and subsequently forwarded to the HLT, where selection algorithms run using more detailed detector information either within the RoI or

across the entire event. These algorithms are designed to resemble offline selection and reconstruction algorithms as much as possible, and are therefore lower-resolution versions of the equivalent offline algorithms. HLT algorithms have the full tracking and vertexing information in the event, which allows for complex decision-making, such as requiring jets to be originating from the decay of a B-hadron.

The HLT reduces the rate from the Level-1 output rate of 100 kHz to approximately 1 kHz, with a processing time of approximately 200 ms. It construct physics objects, such as electrons and jets, with a lower precision than the ones used at analysis level, and applies kinematic requirements on them or on global event quantities, such as the missing transverse momentum. The events passing the requirements of the HLT are kept and stored at the CERN data centre.

The events which pass the ATLAS trigger requirements are stored and can be processed via a distributed computing infrastructure, the Worldwide LHC Computing Grid (WLCG).

3.4 Upgrades for Run-4 and High-Luminosity LHC

After Run-3, the LHC will undergo a long shutdown period, during which it will be upgraded for the High-Luminosity LHC (HL-LHC) programme [66], scheduled to commence in 2029. The HL-LHC will feature ppcollisions at a centre-of-mass energy of $\sqrt{s}$ = 14 TeV and an instantaneous luminosity of up to $7.5 \cdot 10^{34}$ cm^{-2} s^{-1}, a significant increase compared to the peak instantaneous luminosity of $3 \cdot 10^{34}$ cm^{-2} s^{-1} of the ongoing LHC Run 3. Consequently, the average number of inelastic ppinteractions per bunch crossing is expected to reach values as high as 200.

To meet the challenges posed by the high-luminosity conditions at the HL-LHC, an extensive upgrade program, known as the Phase-II Upgrade [67–74], is underway for the ATLAS detector. This upgrade aims to maintain the high performance of particle reconstruction and identification, crucial for the success of the ATLAS physics program. A pivotal aspect of the Phase-II Upgrade involves the complete replacement of the current inner tracking detector system with a new, all-silicon, tracking detector called the Inner Tracker (ITk). The ITk will comprise a Pixel Detector [68] and a surrounding Strip Detector [69].

The Pixel Detector, spanning a pseudorapidity range of $|\eta| < 4$, comprises five flat barrel layers and several inclined and vertical ring-shaped endcap disks. It features a finer pixel pitch of 25×100 μm^2 in the innermost barrel layer, transitioning to a pixel pitch of $50 \times 50 \mu$m^2 elsewhere in the sub-detector. This is a much finer granularity compared to the current ID Pixel Detector, necessary to achieve high efficiency and precision tracking in the high-luminosity environment of Run-4.
The Strip Detector, covering the pseudorapidity range of $|\eta| < 2.7$, consists of four barrel layers and six endcap disks. Each layer features pairs of modules with strips set at a slight stereo-angle, to enhance the z (R) resolution in the barrel (endcap). The strip modules consist of multiple rows of strips with a pitch of 75.5 μm in the barrel and varying from 69 μm to 85 μm in the endcap disks.

Figure 3.8 shows a diagram of the ITk geometry, according to one of its most recent geometry versions, internally referred to as 23-00-03 [75], on which the studies in Chapter 10 are based.

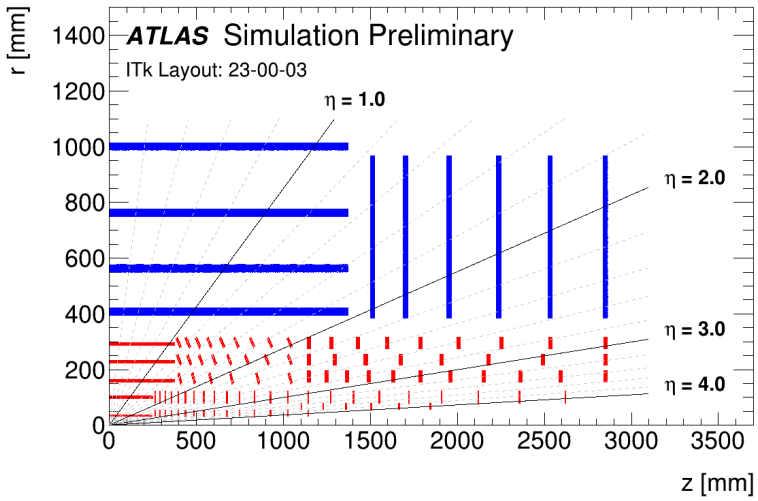

Figure 3.8: ITk geometry with the geometry version internally referred as 23-00-03. The details of this geometry are discussed in Ref. [75]. The red lines represent the Pixel Detector, while the blue lines mark the Strip Detector.

CHAPTER 4

Data and simulation of p-p collisions in ATLAS

In this section, the dataset used for the search presented in this thesis, and the MC simulations of signal and background processes are discussed. The predictions for all signal hypotheses and from the vast majority of the background processes are obtained via MC simulations. The data-driven estimation or correction of the remaining background processes is discussed in Section 6.7.

The relevant experimental backgrounds for this search are:

1. **SM $t\bar{t}$** : SM production of a top-antitop-quark pair. This is by far the biggest background process and it is irreducible, since it has the same final state as the signal process and can also have the same initial state, thus allowing for signal-background interference.
2. **Single-top**: production of a single top or anti-top quark.
3. ***W*+jets**: production of a single W boson, decaying leptonically, plus jets. This is only present in the one-lepton channel.
4. ***Z*+jets**: production of a single Z boson, decaying leptonically, and jets.
5. **$t\bar{t}$ +V**: production of a $t\bar{t}$ pair, in association with a vector boson W or Z.
6. **$t\bar{t}$ +h**: production of a $t\bar{t}$ pair, in association with a SM Higgs boson.
7. **Di-boson**: production of two vector bosons (ZZ, WZ, WW).
8. **Multijet**: QCD production of jets that can mimic a $t\bar{t}$ final state with one leptonically decaying top quark if a jet is misidentified as a lepton.
9. **Fakes**: Events from SM $t\bar{t}$ or W+jets production, with one real and one falsely identified lepton in the final state, mimicking a $t\bar{t}$ event with two leptonically decaying top-quarks.

The estimation of all backgrounds except the multijet is based on MC simulations. The estimation of the multijet background is data-driven and described in Section 6.7.2. Data- or theory-driven corrections to other background processes are specifically mentioned in the following if applied. The W+jets and Z+jets background estimations are corrected via a data-driven approach.
Additional data-driven corrections are applied to simulated samples to account for differences from the data. A correction related to the luminosity profile is applied to all simulated samples. The luminosity

profile is the evolution over time of the instantaneous luminosity delivered to the detector, and depends on the average number of interactions per bunch crossing over time. The instantaneous luminosity in MC simulations does not match the one measured in data, so data-driven corrections are derived centrally in ATLAS and applied via per-event weights (*pile-up weights*). Other corrections related to the performance of object reconstruction algorithms are described in Chapter 5.

4.1 Data sample

In this thesis, ATLAS data from pp collisions at a centre-of-mass energy $\sqrt{s} = 13$ TeV is analysed. The full Run-2 dataset is used, collected between 2015 and 2018, and corresponding to an integrated luminosity of 140 fb^{-1}, with 0.83% uncertainty [76]. All events in the dataset are required to satisfy the *good for physics* conditions (Section 3.1.1). The average number of interactions per bunch-crossing in the whole Run-2 is $\langle\mu\rangle = 33.7$.

4.2 Simulations

The MC simulations of pp collision events follow multiple steps. The first is the simulation of the hard interaction between the initial-state partons, or matrix element (ME) calculation. The large momentum transfers involved in the hard interaction allow for the ME to be calculated perturbatively at a given order in the couplings.
The initial- and final-state partons can radiate gluons and/or produce $q\bar{q}$ pairs, which later hadronise to form colour-neutral showers. These processes cannot be calculated exactly as they are, at least in part, non-perturbative (Section 2.1.3); parton showering (PS) generators are used to simulate them, based on phenomenological models. The emission of initial- and final-state radiation can in principle be seen either as part of the ME calculation or as part of the PS process. For this reason, a matching procedure between the two steps of the simulation is essential to avoid double counting [77].

The hard interaction is accompanied by softer interactions between partons not participating in the hard scattering process, but colour-connected to them. These interactions are known as the *underlying event* (UE). The UE is modelled phenomenologically and its details are controlled by a set of parameters in the MC generators. The choice of parameters in an MC generator is referred to as *tune*.

Finally, since the proton beams are organised in bunches, soft interactions between other protons in the event and in nearby events, not involved in the hard-scattering process, must be simulated. These pile-up interactions (also see Section 3.1.1) are simulated by overlaying QCD multijet simulated events onto the hard-scattering part of the simulation.

All the stable particles produced in the event generation are passed through a full simulation of the ATLAS detector, based on the GEANT4 toolkit [78], to obtain the response of the detector.

4.2.1 SM $t\bar{t}$ production

The production of $t\bar{t}$ pairs at the LHC constitutes the main and irreducible background for searches in $t\bar{t}$ final states. For this reason, a data-driven estimation of it, in a signal-depleted region, is not possible, and the estimation of the expected background contribution in the signal regions has to rely on Monte Carlo simulations.

The SM $t\bar{t}$ background process is simulated at NLO in QCD, using POWHEG BOX v2 [79–83] with the PDF set NNLOPDF3.0NLO [84]. The value of the top quark mass for the simulation is set to m_{top} =172.5 GeV. The functional form for the renormalisation and factorisation scales are set to their default values for the generator, i.e. $\sqrt{m_{\text{top}}^2 + p_T^2}$. The h_{damp} parameter, which regulates the ME/PS matching by changing the amount of initial-state-radiation (ISR) and final-state-radiation (FSR) handled by the ME generator and by the PS generator, is set to 1.5 m_{top} [85].
The PS, hadronisation, and simulation of the UE is simulated by interfacing the ME generator with PYTHIA 8.230, with the A14 [86] tune and using the NNPDF2.3LO PDF set.
The decay of b- and c-quarks is simulated with EVTGEN 1.6.0 [87].

The kinematic variables of the $t\bar{t}$ system are corrected to match a more precise prediction calculated at NNLO in QCD and NLO in electroweak (EW) [88], obtained assuming m_{top} = 173.3 GeV, in agreement with the most recent measurement [23]. It should be noted that, while this prediction is more accurate than the original NLO+PS one in terms of ME calculation, it is not as accurate in the PS calculation; a dedicated uncertainty is defined for this reason, and described in Section 6.8.2. The NNLO-QCD+NLO-EW correction is applied via an event-by-event reweighting and will be therefore referred to as *NNLO reweighting* in the following. The reweighting factors are obtained via an iterative recursive procedure based on the comparison between the parton-level binned distributions of $m_{t\bar{t}}$, $p_T(t)$, and $p_T(\bar{t})$, after FSR. The ratio between the predicted and original distributions in a given bin is used as a reweighting factor; in order to avoid unphysical asymmetries between the p_T distributions for the top and anti-top quarks, the geometrical mean between the $p_T(t)$ and $p_T(\bar{t})$ reweighting factors is used. The reweighting is applied sequentially, based on the $m_{t\bar{t}}$ distribution first, then on the $p_T(t/\bar{t})$ distribution, and again based on the $p_T(t/\bar{t})$ distribution. The whole procedure is repeated multiple times, to ensure the best compatibility with the NNLO-QCD+NLO-EW prediction. More precisely, it was found that three iterations give excellent compatibility with the theoretical calculations, and additional iterations would not yield significant improvements.
The SM $t\bar{t}$ sample is normalised to the NNLO-QCD cross-section, including the resummation of soft-gluon terms at NNLO, calculated with TOP++ 2.0 [89–95]. The calculated cross section at a center-of-mass energy of 13 TeV, using a top-quark mass of 173.3 GeV is $\sigma(t\bar{t})_{\text{NNLO+NNLL}} = 831 \pm 76$ fb.

Alternative samples are used for the estimation of systematic uncertainties related to the modelling of the SM $t\bar{t}$ production, and are described in Section 6.8.2.

4.2.2 Single-top production

The production of a single top quark at LHC proceeds via three processes:

1. ***s*-channel**: quark-antiquark annihilation process, via the exchange of a timelike virtual W boson [96];

2. ***t*-channel**: process in which the top-quark is produced via the exchange of a spacelike virtual W boson;

3. ***Wt***: Associated production of a top-quark with a real W boson [97].

The Wt channel is the biggest source of single-top events in this search and is simulated at NLO with PowhegBoxv2 and using the NNPDF3.0nlo PDF set. At NLO, Wt production can yield the same final state as SM $t\bar{t}$ production, as exemplified in Figure 4.1. This overlap is treated with the diagram removal (DR) scheme, where the $t\bar{t}$-like contribution is removed at the amplitude level [98] from the single-top Wt sample. Pythia 8.307.1 is used for PS and simulation of the UE, with the NNPDF2.3lo PDF set, and EvtGen1.7.0 is used for the decay of b- and c-quarks.

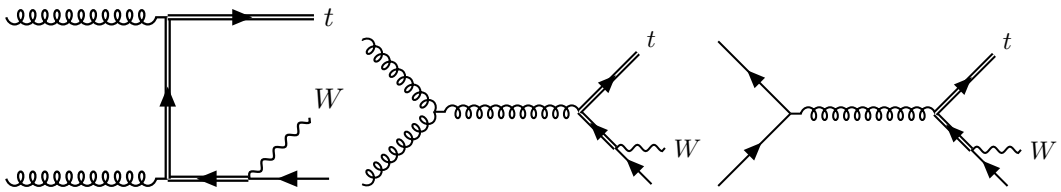

Figure 4.1: Possible NNLO Feynman diagrams of single-top production in the Wt channel. Top and anti-top quarks are represented with double lines.

Single-top production in the s-channel is generated at NLO in QCD, using PowhegBoxv2 with the NNPDF3.0nlo PDF set. PowhegBoxv1 [99] is used for the t-channel instead, with the NNPDF3.04f PDF set and using MadSpin [100] for the decay of top-quarks. For both processes, Pythia 8.230 with the A14 tune and the NNPDF2.3lo PDF set is used for PS, hadronisation and the simulation of the UE. EvtGen1.6.0 is used to decay bottom and charm hadrons.

All three samples are normalised to their respective calculated cross-section, at NNLO+NNLL for Wt [101] and NLO for the s- and t-channels [102, 103].

4.2.3 $t\bar{t}+V$ and $t\bar{t}+h$ productions

Backgrounds from $t\bar{t}+V$ production are simulated at NLO precision in QCD using the MadGraph5_aMC@NLO2.3.3 generator for the ME calculation, with the NNPDF3.0nlo PDF set. The ME generator is interfaced with Pythia 8.210, with the A14 set of tuned parameters and using the PDF set NNPDF2.3lo for the simulation of the PS, the hadronisation and the UE. EvtGen1.2.0 is used for the decays of b- and c-hadrons. The samples are normalised to their theoretical cross-sections, calculated at NLO accuracy in QCD [104].

The ME simulation of the backgrounds from $t\bar{t}+h$ production is obtained via PowhegBoxv1, with the NNPDF3.0nlo PDF set, interfaced with Pythia 8.230. The A14 tune is used for the PS generator, with the NNPDF2.3lo PDF set. The decay of b- and c-hadrons is simulated using EvtGen1.6.0. The sample is normalised to the cross-section calculated at NLO precision in both QCD and EW [105].

4.2.4 W+jets and Z+jets

The production of a single W or Z boson in association with jets in the one-lepton channel is simulated using SHERPA2.2.11, while Z+jets production in the two-lepton channel is simulated with SHERPA2.2.1. The ME is calculated at NLO for up to two final-state partons and at LO for up to five final-state partons with SHERPA2.2.11 and up to four final-state partons with SHERPA2.2.1. The ME simulation is matched with the SHERPA PS [106], using the internal set of tuned parameters MEPS@NLO [107–110], recommended by the SHERPA authors, and adopting the NNPDF3.0nnlo PDF set. Both samples are normalised to their calculated theoretical cross-section, at NLO precision

in QCD [111]. An additional data-driven correction is derived for the Z+jets sample in the two-lepton channel, and is described in Section 6.7.3. Only a data-driven normalisation correction is applied to the W+jets sample in the one-lepton channel, as discussed in Section 6.7.1.

4.2.5 Diboson

The production and decay of vector boson pairs is simulated with SHERPA2.2.1 for fully leptonic decays and SHERPA2.2.2 for semileptonic decays [112]. The ME calculation is at NLO accuracy in QCD for up to one additional parton emission, and at LO accuracy for up to 3 additional emissions. Loop-induced processes initiated by a gluon pair are simulated at LO accuracy. The NNPDF3.0NNLO set of PDF is used. The ME calculations are matched with the SHERPA parton shower based on Catani–Seymour dipole factorisation [106, 113] using the MEPS@NLO set of tuned parameters.

4.2.6 Signal samples

MC samples are produced for the four benchmark models introduced in Section 2.4. The signal process is loop-induced gluon-fusion, $gg \to A/H \to t\bar{t}$, as described in Section 2.4.5. It is generated at LO in QCD with MadGraph v2.6.7 [104], including contributions from t- and b- quarks in the loop, except for the generic (pseudo)scalar model, where only t-quarks are allowed in the loop. The NNPDF3.0NLO set is used for the modelling of parton distribution functions, and the mass of the top quark is set to 173.3 GeV to match the value used in the NNLO reweighting correction to the SM $t\bar{t}$ background. The functional form of the factorisation and renormalisation scales is set dynamically to $\frac{1}{2}\sum_i \sqrt{m_i^2 + p_{T_i}^2}$, where the sum is over all final-state partons. The decay widths of the (pseudo)scalars in the various benchmark models are calculated with 2HDMC v1.8.0 [114] and are used as inputs to the ME calculation. The decays of the top quarks are simulated with MadSpin to correctly account for their spin correlation.
For the statistical interpretation (Section 7.2), pure-signal (S) and signal-plus-interference (S+I) samples need to be generated separately. The S+I matrix elements are generated from the MEs for the inclusive process S+I+B that MadGraph produces. This is done by modifying MadGraph to remove the ME contribution for the LO SM $t\bar{t}$ production from the inclusive process on an event-by-event basis. The simulation of the S+I process using the modified version of MadGraph is validated in Ref. [17], by comparing the $m_{t\bar{t}}$ distribution with the one obtained by generating the inclusive S+I+B process and subtracting the LO SM $t\bar{t}$ events generated with MadGraph. The difference between the two was found to be negligible. The resulting S+I $m_{t\bar{t}}$ distribution has regions with a total negative yield due to the contribution of the interference.

PS, hadronisation and UE are simulated with Pythia 8.244, with the A14 tune and using the NNPDF2.3LO PDF set. EvtGen1.6.0 is used to simulate the decay of b- and c- hadrons. A full simulation of the detector is used, via the GEANT4 toolkit.

Events for the S and S+I samples, for different parameter values in the various benchmark models, are not generated from scratch for all signal hypotheses. In order to save computing resources, a set of pure-signal 2HDM samples after detector simulations is used as input to a reweighting procedure to obtain MC samples under different signal hypotheses. The reweighting factor is the ratio between the matrix elements corresponding to the target and original signal hypotheses, calculated from the

momenta of the partons in the initial and final states, before FSR:

$$w = \frac{\mathrm{ME}\left(\{\text{target parameters}\}, \{p_i,\ p_f\}\right)}{\mathrm{ME}\left(\{\text{original parameters}\}, \{p_i,\ p_f\}\right)} \tag{4.1}$$

The original set of samples for the reweighting is composed of samples Type-II 2HDM samples with $\tan\beta = 0.4,\ 1.0$ and $m_{A/H}$ between 400 GeV and 1400 GeV. The choice of input samples to the reweighting procedure is very important to ensure the accuracy of the estimate. In principle, any gg-initiated process with a $t\bar{t}$ final state could be used, but it must adequately cover the phase space of the final state top quarks, as the reweighting procedure only assigns a new weight to the event, without changing the particle momenta. The 2HDM samples with $\tan\beta = 0.4$ are chosen as they have the widest pure-S $m_{t\bar{t}}$ distribution, hence providing enough statistics to cover a wide $m_{t\bar{t}}$ spectrum. The 2HDM samples with $\tan\beta = 1.0$ were chosen to improve the modelling of narrow interference patterns.
The reweighted samples were validated against a few selected S and S+I generated samples, with the same theoretical parameters, finding a very good agreement between the two. For this reason, no systematic uncertainty is applied to the signal reweighting.

Multiplicative normalisation factors k_S are applied to the S samples of the 2HDM and hMSSM benchmark models, to correct their LO cross-section to a partial NLO cross-section calculated with SusHi v1.7.0 [115–120]. They range from values up to 3-4 in the low-mass, low-$\tan\beta$ region of the parameter space to values of 1-2, in the high-mass, high-$\tan\beta$ region. The corresponding interference term I is also corrected via a multiplicative factor $k_I = \sqrt{k_S \cdot k_B^{\mathrm{LO}}}$, where $k_B^{\mathrm{LO}} = 2.07$ is the ratio between the SM $t\bar{t}$ cross-sections calculated at NNLO in QCD (as used for the MC estimation of the $t\bar{t}$ background) and at LO in QCD (as used for the calculation of the S+I matrix elements). Details on how the normalisation factors are applied can be found in Section 7.2.

CHAPTER 5

Reconstruction and identification of physics objects

The information from various ATLAS subdetectors is used to reconstruct a number of physics objects that are used to select events and calculate kinematic distributions for further statistical analysis. In this chapter, the reconstruction of all physics objects used in the analysis is discussed.

5.1 Basic objects

Basic objects, i.e. tracks and topological clusters, are the building blocks of the physics objects that represent the properties of the final state particles measured in the detector. They are built from localised energy deposits in the different detector layers.

5.1.1 Charged-particles track reconstruction[1]

The reconstruction of charged-particle trajectories in the detector, or *tracking*, involves the following steps, which have been used with the current ATLAS ID during Run-1, -2 and -3, and are expected to be used in a similar form, though with possible detector-specific optimisations, for the ITk.

1. **Formation of clusters and space points:** Signals in adjacent channels of the silicon detectors are combined into clusters, i.e. groups of connected silicon elements (strips or pixels), with a signal over a reconstruction threshold. For each pixel, a *Time over Threshold* (ToT) measurement is performed, both in the ID and in the ITk, while no ToT information is available in the SCT and in the Strip ITk subdetector. Clusters are then converted into space-points, i.e. position measurements based on the signal in each channel, detector geometry and sensor pitch. More precisely, if the ToT information is available, the centre of the cluster is calculated as the charge-weighted average of its constituents, otherwise, the geometric centre is used. A correction for the drift of electron-hole pairs in the silicon sensor due to the ATLAS magnetic field is also applied. In environments with a high density of charged particles, clusters can have energy contributions from multiple particles; these clusters are referred to as *merged*. Merged

[1] This section is largely based on the ATLAS PUB NOTE ATL-PHYS-PUB-2023-022 [121]. I conducted all studies summarised in the note and acted as note editor.

clusters are likely to be used for the reconstruction of multiple tracks and are in this case referred to as *Shared*. More information on cluster merging/sharing is found in Chapter 10.

2. **Track seeding and finding:** Groups of three aligned space-points are combined into *track seeds*. Track seeds are extended to form a track candidate with additional space-points via a combinatorial Kalman Filter [122]. This step yields a set of candidate tracks, including a number of combinatorial or *fake* track candidates, i.e. track candidates that do not correspond to a real particle but are a result of incorrectly assigned space-points.

3. **Ambiguity solving and track fitting:** The ambiguity solving stage is one of the most relevant for tracking performance in dense hadronic environments. In this step, fake-track candidates are rejected and overlaps between track candidates are resolved. Track candidates receive a quality score based on simple measures of track quality, such as the number of clusters (*hits*) on the track, and are processed individually in descending score order. In the processing step, overlaps between tracks sharing clusters are resolved. Clusters cannot be shared by more than two tracks unless they are identified as merged, i.e. due to the contribution of multiple charged particles. Deep Neural Networks are employed to predict the number of particles that have produced the cluster [123, 124]. Preference is given to tracks with higher track scores when deciding to which track a shared cluster should be assigned. Furthermore, a track candidate is not allowed to contain more than two shared clusters. Further details on the treatment of shared clusters in the ambiguity solver can be found in Ref. [125]. Track candidates that pass the ambiguity solver undergo a high-resolution fitting procedure, based on a global χ^2 fit, to determine the final track parameters.

In the current detector, tracks are extended into the transition radiation tracker (TRT), which surrounds the silicon detector layers, before fitting.

An important track-related quantity, which is used in the reconstruction and selection of various physics objects such as electrons and muons, is the *impact parameter* (IP). The IP is the point of closest approach of the track to a reference point, which can be chosen as the interaction point (which is also the origin of the ATLAS reference system), the primary hard-scattering vertex, or a secondary interaction vertex.

5.1.2 Topological clusters

Topological clusters, or topo-clusters, are the basic objects reconstructed in the calorimeters. They are sets of neighbouring cells, with a sufficiently high signal-to-noise ratio. Topo-clusters are seeded by cells with a signal-to-noise (SNR) ratio greater than 4, significantly higher than expected. After a seed cell is identified, neighbouring cells are added to a *proto-cluster* if they have a sufficiently high SNR. The process continues until all cells with a sufficiently high SNR are in a proto-cluster. Proto-clusters are then split if they contain more than one local maximum, i.e. more than one cell with an energy higher than 500 MeV on the electromagnetic scale[2]. The energy of a topo-cluster is given by the sum of the energies of all its constituent cells. Its position in the $\eta - \phi$ plane is obtained by a weighted mean of the $\eta - \phi$ positions of the constituent cells, using the cell energy as weight.

[2] A calibration is necessary to convert the electronic signals in the calorimeter cells into the energy deposited by a particle in an electromagnetic or hadronic shower. The calibrations are performed separately for electromagnetic and hadronic showers.

5.2 Electrons

Electrons lose energy due to bremsstrahlung traversing the detector. The bremsstrahlung photons, in turn, produce electron-positron pairs when interacting with the detector materials, initiating a cascade production of electrons, positrons, and photons known as an electromagnetic shower. Electromagnetic showers are reconstructed in the EM calorimeters. Electrons at the ATLAS experiment are reconstructed by combining the charged-particle information from the ID with the EM topo-clusters in the EM calorimeter. Electron tracks need to be matched to an EM topo-cluster in the $\eta - \phi$ plane [126]. Figure 5.1 shows a schematic of the typical path of a reconstructed electron in the ATLAS detector. Electron reconstruction follows multiple steps.

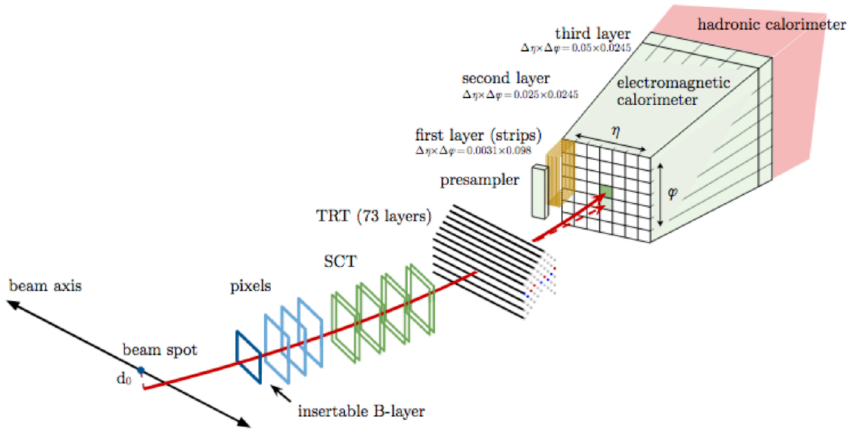

Figure 5.1: Typical path of a reconstructed electron in the ATLAS detector. The dashed line indicates a photon radiated by the electron. Figure taken from Ref. [126]

Seed-cluster reconstruction The first step in electron reconstruction is constructing seed-clusters in the EM calorimeter. The calorimeter is divided into 200×256 towers in the $\eta - \phi$ plane consisting of the three layers of the calorimeter. Seed-clusters are constructed using a sliding-window algorithm [127] to form 3×5 towers in $\eta\times\phi$ with a combined energy of at least 2.5 GeV. The procedure is performed using all cells in the calorimeter as possible tower centres. If two seed-clusters are too close, their energy is used to select the one to retain. If their energies differ by more than 10%, the seed-cluster with the highest energy is kept, otherwise, the one with the highest central tower is kept.

Track reconstruction Charged-particle track reconstruction is the second step in electron reconstruction, and happens in the ID. The details of track reconstruction are found in Section 5.1.1. An additional fitting stage to the ATLAS global χ^2 track fitter is applied to electron tracks. Provided that the electron track-candidate is loosely matched with an EM seed-cluster within $|\Delta\eta| < 0.05$, $-0.20 < \Delta\phi < 0.05$, an additional fit is performed, using an optimised Gaussian-sum filter (GSF) [128] to include the effect of energy loss in the track measurement.

Electron-candidate reconstruction The final step in forming an electron-candidate is the matching between an EM seed-cluster and an electron track. The electron track is required to be matched to a seed cluster within $|\Delta\eta| < 0.05$, $-0.10 < \Delta\phi < 0.05$. If more than one track satisfies the requirement, the primary electron track is selected using an algorithm based on the distance of the tracks from the cluster barycentre in the second layer of the EM calorimeter and ID silicon hit information. The possible matching of the primary electron with a secondary vertex is also considered to obtain a good rejection of converted photons; if the primary electron is matched with a secondary vertex and contains no hits in the Pixel detector, it is classified as a converted photon.

Electron identification A likelihood-based identification procedure is used to select electrons originating from the hard-scattering vertex (*prompt electrons*) against the ones from other vertices (*non-prompt*) and other objects with similar signatures, such as electrons from hadron decays, or hadrons with a large electromagnetic component in their shower [129]. Typical variables used in the likelihood-based identification are the ratio of the energy deposited in the electromagnetic calorimeter, and the momentum of the electron-track, and the hadronic leakage; the hadronic leakage is defined as the ratio between the transverse energy reconstructed in the first layer of the hadronic calorimeter and the transverse energy that is deposited in the EM calorimeter. Three working points are defined for electron identification: *Tight, Medium*, and *Loose*. For all three working points, at least two hits in the Pixel detector are required, along with at least 7 hits across the whole silicon section of the ID; for tight and loose electrons, a hit in the innermost layer of the Pixel detector is also required. The identification efficiency is measured in data, using the well-known processes $J/\Psi \rightarrow ee$ and $Z \rightarrow ee$. Figure 5.2 shows the electron identification efficiency for the three working points.

Electron isolation A prompt electron can be separated from other processes by requiring low electromagnetic activity in its proximity, or *isolation*. Isolation can be calculated based on topo-clusters or charged-particle tracks. With the topo-cluster approach, the transverse energy of calorimeter clusters is measured in a cone of radius ΔR around the electron cluster, while with the track-based approach, the transverse momentum of tracks in a cone around the electron track is measured. The isolation variables are obtained by subtracting the transverse energy or momentum of the electron from the cone. Different strategies can be used to construct the cone. For this search, a track-based approach is used, with a variable-size cone. The size of the isolation cone decreases with the p_T of the electron and is obtained as the minimum between $R = \frac{10\ \text{GeV}}{p_T^e}$ and a maximum radius of 0.2. This reflects the increasing collimation of the decay products of heavy particles with the momentum of the mother particle. The isolation requirement forces the sum of the transverse momenta of tracks in the isolation cone to be less than 6% of the transverse momentum of the electron.

The electron identification and isolation efficiencies in MC-simulated samples do not match the values measured in the data. These efficiencies are calibrated in data via measurements in $Z \rightarrow e^+e^-$ and $J/\psi \rightarrow e^+e^-$ events [130]. Scale factors are applied to simulated samples to reproduce the efficiencies measured in data.

5.3 Muons

Muon reconstruction uses information from the ID, the MS and the calorimeters. At first, the information from each sub-detector is used separately, and then the resulting objects are combined

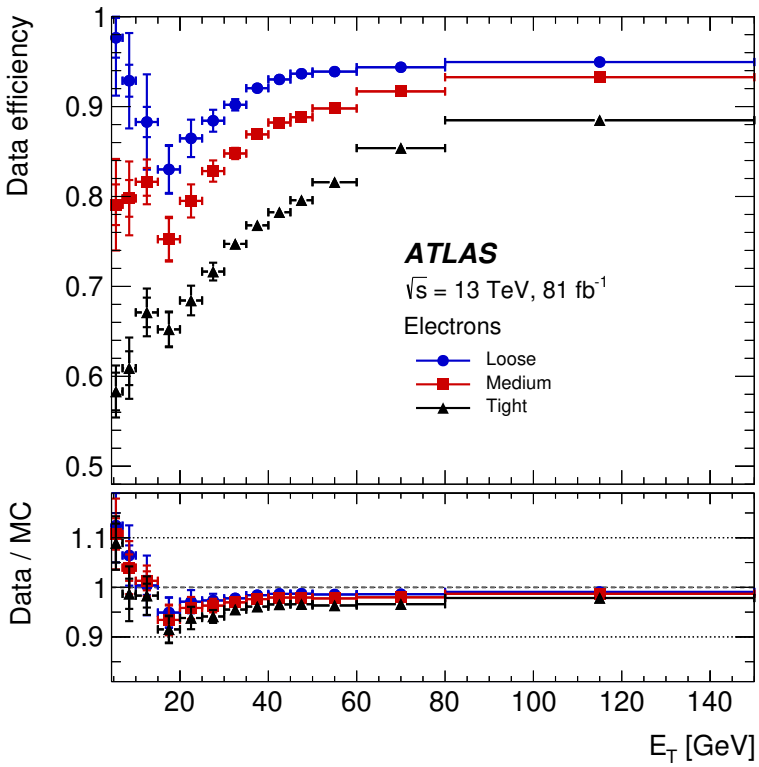

Figure 5.2: Electron reconstruction efficiency for the three working points of the likelihood-based electron identification. Figure taken from Ref. [130]

to form the muon object. The reconstruction of muons in the ID is not different from the standard reconstruction of charged-particle tracks, and was already discussed in Section 5.1.1.

Muon reconstruction in the MS Muon reconstruction in the MS starts with the formation of track segments in the MDTs, RPCs, TGCs and CSCs from hit patterns. After the formation of segments, the track is built by fitting hits from different layers of the detectors. The algorithm is based on a combinatorial algorithm using segments as seeds. The final tracks need to be formed from at least two matched segments, with the only exception of the barrel-endcap transition region, where a single high-quality segment is sufficient to build a track. Hit sharing among multiple track-candidates is possible, and an overlap removal algorithm is used to determine whether a shared hit belongs to a single track or can be used by multiple tracks. After track finding, a global χ^2 fit is performed and candidates undergo a selection process. In track candidates failing the selection, hits with a high contribution to the χ^2 variable are removed, and the fit is repeated.

Combining sub-detector information Four types of muons are defined based on the sub-detectors involved in their reconstruction.

1. *Combined muons* (CB): track reconstruction happens independently in the MS and in the ID, then a combined track is built and re-fit using all hits. Hits from either sub-detector can be

removed to increase the quality of the reconstruction. The fitting strategy is outside-in, meaning that MS tracks are extrapolated inward and matched to an ID track.

2. *Segmented-tagged muons* (ST): this is an inside-out procedure where an ID track is extrapolated into the MS and identified as a muon only if it is matched to at least one segment in the MDT or CSC. This strategy is used mostly for muons traversing only one layer of the MS, either because of their low p_T or because they hit the MS in a region of low acceptance.

3. *Calorimeter-tagged muons* (CT): a track in the ID is matched to a calorimeter deposit compatible with a minimum ionizing particle. This reconstruction strategy has the lowest purity, but it recovers efficiency in regions where the MS has a low acceptance.

4. *Extrapolated muons* (ME): the muon track is reconstructed using only hits in the MS and requiring a loose compatibility with originating from the interaction point. Energy loss in the calorimeters is taken into account in the calculation of track parameters. A muon is required to have hits in at least two layers of the MS chambers, three in the forward region. Extrapolated muons allow muon reconstruction in the pseudorapidity region $2.5 < |\eta| < 2.7$, which is outside of the ID acceptance.

Overlaps between different muon types are removed by prioritisation based on the order above.

Muon identification Muon identification algorithms aim to select prompt muons produced close to the interaction point from non-prompt ones coming from the in-flight decay of charged hadrons. Non-prompt muons are characterised by a *kink* in the reconstructed tracks. For this reason, the fit quality of the resulting reconstructed muon might be poor, and the energies and momenta separately measured in the MS and ID might not be compatible. Muon identification algorithms make use of this information and apply cuts on variables such as the normalised χ^2 of the combined fit and the *q/p significance*, which is defined as

$$\left| \left(\frac{q}{p}\right)_{ID} - \left(\frac{q}{p}\right)_{MS} \right|,$$

where $\left(\frac{q}{p}\right)_{ID}$ and $\left(\frac{q}{p}\right)_{MS}$ are the charge/momentum ratios measured in the ID and MS, respectively.

There are four different definitions of a muon [131], based on different quality requirements:

- **Loose**: All muon types are used, and selection criteria are optimised to maximise reconstruction efficiency.

- **Medium**: The same selection as the Loose category is applied, but only CB and ME tracks are used.

- **Tight**: All CB muons that also have hits in at least two MS stations are used. Tighter quality requirements are applied than for the Medium category.

- **High-p_T**: CB muons passing the Medium requirements, with hits in at least three MS stations are in this category. The selection is optimised to maximise the momentum resolution of muons with $p_T > 100$ GeV.

Muon isolation Muon isolation requirements are defined very similarly to those for electron isolation. As for the electrons, isolation variables are defined both in terms of activity around the ID track and in terms of activity in the calorimeter. For this search, a similar track-based approach as the one used for electron isolation is adopted, with a maximum radius of the isolation cone of 0.3.

Similarly to the electron case, the muon isolation and identification efficiencies are measured in data from $Z \to \mu^+\mu^-$ and $J/\psi \to \mu^+\mu^-$ events [131], and scale factors are applied to simulated samples to reproduce the efficiencies measured in data.

5.4 Jets

At hadron colliders such as LHC, the hard-scattering process is an interaction between the constituent partons of the protons. As introduced in Section 2.1.3, when quarks and gluons are present in the final state of a process, particle-antiparticle pairs are formed from the vacuum due to colour confinement, and interact with the original quarks and gluons to form bound states (hadrons). The resulting cascade of particles is called a hadronic jet. Jets can be viewed as proxies to the quark or gluon from which they originate, with the jet four-momentum ideally representing the four-momentum of the original parton. The reconstructed jet objects need to be calibrated to account for pile-up contributions and energy contributions that might be missed by the detector.

5.4.1 Constructing the jets: the anti-k_T algorithm

Jet reconstruction algorithms start from input objects and cluster them together to form a jet object. A good jet reconstruction algorithm should satisfy the following requirements:

1. it should be **collinear safe**, meaning that if an input is split into two collinear ones, the resulting jet should remain the same;
2. it should be **infrared safe**, meaning that the effect of low-p_T inputs should be small, and vanish when the p_T of the input approaches 0;
3. it should depend as little as possible on detector effects such as noise and resolution;
4. it should be computationally efficient.

A widely used class of jet algorithms is an iterative one that forms jets based on two distances defined as:

$$\begin{cases} d_{ij} = \min\left(k_{T_i}^{2p}, k_{T_j}^{2p}\right)\frac{\Delta R_{ij}}{R^2} \\ d_{iB} = k_{T_i}^{2p} \end{cases}, \tag{5.1}$$

where

- k_{T_i} is the momentum of the i-th proto-jet;
- R_{ij} is the distance between the i-th and j-th proto-jet in the rapidity-azimuthal-angle plane, defined as $\sqrt{\left(y_i - y_j\right)^2 + \left(\phi_i - \phi_j\right)^2}$;
- R and p are parameters of the algorithm.

The quantity d_{ij} represents the distance between the i-th and j-th inputs, while d_{iB} is the distance between the i-th input and the beam. For each input i, the algorithm calculates the distances d_{iB} and d_{ij} for all j other than i; if the minimum distance is found to be d_{iB}, the i-th input is said to form a jet; otherwise, the two closest inputs are combined and the combined object is added to the list of inputs, while the parent inputs are removed. The procedure is repeated until no inputs are left. In the *anti-k_T* algorithm, which is the default in ATLAS, the parameter p is set to -1 and the input distance is based on the inverse transverse momentum:

$$\begin{cases} d_{ij} = \min\left(\frac{1}{k_{T_i}^2}, \frac{1}{k_{T_j}^2}\right)\frac{\Delta R_{ij}}{R^2} \\ d_{iB} = \frac{1}{k_{T_i}^2} \end{cases} \tag{5.2}$$

. The anti-k_T algorithm is infrared-safe as the clustering starts from hard inputs, and soft inputs are then clustered with a hard object, rather than together into a soft object. It is also collinear-safe, as all inputs with $\Delta R_{ij} < R$ are clustered together into a single jet. Finally, another advantage of the algorithm, is that it gives rise to approximately conical jets, with a radius R.

The default value of the R parameter for the reconstruction of small-R jets in ATLAS, which is also used in this search, is 0.4. Other choices of R are also used in the search presented in this thesis, in particular in the construction of reclustered jets (Section 5.4.4).

5.4.2 Building jet inputs: PFlow jets

The first step in the reconstruction of jets is the formation of the input objects to use in the anti-k_T algorithm. Most ATLAS analyses in Run-1 used so-called EM-topo-jets, which used topo-clusters as inputs, corrected by an energy-scale factor [132]. Run-2 analyses rely on PFlow objects [133] as inputs to the anti-k_T algorithm, which are built using both topo-clusters and ID information. The basic idea of PFlow jets is to match tracks in the ID to clusters in the calorimeter and subtract the energy of the matched tracks from the topo-clusters. The matched tracks and energy-subtracted topo-clusters are used as inputs to the anti-k_T algorithm. Since only tracks from non-prompt hadrons are targeted, not all tracks are used as possible PFlow objects: tracks associated with muons and electrons are removed, as well as high-p_T tracks with a transverse momentum higher than 40 GeV. High-p_T tracks are removed as they are often poorly isolated from nearby activity, not allowing the accurate removal of the calorimeter energy associated with the track. Tracks are first matched with a single topo-cluster via angular requirements. The expected energy deposited by the particle in the cluster is parametrised in terms of the track p_T as:

$$\langle E_{\text{dep}} \rangle = p_T^{\text{trk}} \langle E_{\text{clus}}^{\text{ref}} / p_{T,\text{ref}}^{\text{trk}} \rangle, \tag{5.3}$$

where the average energy $E_{\text{clus}}^{\text{ref}}/p_{T,\text{ref}}^{\text{trk}}$ deposited by a track of transverse momentum $p_{T,\text{ref}}^{\text{trk}}$ in a topo-cluster of energy $E_{\text{clus}}^{\text{ref}}$ is derived by special single-particle MC simulations. The estimated energy deposited by the particle is then subtracted from the topo-cluster. It is possible that not all of the energy of a particle is deposited in one topo-cluster. The energy of the cluster associated with the track as well as the deposited energy of the particle are used to determine whether a second cluster should be associated with the track. After the removal of energy deposits associated with tracks from the topo-cluster, a decision is taken on whether to keep the topo-cluster remnant or not. Clusters associated with tracks are assumed to arise from charged hadrons, while the remaining energy deposits

are attributed to neutral hadrons. The remnant is kept if its energy is higher than the width of the $E^{\text{ref}}_{\text{clus}}/p^{\text{trk}}_{T,\text{ref}}$ distribution, otherwise its energy is attributed to a shower fluctuation and the cluster is removed.

Using PFlow objects as inputs for jet reconstruction has multiple advantages. The energy resolution of the calorimeter contains a term proportional to $1/E$ and a term proportional to $1/\sqrt{E}$, while the inverse momentum resolution of a track is proportional to its p_T; this means that using the tracking information improves the jet energy resolution at low energies, while the resolution at high energies is kept at a good level thanks to the calorimeter. Additionally, tracks that would not have passed the calorimeter threshold can be included, as well as very-low-p_T tracks that cannot reach the calorimeter because of their large curvature in the magnetic field. Finally, pile-up contributions can be more easily rejected by associating tracks to vertices.

5.4.3 Jet calibration

The jets reconstructed via the anti-k_T algorithm need to be calibrated to account for energy contributions that were not directly measured by the calorimeters as well as to remove pile-up effects. The main purpose of the jet calibration is to correct the energy scale and direction of the jet to the ones of the initial parton, while at the same time optimising the energy resolution for a more precise estimation of the physical variables of interest in physics analyses.

Jet calibration consists of multiple steps [134]. First, the jets involved in the hard-scatter process are expected to originate from the primary vertex of the event. This correction does not change the energy of the jet, but improves the angular resolution. Next, a pile-up correction is applied, which consists of two steps and removes energy contributions to the jet coming from pile-up particles. The first correction is based on the area of the jet and on the average transverse momentum density of the event, while the residual correction uses MC simulations to parametrise the p_T of the jet in terms of the number of primary vertices (PV) in the event. A Global Sequential Calibration is then applied to improve the p_T resolution of the jet, and a final in-situ calibration is used to account for the remaining differences between jet energies in data and MC simulation.

Area and p_T density pile-up correction For each jet and each event, the pile-up contribution to the jet is calculated as the product ρA, where ρ is the p_T density of the event and A is the area of the jet, calculated as prescribed in Ref. [134]. The pile-up contribution is subtracted from the jet p_T.

Residual pile-up correction After the p_T density-based correction, a residual dependence of the reconstructed jet p_T on pile-up activity remains. An additional calibration is applied by correcting the p_T of the reconstructed jet to correspond to the p_T of a matching truth jet within $\Delta R < 0.3$. Truth jets are defined as anti-k_T jets using all simulated detector-stable particles except muons and neutrinos as inputs. The difference between the reconstructed and truth p_T is parametrised in terms of the number of primary vertices in the event N_{PV} and the average number of interactions per bunch crossing $\langle\mu\rangle$. The correction is parametrised in bins of jet η and p_T. After both pile-up corrections, the jet p_T is written as $p_T^{\text{corr}} = p_T^{\text{reco}} - \rho \times A - (N_{PV} - 1) \times \alpha - \langle\mu\rangle \times \beta$, where α and β are the parameters of the residual pile-up calibration obtained from the comparison between the reconstructed and truth jets.

Absolute MC-based calibrations The absolute *Jet Energy Scale* (JES) and η calibrations correct the four-momenta of the reconstructed jets to the energy scale and pseudorapidity of the final-state

partons. They correct for energy loss in dead material in the calorimeter, out-of-cone contributions to hadronic showers, biases in the η reconstruction, and different responses of the calorimeters to the hadronic and electromagnetic components of showers.

The calibration is parametrised in terms of the reconstructed energy of the jet, E_{reco}, and the pseudorapidity, η_{det}, of the detector elements. The JES correction starts with Gaussian fits to the ratio $E_{\text{reco}}/E_{\text{truth}}$ of the reconstructed and true energies of the jet. The applied calibration factor is $1/\mathcal{R}$, where $\mathcal{R}$ is the mean of the Gaussian fit on $E_{\text{reco}}/E_{\text{truth}}$. The calibration is parametrised in bins of η_{det}. The η calibration corrects the reconstructed pseudorapidity of the jet to match the true one, via fits on the distribution of $\eta_{\text{reco}} - \eta_{\text{truth}}$. The calibration is parametrised in bins of η_{det}.

Note that these calibrations do not correct the whole jet four-momentum, only its energy and η components.

Global sequential calibration The Global Sequential Calibration (GSC) applies additional corrections to the jet four-momentum to correct for fluctuations in its particle content and in the energy distribution within it. For example, the *punch-through* correction reduces the bias in the jet energy distribution due to high-p_T jets which are not fully contained in the calorimeter. Five jet observables, such as the number of tracks in the jet, are used to derive a sequence of multiplicative corrections to the jet four-momentum. Independent corrections are derived for each of the variables, in bins of jet p_T, energy and η_{det}.

In-situ calibrations In-situ calibrations correct for discrepancies between the JES in data and MC simulations. The jet response is measured separately in data and MC and the ratio is used as a correction factor in data.

Three in-situ calibrations are applied. The η-intercalibration corrects the jet response of forward jets in the detector region $0.8 < \eta_{\text{det}} < 4.5$ to match the jet response in the central part of the detector $\eta_{\text{det}} < 0.8$. The second calibration uses Z+jets and γ+jets events and balances the response of jets recoiling against a well-calibrated, leptonically-decaying Z-boson, or photon object. Finally, the multijet balancing calibrates the response of high-p_T jets against a system of low-momentum, well-calibrated jets.

After determining the central value of the JES, also the *Jet Energy Resolution* (JER) is determined. The procedure that is used to measure JER relies on the assumption that, in events containing only two jets, the conservation of momentum in the transverse plane of the detector implies that the transverse momenta of the two jets should be balanced. The jet energy resolution can then be measured by studying the asymmetry between the transverse momenta of the two jets; this is done for jets belonging to the same pseudorapidity region, in order to minimise detector effects.
The JER is thus obtained in $p_T \times \eta$ bins and can be parametrised as follows:

$$\frac{\sigma_{p_T}}{p_T} = \frac{N}{p_T} \oplus \frac{S}{\sqrt{p_T}} \oplus C, \tag{5.4}$$

where N, S, and C are parameters of the model. The first term represents noise, the second corresponds to stochastic fluctuations, and the third term is constant and takes into account effects linked to a non-perfect energy calibration.
The JER distribution is divided in η bins and a fit using the functional form in Eq. 5.4 is performed. More details about JER can be found in reference [135].

No calibration is applied on the jet mass scale (JMS), however a systematic uncertainty is applied on this quantity, and is described in Section 6.8.1.

5.4.4 Reclustered jets

When heavy particles such as top quarks, W bosons, or Higgs bosons decay, the angular separation of the decay products depends on the transverse momentum of the mother particle: the higher the transverse momentum, the smaller the angular separation:

$$\Delta R \sim \frac{2m}{p_T}. \tag{5.5}$$

Hadronic high-p_T decays of heavy particles produce particles that are too close to be reconstructed using multiple small-R jets described in Section 5.4.1; a single large-radius (large-R) jet is usually used to reconstruct such decays. Depending on the inputs and details of the jet algorithm, different large-R jet definitions are possible. The method used in this analysis is *reclustering*, which uses the calibrated R=0.4 anti-k_T PFlow jets (Section 5.4.2) as input, to construct large-R jets. A possible alternative would have been building anti-k_T R=1.0 jets directly from PFlow inputs, which requires a dedicated energy calibration, similar to the one of small-R jets. To this day, only R=0.4 and R=1.0 anti-k_T PFlow jets are centrally calibrated in ATLAS.
The advantage of reclustering is that the input jets are already calibrated, and do not need further calibration, leaving more flexibility for the choice of parameters in the clustering algorithm [136].

The default reclustering algorithm used in this analysis is an anti-k_T algorithm with a p_T-dependent radius parameter, shrinking with increasing jet p_T [137]. The obtained large-R jets are defined as *Variable-Radius Reclustered* jets, or VRC jets. The effective radius of the VRC jet is given by:

$$R = \frac{\hat{\rho} \cdot m_{\text{top}}}{p_T^{\text{jet}}}, \tag{5.6}$$

where the shrinking parameter $\rho = \hat{\rho} \cdot m_{\text{top}}$ is optimised for the reconstruction of high-p_T top-quark decays in this analysis. The maximum radius for VRC jets is chosen as 1.5, in order to capture also decays of top quarks with an intermediate boost ($p_T \lesssim 300$ GeV).

Additionally, an alternative reclustered jet collection (RC), with a fixed radius parameter of 1.0, was tested, which mimics the default anti-k_T R=1.0 collection used as a standard in ATLAS. These studies are summarised in Section 6.6.1.

In order to suppress pile-up effects, input jets to the reclustering algorithm are required to have a transverse momentum higher than 30 GeV, and an additional trimming procedure is applied, that removes all constituent jets with a p_T lower than 5% of the p_T of the reclustered jet.

Table 5.1 summarises the reconstruction criteria for both VRC and RC jets.

5.4.5 *b*-tagging

The identification of a jet as originating from a b-quark is referred to as *b-tagging*. This is a very important procedure for all analyses involving top quarks in the final state, such as the one presented in this thesis. b-hadrons have a long lifetime compared to others, due to the structure of the CKM matrix, so b-jets are often associated with vertices displaced from the primary vertex, and tracks with a high

Table 5.1: Reclustered jet reconstruction criteria.

Feature	Criterion
Variable-R algorithm	
$\hat{\rho}$ parameter	3.5
Maximum radius	1.5
Minimum radius	0.4
Input constituent	anti-k_T $R = 0.4$ PFlow jets (calibrated, $p_T > 30$ GeV)
Fixed-R algorithm	
Radius	1.0
Input constituent	anti-k_T $R = 0.4$ PFlow jets (calibrated, $p_T > 30$ GeV)

distance of closest approach to the beamline. This information is at the base of b-tagging algorithms. The b-tagging algorithm used in this thesis is called DL1r [138], and uses a sequence of deep learning algorithms with properties of tracks associated to the jet as input features. The algorithm consists of two levels, an RNN taking a variable number of tracks associated to the jet as inputs, and a DNN, using the RNN outputs to calculate the probabilities of the jet originating from a light-, a c- or a b-quark. Among the input variables to the RNN are: the distance of the track from the centre of the jet, the fraction of jet p_T carried by the track, a category based on the number of observed, expected, and missing hits in the silicon detectors, and variables based on the impact parameter of the track with respect to the primary vertex.

The DL1r discriminant is constructed based on the light-, c- and b-probabilities and is defined as:

$$\text{DL1r} = \log\left(\frac{p_b}{f_c p_c + (1 - f_c) p_{\text{light}}}\right), \tag{5.7}$$

where the f_c parameter is called *charm fraction*, and can be tuned for better charm-quark identification and/or light-quark rejection.

Different selection criteria based on the DL1r discriminant have different average b-tagging efficiency and c-jet rejection. ATLAS common operating points are provided for b-tagging efficiencies of 70%, 77%, 80% and 85%. The default working point used for the analysis in this thesis is 77%.

Since the b-tagging efficiency calculated from MC simulations does not match the efficiency measured in data, scale factors are derived from data and applied to MC simulated events to obtain the same efficiency measured in data [139].

5.4.6 Missing transverse momentum

Particles that escape detection in ATLAS carry useful information, and they can be detected indirectly by exploiting the conservation of momentum. Since the proton beams travel along the z-axis, the total momentum of the particles after the collision must have no component in the transverse plane. The negative vector sum of the transverse momenta of all objects in the event is called missing transverse momentum $\mathbf{p_T}^{\text{miss}}$ and its magnitude is referred to as missing transverse energy E_T^{miss}. A large missing transverse energy is an indication of the presence of undetected particles in the final state. Small

amounts of E_T^{miss} also arise due to resolution effects or non-perfect calibration.
Neutrinos are a common cause of $\mathbf{p_T}^{\text{miss}}$, as they carry no electric charge and only interact weakly. Similarly, hypothetical BSM particles that interact weakly with matter have the potential to produce $\mathbf{p_T}^{\text{miss}}$.

The E_T^{miss} is used in the analysis presented in this thesis to reconstruct the neutrinos from the semi-leptonic decay of top quarks. Two components go into the definition of the $\mathbf{p_T}^{\text{miss}}$: the selected and calibrated objects in the event, associated with the primary vertex of the interaction; soft tracks not associated with the primary vertex nor with any selected analysis object. The missing transverse momentum is therefore defined as

$$\mathbf{p_T}^{\text{miss}} = -\sum_{i}^{\text{hard}} \mathbf{p_T}^{i} - \sum_{j}^{\text{soft}} \mathbf{p_T}^{j}. \tag{5.8}$$

The magnitude and angle are then defined as:

$$E_T^{\text{miss}} = \sqrt{\left(p_{T,x}^{\text{miss}}\right)^2 + \left(p_{T,y}^{\text{miss}}\right)^2}, \tag{5.9}$$

$$\phi^{\text{miss}} = \tan^{-1}\left(\frac{p_{T,y}^{\text{miss}}}{p_{T,x}^{\text{miss}}}\right). \tag{5.10}$$

The objects used for the definition of the missing transverse momentum can overlap. To avoid double counting of some of its components, a priority sequence is defined, following the order: electrons, photons, hadronically decaying taus, and jets. If an object shares a calorimeter signal with a higher priority one, it is removed from the list of objects to construct the missing transverse momentum. Muons are reconstructed via the ID and MS, while leaving a very characteristic localised deposit in the calorimeter, and usually have little to no overlap with other analysis objects, so they are not part of the priority sequence.

The definition of the missing transverse momentum heavily depends on the collection of objects used to reconstruct it. Two operating points exist in ATLAS, based on the jet requirements [140]. The *Loose* operating point requires all jets to have a p_T higher than 20 GeV and applies additional requirements to jets with $p_T > 60$ GeV with $|\eta| < 2.4$. The *Tight* operating point excludes forward jets ($|\eta| > 2.4$) and 20 GeV $< p_T <$ 30 GeV. This reduces the dependence of the $\mathbf{p_T}^{\text{miss}}$ on pile-up effects, as pile-up mostly affects the forward region of the detector, and is characterised by soft products. This analysis uses the tight working point.

5.4.7 Overlap removal

Analysis objects can share the same deposits in the detector, hence an overlap removal procedure is applied to resolve ambiguities and avoid overlaps. The overlap removal is done sequentially, in the order described in this section. All angular distances ΔR in this procedure are calculated based on rapidity rather than pseudorapidity differences, i.e. as $\sqrt{\Delta y^2 + \Delta\phi^2}$.

First, electron-electron ambiguities are resolved: if two electrons share the same track in the ID, the electron with lower p_T is discarded. Then, electrons sharing the ID track with a muon are discarded, and identified as photons from Bremsstrahlung.

Next, overlaps between jets and leptons are considered. If a jet is within $\Delta R = 0.2$ of an electron, the jet is discarded and assumed to have originated from the electron. If it is within $\Delta R = 0.2$ of a muon, it is discarded if its number of associated tracks is less than 3 or if the muon is ghost-associated to it. Ghost association [141] is a technique to identify which tracks are clustered into a jet. All tracks are treated as objects with infinitesimal momentum and are therefore clustered into jets last, since the anti-k_T algorithm prioritises high-p_T constituents; if a track is clustered into a jet with this procedure, it is said to be ghost-associated to it.
Muons overlapping with a jet can originate from heavy flavour decays inside of the jet. For this reason, muons with angular separation $\Delta R < \left(0.04 + 10\,\text{GeV}/p_T^{\mu}\right)$ from the nearest jet are discarded. This requirement is adapted to maintain a high selection efficiency for muons from top-quark decays, taking into account the collimation of the decay products with increasing p_T of the mother top quark.
Finally, an *electron-in-jet* overlap removal is applied to suppress the background from heavy-flavour decays in the jet, as well as keeping a high reconstruction efficiency for electrons from semi-leptonic decays of top-quarks, which are expected to produce an electron close to a b-jet. This procedure is not standard in ATLAS, and was developed specifically for BSM searches in $t\bar{t}$ final states. If the angular distance between the electron and the jet is $\Delta R < 0.4$, the p_T of the electron is subtracted from the jet. Then, if the jet p_T is lower than 25 GeV, the jet is discarded and assumed to have originated from the electron. Otherwise, the modified jet is kept and the distance ΔR from the electron is recalculated. If $\Delta R_{\text{modified}} > 0.2$, the electron and the modified jet are kept. Otherwise, the electron is thought to have originated from a heavy flavour decay inside the jet and is discarded, while the original jet is kept.

5.5 Baseline object selection

In the following, the selection of the reconstructed objects used in the analysis is discussed. This is the baseline selection and tighter selections are applied in the definition of the signal regions.

5.5.1 Electrons

As described in Section 5, electrons are reconstructed from topo-clusters in the EM calorimeter, matched to a good-quality track in the ID. The Tight identification working point is used for signal electrons, and additional quality requirements are applied. Signal electrons are required to be isolated (Section 5.2) from other tracks in the detector. The pseudorapidity of the electron candidates is required to satisfy $|\eta| < 2.47$, excluding the transition region between the barrel and endcap calorimeters ($|\eta| \notin (1.37,\ 1.52)$). All electrons are required to be matched to the primary vertex by applying requirements on the impact parameter of the associated track with respect to the primary vertex:

- $|z_0 \sin\theta| < 0.5$ mm, where z_0 is the longitudinal impact parameter;
- $d_0/\sigma_{d_0} < 5$, where d_0 is the transverse impact parameter and σ_{d_0} is its uncertainty.

Finally, all electrons are required to have a transverse momentum higher than 25 GeV. A looser electron selection is used for the definition of control regions for data-driven estimation of background processes. Table 5.2 summarises the requirements for electron selection.

Table 5.2: Selection criteria for electrons. Those for looser control region electrons are shown in italics and square brackets.

Feature	**Criteria**
Pseudorapidity range	$(\lvert\eta_{\text{cluster}}\rvert < 1.37) \quad \lvert\rvert \quad (1.52 < \lvert\eta_{\text{cluster}}\rvert < 2.47)$
Transverse momentum	$p_T > 25$ GeV
Track to vertex association	$\lvert d_0/\sigma_{d_0}\rvert < 5$ $z_0 \sin\theta < 0.5$ mm
Identification	Tight *[Medium]*
Isolation	track-based, variable radius *[no isolation]*

5.5.2 Muons

The selection of muons is very similar to that of the electrons. The Medium identification working point is used in the signal regions. Signal muons are required to be isolated from other tracks and have pseudorapidity $|\eta| < 2.5$. Association with the primary vertex is obtained in the same way as electrons. Finally, all muons are required to have $p_T > 25$ GeV. Table 5.3 summarizes the requirements for muon selection.

Table 5.3: Selection criteria for the muons. Those for looser control region muons are shown in italics and square brackets.

Feature	**Criteria**
Pseudorapidity range	$\lvert\eta\rvert < 2.5$
Transverse momentum	$p_T > 25$ GeV
Track to vertex association	$\lvert d_0/\sigma_{d_0}\rvert < 3$ $z_0 \sin\theta < 0.5$ mm
Identification	Medium *[Loose]*
Isolation	track-based, variable radius *[no isolation]*

5.5.3 Small-radius jets

All small-R jets are required to have $p_T > 25$ GeV and $|\eta| < 2.5$. Additionally, to suppress pile-up effects, a jet-vertex-tagging (JVT) technique is applied, based on a multi-dimensional likelihood [142], to jets with $p_T < 60$ GeV and $|\eta| < 2.4$. A selection requirement is applied on the JVT discriminant for jets in the forward region. Table 5.3 summarises the jet selection requirements.

Table 5.4: Small-R jet selection criteria

Feature	**Criteria**
Transverse momentum	$p_T > 25$ GeV
Pseudorapidity range	$\lvert\eta\rvert < 2.5$
Pile-up suppression	JVT> 0.50 for $p_T < 60$ GeV and $\lvert\eta\rvert < 2.4$

5.5.4 Reclustered jets

All reclustered jets in this analysis are required to have a transverse momentum higher than 200 GeV and pseudorapidity $|\eta| < 2.0$. The comparatively low p_T threshold motivates the use of reclustered jets in this analysis in lieu of centrally calibrated DNN-top-tagged anti-k_T R=1 jets, which are only calibrated at $p_T > 350$ GeV [143]. Additionally, reclustered jets are required to have at least two constituent jets, to mitigate JER effects, which are dominant for single-constituent jets. The selection criteria for all reclustered jets in this search are summarised in Table 5.5. They are applied to both VRC and RC jets.

Table 5.5: Reclustered jet selection criteria.

Feature	**Criteria**
Transverse momentum	$p_T > 200$ GeV
Pseudorapidity range	$\|\eta\| < 2.0$
Number of constituents	> 2

CHAPTER 6

Analysis strategy

The analysis presented in this thesis targets the search for heavy (pseudo)scalars decaying to a top-antitop quark pair. This thesis focuses on one-lepton final states, as described in section 2.2.2. Two-lepton final states are also part of the search. Separate sets of selection requirements are used to define orthogonal one- and two-lepton signal regions, which are statistically combined to yield the highest sensitivity to BSM signatures. It is important to highlight that, in the context of this search, the word *lepton* (ℓ) is only used to refer to electrons and muons. Top-quark decays involving τ leptons are not explicitly included in the one- and two-lepton categories, however $t\bar{t}$ decays involving fully-leptonic τ decays lead to ℓ+jets final states and are therefore also selected by the signal-region requirements and accounted for in the calculation of the ℓ+jets $t\bar{t}$ branching ratio.

6.1 Final state and event topologies

The final state of the one-lepton channel is characterised by a charged lepton, large missing transverse momentum, and two to four jets from the $t\bar{t}$ decay, depending on the momentum of the $t\bar{t}$ pair. Two jets are expected to arise from the two b-quarks from the decays of the top and anti-top quark, respectively. The search targets a mass range for the $t\bar{t}$ pair up to 2000 GeV, which results in high-p_T top-quark decays in the tail of the $m_{t\bar{t}}$ spectrum. The decay products of the top quark get more collimated with increasing p_T; this means that in the one-lepton channel, one must consider topologies where the hadronically decaying top quark is not reconstructed using three jets, one for each quark from its decay, but a smaller number of jets. Three topologies are possible in the one-lepton channel:

1. Resolved: the decay of the hadronic top quark is reconstructed using three small-R jets corresponding to the b-jet from the top-quark decay and the two light-quark jets from the decay of the W boson;

2. Semi-merged: two of the jets from the decay of the hadronic top quark merge into a single one, and the top-quark decay is reconstructed using one small-R jet and one large-R jet;

3. Merged: all of the jets from the decay of the hadronic top quark merge into a single one, and the top-quark decay is reconstructed using a single large-R jet.

Figure 6.1 shows a visual representation of the three possible topologies in the one-lepton channel. Of the three topologies, only the resolved and merged ones are included in the event selection and

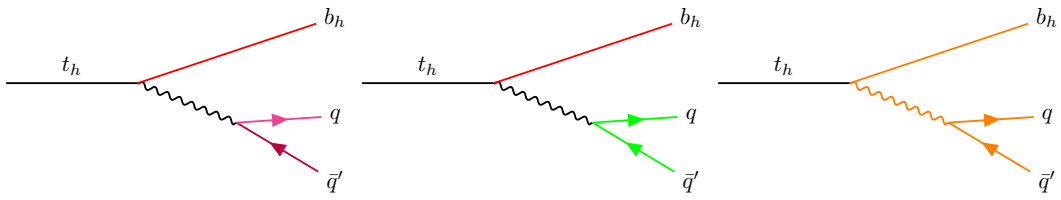

(a) Resolved (b) Semi-merged (c) Merged

Figure 6.1: Schematic depiction of the three possible decay topologies in the one-lepton channel. t_h and b_h represent the hadronically-decaying top quark and the b-quark produced in this decay. Lines of the same colour are reconstructed as a single analysis object. Note that these are not Feynman diagrams, despite the similarity in style.

reconstruction strategy. The introduction of a separate category for events with a Semi-merged topology was investigated and is described in section 6.6 but is not part of the final strategy.

The two-lepton channel is characterised by the presence of two charged leptons in the final state, from the semileptonic decays of the top and the anti-top quark.

6.2 Event selection in the one-lepton channel

6.2.1 Preselection

The preselection requirements in this analysis are based on the recommendation from the Data Preparation Group and are summarised in the following.

Data quality

To ensure good quality of data, data events are required to belong to a luminosity block contained in the Good Run List. This ensures that data collected during temporary malfunctions of the detector, such as incomplete detector information or noise bursts in the LAr calorimeter, is not used in the analysis.

Primary vertex selection

Only events containing a primary vertex with at least two associated tracks are kept. The primary vertex is selected as the vertex with the highest sum of squared transverse momenta of associated tracks in the event; only tracks with $p_T > 0.5$ GeV are considered. This requirement serves to reject events that do not originate from a collision, but from external factors, such as cosmic rays or background radiation in the cavern.

6.2.2 Trigger selection

Events are recorded that pass a variety of different triggers, which require the presence of at least one lepton in the final state. The same trigger selection is applied in simulation as well, and correction factors are applied to the simulated samples to reproduce the performance in data. Both analysis channels rely on an OR combination of single-electron and -muon un-prescaled triggers. Trigger

pre-scaling is a procedure applied to only allow a certain fraction of events satisfying the trigger requirements to be recorded, so that loose trigger requirements can be applied, while keeping the event rate low enough for data acquisition. For this analysis, the loosest un-prescaled electron [144] and muon [145] triggers are used, requiring at least one electron or muon passing with a transverse momentum/energy above a certain threshold. The threshold depends on the data-taking year and the lowest muon p_T (electron E_T) threshold is applied on data collected in 2015 and is equal to 20 (24) GeV. An additional isolation requirement is included in some of the triggers to relax the p_T threshold. Table 6.1 summarises all the used triggers and their requirements.

Table 6.1: Summary of the used triggers and their requirements.

Year	**p_T threshold (GeV)**	**Isolation**
Electron triggers		
2015	24	Yes
2015	60	No
2015	120	No
2016-2018	26	Yes
2016-2018	60	No
2016-2018	140	No
Muon triggers		
2015	20	Yes
2015	50	No
2016-2018	26	Yes
2016-2018	50	No

6.2.3 Common selection

Lepton selection

Events must contain exactly one electron or muon passing the requirements in Sections 5.5.1 and 5.5.2, respectively, and with a transverse momentum higher than 28 GeV. The p_T threshold is higher than all of the trigger thresholds for isolated leptons, to ensure that all triggers are fully efficient. The electron or muon is also required to be matched within $\Delta R < 0.15$ to its corresponding trigger object.

Requirements on $\mathbf{p_T}^{\mathbf{miss}}$

The semileptonic top-quark decay in the one-lepton channel comes with a significant amount of missing transverse energy due to the presence of a neutrino in the final state. Strong multijet production can also come with a typically smaller amount of missing transverse energy due to leptonic decays in heavy-flavoured jets or mismeasurements of jet energy; the requirement $E_T^{\text{miss}} > 20$ GeV is applied to suppress the aforementioned background process. Multijet production has a cross-section orders of magnitude above that for $t\bar{t}$ and is difficult to model, hence its suppression is crucial for the accuracy

of the search. Additionally, events must satisfy the requirement $E_T^{\text{miss}} + m_T^W$ >60 GeV, where

$$m_T^W = \sqrt{2p_T^\ell E_T^{\text{miss}} \left(1 - \cos\Delta\phi(\mathbf{p_T^\ell}, \mathbf{p_T^{\text{miss}}})\right)},$$

in order to suppress background processes in which the $\mathbf{p_T}^{\text{miss}}$ does not arise from a leptonic W boson decay.

6.2.4 Merged selection

Additional requirements are applied on top of the common selection described in Section 6.2.3 to select events with a fully merged hadronic top-quark decay.

For events with a merged topology, we assume both the top and antitop quarks to have a high p_T. This implies that not only the products of the hadronically-decaying top quark are collimated, but also the ones of the semileptonically-decaying top quarks. For this reason, the candidate b-jet from the semileptonic top decay, or b_ℓ-*candidate-jet*, by requiring it to be close to the selected lepton. More precisely, at least one selected small-R jet in the event needs to satisfy the condition $\Delta R(\text{jet, lepton}) < 2.0$. The b_ℓ-candidate-jetis not explicitly required to be b-tagged. However, if more than two jets satisfy the proximity requirement, the b-tagging information is used to resolve the ambiguity. If several or no candidates are b-tagged, the jet with the highest transverse momentum is chosen as b_ℓ-candidate-jet.

For reconstructing the hadronic top-quark decay, at least one selected reclustered large-R jet with a mass higher than 100 GeV is required in the event. The mass condition is a fairly loose top-tagging requirement. Additional requirements to select the topology of a merged hadronic top-quark decay are:

- $\Delta R(\text{RC-jet}, \ell) > R_{\text{max}}$,
- $\Delta R(\text{RC-jet}, b_\ell\text{-candidate-jet}) > R_{\text{max}}$,

where R_{max} is the maximum radius used in the reclustering algorithm described in Chapter 5. The value $R_{\text{max}} = 1.5$ is chosen for the hadronic top-quark candidate. Note that $R_{\text{max}} = 1.0$ is used for the alternative signal region definitions based on fixed-radius reclustered jets described in Section 6.6. The angular requirements ensure that there is no overlap between the decay products from the semileptonic and hadronic top-quark decays and favour events with a loosely back-to-back $t\bar{t}$ topology. At least one b-tagged small-R jet must be present in the event. The choice of not requiring exactly two b-tagged small-R jets comes from the desire to keep a high signal selection efficiency. By dividing the events into b-tagging categories as described in Section 6.4, one is able to keep a high signal selection efficiency, while also defining a region depleted of background events.

6.2.5 Resolved selection

The resolved-topology selection is applied only to events that fail the merged-topology selection. This is because the $m_{t\bar{t}}$ resolution obtained with the merged-topology reconstruction is better than that obtained with the resolved-topology reconstruction, when applicable (see Section 6.6.1). A better $m_{t\bar{t}}$ resolution allows the search to be sensitive to narrower interference patterns.
Events in the resolved topology must have exactly four selected small-R jets: three coming from the hadronic top-quark decay and one from the semileptonic top-quark decay. The $t\bar{t}$ system is

reconstructed using a χ^2-algorithm which is described in section 6.3.3 . Only well reconstructed events, passing the requirement $\log_{10}\chi^2 < 0.9$ are kept. All events must contain at least one b-tagged selected small-R jet.

A summary of all selection requirements for events in the one-lepton channel is in Table 6.2.

In Figure 6.2, the product of selection efficiency and acceptance, including the branching ratio for the ℓ+jets final state, is depicted for both resolved and merged event categories, separately events with an electron (e+jets) and a muon (μ+jets) in the final state. For context, the branching ratio for $t\bar{t}$ to e+jets or μ+jets final states is approximately 17% for each lepton flavour, factoring in leptonic τ-lepton decays [23]. The merged-topology selection dominates the selection efficiency times acceptance for $t\bar{t}$ invariant mass values $m_{t\bar{t}} > 600$ GeV, whereas the resolved-topology selection covers the low-$m_{t\bar{t}}$ region down to the kinematic threshold of the $t\bar{t}$ production. These distributions correspond to the scenario involving a single pseudoscalar A, with similar outcomes observed for a single scalar H.

Table 6.2: Summary of the event selection criteria used in the one-lepton channel.

Selection	**Criteria**
	Common Selection
Run and event cleaning	Data events in GRLs (2015-2018); jet cleaning, primary vertex selection, Remove LAr noise bursts, tile and SCT errors, incomplete events.
Single lepton trigger	Separate single-electron or single-muon triggers
Exactly one lepton	== 1 e or μ with $p_T > 28$ GeV
E_T^{miss} cut	$E_T^{\text{miss}} > 20$ GeV
	$E_T^{\text{miss}} + m_T^W > 60$ GeV
b-tagging	≥ 1 b-tagged jet
	Merged Selection
Large-R jet	≥ 1 large-R jet, $p_T > 200$ GeV
Top tagging	Large-R jet mass consistent with top quark mass: $m > 100$ GeV
Close-to-lepton jet	≥ 1 jet with ΔR (ℓ, R=0.4 jet) $< 2.0 \rightarrow$ **b_ℓ-candidate-jet**
	ΔR (b_ℓ-candidate-jet, ℓ) < 2.0
No overlab between $t\bar{t}$ decay products	ΔR (RC-jet, b_ℓ-candidate-jet) > 1.5
	ΔR (b_ℓ-candidate-jet, ℓ) > 1.5
	Resolved Selection
At least four jets	≥ 4 jets, $p_T > 25$ GeV
Well-reconstructed $t\bar{t}$ system	$\log_{10}(\chi^2) < 0.9$ (Section 6.3.3)
Veto events passing the merged selection	

6.3 Event reconstruction in the one-lepton channel

The reconstruction of the invariant mass $m_{t\bar{t}}$ of the $t\bar{t}$ system in the one-lepton channel is described below. Reconstruction strategies vary based on the event topology.

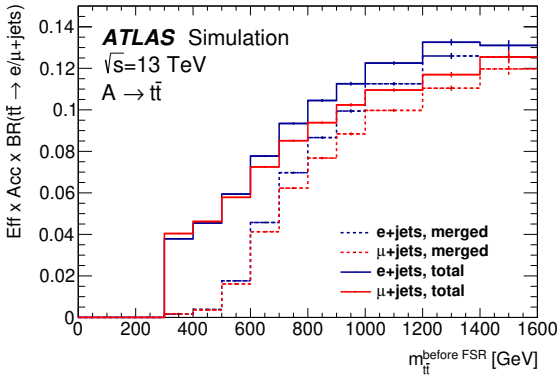

Figure 6.2: Selection efficiency times acceptance times $t\bar{t}$ branching ratio for the ℓ+jets ($\ell \in e, \mu$) final state (Eff x Acc x BR) as a function of the $t\bar{t}$ invariant mass at the parton level before the emission of FSR [19]. The distributions are obtained from all generated type-II 2HDM pure-signal pseudoscalar samples in the mass range 400 – 1400 GeV. The error bars correspond to the statistical uncertainty on the distributions.

6.3.1 Neutrino reconstruction

The first step in the reconstruction of the $t\bar{t}$ system is the reconstruction of the four-momentum of the neutrino from the semileptonic top-quark decay. Its transverse momentum is taken as the missing transverse momentum of the event, $\mathbf{p_T}^{\text{miss}}$. The longitudinal component of the momentum cannot be measured directly, so it is calculated from a kinematic constraint: the Minkowski norm of the four-vector given by the sum of the neutrino and selected lepton four-momenta must yield the squared mass of the W-boson

$$\left(p^{\ell} + p^{\nu}\right)^2 = m_W^2. \tag{6.1}$$

If the resulting quadratic equation has exactly one real solution for p_z^{ν}, this solution is taken as the neutrino longitudinal momentum. If there is no real solution, the missing transverse momentum vector is rescaled and rotated by a minimal amount to obtain exactly one real solution, under the assumption that there has been a mismeasurement of $\mathbf{p_T}^{\text{miss}}$. Finally, if two real solutions exist, two different strategies are followed for the resolved and merged topologies. In the merged topology, the solution with the smallest p_z^{ν} is kept; in the resolved topology, the choice is based on the χ^2 algorithm (see Section 6.3.3) and the solution yielding the smallest χ^2 is kept. Finally, the energy of the neutrino is obtained under the assumption that the neutrino is a massless particle.

6.3.2 Merged topology

In the merged topology, the selected large-R jet passing the requirements in Section 5.5.4 is identified with the hadronically decaying top quark. If more than one selected large-R jet satisfies the requirements, the hadronic top-quark candidate is selected as the jet with the highest transverse momentum. The semileptonically decaying top-quark is reconstructed from the candidate b-jet from the semileptonic top decay b_ℓ-candidate-jet described in Section 6.2.4, and the selected lepton and from the reconstructed neutrino.

6.3.3 Resolved topology

The assignment of the four small-R jets to the hadronically- and leptonically-decaying top quarks in the resolved topology is made by means of a χ^2 minimisation procedure. A χ^2 function is defined as follows:

$$\chi^2 = \left[\frac{m_{jj} - m_W}{\sigma_W}\right]^2 + \left[\frac{(m_{jjb} - m_{jj}) - m_{t_h - W}}{\sigma_{t_h - W}}\right]^2 + \left[\frac{m_{jl\nu} - m_{t_l}}{\sigma_{t_l}}\right]^2 + \left[\frac{(p_{T,jjb} - p_{T,jl\nu}) - (p_{T,t_h} - p_{T,t_l})}{\sigma_{\text{diff}p_T}}\right]^2. \tag{6.2}$$

All permutations of all selected jets are considered, and the jet assignment yielding the minimum χ^2 value is used for the reconstruction of the $t\bar{t}$ system. If two solutions are obtained for the longitudinal momentum of the reconstructed neutrino, both are considered and the one yielding the lower χ^2 is chosen. The number of possible permutations is reduced by allowing the b-tagged jets in the event to be assigned only to one of the b-quarks produced in the decay of the top quarks. The first term in Equation 6.3.3 requires the mass of a jet pair, m_{jj}, to be close to the mass of the W-boson. The second term requires the mass of a three-jet system, m_{jjb}, to be close to the mass of the top quark; in order to reduce the correlation with the first term, the difference of the masses of jjb system and the jj system is matched to mass of the hadronically-decaying-top-minus-W-boson four-vector. The third term is analogous to the second one, but for the semileptonically-decaying top. Finally, the last term constrains the momenta of the two top quarks to be similar. All the parameters in the χ^2 function are derived by Gaussian fits on $Z' \rightarrow t\bar{t}$ MC events, where the lepton, jets and reconstructed neutrino have been matched to the lepton, quarks and neutrino from the hard-scattering process via angular requirements. The parameters m_W, $m_{t_h - W}$, m_{t_ℓ}, and $(p_{T,t_h} - p_{T,t\ell})$ are the central values from the Gaussian fits, while σ_W, $\sigma_{t_h - W}$, σ_{t_l} , and $\sigma_{\text{diff}p_T}$ are the standard deviations.

Scaled χ^2 algorithm

The $m_{t\bar{t}}$ resolution from the χ^2 algorithm is improved by an in-situ calibration making use of the high accuracy of our knowledge of the masses of the top quark and of the W boson. The momenta of the two jets assigned to the decay of the W boson from the hadronic top decay are scaled to yield a total invariant mass equal to the W boson mass. The correction factor α is therefore

$$\alpha = \frac{80.4\ \text{GeV}}{m_{jj}}, \tag{6.3}$$

where m_{jj} is the reconstructed mass of the two-jets system.
Then the momentum of the third jet assigned to the hadronically-decaying top-quark is scaled so that the three-jet system yields the top-quark mass. The correction factor β for the third jet is obtained as the positive solution to the equation

$$m_b^2\beta^2 + \left(m_{jjb}^2 - \alpha m_{jj}^2 - m_b^2\right)\beta - M_{\text{top}}^2 + \alpha m_{jj}^2 = 0, \tag{6.4}$$

where m_{jjb} is the reconstructed mass of the three-jets system, m_b is the mass of the third jet, and $M_{\text{top}} = 173.3$ GeV is the top-quark mass.

The scale factors obtained with this method are in the ranges $0.90 - 1.00$ and $0.88 - 1.10$, respectively. The jet energy corrections are thus consistent with the magnitude of the uncertainties on JES and JER

used in this search [134].

A similar correction to the candidate b-jet from the semileptonic top-quark decay was tested, but the correction factors reached values up to 25%, which are notably larger than the values expected from the JES and JER uncertainties. Thus, no scaling is applied to the jet assigned to the semileptonically-decaying top quark as a sub-optimal reconstruction of this decay is likely linked to the neutrino reconstruction and might come from uncertainties in the estimation of the missing transverse momentum of the event rather than the JER.

6.4 Signal region definition in the one-lepton channel

The selection requirements introduced in Section 6.2 yield two orthogonal event categories, i.e. resolved and merged channels. Events in the resolved channel are further split into two categories, based on the number of b-tagged jets among the selected small-R jets:

- **Resolved 1b:** either the hadronic top-quark candidate or the semileptonic top-quark candidate have a matching b-tagged jet ;
- **Resolved 2b:** both the hadronic and semileptonic top-quark candidates have a matching b-tagged jet.

The matching between the b-tagged jets and the hadronic/semileptonic top-quark candidates is performed by checking whether one of the small-R jets assigned to the $t\bar{t}$ decay by the χ^2-algorithm (section 6.3.3) is b-tagged. Figure 6.3 shows the background composition in the Merged, Resolved 2b and Resolved 1b signal regions. The Resolved 2b region has the highest $t\bar{t}$ purity thanks to the 2 b-jets requirement.

An angular variable $\cos\theta^*$ offers a good discrimination power between the signal and $t\bar{t}$ background processes. θ^* is defined as the angle between the momentum of the semileptonically decaying top quark in the $t\bar{t}$ rest frame and the direction of flight of the $t\bar{t}$ system in the laboratory frame, as illustrated in Figure 6.4. In the presence of a signal $gg \rightarrow A/H \rightarrow t\bar{t}$, the heavy Higgs would decay isotropically, resulting in a flat $\cos\theta^*$ distribution before event selection. This is not the case for the SM $t\bar{t}$ background, which includes t-channel diagrams at first order; for this background, the $\cos\theta^*$ distribution peaks at ± 1, in the kinematic regime considered in this search. In both cases, the distribution of $\cos\theta^*$ is symmetric around 0. Figure 6.5 shows the ratio between the distributions of the $|\cos\theta^*|$ variable for the SM $t\bar{t}$ plus 2HDM sample and for the pure SM $t\bar{t}$ sample; multiple representative signal points are considered, separately in the Resolved 1b and Resolved 2b regions.

A splitting of the signal regions in bins of $|\cos\theta^*|$ allows to isolate regions, at low $|\cos\theta^*|$, where the deviation from the SM, in the presence of a 2HDM signal, is maximal. The signal regions are split according to five bins in $|\cos\theta^*|$ are defined:

- $|\cos\theta^*| < 0.2$;
- $0.2 \leq |\cos\theta^*| < 0.4$;
- $0.4 \leq |\cos\theta^*| < 0.6$;
- $0.6 \leq |\cos\theta^*| < 0.8$;

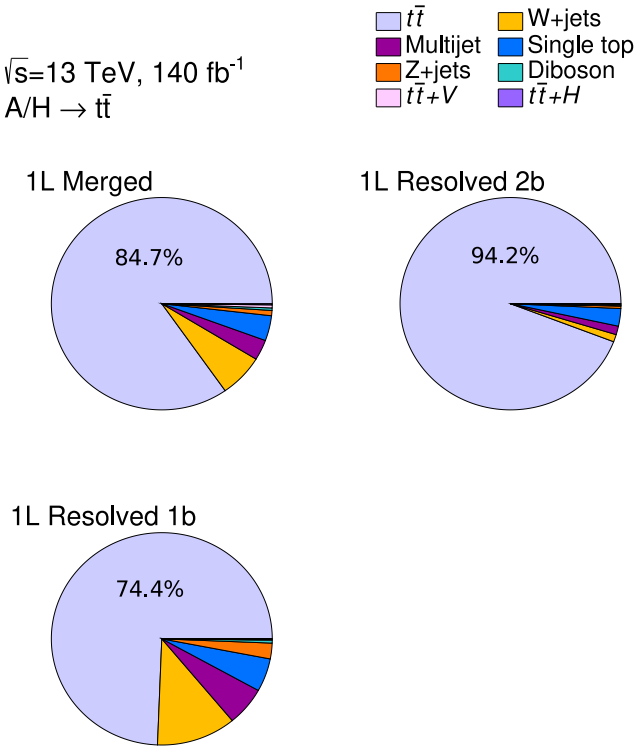

Figure 6.3: Background composition in the merged, resolved 1b and resolved 2b signal regions.

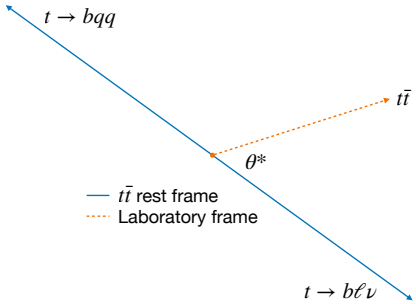

Figure 6.4: Definition of the angular variable θ^*. Momenta in different coordinates systems are shown with lines in different styles and colours

- $0.8 \leq |\cos\theta^*|$.

This results in a total of eleven signal regions, ten in the resolved topology, and one in the merged topology. The gain in sensitivity to the signal processes due to the angular splitting is discussed in Section 6.6. The background composition for the ten orthogonal resolved signal regions is shown in Figure 6.6.

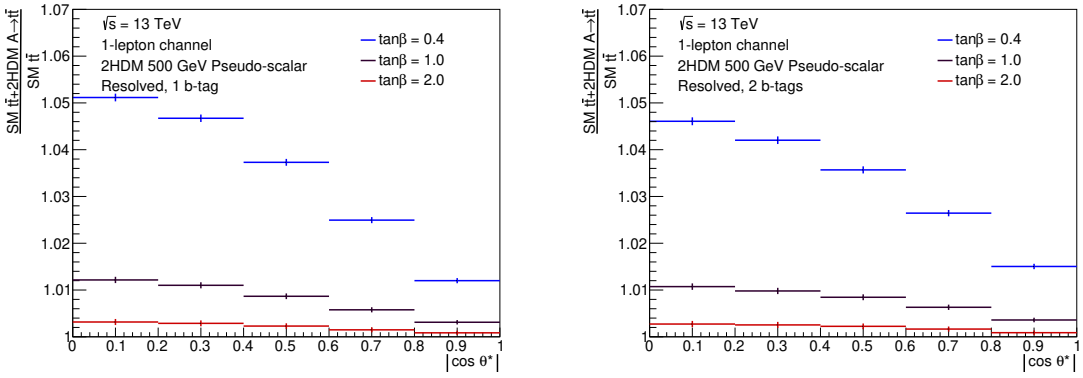

(a) Resolved 1b

(b) Resolved 2b

Figure 6.5: Ratio between the SM $t\bar{t}$ +2HDM (including the contribution of signal-background interference) and SM $t\bar{t}$ distribution of $|\cos\theta^*|$ for a few representative pseudoscalar signals, with a mass of 500 GeV in the Type-II 2HDM model, in the Resolved 1b and Resolved 2b regions.

6.5 Event selection and categorisation in the two-lepton channel

Events in the two-lepton channel must pass the same trigger, data quality, and primary vertex selection as in the one-lepton channel. Additionally, exactly two leptons passing the requirements in Section 5.5.1 or 5.5.2 are required. At least one of the selected leptons must have a transverse momentum higher than 28 GeV and must be matched with the corresponding trigger object using the same criteria as in the one-lepton channel (Section 6.2.3). The two leptons must have opposite charges. At least two small-R jets must be present, and at least one of them must be b-tagged. The mass of the lepton-b-jet pair $m_{\ell b}$ is required to be lower than 150 GeV for at least one of the two possible lepton-b-jet assignments, in order to veto events where the lepton-b-jet pair is not coming from a top-quark decay. The b-jet candidates are chosen as the two b-tagged jets with the largest transverse momentum in the event, if at least two are present; otherwise, the only b-tagged jet is used as one b-jet candidate, while the other is the leading jet in p_T among the remaining ones. Based on the flavour of the selected leptons, three event categories are defined: ee, $e\mu$ and $\mu\mu$. In order to reject contributions to the event yield coming from Z+jets production, additional requirements are applied to the ee and $e\mu$ categories:

- The missing transverse energy in the event must be higher than 45 GeV;
- The mass of the ee or $\mu\mu$ pair must be higher than 15 GeV, to suppress the Drell-Yan process mediated by a photon, and not within the Z-boson mass window, i.e. $\notin [81, 101]$ GeV.

Events are split into five orthogonal signal regions according to equidistant bins of the angular variable $\Delta\phi_{\ell\ell}$, the azimutal angle between the two leptons in the event. Figure 6.7 shows the distribution of the reconstructed $\Delta\phi_{\ell\ell}/\pi$ after the signal selection of the two-lepton channel for the SM backgrounds. In the ratio panel, the expected deviation from the SM in the presence of an interference pattern is shown for two representative Type-II 2HDM hypotheses. The variable $\Delta\phi_{\ell\ell}$ offers a good discrimination power between the SM and the BSM hypothesis.

The invariant mass of the $t\bar{t}$ system cannot be unambiguously reconstructed due to the presence of the two neutrinos from the two semileptonically decaying top quarks in the event. For this reason,

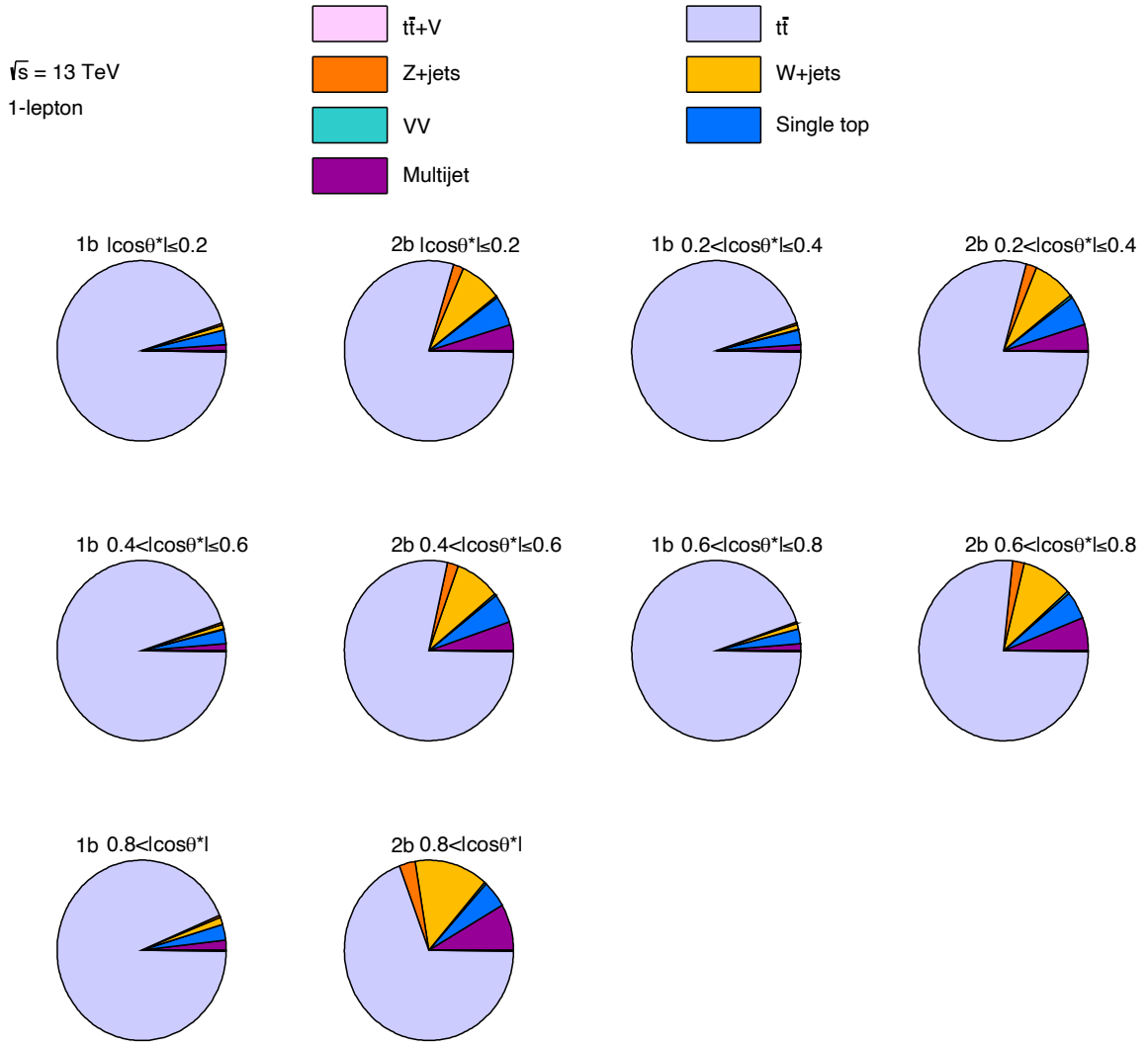

Figure 6.6: Background composition in the ten resolved signal regions. The signal regions are defined based on the number of b-tagged jets in the event (one or two) and according to equidistant bins of the angular variable $\left|\cos\theta^*\right|$.

the invariant mass of the di-lepton plus di-jet system, $m_{\ell\ell bb}$, is used as variable of interest in the two-lepton channel for the statistical analysis.

6.6 Optimisation of the one-lepton signal region definition

The choice of the event categorisation described in Section 6.4 is the result of the studies of different signal-region definitions described in this section. The aim of these studies was to obtain the highest expected sensitivity to the BSM benchmark models considered for the search presented in this thesis.

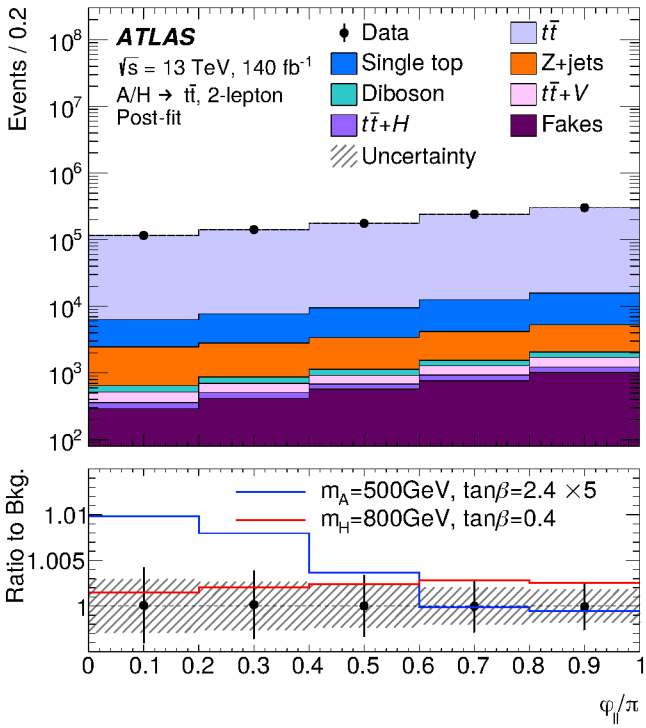

Figure 6.7: Distribution of the reconstructed $\Delta\phi_{\ell\ell}/\pi$ after the signal selection of the two-lepton channel for the SM backgrounds. The expected deviation from the SM in the presence of an interference pattern is also shown for two representative points in the ratio panel [19]

.

In Section 6.6.1, the strategy for the reconstruction of hadronic top-quark decays in a kinematic regime in which the top quark is moderately boosted is discussed. In Section 6.6.2, the effect of the splitting of the signal regions into bins of the angular variable $|\cos\theta^*|$ is presented. This is the first time that a signal region definition based on this variable is used in an ATLAS search in a $t\bar{t}$ final state.

6.6.1 Reconstruction of moderately boosted hadronic top-quark decays

The angular distance between the decay products of a heavy particle is given approximately by Equation 5.4.4 and is inversely proportional to the transverse momentum of the mother particle. The hadronic top-quark decay can follow one of the three topologies described in Section 6.1 (Figure 6.1), depending on the transverse momentum of the top quark and the choice of the radius parameter in the jet algorithm. The Merged topology is realised if the decay products of the top quark are very collimated, i.e. $\Delta R \lesssim 1.0$ and $p_T^{\text{top}} \gtrsim 350$ GeV. The Resolved topology is realised if the decay products of the top quark are well separated, i.e. if $\Delta R \gtrsim 1.5$ and $p_T^{\text{top}} \lesssim 230$ GeV. In order to guarantee a seamless transition from the Resolved to the Merged topology in the region of phase space in which the top quark is moderately boosted (230 GeV $\lesssim p_T^{\text{top}} \lesssim$ 350 GeV), two strategies are possible:

1. **VRC strategy**: Signal regions are only defined in the Resolved and Merged topologies. A variable-radius reclustering algorithm is used for large-R jets in the Merged region, with a

maximum radius of 1.5, as described in Section 5.4.4. This jet algorithm automatically adapts to the kinematics of the top-quark decay. The large maximum radius allows to reconstruct the hadronic top-quark decay using a single large-R jet, even if it is not highly boosted. This is the strategy which was eventually adopted, and details on the event selection and reconstruction for this strategy can be found in Sections 6.2 and 6.3.

2. **RC strategy**: Signal regions are defined for the Resolved, Merged, and Semi-merged topologies. The Semi-merged region ensures high-quality reconstruction of hadronic top-quark decays also if the top quark is moderately boosted. A fixed-radius reclustering algorithm with $R = 1$ is used for large-R jets in the Merged and Semi-merged regions, as described in Section 5.4.4.

Event selection and reconstruction with the RC strategy in the Resolved and Merged regions, closely follow the ones for the VRC strategy, with the only exception of different orthogonality requirements. The orthogonality between the three signal regions in the alternative fixed-radius RC jets based approach is ensured by giving the highest priority to the Merged topology, followed by the Semi-merged one and the Resolved one in this order. For the sake of simplicity, events are not categorised into b-tagging categories nor bins of angular variables for the studies in this section.

Event selection and reconstruction for the Semi-merged topology

Events in the Semi-merged region are required to contain at least one RC jet with a mass compatible with that of a W boson, and two additional selected small-R jets ($60 < m < 100$ GeV). This requirement relies on the assumption that the decay of the W boson from the hadronic top is reconstructed with a single RC jet, and the remaining b-jet from the top decay is reconstructed separately. While the case where the b-jet and a light quark from the W-boson decay merge into a single RC jet is not explicitly considered in this context, events in this topology can still pass the requirements for the Semi-merged topology selection.

The candidate b-jet from the semileptonic top-quark decay is selected exactly as in the case of the Merged-topology selection(Section 6.3.2).

In addition to the mass requirement, events in the Semi-merged topology selection must have at least one selected RC jet passing the following additional requirements to be considered as W-candidate jet:

- No b-tagged-jet within W-candidate jet: ΔR(W-candidate, b-tagged jet(s)) >1.0,
- ΔR (b_ℓ-candidate-jet, ℓ) < 2.0
- ΔR (W-candidate, b_ℓ-candidate-jet) > 1.0
- ΔR (W-candidate, ℓ) > 1.0
- At least 1 selected small-R close to but not within W-candidate jet:
  $1.0 < \Delta R(W\text{-candidate}, \text{small-}R \text{ jet}) < 2.0$.

In the rare cases when there is more than one selected small-R close to the W-candidate jet, the small-R jet with the highest transverse momentum is chosen as candidate b-jet from the hadronic top-quark decay. Additionally, at least one b-tagged jet must be present in the event.

The hadronically decaying top quark in the Semi-merged topology is reconstructed by summing the four-momenta of the W-candidate jet, the b_ℓ-candidate-jetand the candidate b-jet from the hadronic

top-quark decay introduced above. The semileptonically decaying top quark is reconstructed in the same way as in the Merged category (Section 6.3.2).

Mass resolution

A good $m_{t\bar{t}}$ resolution is of great importance to enhance the sensitivity of the search presented in this thesis to narrow interference patterns. For example, in the context of the Type-II 2HDM benchmark, a good $m_{t\bar{t}}$ resolution enhances the sensitivity to high-tanβ hypotheses, which predict a narrow deficit of events at the mass of the BSM (pseudo)scalar state.

The estimation of the $m_{t\bar{t}}$ resolution is based on Gaussian fits on the variable

$$\frac{\Delta m}{m} = \frac{m_{t\bar{t}}^{\text{reco}} - m_{t\bar{t}}^{\text{afterFSR}}}{m_{t\bar{t}}^{\text{afterFSR}}}. \tag{6.5}$$

The resolution is estimated as the standard deviation from the Gaussian fit. No orthogonality requirement on the signal regions is applied for this study. Figure 6.8 shows the $m_{t\bar{t}}$ resolution as a function of the mass m_A of the pseudoscalar A in a type-II 2HDM with $\tan\beta = 0.4$, for all topologies with the different analysis strategies. Pure-signal samples are used for this study.

The mass resolution obtained for the Resolved category is consistently worse than other topologies across the whole mass range. The Semi-merged reconstruction features the best resolution in most of the considered mass range. The superiority of the Semi-merged category with respect to the Resolved one is due to the smaller number of jet combinations in the event, which reduces the chance of mis-reconstructing the $t\bar{t}$ system due to a wrong assignment of the reconstructed jets to the final state partons. The Semi-merged reconstruction also has better performance than the Merged one in the considered mass range, as the hadronically-decaying top quark is only moderately boosted.

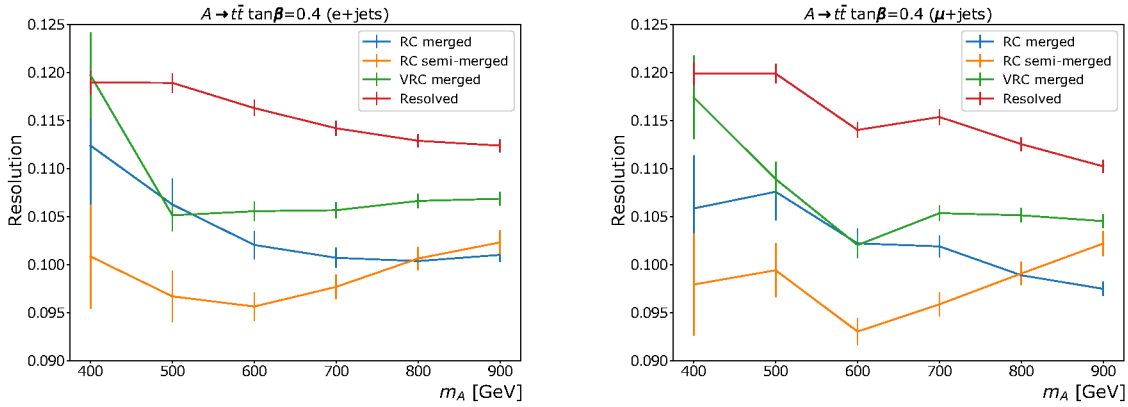

(a) e (b) μ

Figure 6.8: $m_{t\bar{t}}$ resolution as a function of the mass m_A of the pseudoscalar A in a type-II 2HDM with $\tan\beta = 0.4$, for all topologies with the different analysis strategies. Pure-signal samples are used for this study. Events containing an electron or a muon are considered separately. The resolved line is shared by both reclustering strategies.

Event yield

The effect of the jet reclustering and event categorisation strategy on the total number of pure-signal expected events (signal event yield) is discussed in the following. This is relevant not only because a higher count of signal events yields a higher sensitivity to BSM processes, but also because the different event topologies result in different $m_{t\bar{t}}$ resolutions. Hence, the relative contribution of different event topologies to the total event yield affects the sensitivity of the search to the selected BSM benchmark models. The event yield in different signal regions and for the two analysis strategies is shown in Figure 6.9, for multiple pseudoscalar Type-II 2HDM pure-signal hypotheses with $\tan\beta = 0.4$. The choice of reclustering algorithm does not heavily influence the total signal yield, but it affects the relative contribution of the different event categories. The VRC strategy yields a lower fraction of events in the Resolved category compared to the RC strategy. This is beneficial, as the Resolved category has the worst performance in terms of $m_{t\bar{t}}$ resolution.

Upper limits on the signal strength

The final choice of reclustering and event categorisation strategy depends on which one results in the highest sensitivity to BSM signals. In order to assess which strategy is most sensitive to BSM signatures, upper limits at 95% confidence level on the signal strength parameter (Section 7.2) are calculated. This is a different statistical procedure for deriving excluded regions in the BSM benchmark models from the one described in Section 7.5, consisting in determining the highest possible value of the signal strength which is not excluded. This strategy was used as a good proxy for the sensitivity of the search at a time when the final strategy for the statistical interpretation was not fully defined. At this stage, the focus was on the relative sensitivities of the VRC and RC strategies, rather than an accurate estimation of the excluded regions. Upper limits on the signal strength are evaluated neglecting the effect of systematic uncertainties for this study. Figures 6.10 and 6.11 show upper limits on the signal strength, for a selection of representative signal hypotheses involving a single scalar or pseudoscalar in a type-II 2HDM. Three different combinations of signal regions are considered:

- VRC: Merged and Resolved categories, using VRC jets to reconstruct merged top-quark decays.
- RC: Merged, Semi-merged, and Resolved categories, using fixed-radius RC jets to reconstruct the merged W-boson or top-quark decays.
- RC(Combined M+SM): Merged, Semi-merged, and Resolved categories, using fixed-radius RC jets to reconstruct the merged W-boson or top-quark decays. The Semi-merged and Merged categories are combined into a single one to disentangle the effect of the Semi-merged reconstruction from the effect of introducing an additional signal region on the sensitivity to the benchmark model.

The VRC strategy is found to provide the strongest expected sensitivity to the BSM hypotheses tested in this search. Reductions up to 20% in the upper limits are observed compared to the strategies based on RC-jets. Therefore the VRC strategy is chosen for the final signal-region definition in the search presented in this thesis.

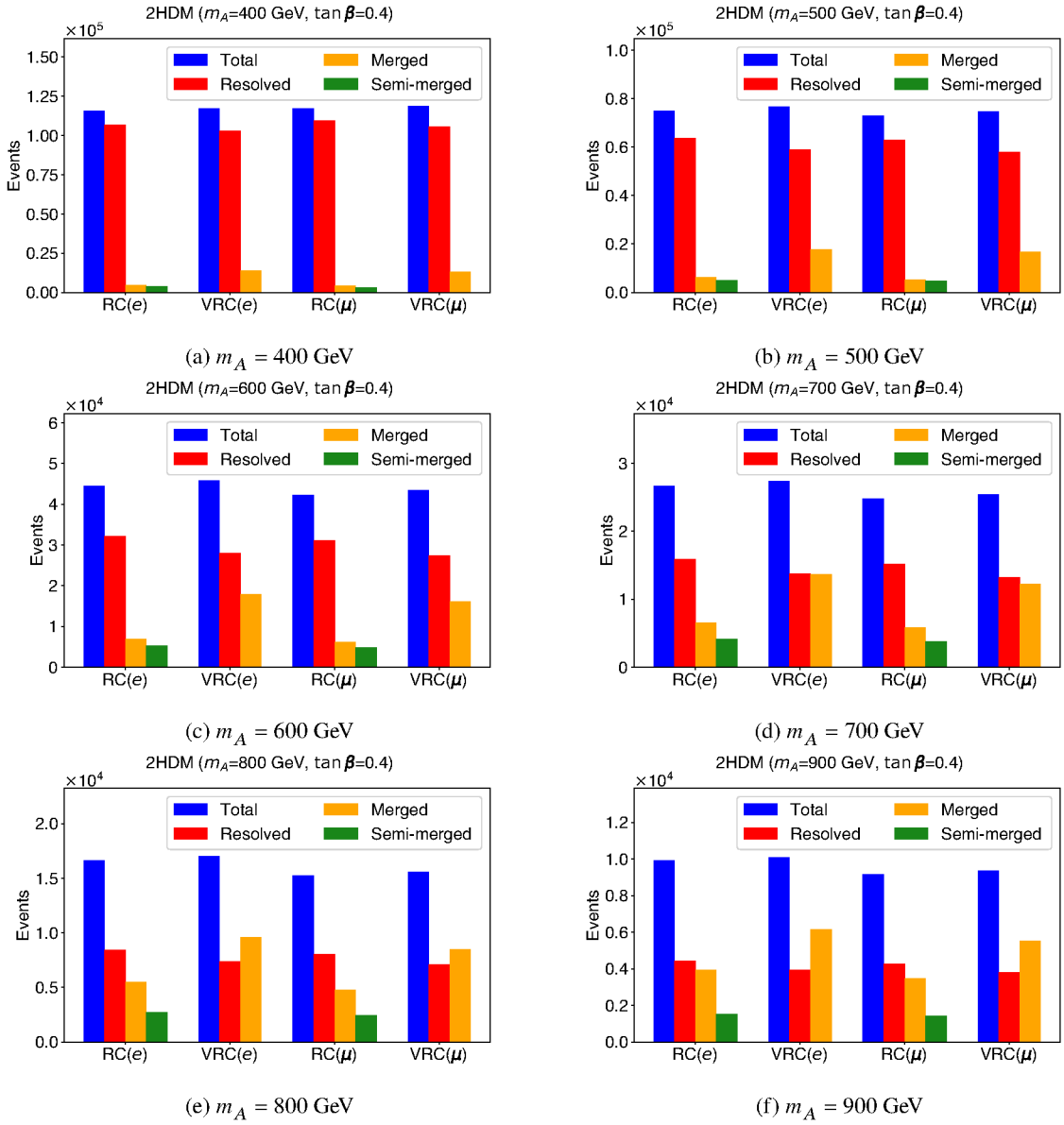

(a) m_A = 400 GeV (b) m_A = 500 GeV

(c) m_A = 600 GeV (d) m_A = 700 GeV

(e) m_A = 800 GeV (f) m_A = 900 GeV

Figure 6.9: Signal yield in different signal regions and for the two analysis strategies, for multiple pseudoscalar Type-II 2HDM pure-signal hypotheses with $\tan\beta = 0.4$. Each group of bars corresponds to a set of event categories for either the baseline VRC-based or the alternative RC-based categories in e+jets and μ+jets events, respectively. The first and third groups correspond to the RC-based categorisation, while the second and fourth groups correspond to the VRC-based baseline categorisation.

6.6.2 Angular categorisation

The splitting of the signal regions into bins of the angular variable $|\cos\theta^*|$ (Section 6.4) was introduced after verifying that it improves the sensitivity to BSM processes compared to a simpler approach in which the signal regions are not split by angular variables. This is an improvement compared to the

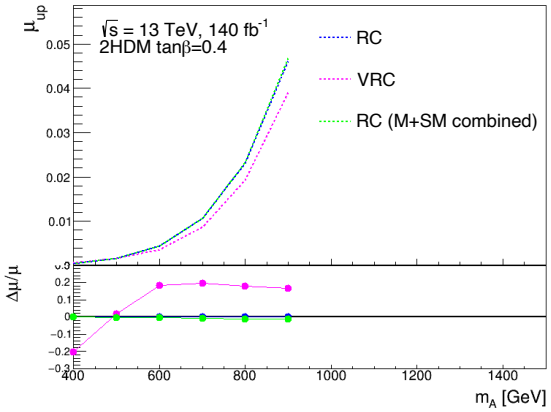

(a) $\tan\beta = 0.4$

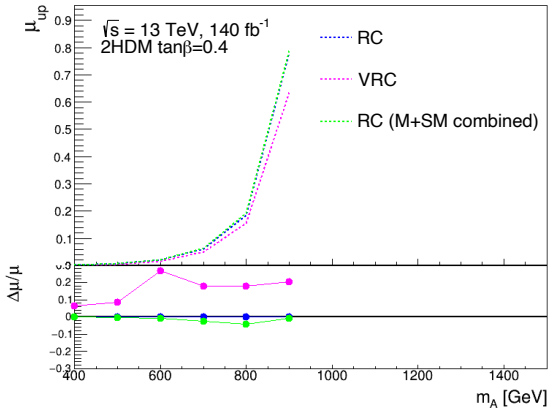

(b) $\tan\beta = 1.0$

Figure 6.10: Comparison of upper limits on the signal strength for a selection of representative signal hypotheses involving a single pseudoscalar in a type-II 2HDM. In the ratio panel, the RC strategy is taken as a reference, and the relative improvement in the upper limits for the other tested strategies is calculated as $\frac{\Delta\mu}{\mu} = \frac{\mu^{up}_{\text{ref}} - \mu^{up}_{\text{test}}}{\mu^{up}_{\text{ref}}}$.

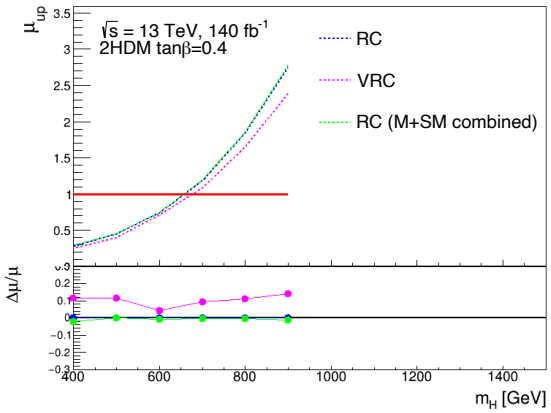

(a) $\tan\beta = 1.5$

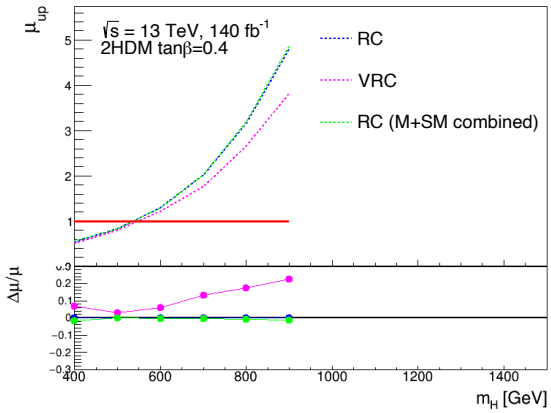

(b) $\tan\beta = 2.0$

Figure 6.11: Comparison of upper limits on the signal strength for a selection of representative signal hypotheses involving a single scalar in a type-II 2HDM. In the ratio panel, the RC strategy is taken as a reference, and the relative improvement in the upper limits for the other tested strategies is calculated as $\frac{\Delta\mu}{\mu} = \frac{\mu^{up}_{\text{ref}} - \mu^{up}_{\text{test}}}{\mu^{up}_{\text{ref}}}$.

previous ATLAS Run-1 result [17], where no angular categorisation was present. Figure 6.12 shows a comparison of upper limits on the signal strength for representative signal hypotheses involving both a scalar and a pseudoscalar with mA=mH in a type-II 2HDM, obtained with a simplified strategy without angular binning and with the more complex strategy relying on angular binning described in Section 6.4.

The splitting of signal regions into bins of $\left|\cos\theta^*\right|$ is found to be highly beneficial to the sensitivity to 2HDM signals. More specifically, the angular categorisation leads to stronger upper limits on the signal strength at different $\tan\beta$ values, with an almost uniform 20% improvement at $\tan\beta = 0.4$.

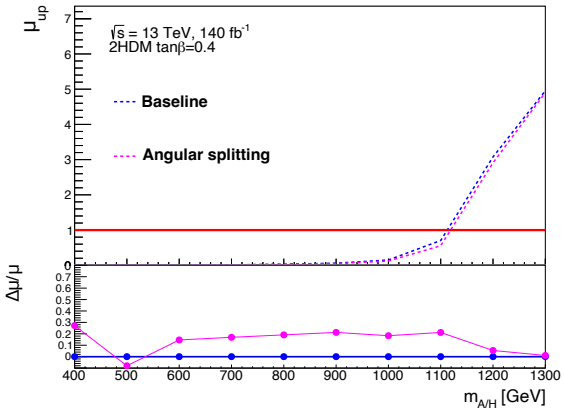

(a) $\tan\beta = 0.4$

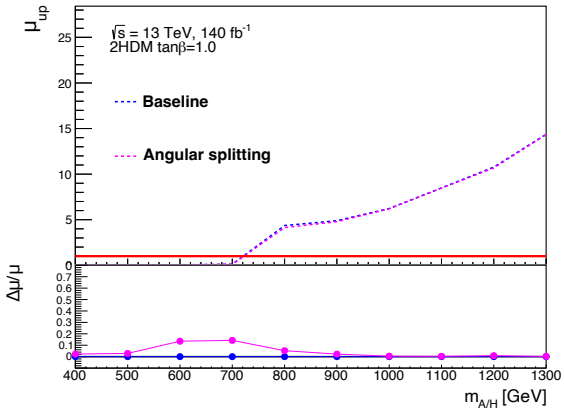

(b) $\tan\beta = 1.0$

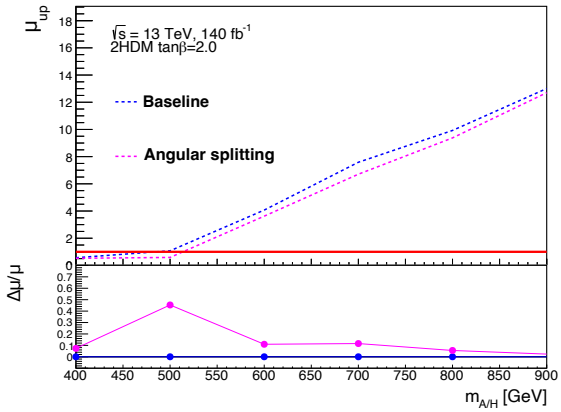

(c) $\tan\beta = 2.0$

Figure 6.12: Upper limits on the signal strength for representative signal hypotheses involving both a scalar and a pseudoscalar with $m_A = m_H$ in a type-II 2HDM, comparing the simplified strategy with the more complex strategy based on $|\cos\theta^*|$ bins. In the ratio panel, the simplified strategy is taken as a reference, and the relative improvement in the upper limits for the other tested strategies is calculated as $\frac{\Delta\mu}{\mu} = \frac{\mu^{up}_{\text{ref}} - \mu^{up}_{\text{test}}}{\mu^{up}_{\text{ref}}}$.

6.7 Data-driven background estimation and correction

6.7.1 W+jets background in the one-lepton channel

The background from W+jets production in the one-lepton channel is estimated with a hybrid strategy: the shape of the relevant kinematic variables is obtained from MC simulations, while the normalisation is corrected via data-driven scale factors. The derivation of scale factors relies on the fact that at pp colliders the production of W^+ bosons is favoured over W^- bosons. This is because the dominant mechanism for W+jets production in pp collisions is the scattering of u- and d- quarks, with $u\bar{d}$ annihilation producing a W^+ boson and $d\bar{u}$ annihilation producing a W^- boson. The u-quark PDF strongly outweighs the d-quark PDF, so the production of W^+ bosons is favoured. The resulting charge asymmetry is known very well and modelled very precisely in MC simulations, and can be used to obtain data-simulation scale factors. The scale factors are determined by comparing the measured W

boson charge asymmetry in data [146] with that predicted by the MC simulation. The total number of W+jets events is calculated in two ways: one purely based on MC simulation and one relying on data. In the data-based method, the number of W+jets events is seen as the product of the number obtained from MC simulation and a correction factor based on the charge asymmetry:

$$N_{W^+} + N_{W^-} = \left(N^+_{\mathrm{MC}} + N^-_{\mathrm{MC}}\right) \frac{D_+ - D_-}{N^+_{\mathrm{MC}} - N^-_{\mathrm{MC}}}, \tag{6.6}$$

where $D_{+(-)}$ is the number of observed data events with a positively (negatively) charged lepton in the same analysis region. Equation 6.6 can be rewritten introducing the ratio r_{MC} of the number of W+jets events with a positively charged lepton to that with a negatively charged lepton obtained from the MC simulation, which is simulated very precisely:

$$N_{W^+} + N_{W^-} = \frac{r_{\mathrm{MC}} + 1}{r_{\mathrm{MC}} - 1}(D_+ - D_-). \tag{6.7}$$

Hence, the number of W+jets events is given by the product of a very precisely simulated term and a charge-asymmetric term which is easily measured in data. Contributions from charge-symmetric processes cancel each out in Equation 6.7, while contributions from charge-asymmetric processes are estimated via MC simulation and subtracted. Since the multi-jet background is charge-symmetric, the W+jets normalisation factors can be derived ahead of the multi-jets estimate described in Section 6.7.2 and also used to correct the W+jets background in the regions used for the multi-jet estimate.

The final scale factor is calculated as the ratio between the total number of events obtained in data and the one obtained via MC simulation. It is important to note that the scale factor can be estimated in a four-jets-1-bjet ($4j1b$) inclusive region as well as separately for any signal region, and for e+jets and μ+jets events. The values obtained separately in the signal regions and in the inclusive $4j1b$ region agree within their statistical uncertainties. The latter can be estimated with higher statistical precision and hence the normalisation factor obtained there is applied in all the signal regions as well as the control and validation regions for the estimation of the multi-jet background.
The value of the normalisation factor obtained as described above is $C_A = 1.125 \pm 0.031$.

6.7.2 Multi-jet background estimation in the one-lepton channel

The multi-jet background in events satisfying the resolved or merged one-lepton selection arises when a non-prompt lepton, or a jet misidentified as a lepton, passes the lepton identification and isolation requirements applied in the signal regions (Sections 5.5.1, 5.5.2), which will from now on be referred to as *tight* lepton requirements. The origin of the multi-jet background is different in e+jets and μ+jets events. In the μ+jets category, the multi-jet background is mostly due to semileptonic decays of hadrons inside of jets, producing non-prompt muons. In the e+jets category, it is dominated by hadronic jets with a large electromagnetic component, e.g. from $\pi^0 \to \gamma\gamma$ decays, which may be misidentified as isolated electrons. The involvement of detector effects in the emergence of this background makes it difficult for it to be modelled with event generators. Hence, a fully data-driven approach via the Matrix Method is chosen. Due to the fundamental difference in the processes generating the background, the estimate is performed separately in the μ+jets and e+jets categories. A detailed description of the method is found in [147, 148].

The matrix method is based on the definition of a lepton selection with looser identification and

isolation requirements, referred to as *loose* lepton requirements in the following. The numbers N_L and N_T of events containing a lepton passing the loose and tight selection requirements, respectively, can be written as

$$\begin{cases} N_L = N_{\text{prompt}} + N_{\text{multi-jet}} \\ N_T = \varepsilon N_{\text{prompt}} + f N_{\text{multi-jet}} \end{cases}, \tag{6.8}$$

where:

- N_{prompt} and $N_{\text{multi-jet}}$ denote the number of events containing a prompt lepton and the number of events containing a non-prompt or fake lepton, respectively;
- the *real rate* ε is an estimator of the probability of a prompt lepton that passes the loose selection requirements to also pass the tight requirements;
- the *fake rate* f is an estimator of the probability of a non-prompt lepton or fake lepton passing the loose selection requirements to also pass the tight requirements.

The fake rate is estimated in data in a control region enriched in fakes, obtained by applying the same selection requirements of the resolved signal regions, but reversing the missing transverse energy and W-transverse-mass cuts. Contributions in the control region coming from prompt processes are estimated via MC simulations and subtracted from the data. The real rate is estimated using $t\bar{t}$ simulated events. The number of multi-jet events in the tight region can be obtained by solving Equation 6.8:

$$f N_{\text{multi-jet}} = \left(\varepsilon N_L - N_T\right) \frac{f}{\varepsilon - f} = \left[\varepsilon N_A - (1-\varepsilon) N_T\right] \frac{f}{\varepsilon - f}, \tag{6.9}$$

where $N_A = N_L - N_T$ is the number of anti-tight events in the loose region, i.e. of events that pass the loose selection but not the tight one.
Technically, the multi-jet estimation in the signal regions is obtained by applying per-event weights to data events in the loose control region, with weight given by

$$w(P_A, P_T) = \left[\varepsilon P_A - (1-\varepsilon) P_T\right] \frac{f}{\varepsilon - f}, \tag{6.10}$$

where P_T (P_A) is equal to 1 if the event satisfies the (anti-)tight requirements, and 0 otherwise.

To improve the modelling of kinematic distributions, such as $m_{t\bar{t}}$, the real and fake rates are derived separately in rectangular bins of the transverse momentum of the lepton and a calorimeter-based isolation variable. In addition, the rates are derived separately for the cases $\Delta R \geq 0.4$ and $\Delta R < 0.4$, where ΔR is the angular distance between the selected lepton and its closest small-R jet. This is done to account for the fake contribution coming from the dedicated overlap removal used in this search (Section 5.4.7).
The fake rates for electrons (muons) vary from 5% to 86% (9% to 84%), with the largest values occurring at high p_T , where the isolation requirement is looser (Sections 5.2 and 5.3).

A conservative 50% uncertainty is applied to the data-driven estimate of this small background, based on the agreement between data and expectation observed in two validation regions obtained by reversing either the E_T^{miss} OR the m_W^T requirement (Section 6.2.3).

6.7.3 Z+jets background in the two-lepton channel

A data-driven correction is applied to the Z+jets MC simulation in the two lepton channel. The correction is derived in a Z+jets control region defined in the same way as the two-lepton signal regions (Section 6.5) but requiring the two leptons to be of the same flavour and within the Z-boson mass window via the requirement $m_{\ell\ell bb} \in [81, 101]$ GeV. A poor modelling of the Z+jets background is observed in the control region, especially for the transverse momentum of the di-lepton pair, $p_T^{\ell\ell}$, and for $m_{\ell\ell bb}$. The mismodelling exhibits a linear trend for both variables, with good agreement at low values, worsening at high values. The correction applied to improve the agreement consists in re-weighting all MC events by a factor

$$w = a(1 - bm_{\ell\ell bb}), \tag{6.11}$$

where the parameters a and b are obtained from a maximum likelihood fit of the $m_{\ell\ell bb}$ distribution in the control region. After applying the correction, a good agreement between the predicted and observed distributions is observed for all relevant kinematic variables. The correction has also also been derived based on the $p_T^{\ell\ell}$ distribution and the difference with respect to the $m_{\ell\ell bb}$ correction is used as a systematic uncertainty.

6.7.4 Fakes background in the two-lepton channel

A small background component in the two-lepton channel is due to events with at least one fake or non-prompt lepton passing the selection requirements described in Sections 5.5.1 and 5.5.2. They are mostly SM $t\bar{t}$, single-top or W+jets events that contain a single prompt lepton, where a fake or non-prompt lepton is also present. The modelling of this *Fakes* background is based on MC simulations and validated in a control region CR_f. The fakes control region is obtained by reversing the opposite-sign requirement in Section 6.5 and requiring at least one reconstructed W boson with transverse mass in the event to be below 100 GeV. Only the $\mu\mu$ and $e\mu$ control regions are used to validate the fakes estimation, while the ee one is not used due to large contribution from processes with two real electrons where one of the two has its charge misidentified.

Based on the comparison between data and the MC expectation in the control regions, the fakes background is accurately described by MC simulations, within a conservative 30% uncertainty. Given the small importance of this background for the overall sensitivity of the two-lepton channel, no data-driven correction is derived.

6.8 Systematic uncertainties

In the analysis presented in this thesis, about 100 systematic uncertainties are considered that alter the shape and normalisation of the $m_{t\bar{t}}$ and $m_{\ell\ell bb}$ distributions in the signal regions. They can be divided into experimental and modelling uncertainties. Experimental uncertainties are related to features of the detector and of the reconstruction algorithms. Modelling uncertainties are directly related to the estimation of backgrounds and signal processes, as well as the simulation of the latter.

6.8.1 Experimental uncertainties

Experimental uncertainties are related to the luminosity measurement of the data used in this search, as well as to the identification efficiency, energy scale and resolution, and isolation (if applicable) of all reconstructed objects. With the only exception of the luminosity uncertainty, which only affects the normalisation of the simulated signal and background samples, they all affect the shape and normalisation of the spectra of interest. In the following, an overview of the experimental uncertainties affecting this analysis is presented.
The most relevant experimental uncertainties are related to small-R jets and flavour tagging (Section 8.3).

Luminosity The uncertainty on the integrated luminosity of the dataset recorded between 2015 and 2018 and used in this analysis set as a simple normalisation variation of 0.83% [76]. It is applied to all simulated signal and background samples.

Pile-up The pile-up weights introduced in Chapter 4, used to correct the luminosity profile of MC simulations to match those of the data, are affected by uncertainties. Variations on pile-up weights are obtained by changing the value of the average number of interactions per bunch-crossing in their calculation, and used as systematic uncertainties.

Electrons and muons The energy scale and resolutions of leptons, as well as the efficiency of their identification and isolation, are calibrated using $Z \to \ell\ell$ and $J/\psi \to \ell\ell$ events [130, 131]. Uncertainties on these calibrations are used as systematic uncertainties.

Jets Small-R jets are the source of many uncertainties, among which are the most relevant experimental uncertainties for this search. Jet uncertainties are related to JES and JER (Section 5.4.3), Jet Mass Scale (JMS), and JVT (Section 5.5.3).
JES-related uncertainties arise in all of the different steps in the jet energy calibration chain: η-intercalibration, Z+jets balance, photon+jets balance, and multijet balance at high p_T. The ATLAS JetEtMiss group provides a set of 30 variations to use as uncertainties on the JES. JER-related uncertainties are obtained by comparing the jet energy resolution in data and MC events. The ATLAS JetEtMiss group provides a set of 13 variations to use as uncertainties on the JER.
A single uncertainty is applied on the JVT discriminant, that takes into account the uncertainty on the selection efficiency for the hard-scatter jets and the uncertainty on the remaining fraction of pile-up jets.

Uncertainties on the JMS are derived for small-R jets and are also propagated to reclustered jets. They are obtained using the R_{trk} [149] method, which is built around the fact that the ATLAS detector provides two independent measurements of the properties of the same jet from the calorimeter and the tracker. Jets formed from ID tracks alone only include energy contributions from their charged-particle constituents. The average calorimeter-to-track jet response

$$R_{\text{trk}} = \langle \frac{m_{\text{calo}}}{m_{\text{trk}}} \rangle \tag{6.12}$$

is proportional to the average calorimeter-to-truth jet response. The ratio of the R_{trk} measured in MC

and in data is taken as an uncertainty on the JMS. The uncertainty is calculated in bins of jet transverse momentum.
No specific uncertainties are applied to (V)RC jets, as they are obtained from pre-calibrated objects. The uncertainties on the small-R constituent jets are propagated to the VRC jets, for example a smearing of the energy of the constituents results in a smearing of the energy of the reclustered jet, which affects its energy scale and resolution. Despite the fact that the uncertainties on small-R jets are calculated for isolated jets, the fact that (V)RC subjets are often not isolated does not have a significant effect on their energy scale and resolution [150]. Therefore, no additional uncertainty is applied.

Flavour tagging Uncertainties related to the scale factors (SF) used to correct the b-, c-, and light-tagging efficiencies in MC simulation (Section 5.4.5) are taken into account. The SFs are obtained via fits to data, with many sources of uncertainty, and in bins of jet p_T . The individual application in ATLAS analyses of all the uncertainties appearing in SF fits would lead to a huge number of systematic uncertainties. Moreover, these uncertainties would be correlated and not independent of each other. For this reason, the *eigenvector variation method* [151] is applied to obtain a reduced set of statistically-independent systematic uncertainties, while keeping the correlations in p_T bins. The method involves the calculation of a covariance matrix between jet p_T bins, for all systematic uncertainties on the b-, c-, and light tagging efficiency SFs. Then a single covariance matrix is obtained by summing together all the single-uncertainty covariance matrices. The total uncertainty matrix is then diagonalised, providing orthogonal variations whose size is given by the square root of the corresponding eigenvalue. The number of eigenvector variations obtained via the eigenvector method is 9, 4, and 4, for $b-$, $c-$ and light-flavour scale factors, respectively. To account for the extrapolation of the SFs to high-p_T regimes, two additional systematic uncertainties are applied. This extrapolation is obtained in MC simulated events, and the main uncertainties on it are related to track reconstruction.

Missing transverse momentum Uncertainties on the inputs to the missing transverse momentum calculation affect the value of $\mathbf{p_T}^{\text{miss}}$, effectively creating an indirect uncertainty on it: changes in the reconstruction of any object in the event change the $\mathbf{p_T}^{\text{miss}}$ value, being the latter a global event object. Three additional uncertainties are applied to the soft-track term in the $\mathbf{p_T}^{\text{miss}}$ calculation: the first is obtained by scaling the soft term up and down in the transverse component of the hard term, while the other two are obtained by smearing the soft-term distribution in the direction parallel and perpendicular to the transverse component of the hard term, respectively.

6.8.2 Modelling uncertainties

Modelling uncertainties include uncertainties on the signal processes and the dominant background processes, most importantly SM $t\bar{t}$, single-top production, Z+jets (two-lepton), and W+jets (one-lepton).
There are multiple sources of uncertainty for purely MC-based background estimates. Missing higher orders in the perturbative expansion of partonic cross-sections lead to an unphysical dependence on the renormalisation and factorisation scales; uncertainties are applied by varying the scales. The choice of PDF (Section 2.2.1) set and uncertainties on the nominal PDF set is a source of uncertainty. Uncertainties are derived on the choice of PS, the ME-PS matching and the choice of ME generator, by comparing samples from different ME generators or by changing parameters in the nominal generator.

Uncertainties on the PS simulation itself are obtained by using different PS generators. The PS generators also come with a number of tunable parameters that affect the details of hadronisation, emission of initial and final state radiation, and the properties of the UE. Choices of these parameters different from the nominal are used as systematic uncertainties. Finally, uncertainties on the top-quark mass affect the SM $t\bar{t}$, single-top, $t\bar{t}$+V, and $t\bar{t}$+h backgrounds, as well as the signal modelling.

Modelling uncertainties are also derived separately for the signal (S) and signal-plus-interference ($S + I$) samples and varied in a fully correlated way in the statistical analysis 8.1. The modelling uncertainties are derived for S and $S + I$ samples with the same means as the $t\bar{t}$ background and include: renormalisation and factorisation scales, PDF uncertainties, variations of the parameters of the PS generator and top-quark mass uncertainty.

Modelling of the SM $t\bar{t}$ background

The uncertainty on the $t\bar{t}$ cross-section is one of the main sources of systematic uncertainty and only affects the normalisation of the invariant mass spectra (one spectrum per signal region), not their shape. A $^{+5.6\%}_{-6.1\%}$ variation is applied to the total cross-section. The main sources for this uncertainty are the choice of renormalisation and factorisation scales, the choice of PDF set, the top-quark mass uncertainty, and the uncertainty on the strong coupling constant α_S [89–95].

As described in Section 4.2.1, the $t\bar{t}$ prediction is obtained via MC simulations at NLO+PS and a subsequent reweighting of the main $t\bar{t}$ kinematic variables to higher order precision (NNLO-QCD+NLO-EW). The modelling systematics scheme for this background follows this pattern.
Three types of modelling systematics for the SM $t\bar{t}$ background can be defined in this context.

1. **Uncertainties relying on alternative MC samples:** Different MC setups are available to estimate uncertainties on the NLO+PS calculation. These alternative samples are reweighted to NNLO-QCD+NLO-EW with the same technique as used for the nominal sample. This is done because, while these uncertainties do not affect the parton-level quantities used for the reweighting, they still have a residual effect on the final observables after reweighting, due to different correlations between the reweighting variables or other event properties.

2. **Uncertainties on higher-order MC predictions:** These are uncertainties on quantities that affect the parton-level quantities used for the reweighting, on the reweighting procedure itself, or arising from diagram contributions that are not present in the NLO+PS prediction.

3. **Uncertainties on the NLO+PS prediction with no corresponding uncertainty at higher order:** These are uncertainties that are not *reduced* by the reweighting, i.e. that are not reweighted to the same higher order as nominal. This is done either because they do not affect the distributions of the reweighting variables, nor their correlations, or in order to apply a more conservative uncertainty not reduced by the reweighting. From a technical point of view, no specific reweighting is applied in this case. Instead, the same reweighting factor as for the nominal sample is used.

Systematic uncertainties on NLO+PS prediction - type 1 and 3 The following systematic uncertainties on the NLO+PS prediction are taken into account:

- PS & hadronisation (type-3): uncertainty related to the choice of parton showering and hadronisation scheme. It is estimated by comparing the nominal POWHEG+PYTHIA prediction with the one obtained by interfacing POWHEG with HERWIG 7.1.3. Since it only affects the choice of the parton shower generator, no specific NNLO reweighting is applied to this uncertainty.

- PS-ME matching (type-1): uncertainty related to the ME-PS matching. It is estimated by changing the nominal value of the POWHEG p_T^{hard} parameter in PYTHIA [152]. This is the recommended way to access the ME-PS matching uncertainty according to the PYTHIA 8 authors [153].

- ME-PS h_{damp} (type-1): another uncertainty relating to the ME-PS matching. It controls the amount of initial state radiation handled by the ME and PS parts of the simulation. This is done by increasing the h_{damp} parameter in POWHEG by a factor two with respect to its nominal value.

- Lineshape (type-3): uncertainty related to the spin correlation between the top and anti-top quarks in the final state. It is obtained by generating a SM $t\bar{t}$ sample in the same way as the nominal one, but decaying the top quarks with MADSPIN instead of POWHEG. This uncertainty indirectly affects the ME-PS matching as it changes the last step of the ME prediction.

- Renormalisation (μ_R) and factorisation (μ_F) scales (type-1): two uncertainties controlling the QCD renormalisation and factorisation scales in the ME calculation. They are estimated by varying them independently by a factor of 2 and 0.5.

- ISR A14 (type-3): uncertainty affecting the renormalisation scale in the ISR parton shower. It is obtained by varying a parameter in the A14 tune of the PS generator. Since the effect of this uncertainty is found to be negligible on the parton-level quantities used for the NNLO-QCD+NLO-EW reweighting, no specific reweighting is applied and the nominal reweighting factors are used.

- FSR (type-1): uncertainty affecting the renormalisation scale in the FSR parton shower.

- m_{top} (type-3): uncertainty on the top-quark mass. It is estimated by using two alternative POWHEG+PYTHIA8 samples with m_{top} varied by ±1.5 GeV. The resulting variation histograms are scaled by a factor of 0.5 to obtain the variations corresponding to a 0.76 GeV uncertainty on the top-quark mass [154].

Systematic uncertainties on the theory prediction and on the reweighting - type 2 The following higher-order-specific uncertainties are applied:

- QCD scale variations: changes in the renormalisation and factorisation scales affect the parton-level variables used as input to the reweighting. Four specific systematic uncertainties are applied to take this into account, obtained by independently scaling them up and down by a factor two, separately for the two parton-level reweighting variables. The resulting uncertainties are called $t\bar{t}$ NNLO μ_R ($p_{T,\text{top}}$), $t\bar{t}$ NNLO μ_F ($p_{T,\text{top}}$), $t\bar{t}$ NNLO μ_R ($m_{t\bar{t}}$), $t\bar{t}$ NNLO μ_F ($m_{t\bar{t}}$).

- PDF uncertainty on the NNLO-QCD prediction taken from Ref. [88], where it is calculated as the envelope of the PDF variations of the nominal LUXQED PDF set [155].

- EW correction uncertainties: the effect of different treatments of the photon PDF is considered as part of the uncertainty on the EW component of the higher-order prediction. A set of parton-level predictions is obtained with an alternative NNPDF3.0QED PDF set [156], which has a very different treatment of the photon PDF with respect to the nominal LUXQED PDF set.

- Reweighting order: as described in Section 4.2.1, the higher-order reweighting follows a specific but arbitrary order. An uncertainty obtained by reversing the reweighting order is applied.

- Top parton definition: an additional uncertainty is applied to account for ambiguities in the definition of the top quarks at the parton level. Strictly speaking, there is not a perfect coherence between the parton-level theory predictions, which are NNLO in QCD, and the parton-level MC predictions, which are NLO in QCD plus parton shower applied. The NNLO-QCD theory prediction only allows for two real emissions from the final-state top quarks; the NLO+PS MC prediction allows for an infinite number of real emissions from the top quarks, one handled by the ME generator, and the rest by the PS. In order to deal with this inconsistency, an alternative $t\bar{t}$ MC sample is generated, with the nominal Powheg+Pythia8 setup, where only one emission at PS level is allowed, effectively allowing for a total of 2 real emission and obtaining a parton-level NLO+PS prediction coherent with the NNLO prediction. The alternative sample is then used as a target for the reweighting of the nominal NLO+PS prediction.

  The difference between this reweighted sample and the nominal NLO+PS prediction is used as an uncertainty of type-2.

Modelling of the single-top background

The main uncertainty on the modelling of single-top quark production arises from the comparison between two possible schemes for the treatment of interference effects and overlaps between SM $t\bar{t}$ and Wt production. In the Diagram Removal (DR) scheme, resonant $t\bar{t}$ effects are removed from the Wt sample at the amplitude level, while in the Diagram Subtraction scheme, they are removed at the cross-section level [157]. The uncertainty is obtained by comparing the nominal Wt sample, generated via the DR scheme, with an alternative sample generated with the DS scheme.
The uncertainties related to the choice of the PS & hadronisation model and to the ME-PS matching in the Wt sample are evaluated analogously to the corresponding $t\bar{t}$ uncertainties, without the additional complications stemming from the higher-order reweighting, and are found to be negligible.
Uncertainties on the renormalisation and factorisation scales and choice of PDF set were also considered and found to be negligible.
Theoretical uncertainties on the calculated cross-sections for Wt- [101], s- [102], and t-channel [103] production of single-top events are applied as pure normalisation uncertainties on the respective components.

Modelling of the W+jets background

In the one-lepton channel, a conservative 20% normalisation uncertainty is applied to the W+jets estimate after the data-driven charge asymmetry correction described in Section 6.7.1. It is applied separately in the Resolved $1b$, Resolved $2b$ and Merged regions to account for any remaining mis-modelling of the relative contributions from W-boson production in association with heavy-flavour

jets [158]. Additionally, modelling uncertainties related to factorisation and renormalisation scales, and PDF choice are included, but found to be negligible and pruned from the final fit.

In the two-lepton channel, W+jets production is included in the fake-lepton background component that is discussed below.

Modelling of the Z+jets background

In the one-lepton channel, a conservative 30% normalisation uncertainty is applied, accounting for both a cross-section uncertainty and possible mismodelling of the jet multiplicity, which has an effect on acceptance.
In the two-lepton channel, an alternative MC reweighting based on $p_T^{\ell\ell}$ instead of the nominal one based on $m_{\ell\ell bb}$ is used to derive an uncertainty, as mentioned in Section 6.7.3, amounting to a 3% variation of the reweighting factor. An additional 30% normalisation uncertainty is also applied in the two-lepton channel to cover for any residual mismodellings in the production of heavy-flavour jets.

Modelling of other minor backgrounds

For the multijet background in the one-lepton channel, and fake estimate in the two-lepton channel, conservative normalisation uncertainties are applied, amounting to 50% for the multijet estimate (Section 6.7.2) and 30% for the fake estimate (Section 6.7.4).

For the backgrounds from $t\bar{t}+Z$, $t\bar{t}+W$, and $t\bar{t}+h$ production, only uncertainties in the respective higher-order cross-sections are taken into account, and amount respectively to $^{+10.4}_{-12.0}$, $^{+13.3}_{-12.0}$, and $^{+6.8}_{9.8}$.

A conservative 50% normalisation uncertainty is applied for the background from diboson production to account for any possible mismodelling from the production of heavy-flavour jets [159] and additional jets [160].

All normalisation uncertainties are summarised in Table 6.3.

Table 6.3: Summary of normalisation uncertainties applied to different background components.

Background process	Up variation	Down variation
$t\bar{t}$	+5.6%	-6.1%
Single-top: Wt-channel (both)	+5.4%	-5.4%
Single-top: t-channel (both $t, \bar{t}$)	+4.3%	-3.7%
Single-top: s-channel (both $t, \bar{t}$)	+4.4%	-4.1%
$t\bar{t}+Z$	+10.4%	-12.0%
$t\bar{t}+W$ (both W^+, W^-)	+13.3%	-12.0%
$t\bar{t}+h$	+6.8%	-9.8%
Diboson	+50.0%	-50.0%
Z+jets	+30.0%	-30.0%
W+jets	+20.0%	-20.0%
Multijet	+50.0%	-50.0%
Fakes (two-lepton)	+30.0%	-30.0%

CHAPTER 7

Statistical methods

The agreement between the data and the SM background prediction, as well as with a variety of BSM hypotheses, is assessed via *profile likelihood* fits on the expected and observed distributions of $m_{t\bar{t}}$ in the one-lepton channel and $m_{\ell\ell bb}$ in the two-lepton channel (variables-of-interest), in histogram format. In the profile likelihood fit, the expected distributions are allowed to vary within systematic uncertainties to match the observed. The fit is performed simultaneously in the eleven one-lepton signal regions and the five two-lepton signal regions. The profile likelihood is also used as a building block for hypothesis tests that quantify the probability of measuring the observed dataset, under the SM or BSM hypotheses.
In this section, the basics of the profile likelihood method and its use in hypothesis tests are introduced, and the complications and peculiarities arising from the presence of signal-background interference are discussed.
The statistical analysis is implemented in the `TRExFitter` framework [161] and private code based on the `xRooFit` library [162] for binned template profile likelihood fits. `TRExFitter` is used mostly for the creation of *workspaces* encoding the information about the expected and observed content of histograms their uncertainties, and standalone fits. The private code based on `xRooFit` uses the `TRExFitter` workspaces to build test statistic and perform hypothesis testing.

7.1 Profile likelihood fits

One important step in all searches is to quantify the agreement of the observed dataset with a specific BSM hypothesis. This is done via profile likelihood fits.

The basics of negative-log-likelihood minimisation

Data analyses in particle physics work with an observed dataset X which is modelled in terms of theoretical parameters $\boldsymbol{\theta}$. These parameters can refer to physical quantities that one would like to measure. A likelihood function is the probability of observing X, if the true values of the parameters are $\boldsymbol{\theta}$:

$$\mathcal{L} = P\left(X\,|\boldsymbol{\theta}\right). \tag{7.1}$$

The idea of maximum-likelihood parameter estimation is that the most probable value of these parameters is obtained by maximising the likelihood. From a technical point of view, this is usually

achieved by minimising the negative-log-likelihood NLL = $-\log \mathcal{L}$.
Calling $\hat{\boldsymbol{\theta}}$ the values of the parameters that minimise the NLL, i.e. the best-fit values, their uncertainty is often evaluated via the covariance matrix:

$$\hat{V}_{ij} = - \left. \frac{\partial^2 \log \mathcal{L}}{\partial \theta_i \partial \theta_j} \right|_{\hat{\theta}_i \hat{\theta}_j}, \tag{7.2}$$

where the indices i, j run over the number of parameters in the vector $\boldsymbol{\theta}$. The uncertainty on each parameter in the vector $\boldsymbol{\theta}$ is obtained from the inverse $\hat{V}^{-1}$ of the covariance matrix:

$$\Delta\theta_k = \sqrt{\hat{V}^{-1}_{kk}}. \tag{7.3}$$

A more precise evaluation is sometimes obtained via a method that consists in shifting the NLL up by $1/2$ from its minimum, and can lead to asymmetric uncertainties:

$$\text{NLL}\left(\boldsymbol{\theta} \pm \Delta\theta_k^{\text{up/down}}\right) - \text{NLL}\left(\boldsymbol{\theta}\right) = \frac{1}{2}. \tag{7.4}$$

In many searches, including the one presented in this thesis, the analysis is performed on binned distributions, i.e. histograms; neglecting systematic uncertainties, each bin can be treated like an independent Poisson experiment, with an expected number of events $\nu_i(\boldsymbol{\theta})$ and number of observed events n_i. The negative-log-likelihood can be written as:

$$\text{NLL}(\boldsymbol{\theta}) = \sum_i^{\text{N}_{\text{bins}}} \left[\nu_i(\boldsymbol{\theta}) - n_i \log \nu_i(\boldsymbol{\theta})\right] + \text{const.}, \tag{7.5}$$

where N_{bins} is the total number of bins in the histogram, and the constant term is independent of the vector of parameters $\boldsymbol{\theta}$.

The basics of profiling

In this and many other searches, the amount of BSM signal is parametrised in terms of a single continuous *parameter-of-interest* (POI) μ. Other parameters in the fit are referred to as *nuisance parameters* (NP) and are introduced to model the impact of systematic uncertainties on the distribution of interest. If the nominal bin expectation in a histogram is $\nu_i^{\text{nom}}(\mu)$, and a systematic uncertainty j shifts the bin content by a relative amount Σ_i^j, the expected bin content can be parametrised as:

$$\nu_i(\mu, \boldsymbol{\theta}) = \nu_i^{\text{nom}}(\mu) \prod_j^{N_{\text{syst}}} \left(1 + \Sigma_i^j \theta_j\right), \tag{7.6}$$

where θ_j are NPs, whose value decides the impact of the systematic variations on the bin expectation. MC statistical uncertainties can be treated in a similar way as systematic uncertainties by introducing an independent NP per each bin. NPs related to MC statistical uncertainties are commonly referred to as γ-parameters. Before fitting, the values of the NPs are assumed to be equal to 1, so that the the bin expectation coincides with its nominal value for all bins. It should be noted that the presence of NPs

introduces correlations between bins, as a variation of the value of a NP yields a coherent variation of the number of expected events in all bins. A constraint term, which can be interpreted as the prior distribution of the NP, is also usually added to the likelihood for each NP. The constraint terms serve as penalty terms that keep the fit from deviating too flexibly from the expected values of the NPs, which would compromise the ability of the fit to discern the presence of the signal process. A typical choice is a Gaussian constraint, but also Poisson and log-normal constraints are sometimes used. All NP prior distributions are assumed to have a mean of 0 and a variance of 1. This expands the NLL of Eq. 7.5 as:

$$\mathrm{NLL}(\mu, \boldsymbol{\theta}) = \sum_{i}^{\mathrm{N_{bins}}} \left[\nu_i(\mu, \boldsymbol{\theta}) - n_i \log \nu_i(\mu, \boldsymbol{\theta})\right] - \sum_{j}^{\mathrm{N_{syst}}} \left[\log \mathcal{F}_j(\theta_j)\right] + \text{const.}, \tag{7.7}$$

where $\mathcal{F}_j(\theta_j)$ is the constraint term of the NP θ_j.

7.2 Profile likelihood parametrisation in the presence of interference

The expected bin content of the $m_{t\bar{t}}$ and $m_{\ell\ell bb}$ histograms in the presence of a BSM signal interfering with the SM $t\bar{t}$ background is parametrised in terms of the *signal strength* μ:

$$\nu_i = \mu k_S S_i + \sqrt{\mu} k_I I_i + B_i = \left(\left(\sqrt{\mu}\right)^2 k_S - \sqrt{\mu} k_I\right) S_i + \sqrt{\mu} k_I (S+I)_i + B_i,\ i = 1, ..., N_{\mathrm{bins}} \tag{7.8}$$

The S_i- and $(S+I)_i$-terms denote the contributions of the pure signal and signal-plus-interference samples to the bin i for the BSM hypothesis under consideration, while the B_i-term stands for the total SM background contribution. The contribution from signal-background interference in Equation 7.2 is scaled by the square root of the signal strength $\sqrt{\mu}$ instead of μ, as the interference term in the $gg \to t\bar{t}$ cross-section scales with the first power of the BSM scattering amplitude, differently from the signal term, which scales with the second power (cf. Equation 2.4.5). The k_S and k_I factors are introduced to correct the S- and $(S+I)$- samples to their calculated NLO cross-section, as described in Section 4.2.6; if no correction factor is applied, $k_S = k_I = 1$. The POI in the fit is $\sqrt{\mu}$.
The values $\sqrt{\mu} = 0$ and $\sqrt{\mu} = 1$ correspond to the SM-only and to the signal hypothesis under consideration, respectively. It should be pointed out that this parametrisation of the likelihood assumes that, under a given signal hypothesis, the shape of the S and S+I distributions of the variable-of-interest does not change with $\sqrt{\mu}$, although the relative contribution of the pure-signal and pure-interference terms does. This also implies that the decay width of the hypothetical new particle does not change with $\sqrt{\mu}$. This is a simplifying assumption because in the models under consideration (except the generic scalar model of Section 2.4.4), the decay width is a function of the mass of the BSM particle and of $\tan\beta$.

7.2.1 Technical implementation via the offset method

The $S+I$ template histograms contain bins with negative content, as the $S+I$ samples the relative deviation from the SM $t\bar{t}$ expectation, but do not represent physical processes. Histograms containing bins with negative content cannot be processed by common statistical frameworks, so they cannot enter the statistical analysis as they are. A method based on the use of an offset histogram O is implemented to allow the $S+I$ samples to be processed within `TRExFitter`. The method is described

in the following:

1. An offset histogram is added to the $S + I$ template histogram, so that it only contains positive bins;

2. an additional *counter-term* is included in the parametrisation of the bin expectation, identical to the offset, but with a negative normalisation factor. The counter-term is used to subtract the contribution from the offset.

The bin expectation from Equation 7.6 becomes

$$\nu = \left(\left(\sqrt{\mu}\right)^2 - \sqrt{\mu}\right) S + \sqrt{\mu}(S + I + O) - \sqrt{\mu} O + B, \tag{7.9}$$

where the correction factors are neglected, for the sake of simplicity. The bin content of all histograms is now positive, but the total expectation has not changed. The offset approach involves different MC statistical errors compared to an implementation without the offset histograms, which could lead to different constraints for the γ-parameters. To correct for this, the MC statistical uncertainties for the offset and counter-term histograms are disabled, and separate γ-parameters are introduced for the $(S + I)$ histograms.

The offset method is validated in simplified fits that do not involve interference terms. Profile-likelihood fits are performed using two different parametrisations of the bin expectation in the presence of signal:

- **S+B:** $\nu = \mu S + B$;
- **S+O+B:** $\nu = \mu(S + O) - \mu O + B$.

The data used for these fits is an Asimov dataset with expected value $\sqrt{\mu} = 1$. An Asimov dataset is a set of *pseudodata* constructed in such a way that all estimators correspond to their expected value, but reflecting the statistical uncertainties of real data [163]. An Asimov dataset with expected value $\sqrt{\mu} = 1$ is a dataset corresponding to the BSM expectation. In Figures 7.1 and 7.2 the pulls on the NPs after the fits to the Asimov dataset are shown, respectively for the experimental and modelling uncertainties (see Section 6.8), under a Type-II 2HDM scalar signal hypothesis, with $m_H = 500$ GeV and $\tan\beta = 1.0$, for the parametrisations with and without an offset term. The pull on a NP θ is defined as

$$\text{Pull}(\theta) = \frac{\hat{\theta} - \theta_0}{\Delta\theta}, \tag{7.10}$$

where $\hat{\theta}$ is the best-fit value of the NP, θ_0 is its pre-fit value (typically 0) and $\Delta\theta$ is the width (typically 1) of the prior distribution of the NP (Section 7.1). The constraints for all NPs are perfectly consistent between parametrisations, and both fits result in a best-fit value of the POI $\hat{\mu} = 1.00 \pm 0.17$. This underlines the validity of the offset method, as fit results are independent of whether the method is used or not.

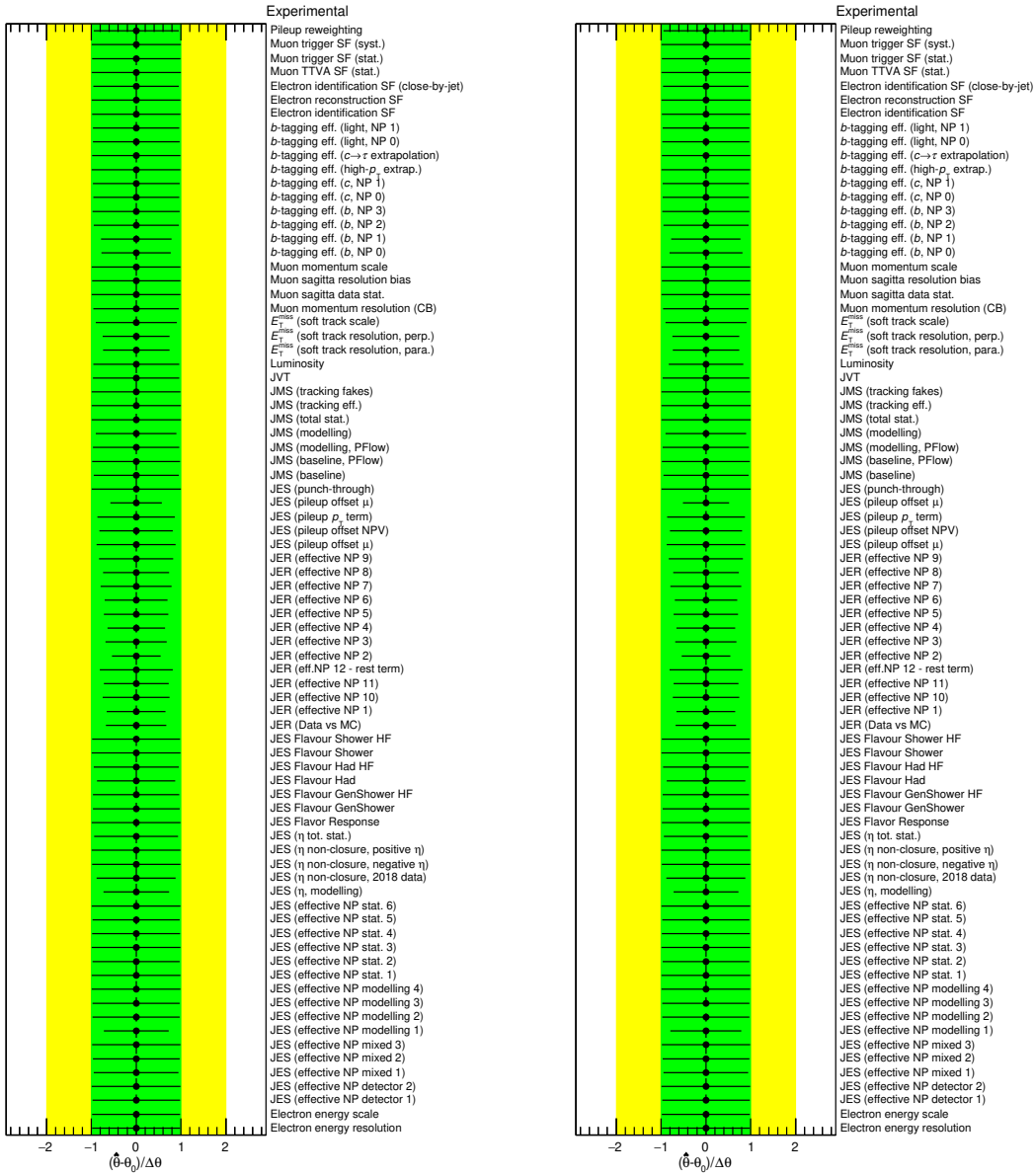

(a) S+B

(b) S+O+B

Figure 7.1: Pulls on the NPs after the fits to the Asimov dataset for the experimental uncertainties, under a Type-II 2HDM scalar signal hypothesis, with $m_H = 500$ GeV and $\tan\beta = 1.0$, for the parametrisations without (a) and with (b) and offset term.

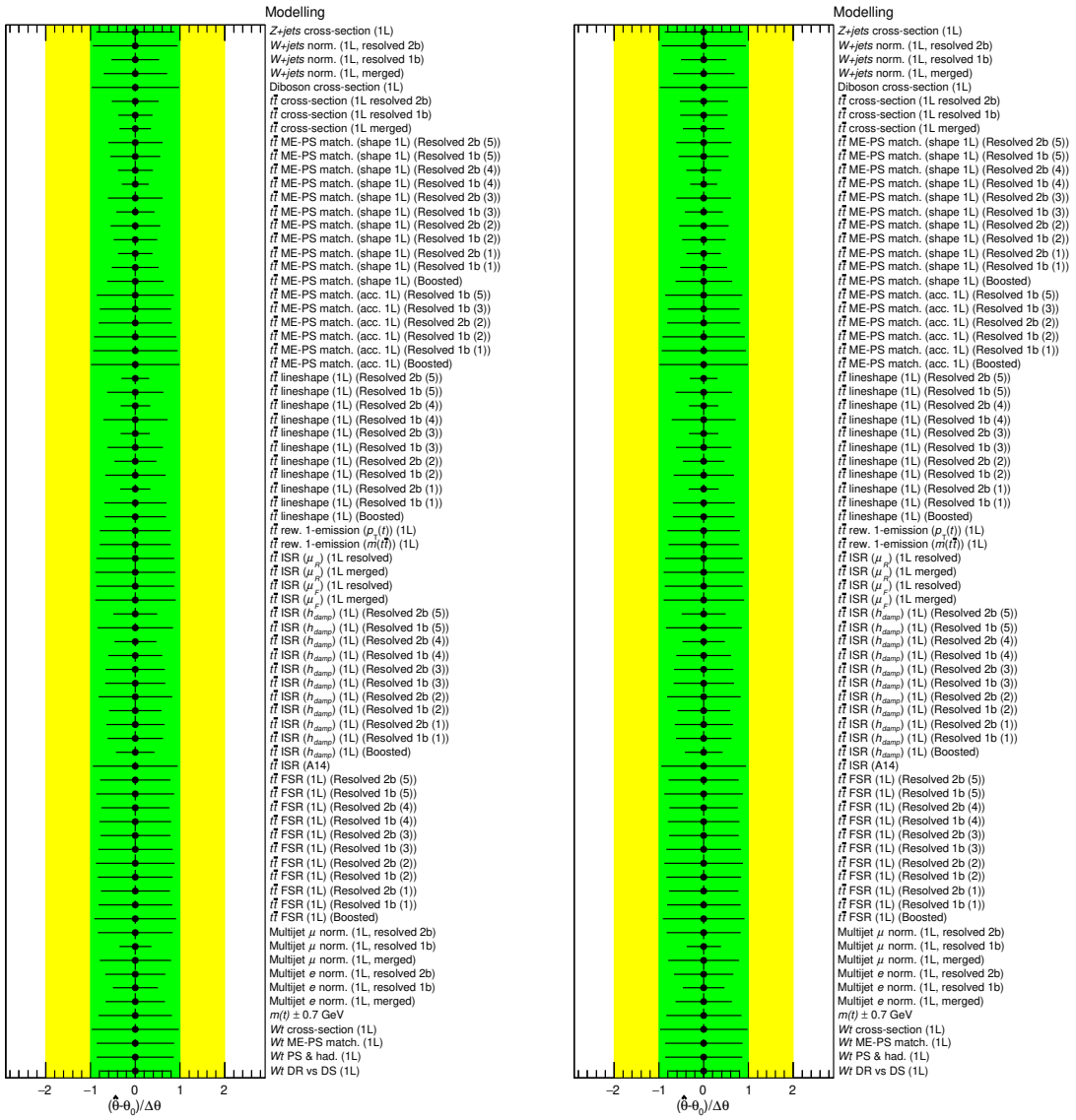

(a) S+B

(b) S+O+B

Figure 7.2: Pulls on the NPs after the fits to the Asimov dataset for the modelling uncertainties, under a Type-II 2HDM scalar signal hypothesis, with $m_H = 500$ GeV and $\tan\beta = 1.0$, for the parametrisations without (a) and with (b) and offset term.

7.3 Statistical inference

The problems of claiming the significance of a discovery or finding an excluded region in the parameter space of a BSM model, based on the measured data, both fall in the realm of hypothesis testing and relate to the fundamental question: is the observed data made of background events only, or is it a mixture of signal and background events?

7.3.1 Hypothesis tests

All hypothesis tests start from the definition of two opposing hypotheses, a *null* one, which is the one usually assumed to be true, and an alternative one. A *test statistic* t is then defined as a random variable designed to discriminate between the two hypotheses, whose distribution under the two hypotheses must be known in order to perform the test. Assuming that the test statistic takes lower values under the null hypothesis than under the alternative hypothesis, the exclusion of the null hypothesis in favour of the alternative one, with a confidence level CL $= 1 - \alpha$ works in the following way.

1. A p-value under the null hypothesis is calculated, i.e. the probability of measuring a value of the test statistic higher than what is observed $p_{\text{null}} = P(t > t_{\text{obs}}|\text{null})$;
2. If $p_{\text{null}} < \alpha$, the null hypothesis is excluded in favour of the alternative one, with confidence level $1 - \alpha$.

This means that the probability that the test statistic assumes a value equal or higher than the observed one due to a statistical fluctuation is less than α, if the null hypothesis is true. Of course, for a powerful test, we aim to maximise its strength, or alternative p-value, at a fixed confidence level, defined as $\beta = P(t > t_{\text{obs}}|\text{alt})$. According to the Neyman-Pearson lemma [164], the test statistic that maximises the strength of the test, at a fixed CL, is the likelihood ratio between the two hypotheses.

Two different hypothesis tests are considered in this thesis. The first is the *search* test, where the SM is the null hypothesis, and the BSM models are used as alternative hypotheses. The idea of this test is to quantify the significance of possible observed deviations of the data from the SM expectation. Often, the null p-value in this test is expressed in terms of a *significance* Z, defined as the number of standard deviations in a standard normal distribution that would yield that p-value:

$$Z = \Phi^{-1}\left(1 - p_{\text{null}}\right), \tag{7.11}$$

where $\Phi^{-1}(x)$ is the inverse of the standard normal cumulative.
The second is the *exclusion* test, where the BSM model, with a specific set of parameters, is the null hypothesis, while the SM is the alternative hypothesis. This is used to assess which points in the parameter space of the BSM model are excluded at a fixed CL, in favour of the SM.

The search test

Discrepancies between the observed data and the SM expectation are quantified using a profile likelihood ratio test statistic

$$q_0 = -2\log\frac{\mathcal{L}\left(\sqrt{\mu} = 0, \hat{\hat{\boldsymbol{\theta}}}_0\right)}{\mathcal{L}\left(\sqrt{\hat{\mu}}, \hat{\boldsymbol{\theta}}\right)}, \tag{7.12}$$

where $\hat{\hat{\boldsymbol{\theta}}}_0$ indicates the values of the NPs that maximise the likelihood for $\sqrt{\mu} = 0$, while $\hat{\sqrt{\mu}}$ and $\hat{\boldsymbol{\theta}}$ are the values of the POI and NPs that jointly maximise the likelihood.
The search test statistic allows for a test of the SM against a broad class of interference patterns, obtained from S and $S + I$ by varying $\sqrt{\mu}$ according to Eq. 7.6.

In the Type-II 2HDM, hMSSM, and 2HDM+a models (Section 2.4), a best-fit value of $\hat{\sqrt{\mu}} \neq 1$ does not indicate agreement with the signal hypothesis under consideration, i.e. the one for which the samples S and $S + I$ in Eq. 7.6 are obtained. In fact, values of $\sqrt{\mu} \neq 1$ do not correspond to the interference pattern of the benchmark model in study, as the decay width of the heavy Higgs and its coupling to top quarks are not independent and both depend on the heavy Higgs mass and $\tan\beta$. Deviations of $\sqrt{\mu}$ from 1 correspond to variations of the Higgs-$t\bar{t}$ coupling, but do not produce a corresponding change in decay width, resulting in an interference pattern outside of the benchmark model.
In the generic (pseudo)scalar model, where the width of the pseudoscalar is independent from its coupling to top quarks, there is a perfect correspondence between the $\sqrt{\mu}$ parameter and the Higgs-$t\bar{t}$ coupling, via the relation $\sqrt{\mu} = g^2_{A/Ht\bar{t}}$. One can easily convince themselves of this relation by comparing the bin content parametrisation in Equation 7.2 with the expression of the $gg \to t\bar{t}$ cross-section in terms of the signal and background scattering amplitudes given by Equation 2.4.5.
The search test is performed in the generic (pseudo)scalar interpretation, which allows for a test of the SM against a broad class of physically valid interference patterns, thanks to the equivalence between $\sqrt{\mu}$ and consequently $g_{A/Ht\bar{t}}$).

An asymptotic formula in Ref. [165] is used for approximating the distribution of the search test statistic in the large sample limit.

The exclusion test

A different test statistic from the one employed at the search stage is used at the exclusion stage with the CLs frequentist formalism (see section 7.3.2), in order to quantify the level at which the data excludes a given signal hypothesis, if no significant deviation from the background-only hypothesis is observed in the data.
The exclusion test statistic is based on the likelihood ratio between the $\sqrt{\mu} \neq 0$ hypothesis and the SM hypothesis $\sqrt{\mu} = 0$:

$$r_{\sqrt{\mu}} = -2 \log \frac{\mathcal{L}\left(\sqrt{\mu}, \hat{\hat{\boldsymbol{\theta}}}_{\sqrt{\mu}}\right)}{\mathcal{L}\left(0, \hat{\hat{\boldsymbol{\theta}}}_0\right)}. \tag{7.13}$$

For exclusion in the 2HDM, 2HDM+a and hMSSM parameter spaces, only the r_1 test statistic is used, by calculating p-values in the context of the CLs formalism just for $\sqrt{\mu} = 1$. This is motivated by the fact that the exclusion stage aims at quantifying the rejection of the specific benchmark scenario under consideration, which corresponds to the value of $\sqrt{\mu} = 1$, while values of $\sqrt{\mu} \neq 1$ do not produce the interference pattern of the benchmark model in study.
For the generic scalar model, where there is a perfect correspondence between the $\sqrt{\mu}$ parameter and the Higgs-$t\bar{t}$ coupling, the whole class of test statistic $r_{\sqrt{\mu}}$ is used for exclusion in its parameter space. Each value of $\sqrt{\mu}$ is used to test the exclusion of a different coupling value; for example, the p-values for the exclusion of $g_{A/Ht\bar{t}} = 2$ are calculated using the r_4 test statistic.

Asymptotic formulas for the distribution of the exclusion test statistic are obtained via analogous

calculations as in Ref. [165], where they are only derived for $\sqrt{\mu} = 1$. The derivation of the asymptotic formulas for the broader $\sqrt{\mu} \neq 1$ case is derived as follows. The exclusion test statistic can be written as a combination of profile-likelihood-ratio test statistic:

$$r_{\sqrt{\mu}} = -2\log\frac{\mathcal{L}\left(\sqrt{\mu}, \hat{\hat{\boldsymbol{\theta}}}_{\sqrt{\mu}}\right)}{\mathcal{L}\left(\hat{\sqrt{\mu}}, \hat{\boldsymbol{\theta}}\right)} + 2\log\frac{\mathcal{L}\left(0, \hat{\hat{\boldsymbol{\theta}}}_{0}\right)}{\mathcal{L}\left(\hat{\sqrt{\mu}}, \hat{\boldsymbol{\theta}}\right)}. \tag{7.14}$$

Under the Wald approximation, the profile-likelihood-ratio can be written as

$$-2\log\frac{\mathcal{L}\left(\sqrt{\mu}, \hat{\hat{\boldsymbol{\theta}}}_{\sqrt{\mu}}\right)}{\mathcal{L}\left(\hat{\sqrt{\mu}}, \hat{\boldsymbol{\theta}}\right)} = \frac{\left(\sqrt{\mu} - \hat{\sqrt{\mu}}\right)^2}{\sigma^2} + O\left(1/\sqrt{N}\right), \tag{7.15}$$

where N is the size of the sample. Here, $\hat{\sqrt{\mu}}$ follows a Gaussian distribution with mean $\sqrt{\mu}'$ equal to the real value of the $\sqrt{\mu}$ parameter, and variance σ^2. Based on the discussions above, $\sqrt{\mu}' = 0$ in the SM hypothesis, while for the 2HDM, 2HDM+a, and hMSSM hypotheses $\sqrt{\mu}' = 1$, and for the generic scalar model $\sqrt{\mu}' = g^2_{A/Ht\bar{t}}$. The exclusion test statistic can therefore be approximated by

$$r_{\sqrt{\mu}} = \frac{\left(\sqrt{\mu} - \hat{\sqrt{\mu}}\right)^2}{\sigma^2} - \frac{\hat{\sqrt{\mu}}^2}{\sigma^2} = \frac{\sqrt{\mu}^2 - 2\sqrt{\mu}\hat{\sqrt{\mu}}}{\sigma^2}, \tag{7.16}$$

and is normally distributed, with mean and variance given by

$$E\left[r_{\sqrt{\mu}}\middle|\sqrt{\mu}'\right] = \frac{\sqrt{\mu}^2 - 2\sqrt{\mu}\sqrt{\mu}'}{\sigma^2}, \quad VAR\left[r_{\sqrt{\mu}}\right] = \frac{4\sqrt{\mu}^2}{\sigma^2}. \tag{7.17}$$

It should be noted that the parameter σ in Eq. 7.17 depends on $\sqrt{\mu}'$, so the width of the test statistic distribution is different under the null and alternative hypotheses. Details on the methods for the estimation of the σ parameter are found in Ref. [165].

The asymptotic formulas for the distribution of the exclusion test statistic are validated via toy experiments. More precisely, 500 MC toy experiments, corresponding in size to the 140 fb^{-1} Run-2 ATLAS dataset, are generated under both the null hypothesis (including signal-background interference) and the alternative hypothesis (only background events). For each pseudo-experiment, the value of the test statistic is calculated, and histograms of the test statistic distribution, under the two hypotheses, are constructed. The histograms from the pseudo-experiments are then compared to the distributions obtained via the asymptotic formulas. Figure 7.3 shows the distribution of the exclusion test statistic for two selected 2HDM hypotheses, under the null and alternative hypotheses, estimated using toy experiments and asymptotic formulas. A very good agreement between asymptotic and toy MC distributions is observed, showing that the asymptotic formula approximates the true probability density distribution very well.

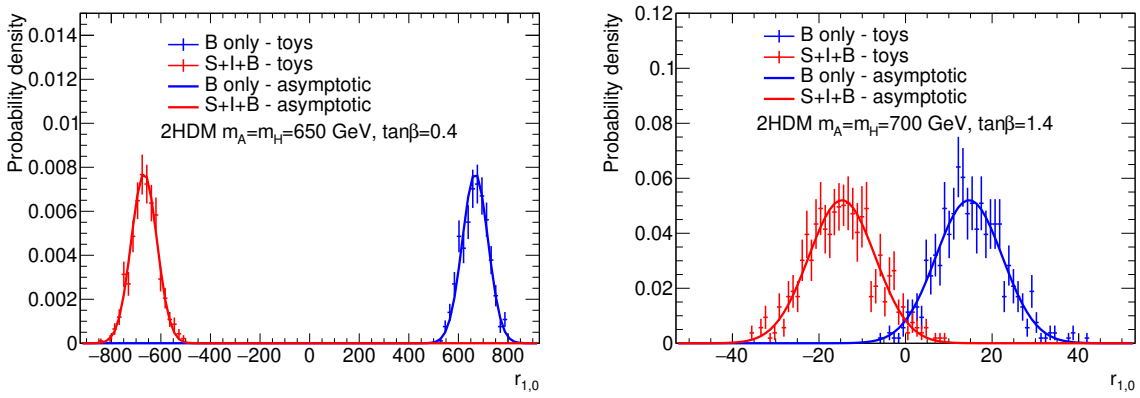

(a) $m_A = m_H = 650$ GeV, $\tan\beta = 0.4$ (b) $m_A = m_H = 700$ GeV, $\tan\beta = 1.4$

Figure 7.3: Distribution of the exclusion test statistic for two selected 2HDM hypotheses, under the null (BSM) and alternative (SM-only) hypotheses, estimated using toy experiments (data points) and asymptotic formulas (solid lines).

7.3.2 The CL_s method for quantifying exclusion in the BSM parameter space

Before the LHC era, parameter exclusion was based on the standard procedure described in Section 7.3.1. The parameters defining the null (signal+background) hypothesis were excluded at CL $= 1 - \alpha$ if the p-value under the null hypothesis is smaller than α. This procedure, known under the name of frequentist approach, had the great drawback of leading to exclusion in regions of the parameter space where the experiment is not sensitive, i.e. regions where the test statistic has poor discrimination power between the null and alternative (background-only) hypotheses.
To solve this issue, a modified approach is used, where both p-values corresponding to the null and alternative hypotheses are calculated:

$$\begin{cases} p_{\text{null}} = P\left(t \geq t_{\text{obs}} \,|\text{null}\right) \\ p_{\text{alt}} = P\left(t \geq t_{\text{obs}} \,|\text{alt}\right) \end{cases} . \tag{7.18}$$

From those probabilities, a new quantity is derived:

$$p_{\text{CL}_s} = \frac{p_{\text{null}}}{p_{\text{alt}}}. \tag{7.19}$$

The null hypothesis is excluded with CL $= 1 - \alpha$, in favour of the alternative one, if $p_{\text{CL}_s} < \alpha$. This approach is more conservative than the standard frequentist approach, but behaves very similarly in regions where the experiment is sensitive to the null hypothesis. Figure 7.4 exemplifies the behaviour of the p_{CL_s} method:

1. If there is a good separation between the distributions of the test statistic under the null and alternative hypotheses, the alternative p-value is very close to one, and $p_{\text{CL}_s} \sim p_{\text{null}}$.

2. If the distributions of the test statistics under the null and alternative hypothesis significantly overlap, the alternative p-value in the denominator prevents p_{CL_s} from becoming too small.

This is desirable behaviour, because it means that hypotheses that are hardly distinguishable from the background-only hypothesis are not excluded just because of statistical fluctuations in data.

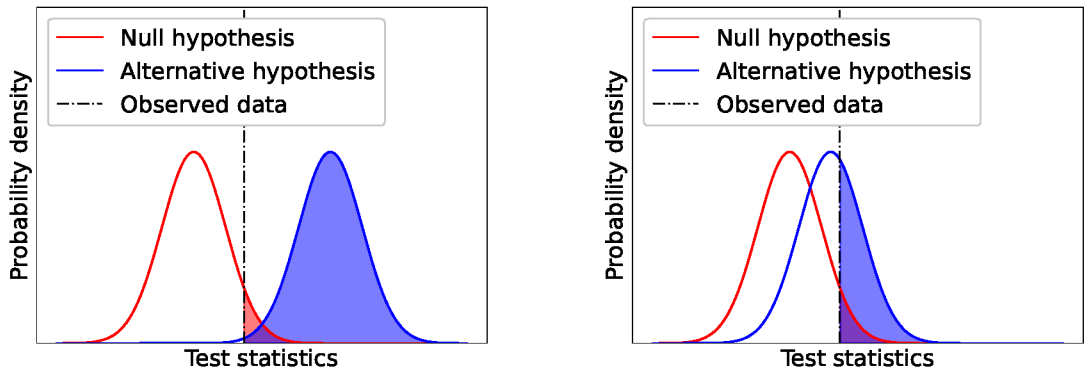

(a) (b)

Figure 7.4: Illustration of the application of the CL_s method in case of well-separated distributions of the test statistic under the null and alternative hypotheses (left) and in case of largely overlapping distributions (right), where the experiment has poor sensitivity to the signal. The shaded areas under the curves represent p-values.

7.4 p-value variations in the presence of interference

When reporting the excluded area in the parameter space of a model, usually both an observed and an expected excluded region are shown. The region expected to be excluded is the region in the parameter space of the model that is excluded if only background events are observed, i.e. the excluded region under the alternative hypothesis. Given that the test statistic is a random variable, it is subject to statistical fluctuations, which alter the CL_s p-value, resulting in a different excluded region. Hence, also $N\sigma$ variations on the region expected to be excluded, under the alternative hypothesis, are reported. The $N\sigma$ variations on the region expected to be excluded are the excluded regions according to a fluctuation of the test statistic corresponding to N standard deviations of a normal distribution. Since a fluctuation of the test statistic affects p-values, we can also see the problem as one of finding the p-value variations under the alternative hypothesis.

The previous baseline approach in ATLAS searches of reporting expected $N\sigma$ variations of CL_s p-values is the **contour** method. It involves the determination of a dataset representative of the $N\sigma$ fluctuation of the test statistic under the alternative hypothesis. This is equivalent to finding a representative dataset A_N yielding a maximum likelihood estimation of the parameter of interest μ which is $N\sigma$ away from its expected value, where σ is the (unknown) standard deviation of the distribution. If, as it is common in ATLAS searches, the test statistic for the hypothesis test is a profile-likelihood-ratio

$$q_\mu = -2\log\frac{\mathcal{L}\left(\mu,\hat{\hat{\boldsymbol{\theta}}}_\mu\right)}{\mathcal{L}\left(\hat{\mu},\hat{\boldsymbol{\theta}}\right)},$$

built from histograms whose bin expectation is linear in the parameter of interest, this dataset can be found by solving an equation involving the exclusion test statistic. More precisely, A_N is the dataset with a true value of $\mu = \mu_N$, where μ_N solves the equation $q_{\mu_N} = N^2$. It should be noted that if the bin expectation is not linear in the parameter of interest, the aforementioned equation is not always successful in finding the $N\sigma$ variation of $\hat{\mu}$. This can eventually result in a non-physical crossing of the median expected and/or the $1/2\sigma$ exclusion contours, making the contour method non-applicable. The CL_s p-values obtained with A_N as data are the $N\sigma$ variations on the expected p-values.

In this search, the histogram bin expectations are not linear in the parameter of interest, so the contour method is not applicable. Additionally, the test statistic for the exclusion stage is not the profile-likelihood-ratio, so, even if the bin expectations were linear in the POI, the calculation of the $\hat{\mu}$ variations would require the additional evaluation of the profile-likelihood-ratio in addition to the exclusion test statistic, making the calculation of the p-value variations unnecessarily convoluted. A different method for finding CL_s p-value variations is used, named **band method**, which has now been adopted as the new baseline in the `TRExFitter` framework and hence in the majority of ATLAS searches. The method consists in explicitly finding the values of the test statistic r_1 corresponding to $N\sigma$ fluctuations under the alternative hypothesis. This is done by finding the value r_1^N related to the cumulative of a standard Gaussian $\Phi(N)$ by the equation

$$P\left(r_1 > r_1^N \middle| \mathrm{alt}\right) = 1 - \Phi(N). \tag{7.20}$$

The CL_s p-values obtained using the values r_1^N of the test statistic are the $N\sigma$ variations of the expected p-values. It should be noted that this is the natural way of calculating variations on p-values, although the contour method is equivalent to it, with the right choice of test statistic and bin expectation parametrisation discussed above. The band method is therefore suited for the calculation of p-value variations regardless of the choice of test statistic. It is also worth noting that the median expected p-value is obtained for $N = 0$.
The area between the $+1(2)\sigma$ and $-1(2)\sigma$ excluded regions in the parameter space is called $1(2)\sigma$ band.

7.5 From p-values to exclusion regions

A point in the parameter space of the model under investigation is excluded at 95% CL if its CL_s p-value for $\sqrt{\mu} = 1$ is lower than 0.05. In this regard, it is worth noting that many searches for BSM physics, do not test a single value of the POI against the background-only hypothesis, but rather a wide range of values, and set an upper limit on POI, i.e. its highest possible value resulting in a p_{CL_s} higher than 0.05. In searches not including signal-background interference, there is a correspondence between the POI (signal strength) and the signal cross-section, and the upper limits on the POI trivially translate into upper limits on the signal cross-section. This approach is not possible in the analysis presented in this thesis, because values of $\sqrt{\mu} \neq 1$ do not produce the interference pattern of the benchmark model under consideration (Section 7.3.1), and because there is no clear correspondence between $\sqrt{\mu}$ and the BSM cross-section, due to the signal-background interference.
Due to the quadratic dependence of the histogram bin content expectation on $\sqrt{\mu}$, the CL_s p-value is not a monotonic function of $\sqrt{\mu}$, as exemplified by Figure 7.5 for one of the signal hypotheses used in this search. The function $p_{\mathrm{CL}_s}\left(\sqrt{\mu}\right)$ can cross the 0.05 value multiple times, resulting in

disjoint confidence intervals for the POI, which do not allow for a unique definition of an upper limit. Additionally, the crossing value can differ significantly between the median and $\pm N\sigma$ curves, for the same signal hypothesis. Finally, the behaviour of the $p_{\mathrm{CL}_s}\left(\sqrt{\mu}\right)$ curve strongly depends on the parameters of the model, and different points in the same model can have single or multiple crossings of the 0.05 value.

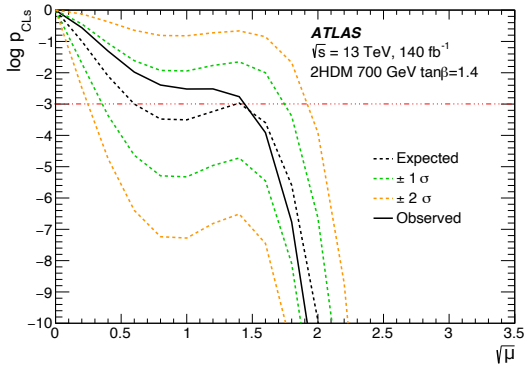

Figure 7.5: Example of a p_{CL_s} scan as a function of $\sqrt{\mu}$ for the Type-II 2HDM signal hypothesis with $m_A = m_H = 700$ GeV and $\tan\beta = 1.4$. The expected and observed lines, as well as $\pm 1\sigma$ and $\pm 2\sigma$ lines do not exhibit a monotonic behaviour in terms of the POI $\sqrt{\mu}$. The red horizontal line corresponds to the p_{CL_s} value of 0.05 used as a threshold for the exclusion; values with $p_{\mathrm{CL}_s} < 0.05$ are excluded at 95% CL.

It is then interesting to take a closer look at how exclusion regions are derived in this search, as the statistical method is relevant for all searches where an upper limit on the POI cannot be defined due to the p_{CL_s} behaviour as a function of the POI $\sqrt{\mu}$.
In the Type-II 2HDM, hMSSM, and 2HDM+a interpretations, the exclusion region is obtained by calculating $P_{\mathrm{CL}_s} := p_{\mathrm{CL}_s}\left(\sqrt{\mu} = 1\right)$ in a fine grid of points in the $m_A - \tan\beta$ plane. In the generic (pseudo)scalar interpretation, it is obtained by calculating $P_{\mathrm{CL}_s} := p_{\mathrm{CL}_s}\left(\sqrt{\mu} = g^2_{A/Ht\bar{t}}\right)$ in a fine grid of points in the $m_{A/H} - g_{A/Ht\bar{t}}$ plane. A linear interpolation method is used between the points to find the level curves $P_{\mathrm{CL}_s} = 0.05$. This is opposed to a common procedure in which upper limits on the POI are calculated for a grid of points and then an interpolation is used to find the level curve where the upper limits are equal to 1.
The technique used in this analysis bypasses the calculation of upper limits and can therefore be used in all searches where upper limits cannot be reasonably defined or calculated. Moreover, it can also be used in traditional searches, and in this case it gives equivalent results to those obtained with the method based on the upper-limit calculation.

CHAPTER 8

Statistical inference and results

The results of the statistical analysis are presented in this section. First, profile likelihood fits to data are performed under the background-only hypothesis, where the parameter of interest is fixed at the SM value $\sqrt{\mu} = 0$ and only the NPs are allowed to vary, to quantify the post-fit agreement of the collected data with the SM expectation. Then, a search stage is performed, where deviations of the data from the SM are quantified. Finally, not observing any significant deviation of the data from the SM, exclusion regions in the parameter spaces of the benchmark models are derived.

8.1 Construction of the profile likelihood

The profile likelihood is built as described in Chapter 7 from the $m_{t\bar{t}}$ (one-lepton channel) and $m_{\ell\ell bb}$ (two-lepton channel) histograms. As outlined in Sections 6.4 and 6.5, sixteen signal regions enter the fit, eleven of which are in the one-lepton channel, while five are in the two-lepton channel. The eleven one-lepton signal regions result from categorising events by decay topology (Merged and Resolved), by the number of selected b-tagged jets ($1b$ or $2b$), and in bins of the angular variable $\left|\cos\theta^*\right|$. The 5 two-lepton signal regions are defined in bins of the angular variable $\Delta\phi_{\ell\ell}$. The binning of the histograms in both channels is optimised with the goal of maximising the number of bins, so that the interference pattern is reconstructed with as high a resolution as possible, without having bins narrower than the experimental resolution of the variable of interest.

Uncertainty correlation scheme Systematic uncertainties are introduced in profile likelihood fits via NPs, as described in Section 7.1. When a single NP is used across multiple regions (samples), for the same uncertainty, it is said that the uncertainty is correlated across regions (samples).
All experimental uncertainties are treated as fully correlated across samples and across the signal regions of both the one-lepton and two-lepton channels, as their sources are independent of the final state of the event.
The modelling uncertainties for the different signal and background processes are treated as uncorrelated between samples, as they come from different sources. The only exception is the uncertainty on the mass of the top quark, which is correlated between the signal, signal-plus-interference, and SM $t\bar{t}$ samples.
The uncertainties on the SM $t\bar{t}$ background related to PS, hadronisation, and the matching of the PS and ME simulations, including the choice of the h_{damp} Powheg parameter are all obtained by a

simple comparison of the nominal sample with an alternative sample. This is a notable yet necessary simplification, as there is only a limited number of MC generators for the PS that can be matched to POWHEG, and this leads to very conservative uncertainties. For this reason, these uncertainties are uncorrelated across the eleven one-lepton and five two-lepton signal regions.
The uncertainties on the SM $t\bar{t}$ process related to renormalisation and factorisation scales, and levels of ISR and FSR have a dependence on the kinematics of the event and are therefore uncorrelated between the one-lepton and two-lepton channels, and between the Merged and Resolved topologies of the one-lepton channel. They are, however, treated as correlated across bins of the $\left|\cos\theta^*\right|$ and $\Delta\phi_{\ell\ell}$ angular variables. The same treatment is reserved to the uncertainty on the SM $t\bar{t}$ cross-section, in an attempt to have a conservative approach. All other uncertainties are treated as correlated across channels and signal regions.

Smoothing and pruning of systematic uncertainties Statistical fluctuations in systematic uncertainties can match fluctuations in the data by chance and alter the results of fits. They can also lead to a double-counting of statistical uncertainties if the fluctuations in the systematic uncertainties arise from statistical fluctuations in the same dataset. In order to avoid this, a *smoothing* procedure is applied to systematic variations histograms, which averages out the fluctuations, resulting in a smoother histogram. The smoothing procedure is implemented as part of the `TRExFitter` tool and it works as follows[161].

1. If the combined statistical uncertainty on the variation histogram is larger than 5%, average all bins, resulting in a flat uncertainty.
2. If the combined statistical uncertainty on the variation histogram is lower than 5%, merge the pair of adjacent bins with the smallest sum of squared differences between the original bin contents and the average bin content. The new bin contents will be the average between the two original contents.
3. Repeat step 2 until the variation histogram has at most three changes in slope.
4. Starting from the right, merge every bin with a statistical uncertainty larger than 5% with the one on its left, until no bin has an uncertainty larger than 5%.

In order to improve the numerical stability of the NLL minimisation, a *pruning* procedure is also applied to remove nuisance parameters with negligible impact on the final result, dropping all uncertainties containing no bin with a variation greater than 0.01‰ compared to the nominal.

8.2 Profile likelihood fits under the background-only hypothesis

The agreement between the observed data and the SM expectation is tested via a profile-likelihood fit under the background-only hypothesis ($\sqrt{\mu} = 0$). Only the NPs are allowed to vary in the fit. Figures 8.1, 8.2, 8.3 show the reconstructed distributions of $m_{t\bar{t}}$ in the signal regions of the one-lepton channel, and of $m_{\ell\ell bb}$ in the signal regions of the two-lepton channel. The data points are in good agreement with the SM expectation, within the post-fit constrained uncertainty bands.

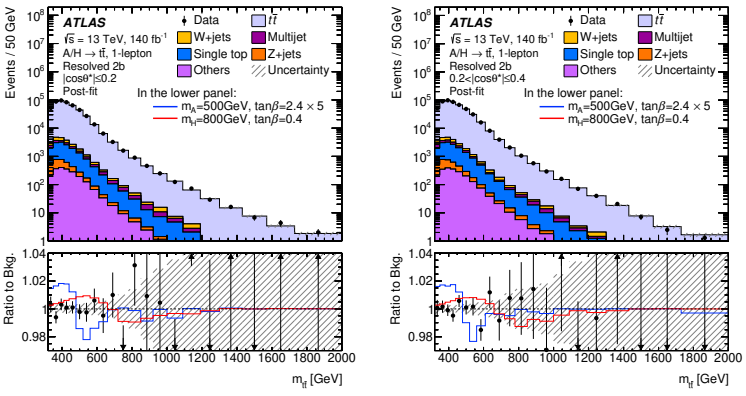

(a) Resolved $2b$, $|\cos\theta^*| < 0.2$

(b) Resolved $2b$, $0.2 < |\cos\theta^*| < 0.4$

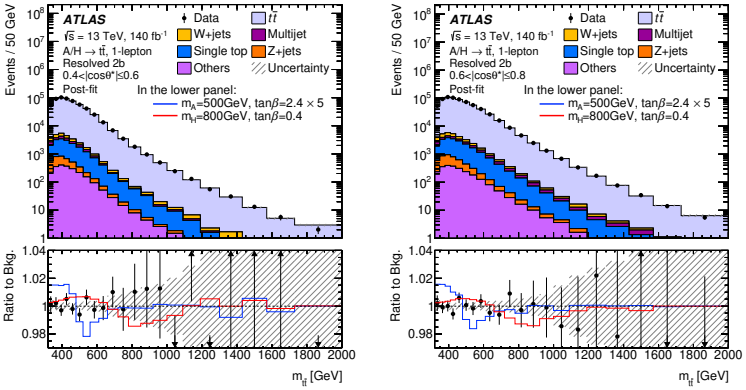

(c) Resolved $2b$, $0.4 < |\cos\theta^*| < 0.6$

(d) Resolved $2b$, $0.6 < |\cos\theta^*| < 0.8$

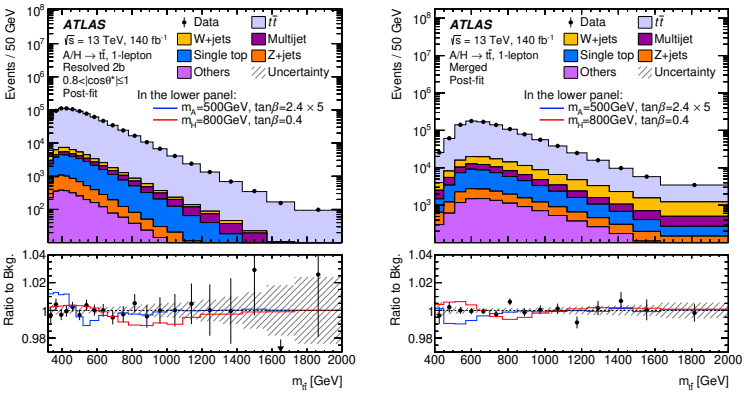

(e) Resolved $2b$, $0.8 < |\cos\theta^*| < 1.0$

(f) Merged

Figure 8.1: Distributions of the reconstructed $m_{t\bar{t}}$ in (a-e) the five Resolved signal regions with 2 b-tags and (f) the Merged signal region of the one-lepton channel, after fit under the background-only hypothesis. In the top panel, the data points are overlaid on the SM prediction, while in the bottom panel, the ratio between the observed data and the post-fit SM expectation is shown. The ratio between the expected distributions under the BSM and the SM hypotheses is also shown in the bottom panel for two representative signal hypotheses. Figure published in Ref. [19].

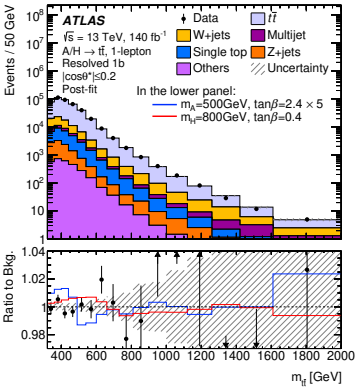

(a) Resolved $1b$, $|\cos\theta^*| < 0.2$

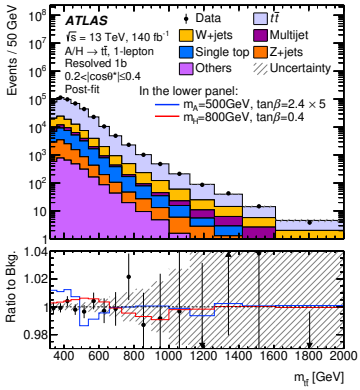

(b) Resolved $1b$, $0.2 < |\cos\theta^*| < 0.4$

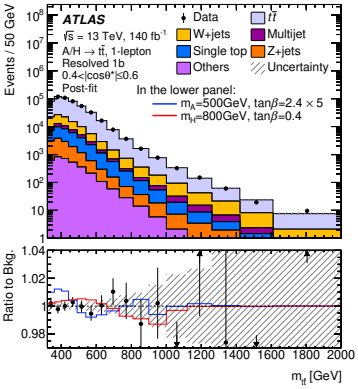

(c) Resolved $1b$, $0.4 < |\cos\theta^*| < 0.6$

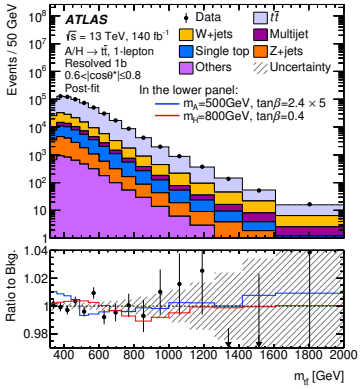

(d) Resolved $1b$, $0.6 < |\cos\theta^*| < 0.8$

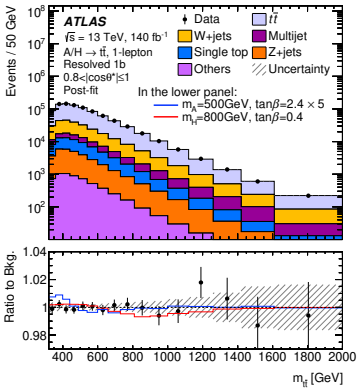

(e) Resolved $1b$, $0.8 < |\cos\theta^*| < 1.0$

Figure 8.2: Distributions of the reconstructed $m_{t\bar{t}}$ in the five Resolved signal regions with 1 b-tag of the one-lepton channel, after fit under the background-only hypothesis. In the top panel, the data points are overlaid on the SM prediction, while in the bottom panel, the ratio between the observed data and the post-fit SM expectation is shown. The ratio between the expected distributions under the BSM and the SM hypotheses is also shown in the bottom panel for two representative signal hypotheses. Figure published in Ref. [19].

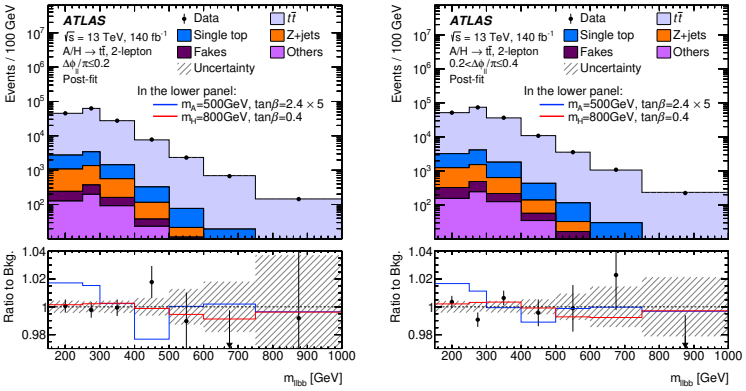

(a) $0.0 < \Delta\phi/\pi < 0.2$

(b) $0.2 < \Delta\phi/\pi < 0.4$

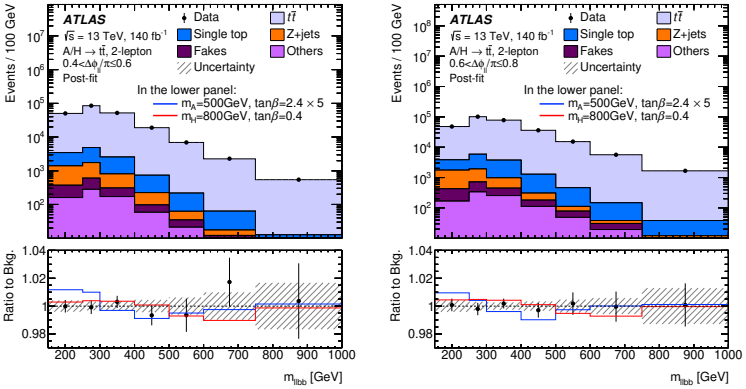

(c) $0.4 < \Delta\phi/\pi < 0.6$

(d) $0.6 < \Delta\phi/\pi < 0.8$

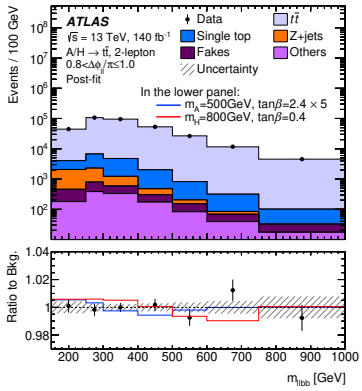

(e) $0.8 < \Delta\phi/\pi < 1.0$

Figure 8.3: Distributions of the reconstructed $m_{\ell\ell bb}$ in the five signal regions of the two-lepton channel, after fit under the background-only hypothesis. In the top panel, the data points are overlaid on the SM prediction, while in the bottom panel, the ratio between the observed data and the post-fit SM expectation is shown. The ratio between the expected distributions under the BSM and the SM hypotheses is also shown in the bottom panel for two representative signal hypotheses. Figure published in Ref. [19].

8.3 Impact and ranking of systematic uncertainties

The importance of each systematic uncertainty in the statistical model is evaluated via fits under the signal+interference+background hypothesis. Two signal hypotheses are considered, based on the Type-II 2HDM benchmark model.
Two post-fit impacts are calculated for each NP, corresponding to an upward and a downward fluctuation of the NP. The *up* (*down*) post-fit impact of each NP is calculated as the difference between two best-fit values of the parameter of interest $\sqrt{\mu}$: the first value comes from an unconditional fit; the second value comes from a conditional fit in which the corresponding NP is fixed at the value corresponding to its post-fit $+1\sigma$ (-1σ) variation. This procedure yields a ranking of post-fit impacts of all NPs in the fit. NPs corresponding to the same uncertainty or to uncertainties with a similar source are then grouped, so that the impact of the main sources of uncertainties can be better visualised. The impact of a given group is evaluated as the sum-in-quadrature of the individual uncertainties in the group. The fractional impact of the group is calculated as the ratio between the impact of the group and the total uncertainty on the best-fit value $\hat{\sqrt{\mu}}$ for the POI. The total systematic uncertainty is obtained as the sum-in-quadrature of all the impacts of individual uncertainties. The total statistical uncertainty is obtained by subtracting in quadrature the total systematic uncertainty from the total uncertainty on the best-fit value $\hat{\sqrt{\mu}}$ for the POI.

Table 8.1 shows the fractional impacts of all groups of systematic uncertainties. The dominant uncertainties are related to the modelling of the SM $t\bar{t}$ background. This is an expected result, as the SM $t\bar{t}$ production is the main, irreducible background for the search presented in this thesis. This result also highlights the important role that reducing these uncertainties via a reweighting of the SM $t\bar{t}$ prediction to NNLO-QCD+NLO-EW played for the sensitivity of the search to the BSM models. The largest contributions to the uncertainty on $\hat{\sqrt{\mu}}$ are related to the NNLO prediction and reweighting procedure, to the ME-PS matching (p_T^{hard}, h_{damp}), and to the $t\bar{t}$ spin correlation (lineshape).
The dominant experimental uncertainties are those on the JES, JER, and flavour tagging SFs.

Table 8.1: Post-fit fractional impacts [19] of different uncertainty groups, relative to the total uncertainty on the best-fit value $\hat{\sqrt{\mu}}$ of the POI, for two representative signal hypotheses in the Type-II 2HDM benchmark model: a single pseudoscalar with $m_A = 800$ GeV and $\tan\beta = 0.4$ and a scenario with both a scalar and a pseudoscalar, with $\tan\beta = 2.0$ and $m_A = m_H = 500$ GeV. The statistical uncertainty is obtained by subtracting in quadrature the total systematic uncertainty from the total uncertainty on $\hat{\sqrt{\mu}}$. The observed best-fit value of the POI is $\hat{\sqrt{\mu}} = -0.147 \pm 0.104$ for the hypothesis with $m_A = 800$ GeV and $\hat{\sqrt{\mu}} = +0.071 \pm 0.224$ for $m_A = m_H = 500$ GeV. Note that the total sum in quadrature of all impacts does not precisely reach 100% because of the rounding precision of the numbers provided within this table.

Uncertainty component	Fractional contribution [%]	
	$m_A = 800$ GeV, $\tan\beta = 0.4$	$m_A = m_H = 500$ GeV, $\tan\beta = 2.0$
Experimental	**30**	**42**
Small-R jets (JER, JES)	22	29
Large-VR jets	11	20
Flavour tagging	13	17
Leptons	4	5
Other (MET, luminosity, pile-up, JVT)	10	14
Modelling: SM $t\bar{t}$ and signal	**91**	**79**
$t\bar{t}$ NNLO	49	28
$t\bar{t}$ lineshape	27	29
$t\bar{t}$ ME-PS ($p_{\mathrm{T}}^{\mathrm{hard}}$)	36	30
$t\bar{t}$ ME-PS (h_{damp})	41	25
$t\bar{t}$ ISR& FSR	9	13
$t\bar{t}$ PS	29	41
$t\bar{t}$ cross-section	21	31
$t\bar{t}$ scales & PDF	21	16
m_t	6	4
Signal	19	9
Modelling: other	**41**	**16**
W+jets	11	8
Z+jets	1	2
Multijet	27	10
Fakes	<1	1
Other bkg.	29	10
MC statistics	**18**	**26**
Total systematic uncertainty	**±100**	**±100**
Total statistical uncertainty	**< 1**	**< 1**

8.4 Search stage

Deviations of the observed data from the SM expectation are quantified via the search test described in Section 7.13. Three different tests are performed : a search for resonant excesses, a search for localised deficits, and a search for interference patterns. All three tests are performed using samples generated in the context of the generic (pseudo)scalar model (Section 2.4.4), with the search for interference patterns. The searches for excesses and deficits are performed to keep the search stage as general as possible, as the search presented in this thesis is the first one probing the $m_{t\bar{t}}$ spectrum on the ATLAS full Run-2 dataset.

Different bin content parametrisations are employed for the different tests, involving the same signal and interference samples:

1. $\nu = \mu S + B$ for the **resonance search**;
2. $\nu = -\mu S + B$ for the **deficit search**;
3. $\nu = \left(\mu - \sqrt{\mu}\right) S + \sqrt{\mu}\,(S + I) + B$ for the **interference search**.

Only the contribution of either the pseudoscalar A or the scalar H is assumed to be present in the spectra of the variables of interest, under the BSM hypothesis.

The most significant resonant excess is observed at a mass of 850 GeV, under the scalar hypothesis, and with a relative width $\Gamma_{H\to t\bar{t}}/m_H = 5\%$. It constitutes a deviation from the SM expectation with a significance of 2.5σ. This deviation from the SM expectation is driven by an excess of events in the one-lepton Merged channel, specifically in the $m_{t\bar{t}}$ bin between 770 GeV and 850 GeV (cf. Figure 8.1). Similar deviations above 2σ are observed also for other widths and for the pseudoscalar hypothesis. The most significant deficit is observed at a mass of 1200 GeV, under the scalar hypothesis, and amounts to a deviation from the SM of about 2.4σ. A similar 2σ variation is observed under the pseudoscalar hypothesis at a 1150 GeV mass.
More details about the resonant excess and localised deficit searches can be found in Appendix A.

Figures 8.4 and 8.5 show the local p-values under the background-only hypothesis as a function of the mass of the BSM (pseudo)scalar, for the interference search. The p-values are obtained separately in the one-lepton and two-lepton channels, and by combining both. It is interesting to note that the p-values obtained by combining the one- and two-lepton channels are close to the ones obtained in the one-lepton channel alone; this means that the sensitivity to BSM signatures is dominated by the one-lepton channel.
The most significant interference pattern is observed for a pseudoscalar hypothesis, with $m_A = 800$ GeV and a relative width of 10%. The observed deviation from the SM has a significance of 2.3σ and corresponds to a best-fit value of the parameter of interest of $\hat{\sqrt{\mu}} = 4.08$. Given the equivalence between $\sqrt{\mu}$ and the coupling modifier in the generic pseudoscalar model, this corresponds to a best-fit value of the A-$t\bar{t}$ coupling of $\hat{g}_{At\bar{t}} \approx 2.02$.
It is not by chance that the most significant interference pattern and the most significant resonant pattern are observed at similar masses. In fact, under the interference hypothesis, at high values of $\sqrt{\mu}$, such as the best-fit value $\hat{\sqrt{\mu}} = 4.0$, the pure-signal term S in the bin content parametrisation dominates over the interference term, making the interference pattern more *resonance-like*. This is also exemplified in Figure 2.8, recalling the relation $\sqrt{\mu} = g^2_{A/Ht\bar{t}}$ in the generic (pseudo)scalar model.

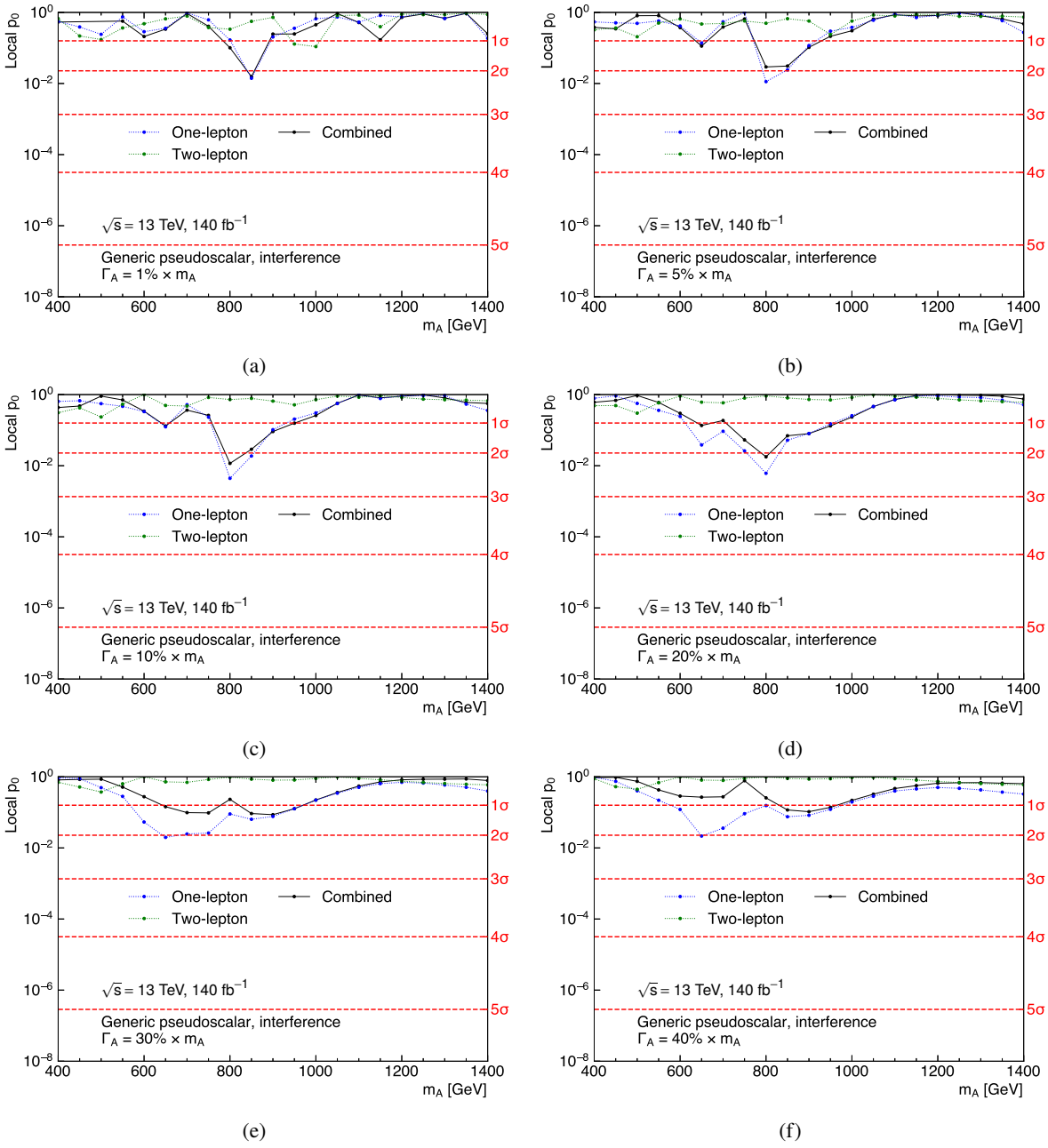

Figure 8.4: Observed local p-values under the background-only hypothesis, against a pseudoscalar interference hypothesis, as a function of m_A for different values of the relative width of the pseudoscalar A: (a) 1%, (b) 5%, (c) 10%, (d) 20%, (e) 30%, (f) 40%. The p-values are calculated separately in the one-lepton and two-lepton channels, and by combining both. On the right-hand y-axis, the Gaussian significances corresponding to the p-values on the left-hand y-axis are reported.

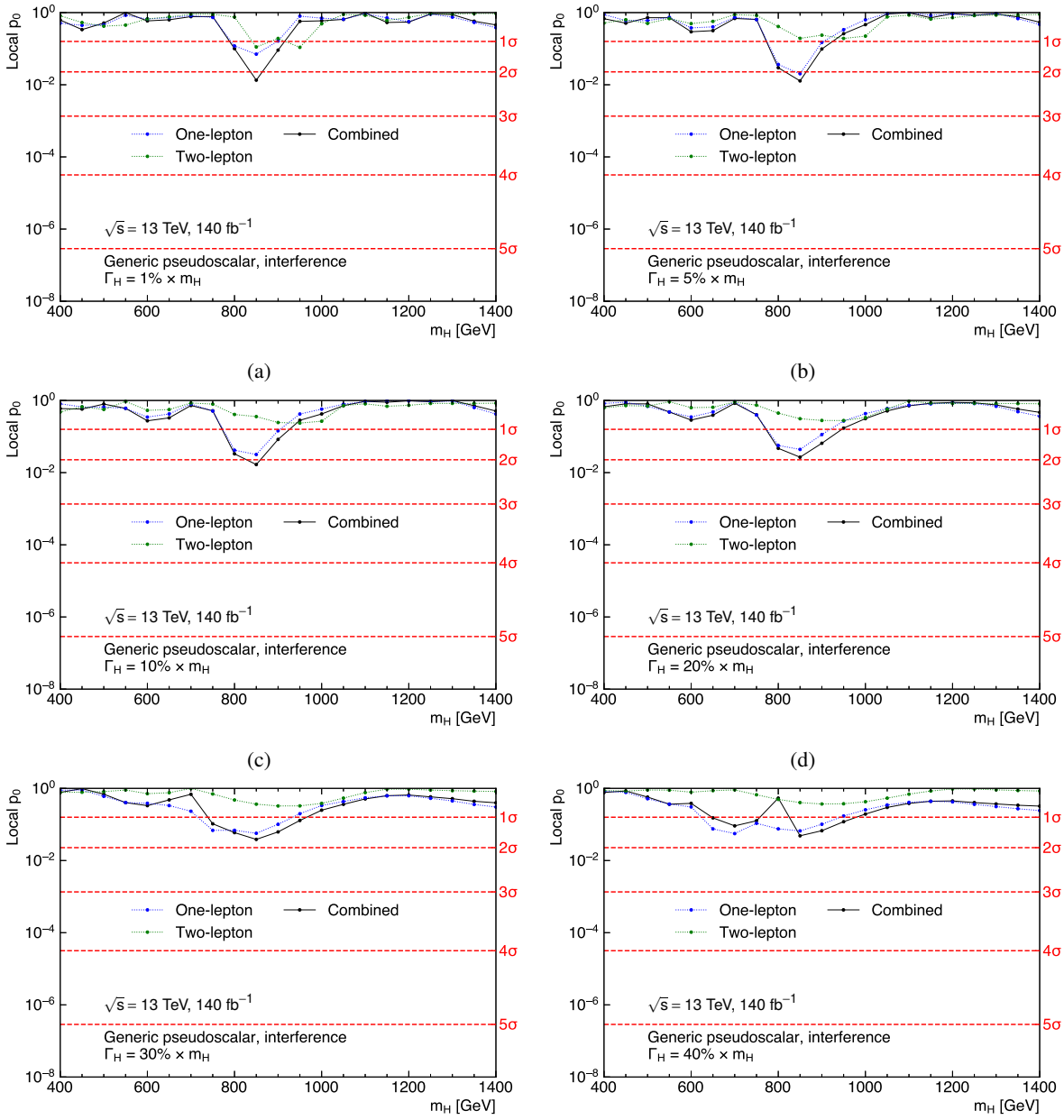

Figure 8.5: Observed local p-values under the background-only hypothesis, against a scalar interference hypothesis, as a function of m_H for different values of the relative width of the scalar H: (a) 1%, (b) 5%, (c) 10%, (d) 20%, (e) 30%, (f) 40%. The p-values are calculated separately in the one-lepton and two-lepton channels, and by combining both. On the right-hand y-axis, the Gaussian significances corresponding to the p-values on the left-hand y-axis are reported.

8.5 Exclusion in the BSM parameter space

In the absence of significant deviations from the SM expectation, excluded regions are calculated in the parameter spaces of the benchmark models, using the approach described in Chapter 7.

Figure 8.6 shows the regions in the $m_A - \tan\beta$ plane, for the Type-II 2HDM and hMSSM benchmarks, excluded at 95% CL. The interference pattern for both the pseudoscalar A and the scalar H are assumed to contribute to the spectra of the variables of interest in both cases. In the type-II 2HDM hypothesis, the masses of A and H are assumed to be equal, and the relation $\cos(\beta - \alpha) = 0$ is required, as mentioned in Section 2.4.1. The lowest tested $\tan\beta$ value of 0.4 is excluded for masses up to $\approx$ 1200 GeV in both benchmark models. Values of tan $\tan\beta$ smaller than 3.49 (3.52) are observed (expected) to be excluded for $m_A = m_H = 400$ GeV in the 2HDM benchmark. In the hMSSM benchmark, values of $\tan\beta$ smaller than 3.16 (3.37) are observed (expected) to be excluded for $m_A = 400$ GeV. The observed exclusion is stronger than expected in both models at a mass of $\approx$ 800 GeV, by approximately 2σ, consistent with the excess of events observed in the search stage. In both the 2HDM and hMSSM benchmarks, the signal-background interference results in a deficit of events compared to the SM expectation for values of $m_{t\bar{t}}$ close to the mass of the heavy Higgs. Hence, an excess of events in the data results in a stronger-than-expected exclusion.

Constraints on the 2HDM+a benchmark, in the $\tan\beta - m_a$ plane are also derived and shown in Figure 8.7. The value of the A-a mixing angle θ is chosen such that $\sin\theta = 0.35$ and 0.7, respectively, and the masses of the charged and neutral Higgs bosons of the 2HDM are set to $m_A = m_H = m_{H^\pm} = 600$ GeV. For the benchmark case with $\sin\theta = 0.35$ (0.70), values of $\tan\beta$ up to almost 1.2 (1.0) are excluded. Only a moderate dependence of the excluded regions is observed in terms of m_a, due to two opposing effects balancing each other out: the first is the decrease in the production cross-section of the mediator a with increasing m_a, and the second is an increase of the branching ratio for the decay $A \to t\bar{t}$ with increasing m_a. The latter is related to the fact that the branching ratio for the decay $A \to ah$ decreases with increasing m_a.

For the generic (pseudo)scalar model (Section 2.4.4), constraints on the parameter space are shown separately for the pseudoscalar and scalar hypotheses, in the $m_{A/H} - g_{A/Ht\bar{t}}$ plane, in Figures 8.8 and 8.9[1], respectively. Only the interference pattern of either the pseudoscalar A or the scalar H is assumed to contribute to the spectra of the variables of interest in this benchmark model. The excluded regions are derived separately for different hypotheses of the width $\Gamma_{A/H}$. At a fixed width, not all values of the coupling modifier lead to a physical scenario. This is because for large couplings, the partial width $\Gamma_{A/H\to t\bar{t}}$, which depends on the coupling modifier, can exceed the total width $\Gamma_{A/H}$. The regions of the parameter space which are not physically allowed are marked by a hatched area. The constraints on the pseudoscalar hypothesis are stronger than the ones obtained in the scalar hypothesis, as the pure-signal production cross-section for a single pseudoscalar is generally higher than the pure-signal production cross-section of scalars. For values of the relative width $\Gamma_{A/H\to t\bar{t}}/m_A$ of the (pseudo)scalar lower than 10%, the observed constraints are slightly weaker than expected by around 2σ, in the mass region 800 – 850 GeV. This is consistent with the 2σ-discrepancy from the SM observed in same mass region at the search stage (Section 8.4). A discrete "island" is observed in the excluded region for the scalar hypothesis, with $\Gamma_A = 20\%$. This is due to the fact that the likelihood,

[1] This thesis was written and submitted to Universität Hamburg before the publication of the final results from the ATLAS collaboration in the Journal of High Energy Physics, in August 2024 [19]. The constraints on the parameter space of the generic (pseudo)scalar model presented in this thesis are obtained without applying any correction factor to NLO precision to the S and S+I samples, differently from the ones shown in Ref. [19]. More details can be found in Appendix B.

and consequently the CL_s p-value, has a local minimum for $\sqrt{\mu} > 1$ for these two hypotheses, at a mass of 850 GeV, and is not monotonic in $\sqrt{\mu}$ (see also Section 7.5); this results in the CL_s p-value crossing the exclusion threshold 0.05 multiple times. Since there is a perfect equivalence between $\sqrt{\mu}$ and the coupling modifier, via the relation $\sqrt{\mu} = g^2_{A/Ht\bar{t}}$, this results in an "island" in the observed contour.

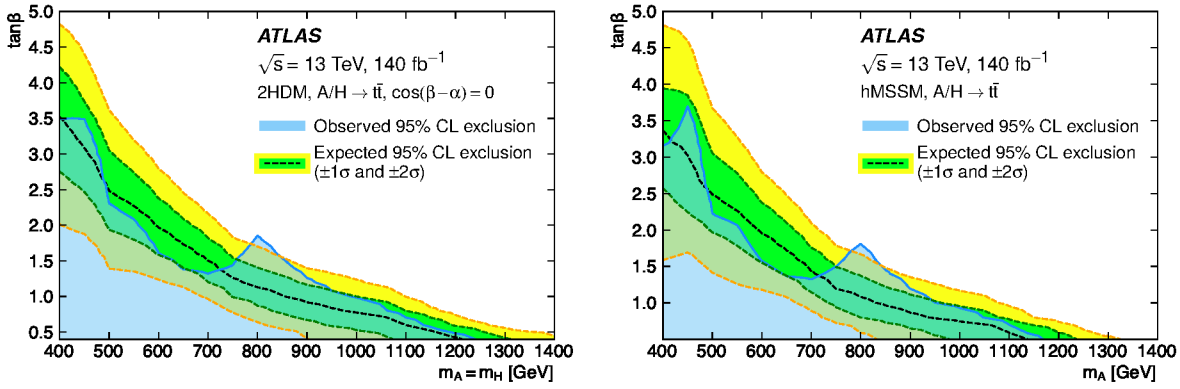

(a) Type-II 2HDM (b) hMSSM

Figure 8.6: Observed and expected exclusion regions in the $m_{A/H} - \tan\beta$ plane of a (a) Type-II 2HDM in the alignment limit ($\cos(\beta - \alpha) = 0$) with mass-degenerate pseudoscalar and scalar states, and the (b) hMSSM. The observed exclusion regions are indicated by the shaded area. The boundary of the expected exclusion region under the background-only hypothesis is marked by the dashed line. The surrounding shaded bands correspond to the $\pm 1(2)\sigma$ variations of the expected excluded regions. Figure published in Ref. [19].

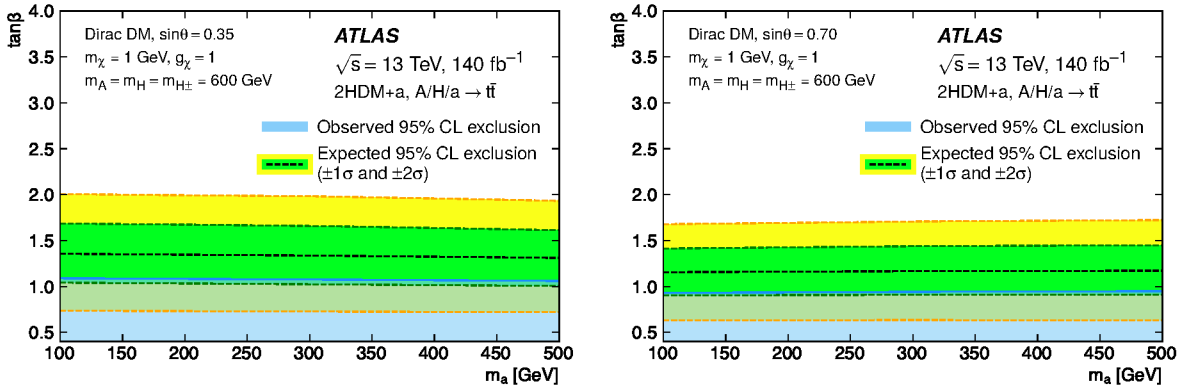

(a) $\sin\theta = 0.35$ (b) $\sin\theta = 0.70$

Figure 8.7: Observed and expected exclusion regions in the $m_a - \tan\beta$ plane for the 2HDM+a with $m_A = m_H = m_{H^\pm} = 600$ GeV and (a) $\sin\theta = 0.35$, (b) $\sin\theta = 0.70$. The observed exclusion regions are indicated by the shaded area. The boundary of the expected exclusion region under the background-only hypothesis is marked by the dashed line. The surrounding shaded bands correspond to the $\pm 1(2)\sigma$ variations of the expected excluded regions. Figure published in Ref. [19].

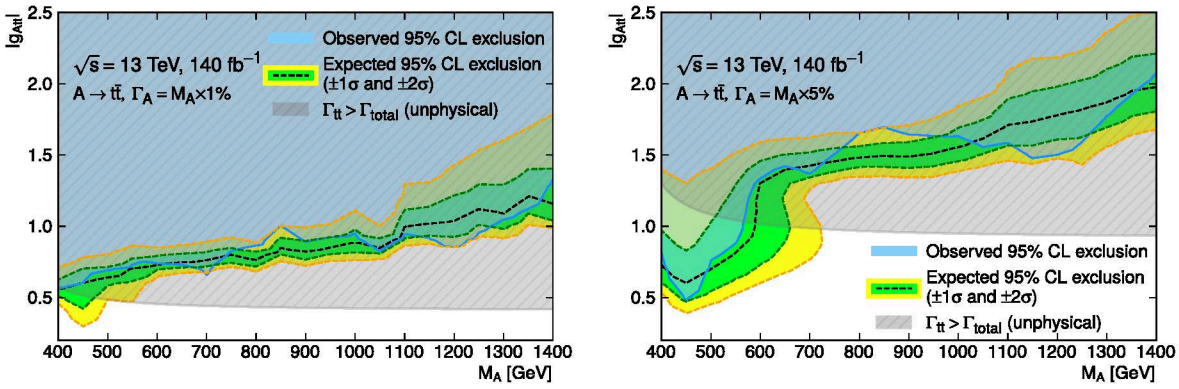

(a) $\Gamma_{A\to t\bar{t}}/m_A = 1\%$

(b) $\Gamma_{A\to t\bar{t}}/m_A = 5\%$

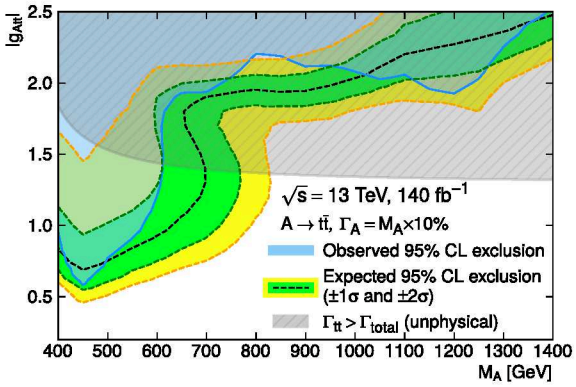

(c) $\Gamma_{A\to t\bar{t}}/m_A = 10\%$

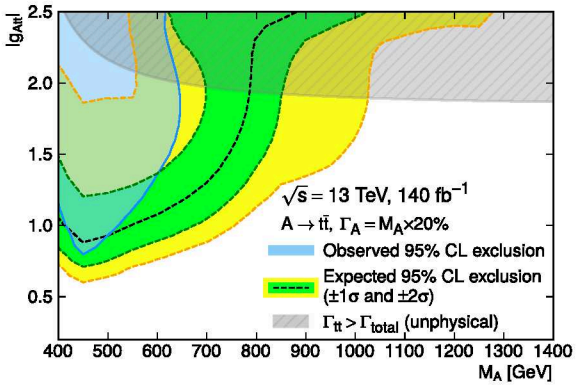

(d) $\Gamma_{A\to t\bar{t}}/m_A = 20\%$

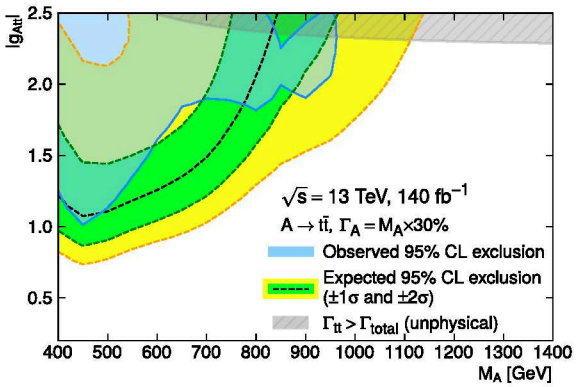

(e) $\Gamma_{A\to t\bar{t}}/m_A = 30\%$

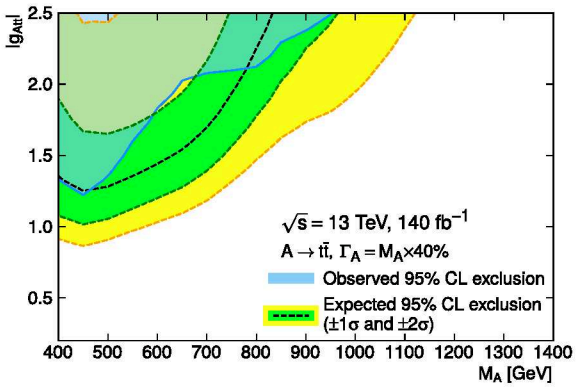

(f) $\Gamma_{A\to t\bar{t}}/m_A = 40\%$

Figure 8.8: Constraints on the coupling strength modifier $g_{At\bar{t}}$ as a function of m_A for different values of the relative width of the pseudoscalar A: (a) 1%, (b) 5%, (c) 10%, (d) 20%, (e) 30%, (f) 40%. The hatched area marks the unphysical region of parameter space where the partial width $\Gamma(A \to t\bar{t})$ is larger than the total width of A. The observed exclusion regions are indicated by the shaded area. The boundary of the expected exclusion region under the background-only hypothesis is marked by the dashed line. The surrounding shaded bands correspond to the $\pm 1(2)\sigma$ variations of the expected excluded regions.

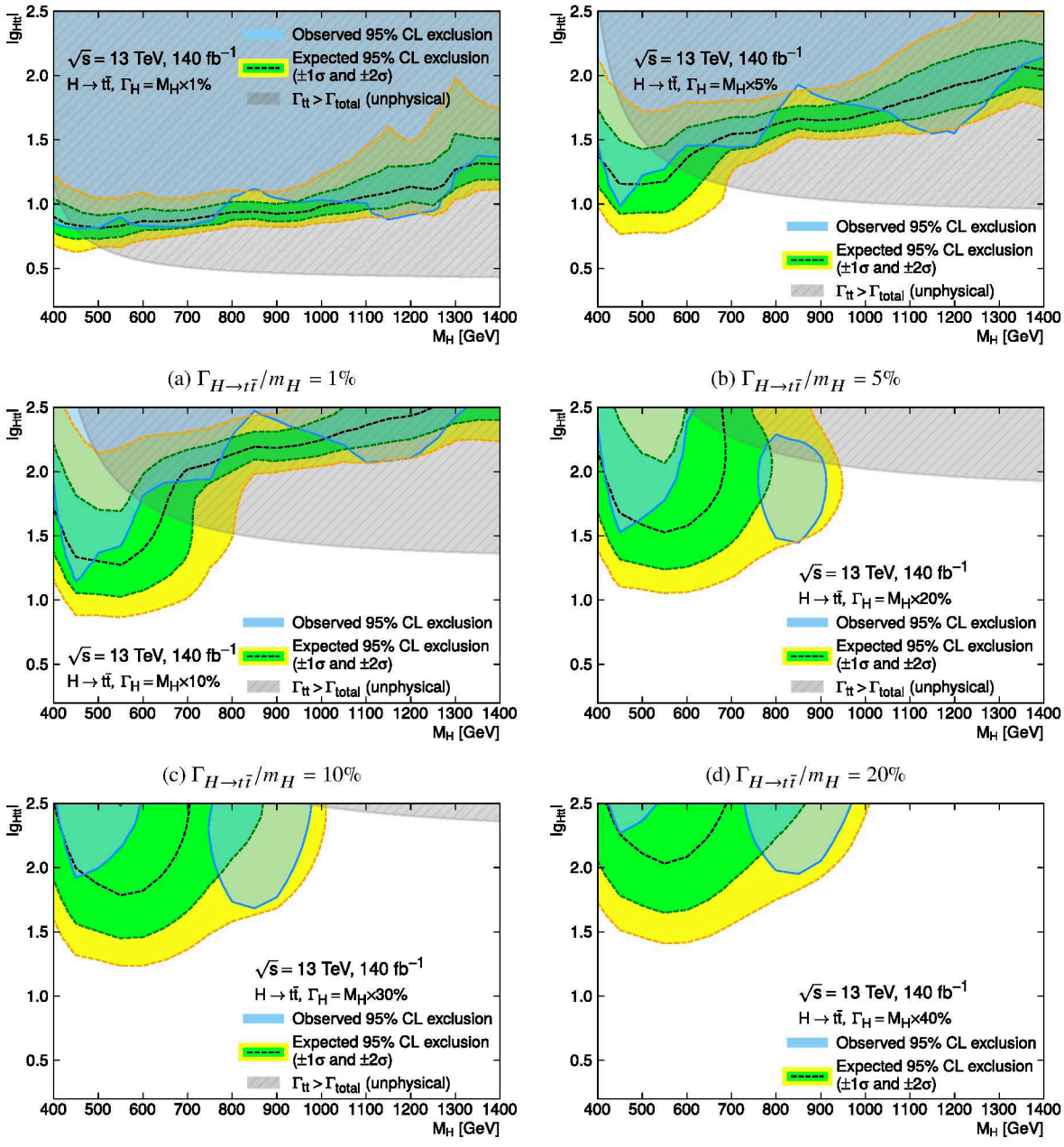

(a) $\Gamma_{H\to t\bar{t}}/m_H = 1\%$

(b) $\Gamma_{H\to t\bar{t}}/m_H = 5\%$

(c) $\Gamma_{H\to t\bar{t}}/m_H = 10\%$

(d) $\Gamma_{H\to t\bar{t}}/m_H = 20\%$

(e) $\Gamma_{H\to t\bar{t}}/m_H = 30\%$

(f) $\Gamma_{H\to t\bar{t}}/m_H = 40\%$

Figure 8.9: Constraints on the coupling strength modifier $g_{Ht\bar{t}}$ as a function of m_H for different values of the relative width of the scalar H: (a) 1%, (b) 5%, (c) 10%, (d) 20%, (e) 30%, (f) 40%. the hatched area marks the unphysical region of parameter space where the partial width $\Gamma(H \to t\bar{t})$ is larger than the total width of H. The observed exclusion regions are indicated by the shaded area. The boundary of the expected exclusion region under the background-only hypothesis is marked by the dashed line. The surrounding shaded bands correspond to the $\pm 1(2)\sigma$ variations of the expected excluded regions.

CHAPTER 9

Discussion and outlook

The search for heavy Higgs bosons decaying to a $t\bar{t}$ pair has been conducted for the first time with the full Run-2 dataset at the centre-of-mass energy of 13 TeV at an LHC experiment. In this chapter, the results of the search are discussed and compared to existing constraints on the signal process under consideration, in the context of the benchmark models used in this thesis. An outlook on future perspectives and potential improvements of the search concludes the chapter.

9.1 Comparison with existing constraints

The search presented in this thesis supersedes the previous ATLAS interference search conducted on $\sqrt{s} = 8$ TeV data from LHC Run-1 [17]. Numerous improvements were made with respect to this first LHC interference search.
The first interference search was based only on a single decay channel, the one-lepton channel. The search presented in this thesis relied on an additional two-lepton channel. The results from the two channels are statistically combined for optimal sensitivity to the signal process under consideration. The two-lepton channel features a lower branching ratio compared to the one-lepton channel and does not allow for the complete reconstruction of the final-state particles, which reduces the resolution of the interference pattern. However, the introduction of additional SRs in this channel increases the expected number of signal events and allows for better control over systematic uncertainties that can be constrained across different signal regions. This results in a notable improvement in sensitivity with respect to a search relying only on the one-lepton channel. The statistical combination with the two-lepton channel yields the largest improvement in sensitivity at low $\tan\beta$ values. In the Type-II 2HDM interpretation, for $m_{A/H} = 400$ GeV, the observed (expected) exclusion range in $\tan\beta$ is 11% (5%) larger with the one- and two-lepton channel combination than with the one-lepton channel alone. In the one-lepton channel, a dedicated signal region was introduced for the reconstruction of merged hadronic top-quark decays, in order to increase the sensitivity to the signal process at high values of $m_{t\bar{t}}$. The signal selection efficiency is dominated by the resolved SR for $m_{t\bar{t}} > 600$ GeV, as indicated by Figure 6.2 and discussed in Chapter 6.
Figure 9.1 shows a comparison of the excluded regions obtained in the ATLAS Run-1 interference search and in the search presented in this thesis, in the $m_{A/H} - \tan\beta$ plane for a type-II 2HDM in the alignment limit with $\cos(\beta - \alpha) = 0$.

Another improvement of the ATLAS Run-2 result presented in this thesis with respect to the Run-1

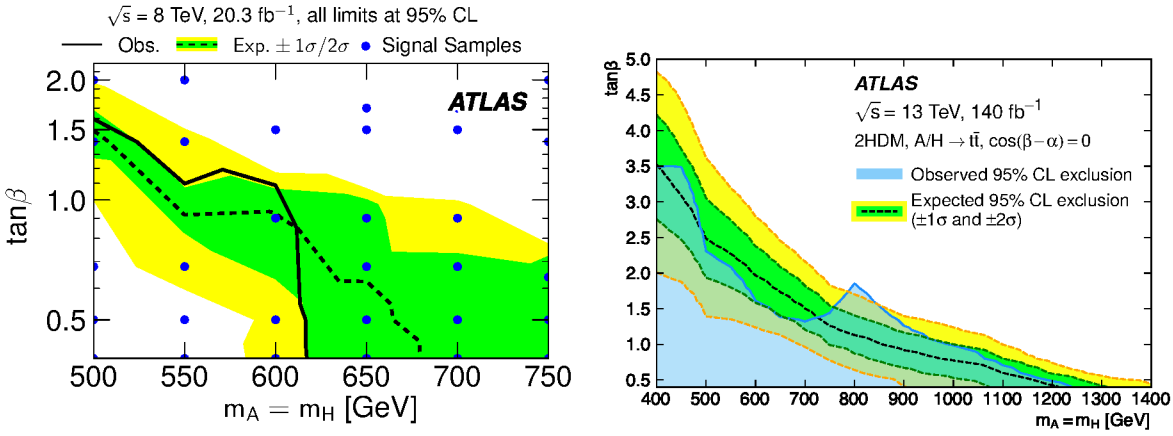

(a) (b)

Figure 9.1: Observed and expected exclusion regions in the $m_{A/H} - \tan\beta$ plane of a type-II 2HDM in the alignment limit ($\cos(\beta - \alpha) = 0$) with mass-degenerate pseudoscalar and scalar states, from (a) the previous search on 8 TeV data [17], and (b) the search presented in this thesis [17].

result, is the interpretation of the results in terms of a wider range of BSM benchmark models. In addition to the Type-II 2HDM, the results are interpreted in terms of two models predicting a second Higgs doublet (hMSSM, 2HDM+a), and one model predicting a single additional (pseudo)scalar. Broadening the range of benchmark models is important in order to enhance the sensitivity of the search to a wide variety of interference patterns. In fact the interference pattern depends strongly on the BSM benchmark under consideration, which makes it difficult to re-interpret the search in the context of other benchmark models without repeating the full profile likelihood fit. The introduction of the generic (pseudo)scalar interpretation is particularly useful in this regard, as few assumptions are made on the underlying BSM theory.

The hMSSM is used as a common benchmark to compare ATLAS searches targeting extra neutral (A/H) and charged ($H^{\pm}$) Higgs bosons. A summary of ATLAS results providing the excluded regions in the $m_A - \tan\beta$ hMSSM plane is shown in Figure 9.2. The search presented in this thesis provides the strongest constraints up to date in the high-mass, low-tan β region of the parameter space, with an observed (expected) exclusion of m_A = 950 GeV (850 GeV) at $\tan\beta = 1$. Constraints on the hMSSM parameter space are also available from the CMS collaboration, based on an interference search on 35.9 fb^{-1} of data collected by the CMS experiment during the first part of Run-2 (2015-2016) [18][1]. They are shown in Figure 9.3. The CMS partial-Run-2 search reported a deviation from the SM expectation with a global (local) significance of 1.9 (3.5)σ, compatible with a pseudoscalar particle with a mass of 400 GeV and a relative width of 4%. This and similar signal hypotheses are now strongly excluded based on the results presented in this thesis.

[1]This thesis was written before the publication of a search for scalar and pseudoscalar particles from the CMS collaboration using the whole Run-2 dataset [167].

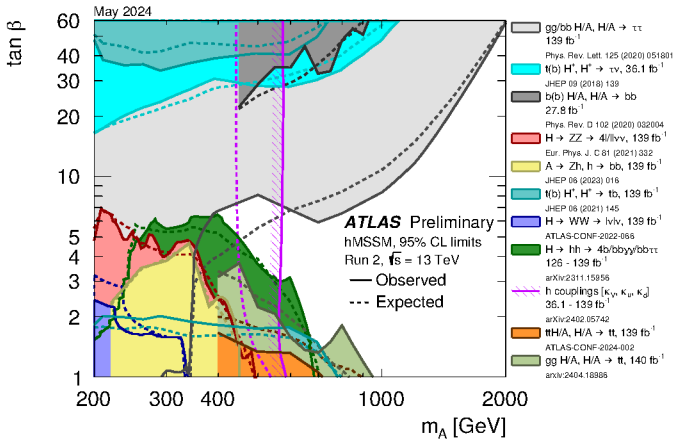

Figure 9.2: Observed and expected constraints on the hMSSM benchmark in the $m_A - \tan\beta$ plane derived from a variety of different ATLAS searches using Run-2 data, from Ref. [166].

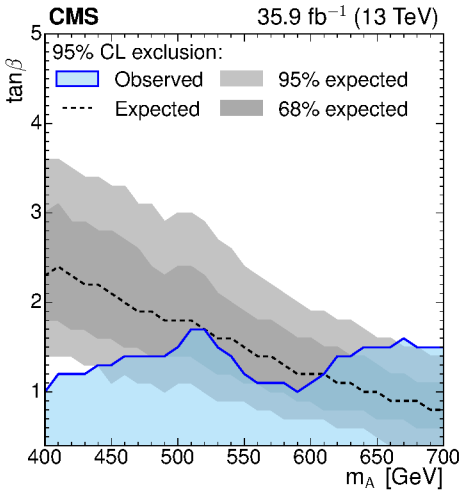

Figure 9.3: Observed and expected exclusion regions in the $m_A - \tan\beta$ hMSSM plane from the CMS search in Ref. [18]

.

Constraints on the parameter space of the Type-II 2HDM benchmark in the alignment limit and with $m_A = m_H$, have also been published in the context of an ATLAS search for heavy (pseudo)scalar particles decaying to $t\bar{t}$, in association with a $t\bar{t}$ pair [168]. The Feynman diagram for the signal process on which this search is focused is shown in Figure 9.4. This process does not interfere strongly with the main background from SM $t\bar{t}t\bar{t}$ production. Hence, the search for heavy (pseudo)scalar particles in the $t\bar{t}t\bar{t}$ final state targets resonant enhancements compared to the SM expectation. The region observed to be excluded in the $m_{A/H} - \tan\beta$ plane for a type-II 2HDM in the alignment limit with $\cos(\beta - \alpha) = 0$ is shown in Figure 9.5. The search presented in this thesis offers stronger constraints at low $m_{A/H}$ than the resonant search. At $m_A = m_H = 1$ TeV, both searches yield the same expected constraint $\tan\beta > 0.8$, with the interference search reporting the strongest observed constraint $\tan\beta > 1.0$.

ATLAS results constraining the parameter space of 2HDMs with an additional dark matter pseudoscalar mediator (2HDM+a) have also been published in Ref. [169]. Figure 9.6 combines all the constraints from the most recent ATLAS analyses on the 2HDM+a parameter space, showing the excluded regions at 95% CL in the $m_a - \tan\beta$ plane, with $m_A = m_H = 600$ GeV and with two possible values of $\sin\theta$. The ATLAS search presented here has the best *expected* sensitivity to 2HDM+a signatures for 400 GeV $\lesssim m_a \lesssim$ 500 GeV. However, due to a downward fluctuation of the observed

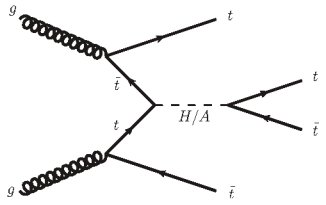

Figure 9.4: Feynman diagram for the production of a heavy (pseudo)scalar particle, H/A, produced in association with a pair of top quarks, with the (pseudo)scalar decaying into $t\bar{t}$, from Ref. [168].

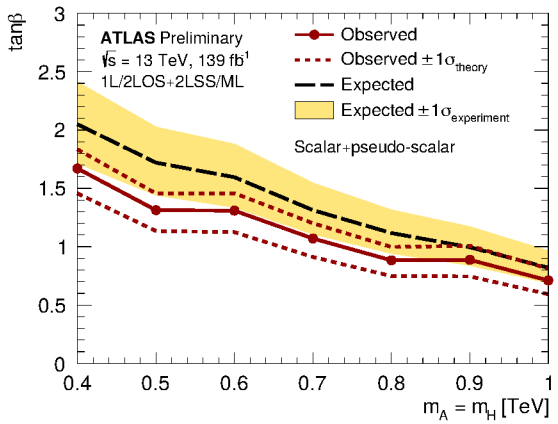

Figure 9.5: Observed (red solid line) and expected (black dashed line) 95% CL lower limits on $\tan\beta$ as a function of the $m_A = m_H$, assuming type-II 2HDM in the alignment limit [168]. The yellow bands illustrate the $\pm 1\sigma$ bands of the expected limits. The two red dashed lines correspond to the observed limits obtained with a variation of the theory cross sections by $\pm 1\sigma$.

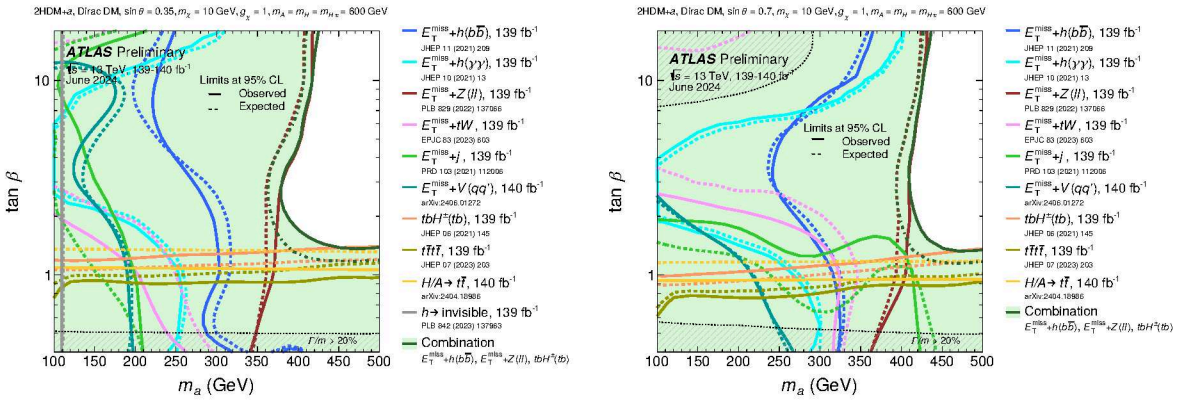

(a) (b)

Figure 9.6: Observed and expected exclusion regions in the $m_a - \tan\beta$ plane for the 2HDM+a with $m_A = m_H = m_{H^\pm} = 600$ GeV and (a) $\sin\theta = 0.35$, and (b) $\sin\theta = 0.70$, combining multiple results from searches on the full Run-2 ATLAS dataset, from Ref. [170] .

exclusion contour, it does not provide the strongest *observed* constraint for this BSM benchmark. It is also worth noting that in this mass region, the only search which is competitive in sensitivity with the search presented in this thesis, namely the search for charged Higgs bosons decaying to a top and a bottom quark [171], relies on a calculation of the signal cross section at NLO precision. The search presented in this thesis relies on a calculation of the signal cross-section at LO precision, which underestimates the amount of signal and the importance of the signal-background interference, resulting in a more conservative excluded region. NLO calculations do not exist for the process $gg \to a/A \to t\bar{t}$ targeted in this thesis. Future iterations of this analysis are very promising for further constraining the parameter space of the 2HDM+a benchmark.

9.2 Outlook

The Run-3 data-taking period of the ATLAS experiment is currently ongoing, at the end of which more data than ever before will be available. An integrated luminosity of about 200 fb^{-1} is targeted by the end or Run-3. A new search for the same signal process as the one presented in this thesis will be performed on the Run-3 dataset. The statistical tools developed in the context of this thesis will form a basis onto which the new search will be built, and the lessons learned will be used to improve the sensitivity to the signal process.

The current MC simulations of the benchmark BSM processes are generated at LO in QCD. Additional correction factors are applied to correct the pure-signal and interference terms to the signal cross-section calculated at NLO for the pure-signal component. The correction factors can reach values up to about four in the low-mass, low-tan β region. Since different correction factors are applied to the pure-signal and interference terms, they affect the shape of the interference pattern on the $m_{t\bar{t}}$ spectrum. Simulations at NLO [172] would allow for a more precise calculation of the expected interference pattern as a function of $m_{t\bar{t}}$, and significantly reduce modelling uncertainties on the signal process.

The current MC prediction of the SM $t\bar{t}$ background is generated at NLO in QCD, with a full PS

simulation, and reweighted so that the mass of the $t\bar{t}$ system and the transverse momenta of the two top-quarks match the theoretical prediction at NNLO precision in QCD and NLO in electroweak (NNLO-QCD+NLO-EW). A full NNLO-QCD+NLO-EW simulation is under consideration for future iterations of the search, which would give a more reliable estimation of the full kinematics of the main and irreducible background for this search.

The reconstruction of the $t\bar{t}$ system in the one-lepton channel can be improved for both the resolved and merged topologies. In the resolved topology, machine learning algorithms such as SPANet [173] are available to improve the assignment of jets to partons in final states with two or more top quarks and/or additional heavy particles. More modern ML tools, such as GNNs [174], can also be used for this purpose. Similar tools can be used to improve signal-background discrimination, too.
In the merged topology, a simple set of requirements based on mass and p_T thresholds is used for the identification of large-R jets produced in the hadronic decay of top-quarks (top-tagging). Improvements in top-tagging would certainly increase the mass reach of the search, by allowing for better rejection of background events without a merged hadronic top-quark decay. Currently, centrally-calibrated ATLAS top-tagging algorithms [143] are only available for large-R jets with $R = 1$ (see Section 5.4.1 for the definition of the R parameter in the anti-k_T jet algorithm), and calibrated for $p_T > 350$ GeV. This transverse momentum threshold does not guarantee a seamless transition from the resolved to the merged regime in the region of phase space where top quarks have an intermediate boost (700 GeV $\lesssim m_{t\bar{t}} \lesssim$ 1 TeV). This intermediate boost region is relevant for the interference search presented in this thesis because type-II 2HDM and similar BSM signatures predict an off-shell peak in the $m_{t\bar{t}}$ distribution at low values of $m_{t\bar{t}}$, for low values of $\tan\beta$. An extension of the ATLAS top-tagger calibration to lower transverse momentum, in addition to the definition of a semi-merged topology similar to the one of Section 6.6.1 would be a way to improve the reconstruction and identification of hadronic top-quark decays for $m_{t\bar{t}}$ values close to 1 TeV. An alternative route consists in developing a top-tagger for VR reclustered jets, while keeping the current categorisation based on the resolved and merged topologies only. In order to achieve the best top-tagging performance, it would be beneficial to use $R = 0.2$ anti-k_T jets as input to the reclustering algorithm, so that the sub-structure of the reclustered jet is better described by its constituents. Sub-structure variables could be used directly or as inputs to a multivariate algorithm to identify jets originating from top quarks. The energy calibration of these smaller constituent jets and the substructure variables calculated from them would, however, necessitate significant effort at the collaboration level, given the complexity of the jet calibration procedure (Section 5.4.3).

The analysis presented in this thesis constrains the parameter space of a wide variety of benchmark models predicting interference effects between the SM $t\bar{t}$ production and the gg-initiated production of heavy BSM (pseudo)scalars. This is the most sensitive direct search to date for neutral (pseudo)scalar particles decaying to $t\bar{t}$ in an LHC experiment. Investing in the new iteration of the search based on the data collected in Run-3 would be highly beneficial to the ATLAS physics programme.

CHAPTER 10

The future of charged particle reconstruction in ATLAS

Highly efficient and accurate reconstruction of charged-particle trajectories (*tracks*) from the energy deposits (*clusters*) of charged particles within the different layers of the ITk (Section 3.4) is of the utmost importance for the reconstruction of all other physics objects and hence all physics analyses at the HL-LHC. This is particularly true for analyses relying on the identification of heavy-flavour jets, such as di-Higgs measurements and searches with top quarks in the final state.

Reconstructing tracks becomes particularly challenging in environments characterised by a high density of ionising particles. Within these *dense environments*, the energy deposits left by different nearby particles in the same detector layer have a considerable likelihood of overlapping, thereby forming a single *merged* cluster, with energy contributions from multiple particles. This effect is particularly pronounced in the innermost layers of the Pixel Detector. Cluster merging impacts both the efficiency of track reconstruction and the precision with which track parameters can be estimated. The decrease in track reconstruction efficiency largely arises from the penalisation of track candidates in the reconstruction process for sharing clusters with other tracks, which aims at reducing the occurrence of tracks resulting from incorrect combinations of clusters (*fake tracks*). Similarly, the degradation of track parameter resolution is primarily due to the fact that the position of the merged cluster typically does not align with the position of any of the individual charged particles which contributed to it. Accurately estimating track parameters is crucial for many applications, especially in unambiguously associating tracks with vertices. This necessity is particularly relevant for identifying tracks from concurrent proton-proton collisions (*pile-up tracks*) and discerning the displaced decay vertices of heavy-flavour hadrons (b- and c-hadrons) [175, 176]. Dense environments most prominently occur in the cores of hadronic jets with high transverse momentum. The reconstruction of these jets and the identification of heavy-flavour hadron decays within these jets is of key importance for the HL-LHC physics programme.

Within the current ATLAS track reconstruction chain, machine learning algorithms are applied for the identification of merged clusters [123, 124], as well as for assessing the positions and associated uncertainties of the sub-clusters linked to individual particles contributing to a merged cluster [177]. While the enhanced spatial resolution of the ITk compared to the current Inner Detector is anticipated to reduce cluster merging rates, the importance of tracking in dense environments persists, compounded by the increased complexity due to higher levels of pile-up, resulting in additional particle tracks,

at the HL-LHC. Consequently, the algorithms used in the context of Clustering and Tracking in Dense Environments (CTIDE) need to be examined and optimised in anticipation of operations at the HL-LHC.

The performance of CTIDE with the ITk has previously been explored in the context of the ITk Pixel Technical Design Report (TDR) [68]. However, since the TDR release, significant advancements have been made in the ITk layout and corresponding reconstruction software. Notably, tracking analyses based on a recent ITk layout and software architecture have not focused on dense environments [75]. This chapter draws from an ATLAS PUBNOTE[1] [121], which builds upon and extends prior investigations, focusing specifically on the performance of CTIDE with a recent ITk layout, with particular emphasis on the Pixel Detector.

10.1 Classification of clusters and tracks

The penalisation of shared clusters during the ambiguity solving phase (Section 5.1) results in a reduction of the tracking efficiency in dense environments, unless additional algorithms are employed to identify merged clusters. Identifying merged clusters via machine learning techniques allows tracks to utilise shared clusters without penalty, while also avoiding an increase in the rate of falsely identified tracks.

In the following simulation-based studies, tracks that include at least one merged cluster, whether in the Pixel or Strip Detectors, are termed *merged* tracks. Tracks are classified further based on the presence of a merged cluster in either the Pixel or Strip sub-detector. Clusters can be categorised based not only on the number of contributing particles, but also on the number of tracks to which they belong. Clusters which are not identified as merged during event reconstruction, and are used for reconstructing multiple tracks, with penalty, are referred to as *shared* clusters.

In the current track reconstruction software for the ID, cluster classification relies on a Neural Network (NN), using inputs such as the *time-over-threshold* (ToT) of each pixel within the cluster. The NN algorithm classifies pixel clusters into three classes:

1. 1-particle cluster: only one contributing particle;
2. 2-particle cluster: two contributing particles;
3. Many-particle cluster: three or more contributing particles.

Clusters falling into classes 2 and 3 are identified as merged. In the current ID, cluster classification is solely performed in the Pixel sub-detector, where ToT data is available. No reconstruction-level classification algorithm has been devised for the ITk yet. Instead, a truth-based NN emulation, based on Run 2 performance, is employed. This emulation identifies 1-particle clusters with perfect efficiency and 2/many-particle clusters with a custom efficiency denoted as ε. Throughout this chapter, $\varepsilon = 0$ is assumed to evaluate the baseline CTIDE performance with the ITk without any cluster classification. In Section 10.5, $\varepsilon = 1$ is employed for comparison, illustrating the potential benefit of implementing a perfect cluster classification algorithm for the ITk. No classification is employed for strip clusters, following the track reconstruction methodology of the current ID.

[1] This chapter is largely based on the ATLAS PUB NOTE ATL-PHYS-PUB-2023-022 [121], and some parts are taken verbatim from it. I conducted all studies summarised in the note and acted as note editor.

10.2 Track selection and matching to jets

The primary set of tracks analysed in this chapter consists of tracks with $p_T > 1$ GeV and $|\eta| < 4.0$. Additionally, tracks must satisfy the following set of *loose* selection criteria regarding the number of pixel and strip hits, holes, dead sensors, and shared hits:

- $N_{\text{pixHits}} + N_{\text{stripHits}} + N_{\text{pixDead}} + N_{\text{stripDead}} \geq 7$
- $N_{\text{pixShared}} + 0.5 \cdot N_{\text{stripShared}} \leq 1$
- $N_{\text{pixHoles}} + N_{\text{stripHoles}} \leq 2$
- $N_{\text{pixHoles}} \leq 1$.

For the studies in Sections 10.4 and 10.5, a stricter requirement of track $p_T > 10$ GeV is adopted. This choice aligns with earlier studies of the CTIDE performance in the ID in Ref. [178], allowing for a direct comparison of the results in Section 10.5 with those in Ref. [178]. This higher p_T threshold also serves the purpose of mitigating biases due to differences in the track p_T distributions, when comparing the properties of tracks with and without merged clusters. In fact, cluster merging occurs predominantly in high-p_T tracks. Any residual biases due to remaining differences in the track p_T distributions can be corrected through a track-p_T reweighting, as described in Section 10.4. It is worth noting that, qualitatively, the conclusions drawn in Section 10.4 are also applicable to tracks with $p_T > 1$ GeV.

At the simulation level, hadronic jets are reconstructed from truth particles, excluding muons and neutrinos. The term truth particles refers to MC simulated particles produced as a result of the PS process (Chapter 4). The anti-k_t algorithm with a radius parameter $R = 0.4$ is used. These jets must have $p_T > 25$ GeV and $|\eta| < 4.0$. Tracks are matched to jets based on their angular separation $\Delta R(\text{track}, \text{jet})$ from the jet axis. For a track to be associated with a jet, $\Delta R(\text{track}, \text{jet}) < 0.4$ is required.

10.3 Simulation

The ITk layout version 23-00-03, described in Section 3.4, has been simulated using GEANT4 [78]. Details of the simulation are documented in Ref. [75]. The following MC samples are considered in the CTIDE performance studies presented in this chapter:

- $t\bar{t}$ PU0: SM production of $t\bar{t}$ pairs. No pile-up is simulated in this sample ($\langle\mu\rangle = 0$).
- $t\bar{t}$ PU200: SM production of $t\bar{t}$ pairs. An average of 200 pile-up collisions per bunch crossing ($\langle\mu\rangle = 200$) are simulated in this sample. The comparison between the two $t\bar{t}$ samples allows for a study of the effects of pile-up on cluster and track merging.
- $Z' \rightarrow$ had: Production of a heavy vector boson Z' with mass $m_{Z'} = 4$ TeV decaying with roughly equal probabilities into b-, c-, and light-quark jets. The sample is constructed in a way that the resulting jet p_T spectrum is roughly flat up to 5 TeV. This sample is especially suited for studying dense hadronic environments, as it is enriched in high-p_T jets. Its average jet p_T is 640 GeV, compared to 31 GeV (32 GeV) for the $t\bar{t}$ PU0 (PU200) samples. No pile-up is simulated in this sample.

All processes were simulated assuming pp collision events at a centre-of-mass energy $\sqrt{s}$ = 14 TeV. The $t\bar{t}$ events were generated using the PowhegBoxv2 generator at NLO in QCD, with the NNPDF3.0nlo set of PDFs and the h_{damp} parameter set to 1.5 times the mass of the top quark, with m_{top} = 172.5 GeV. The parton shower, hadronisation, and the UE were simulated using Pythia v8.2.40.4 [179] with the A14 set of tuned parameters. The Z' sample was generated using Pythia 8.2.40.4 with the same tune and PDF set. EvtGen1.7.0 [87] was used to model the decays of b- and c-hadrons. Minimum-bias interactions were generated using Pythia v8.244 with the A3 set of tuned parameters [180] and overlaid on the $t\bar{t}$ events to model the effect of pileup. Particles are passed through the ATLAS detector simulation based on GEANT4.

In Figure 10.1, the distributions of the jet transverse momentum p_T and absolute pseudorapidity $|\eta|$, all normalised to unity, are shown. The jet p_T spectrum for the $Z' \rightarrow$ had sample is flat by construction, as described above, while the corresponding distributions for the $t\bar{t}$ samples decrease with increasing jet p_T. Differences are also visible in spectra of the jet absolute pseudorapity η^{jet}, with the $Z' \rightarrow$ had process, being an s-channel process, producing more central jets compared to $t\bar{t}$ production, which is t- and u-channel dominated.

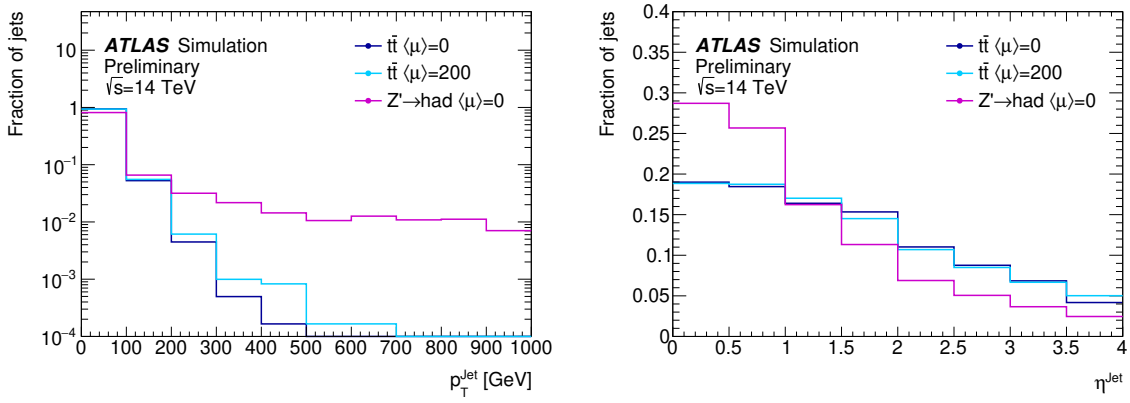

(a) (b)

Figure 10.1: Comparison of (a) the jet p_T and (b) the jet absolute pseudorapidity η^{jet} distributions for the $t\bar{t}$ PU0, $t\bar{t}$ PU200, and $Z' \rightarrow$ had samples. All distributions are normalised to unity.

10.4 Effect of cluster merging on track parameters

Track parameters represent the global properties of tracks and are derived from the final track fit. Typically, these parameters are determined at the *perigee* of the track, which is the point on the track where its projection onto the x-y plane is closest to the origin. In this analysis, the origin is defined as the beamspot. The key parameters used to describe a track are:

- ϕ and θ: the angular coordinates of the track at the perigee.
- q/p_T: the ratio of the charge associated with the track to its transverse momentum.
- d_0 and z_0: Coordinates of the IP (Section 5.1.1). The *transverse IP* (d_0) refers to the component perpendicular to the beamline, while the *longitudinal IP* (z_0) is parallel to the beam line. The

transverse IP is particularly important for identifying heavy-flavour jets, while the longitudinal IP helps differentiate between tracks originating from the hard-scatter vertex and those from the pile-up.

The quality of a track parameter P can be assessed through its residuals and pulls, defined as:

$$\text{Residual} = P - P^{\text{truth}}, \tag{10.1}$$

$$\text{Pull} = \frac{P - P^{\text{truth}}}{\sigma(P)}, \tag{10.2}$$

where P^{truth} represents the parameter value for the truth particle associated with the track, and $\sigma(P)$ is the uncertainty in the parameter estimation. A Gaussian-shaped pull distribution with a mean of zero and a width of one indicates good parameter estimation quality. A width less than one suggests potential overestimation of the track parameter error, while a non-zero mean indicates a bias in the estimation.

The influence of merged clusters on the θ, ϕ, and q/p_T tracking parameters is initially examined in the Z' sample. Given the importance of the d_0 and z_0 parameters for flavour tagging and their susceptibility to pile-up effects, this is followed by more detailed investigations on the impact of merged clusters upon them in both the Z' and $t\bar{t}$ samples with different mean pile-up ($\langle\mu\rangle = 0$ and $\langle\mu\rangle = 200$).

In Figure 10.2, the distributions of residuals and pulls for the track parameters θ, ϕ, and q/p_T are presented, distinguishing between tracks without merged clusters and tracks with at least one merged cluster in the Pixel Detector. To disentangle merging effects from track p_T effects, the distributions for tracks containing merged clusters are reweighted to match the track p_T spectrum of tracks without merged clusters. This is done for all the figures in this section.
The widths of the residual and pull distributions are summarised in Tables 10.1 and 10.2. It is determined iteratively, with the following procedure:

1. Evaluate the mean μ and the standard deviation σ of the distribution.
2. Restrict the distribution to the interval $[\mu - 3\sigma, \mu + 3\sigma]$.
3. Go to point 1 and repeat until the range remains stable, i.e. changes between two consecutive iterations are negligible.

Track merging notably worsens the quality of the track parameter estimation for the track parameters θ, ϕ, and q/p_T.

In Figures 10.3 and 10.4, the distributions of the residuals and pulls on the track impact parameters d_0 and z_0, respectively, are shown separately for tracks without any merged clusters and with at least one merged cluster in the Pixel Detector. The widths of these distributions, determined through the iterative method outlined earlier, are listed in Tables 10.3 to 10.6. The merging of tracks significantly degrades the quality of the impact parameter estimation across all analysed scenarios. Furthermore, pile-up effects broaden the residual distributions for tracks with merged clusters, probably due to additional energy deposits unrelated to tracks originating from the hard-scattering process. However, this effect is not evident in the pull distributions for d_0 and z_0, which are narrower for the $t\bar{t}$ $\langle\mu\rangle = 0$ samples compared to the $t\bar{t}$ $\langle\mu\rangle = 200$ samples. This is an indication that the uncertainties on these

track parameters also increase in the presence of pile-up, as can be reasonably expected, leading to on average smaller pulls.

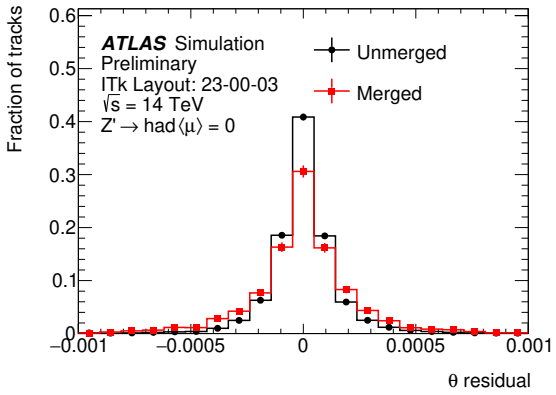

(a) θ residual

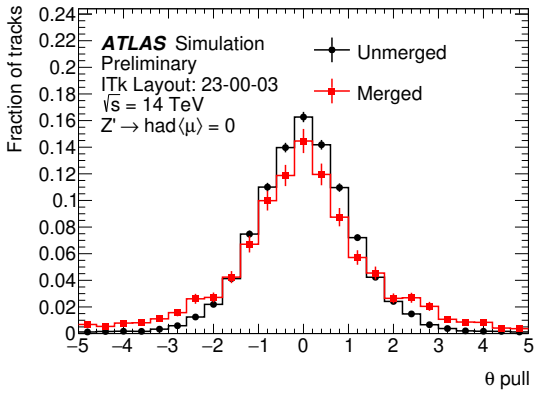

(b) θ pull

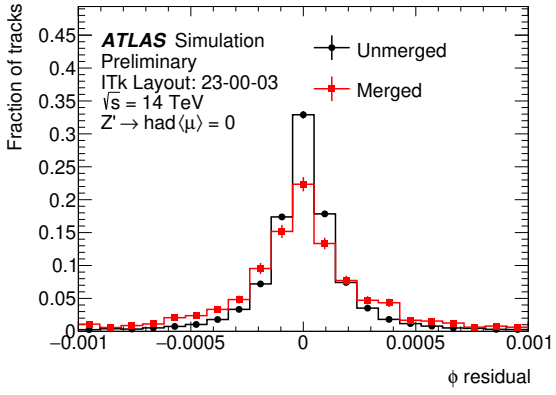

(c) ϕ residual

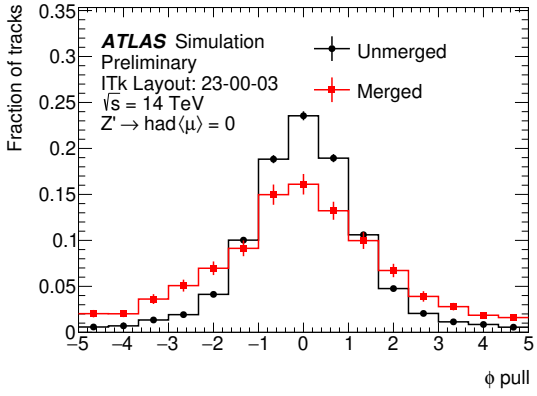

(d) ϕ pull

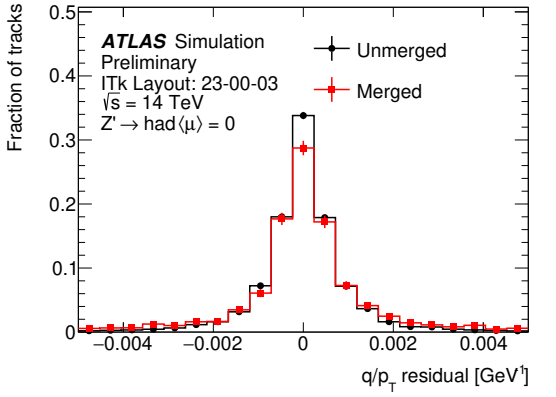

(e) q/p_T residual

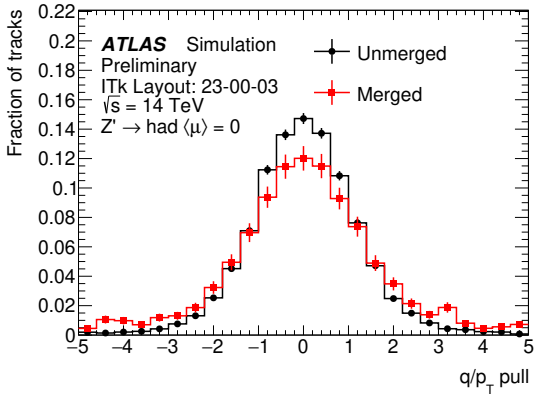

(f) q/p_T pull

Figure 10.2: Residuals (left) and pulls (right) on track θ (upper row), ϕ (middle row), q/p_T (bottom row) in $Z' \rightarrow$ had events. Two curves are shown separately for tracks containing and not containing a merged cluster.

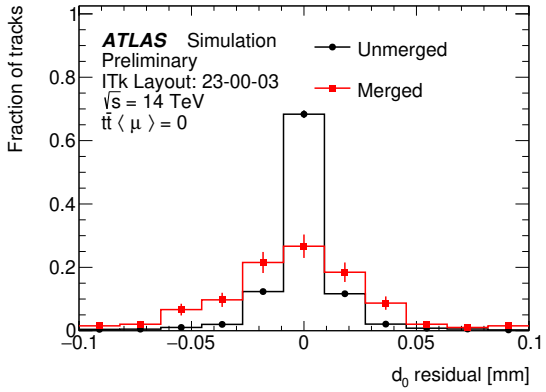

(a) d_0 residual, $t\bar{t}$ $\langle\mu\rangle = 0$

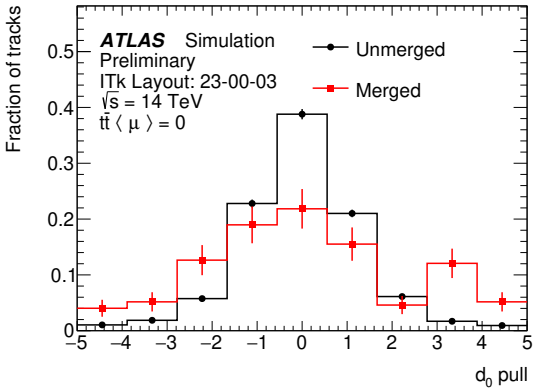

(b) d_0 pull, $t\bar{t}$ $\langle\mu\rangle = 0$

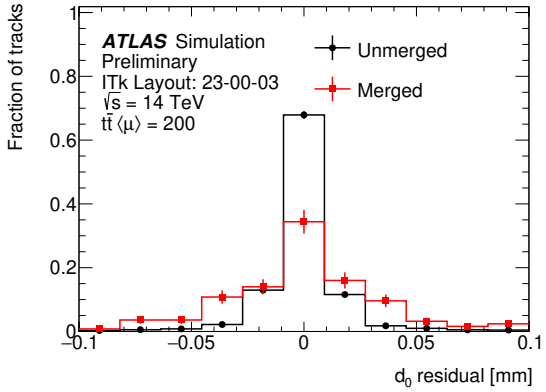

(c) d_0 residual, $t\bar{t}$ $\langle\mu\rangle = 200$

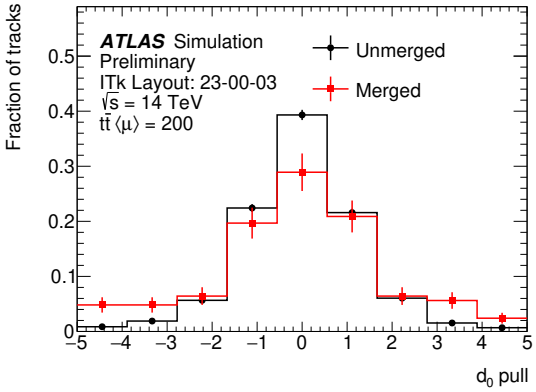

(d) d_0 pull, $t\bar{t}$ $\langle\mu\rangle = 200$

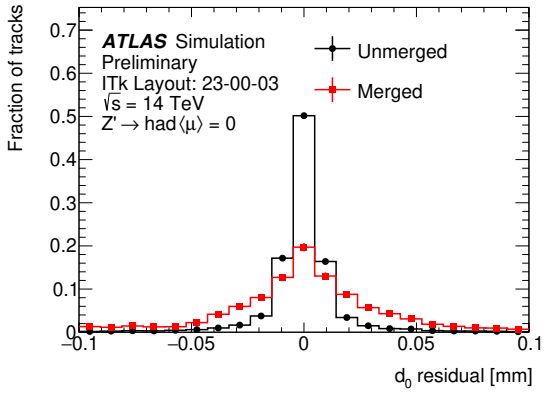

(e) d_0 residual, $Z' \rightarrow$ had

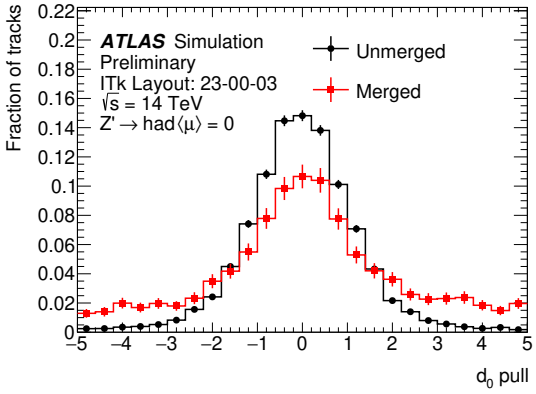

(f) d_0 pull, $Z' \rightarrow$ had

Figure 10.3: Residuals (left) and pulls (right) on track d_0 in $t\bar{t}$ $\langle\mu\rangle = 0$, $t\bar{t}$ $\langle\mu\rangle = 200$, and $Z' \rightarrow$ had events. Two curves are shown separately for tracks containing and not containing a merged cluster.

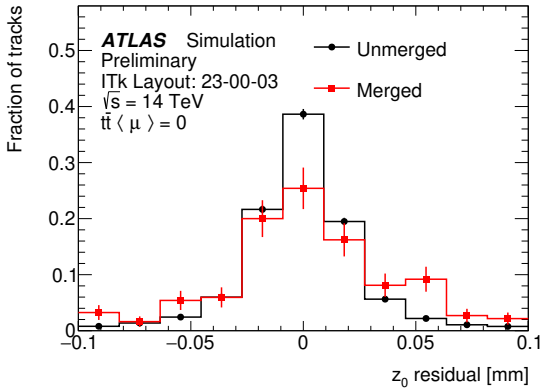

(a) z_0 residual, $t\bar{t}$ $\langle\mu\rangle = 0$

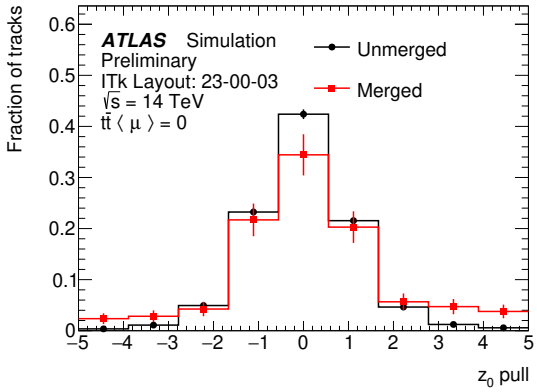

(b) z_0 pull, $t\bar{t}$ $\langle\mu\rangle = 0$

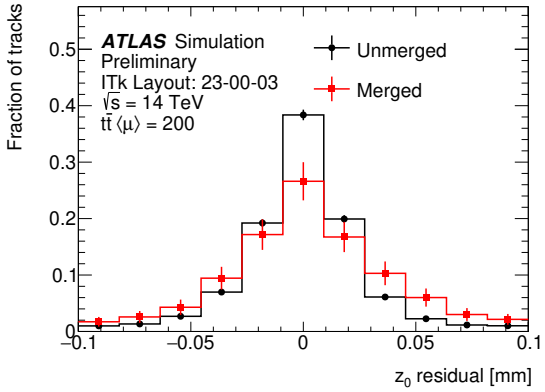

(c) z_0 residual, $t\bar{t}$ $\langle\mu\rangle = 200$

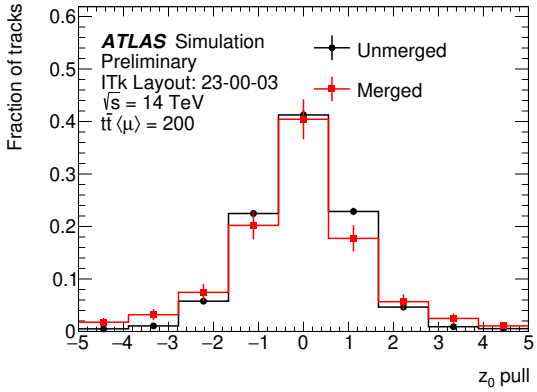

(d) z_0 pull, $t\bar{t}$ $\langle\mu\rangle = 200$

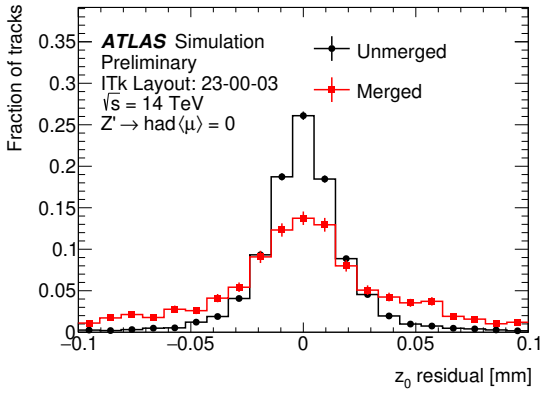

(e) z_0 residual, $Z' \rightarrow$ had

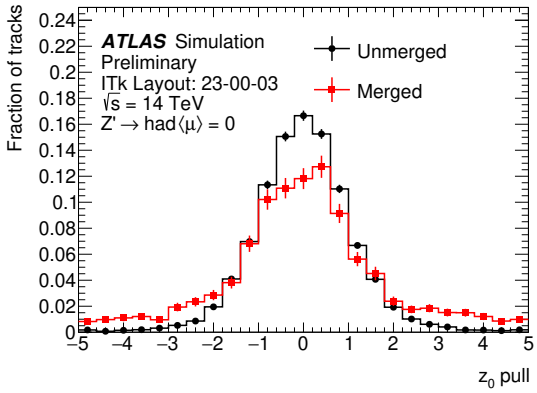

(f) z_0 pull, $Z' \rightarrow$ had

Figure 10.4: Residuals (left) and pulls (right) on track z_0 in $t\bar{t}$ $\langle\mu\rangle = 0$, $t\bar{t}$ $\langle\mu\rangle = 200$, and $Z' \rightarrow$ had events. Two curves are shown separately for tracks containing and not containing a merged cluster.

Table 10.1: Width of the residual distributions for the track parameters θ, ϕ, q/p_T in $Z' \rightarrow$ had events.

Residual on	Not merged	Merged
$\theta \left(\times 10^3\right)$	0.150 ± 0.001	0.190 ± 0.003
$\phi \left(\times 10^3\right)$	0.188 ± 0.002	0.305 ± 0.006
$q/p_T \left(\times 10^3 \text{ GeV}^{-1}\right)$	0.96 ± 0.01	1.06 ± 0.02

Table 10.2: Width of the pull distributions for the track parameters θ, ϕ, q/p_T in $Z' \rightarrow$ had events.

Pull on	Not merged	Merged
θ	1.07 ± 0.01	1.57 ± 0.03
ϕ	1.25 ± 0.01	3.46 ± 0.06
q/p_T	1.14 ± 0.01	1.69 ± 0.03

Table 10.3: Width of the residual distributions for the track parameter d_0 in $t\bar{t}$ $\langle\mu\rangle = 0$, $t\bar{t}$ $\langle\mu\rangle = 200$, and $Z' \rightarrow$ had events.

Process	Not merged	Merged
$t\bar{t}$ $\langle\mu\rangle = 0$	12.4 ± 0.1	34 ± 2
$t\bar{t}$ $\langle\mu\rangle = 200$	12.3 ± 0.1	39 ± 2
$Z' \rightarrow$ had	9.57 ± 0.08	33.4 ± 0.6

Table 10.4: Width of the pull distributions for the track parameter d_0 in $t\bar{t}$ $\langle\mu\rangle = 0$, $t\bar{t}$ $\langle\mu\rangle = 200$, and $Z' \rightarrow$ had events.

Process	Not merged	Merged
$t\bar{t}$ $\langle\mu\rangle = 0$	1.35 ± 0.01	2.2 ± 0.1
$t\bar{t}$ $\langle\mu\rangle = 200$	1.32 ± 0.01	1.92 ± 0.09
$Z' \rightarrow$ had	1.15 ± 0.01	3.43 ± 0.06

Table 10.5: Width of the residual distributions for the track parameter z_0 in $t\bar{t}$ $\langle\mu\rangle = 0$, $t\bar{t}$ $\langle\mu\rangle = 200$, and $Z' \rightarrow$ had events.

Process	Not merged	Merged
$t\bar{t}$ $\langle\mu\rangle = 0$	25.0 ± 0.3	45 ± 2
$t\bar{t}$ $\langle\mu\rangle = 200$	25.7 ± 0.3	51 ± 2
$Z' \rightarrow$ had	19.3 ± 0.2	37.8 ± 0.7

Table 10.6: Width of the pull distributions for the track parameter z_0 in $t\bar{t}$ $\langle\mu\rangle = 0$, $t\bar{t}$ $\langle\mu\rangle = 200$, and $Z' \rightarrow$ had events.

Process	Not merged	Merged
$t\bar{t}$ $\langle\mu\rangle = 0$	1.14 ± 0.01	1.72 ± 0.08
$t\bar{t}$ $\langle\mu\rangle = 200$	1.14 ± 0.01	1.47 ± 0.06
$Z' \rightarrow$ had	1.02 ± 0.01	1.93 ± 0.03

Figure 10.5 shows the width of the d_0 pull distribution as a function of the number of merged pixel clusters per track in $Z' \rightarrow$ had events. A roughly linear increase of the width of the distribution is observed as a function of the number of merged pixel clusters per track. This shows that an increase in the number of merged clusters causes greater degradation in the quality of track reconstruction. It can be noted that the width obtained for tracks with exactly one merged pixel cluster is roughly consistent with that obtained for the inclusive distribution of tracks with at least one merged cluster in Figure 10.3(f), which is naturally dominated by tracks with exactly one merged cluster.

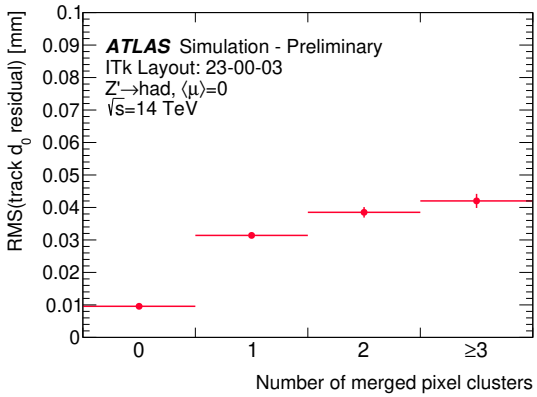

Figure 10.5: Width of the d_0 residual distribution as a function of the number of merged pixel clusters per track in $Z' \rightarrow$ had events.

10.5 Tracks inside of jets

The cores of high-p_T jets are characterised by a high local density of charged particles due to the small angular distance of highly Lorentz-boosted particles in the laboratory frame. This makes them the ideal environment to study cluster merging and its effect on tracking performance. Additionally, efficient tracking in jets is crucial for the performance of jet flavour-tagging algorithms.

10.5.1 Cluster merging

The impact of cluster merging within jet cores can be studied by evaluating the average number of hits per track, either inclusively or across individual layers of the detector. Tracks are required to be associated with a truth particle originating from a vertex less than 34 mm from the beamline, to

exclude tracks originating beyond the innermost layer, such as those produced from decays of high-p_T B-hadrons.

In Figure 10.6, the number of pixel clusters per track is shown as a function of (a) the angular separation ΔR between the track and the jet axis and (b) the jet p_T. Only tracks within the jet core ($\Delta R < 0.02$) are considered in the latter case, to examine a dense environment rich in close-by tracks. The number of pixel hits per track decreases for small ΔR values with increasing jet p_T. This decrease is attributed to the high track density and consequently increased rate of shared clusters, in combination with the ambiguity-solver condition requiring that tracks can share only a limited number of clusters; these shared clusters are eliminated from tracks with lower track scores. The same quantities are shown in Figures 10.7 and 10.8 for the innermost and next-to-innermost pixel layers, respectively. In the innermost layer, the decrease in pixel hits with increasing jet p_T is more pronounced than across the entire Pixel Detector, with a loss of hits also observed outside the jet core at low ΔR values. This is due to higher track density in detector regions closer to the interaction point. The drop in pixel hits at high jet p_T within the next-to-innermost pixel layer is not as significant as in the innermost layer, indicating that the overall reduction observed in Figure 10.6 is mostly due to the innermost layer. No comparable reduction in hits is observed for the Strip Detector (Figure 10.9), which is at a considerably larger distance from the interaction point, where particle densities are lower due to geometric factors.

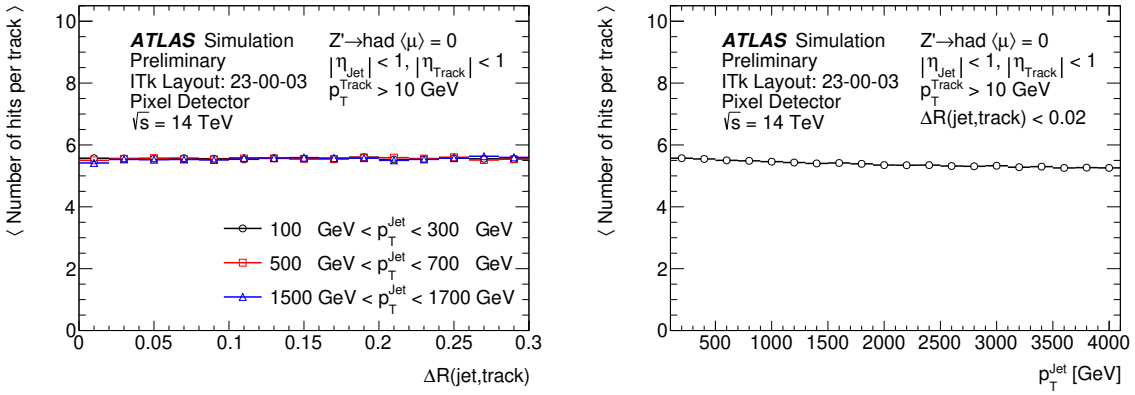

(a) (b)

Figure 10.6: Average number of pixel hits per track as a function of (a) the ΔR between the track and the center of the jet and (b) the p_T of the jet, obtained in $Z' \rightarrow$ had events.

In Figures 10.10 and 10.11, the fraction of shared pixel clusters per track is shown as a function of ΔR(jet, track) and jet p_T, across all pixel layers and in the Pixel innermost layer, respectively. In Figure 10.12, the number of shared strip clusters per track is shown, again as a function of ΔR(jet, track) and jet p_T. The observations in this Section are consistent with the reasonable assumption that the cluster merging rate is highest in the jet core, increases with jet p_T , and is largest in the innermost layers of the detector due to the higher particle densities closer to the interaction point.

10.5.2 Tracking efficiency

An important measure of the track reconstruction performance is the track reconstruction efficiency, i.e. the fraction of all charged particles successfully reconstructed as tracks. Track reconstruction

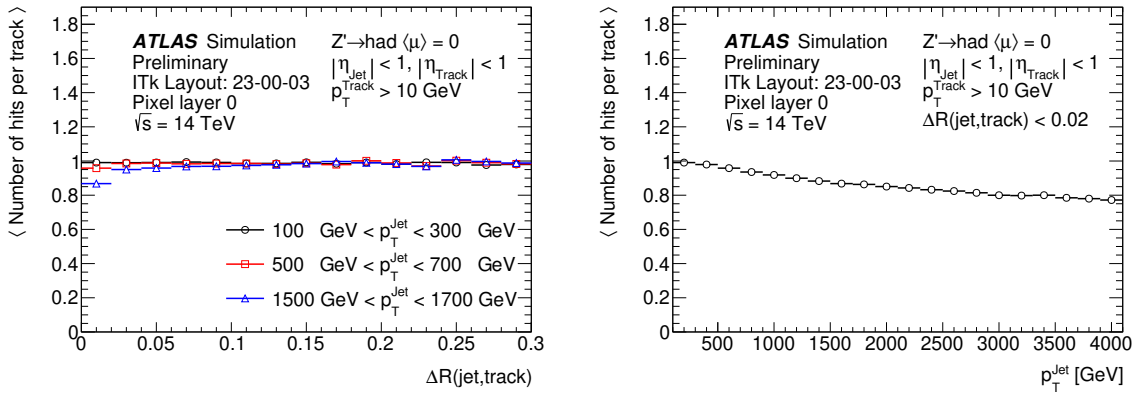

(a) (b)

Figure 10.7: Average number of pixel hits per track in the innermost layer of the Pixel Detectoras a function of (a) the ΔR between the track and the center of the jet and (b) the p_T of the jet, obtained in $Z' \rightarrow$ had events.

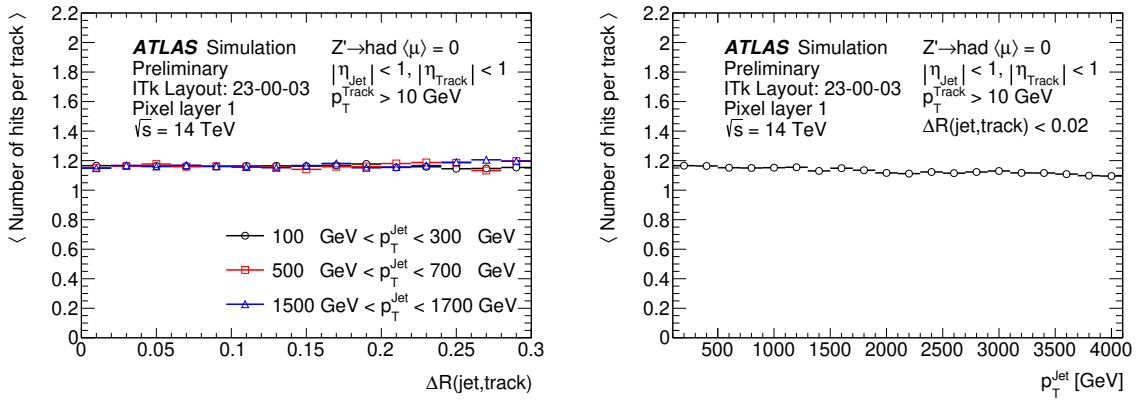

(a) (b)

Figure 10.8: Average number of all pixel hits per track in the next-to-innermost layer of the Pixel Detectoras a function of (a) the distance ΔR between the track and the center of the jet and (b) the p_T of the jet, obtained in $Z' \rightarrow$ had events.

inefficiencies may stem from various factors. First, interactions with detector material, like multiple scatterings, can induce energy losses or alter the trajectory of a particle track. This may result in track candidates failing to meet the quality standards required at the selection stage of the ambiguity solver. This effect is independent of the local charged-particle density, and more prominent at low p_T due to the higher probability of multiple scattering, and at larger $|\eta|$ due to the increased material density. Secondly, in dense environments, track candidates may incur penalties at the ambiguity solver stage for sharing a large number of hits with nearby track candidates (Section 5.1). To mitigate the first set of contributions to the track reconstruction inefficiency outlined above, which are unrelated to local particle density, only truth particles with $p_T > 10$ GeV and central jets ($|\eta| < 1.2$) are considered. Figure 10.13 shows the efficiency of charged particles being reconstructed within a jet, as a function of the jet p_T, for all tracks within the jet, and those in the jet core, separately. A decrease in the tracking

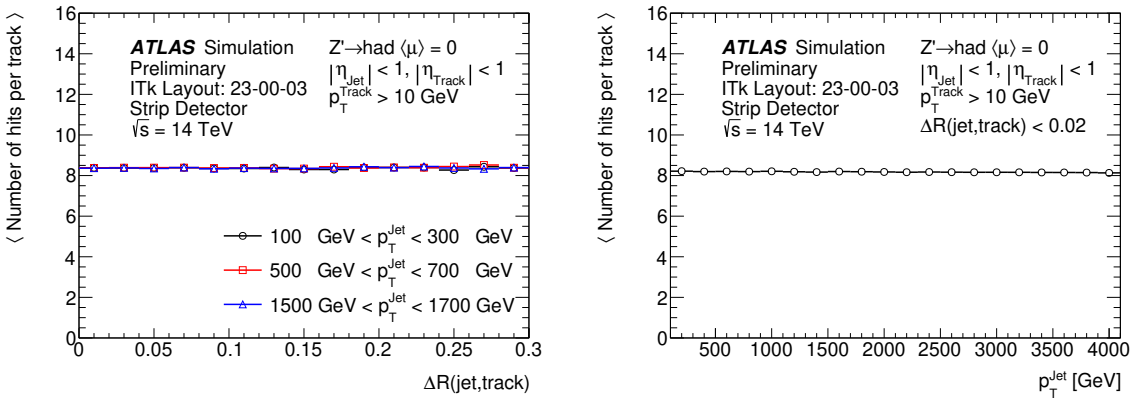

(a) (b)

Figure 10.9: Average number of strip hits per trackas a function of (a) the ΔR between the track and the center of the jet and (b) the p_T of the jet, obtained in $Z' \rightarrow$ had events.

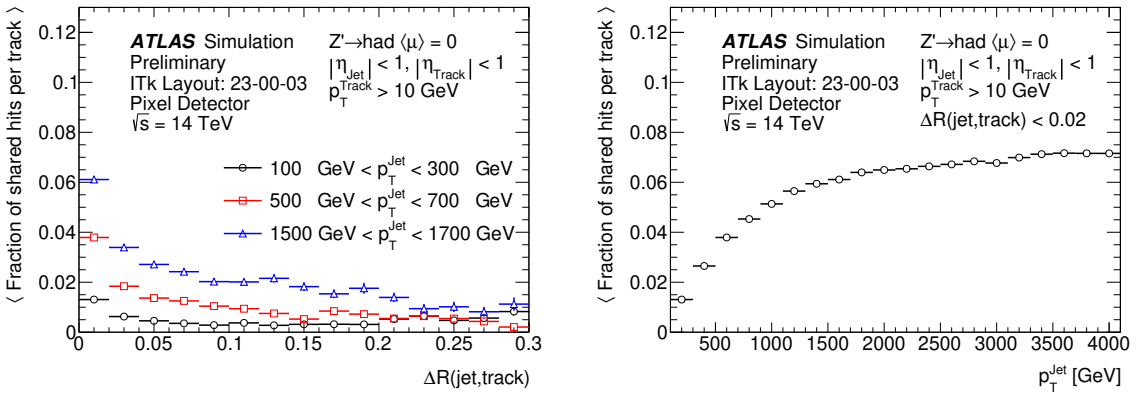

(a) (b)

Figure 10.10: Fraction of shared pixel hits per trackas a function of (a) the ΔR between the track and the center of the jet and (b) the p_T of the jet, obtained in $Z' \rightarrow$ had events.

efficiency of approximately 8% is observed as the jet p_T increases from 500 to 2500 GeV.

The impact of introducing an algorithm to identify merged clusters during the ambiguity solving phase is shown in Figure 10.14. Here, the tracking efficiency for tracks within the cores of jets is compared across different jet p_T ranges between the baseline scenario (no merged-cluster classification, $\varepsilon = 0$) and a scenario with perfect classification of merged clusters ($\varepsilon = 1$). In the scenario with perfect merged-cluster classification, a 4% reduction in tracking efficiency is observed at a jet p_T of 2500 GeV, compared to the efficiency at 500 GeV, against the 8% reduction observed in the absence of merged-cluster classification. This comparison demonstrates the advantage of using a cluster classification algorithm, such as the NN-based classifier employed in the current ID, for ITk tracking. Moreover, it highlights that, despite an optimally performing identification algorithm, a decline in tracking efficiency still occurs within the cores of high-p_T jets. This decrease is likely due to inefficiencies in the track seeding phase, which remain unaddressed by a cluster classification

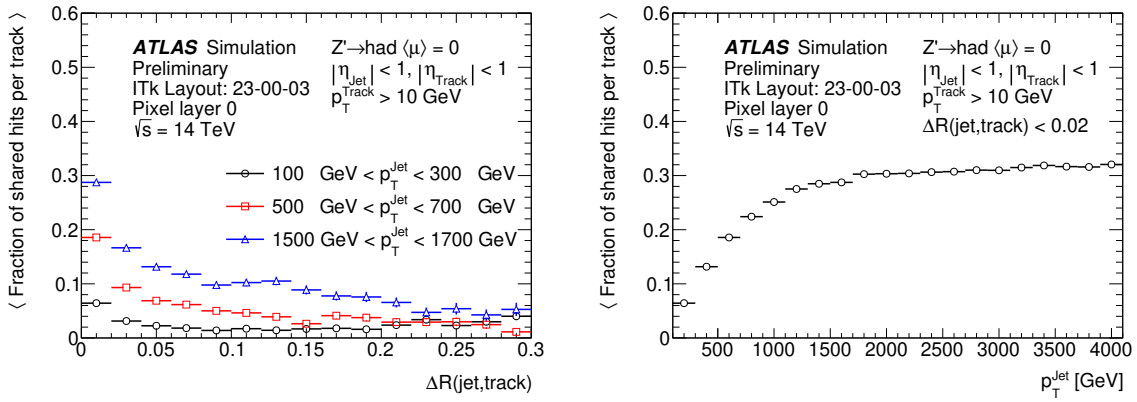

(a) (b)

Figure 10.11: Fraction of shared pixel hits per track in the innermost layer of the Pixel Detectoras a function of (a) the ΔR between the track and the center of the jet and (b) the p_T of the jet, obtained in $Z' \rightarrow$ had events.

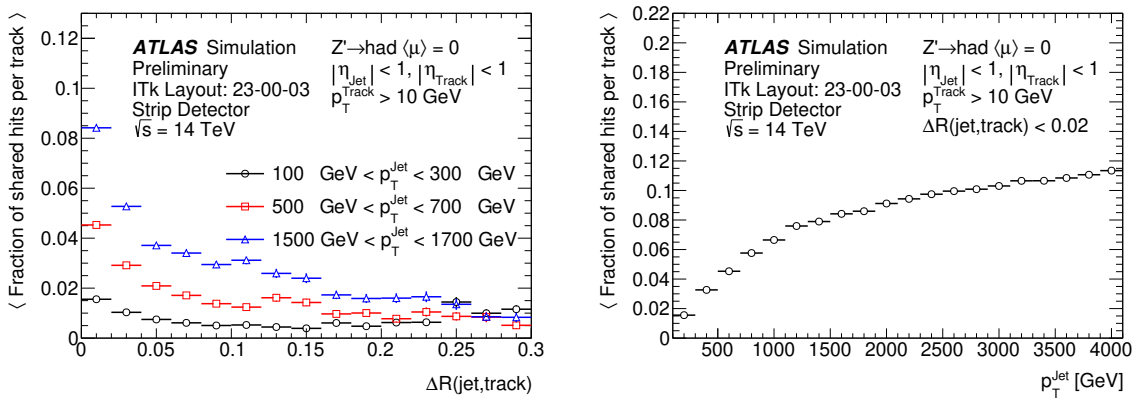

(a) (b)

Figure 10.12: Fraction of shared strip hits per trackas a function of (a) the ΔR between the track and the center of the jet and (b) the p_T of the jet, obtained in $Z' \rightarrow$ had events.

algorithm at the subsequent ambiguity solver stage.

The dependence of the track reconstruction efficiency in the jet core as a function of jet p_T has also been studied for the current ID, as documented, for example in Fig. 1 of Ref. [178]. A deterioration of approximately 20% in tracking efficiency within the jet core is observed for jet p_T between 500 GeV and 2500 GeV. It is worth highlighting that this reduction in efficiency is observed in ID track reconstruction, including the use of NNs to identify merged clusters and other dedicated algorithms to correct the cluster positions and uncertainties. The comparison with the corresponding 8% efficiency loss obtained for the ITk without merged-cluster classification illustrates the improvements in tracking efficiency in dense environments thanks to the increased granularity of the ITk Pixel detector in comparison to the current ID Pixel system.

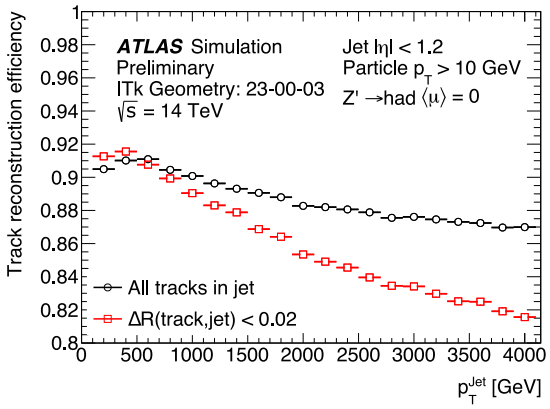

Figure 10.13: Track reconstruction efficiency for tracks inside jets as a function of jet p_T in $Z' \rightarrow$ had events.

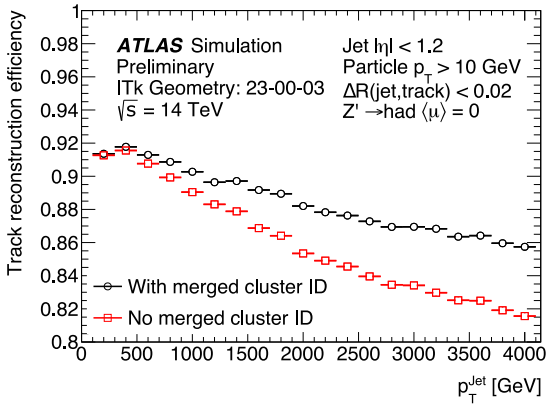

Figure 10.14: Track reconstruction efficiency for tracks in the core of jets as a function of jet p_T in $Z' \rightarrow$ had events, comparing a reconstruction scenario with no classification of merged clusters with a scenario with perfect classification of merged clusters.

10.6 Summary

In this chapter, the expected CTIDE performance using a recent ITk was studied.
Cluster merging is found to reduce the resolution of track parameters, particularly that of the transverse impact parameter d_0, crucial for flavour tagging. For instance, the d_0 pull resolution worsens by a factor of three even for tracks containing a single merged cluster compared to those containing none. In the core of jets and especially with increasing jet p_T, the rate of cluster merging increases significantly. This results in pixel hits losses for tracks within high-p_T jets and an overall decline in tracking reconstruction efficiency within the core of high-p_T jets, with observed reductions of up to 8% for jet transverse momenta of 2500 GeV compared to 500 GeV, when no merged-cluster identification algorithm is employed.

Studies utilising an ideal, truth-based cluster identification method suggest that an algorithm designed to identify merged clusters, similar to the NN-based approach employed in the current ID, can reduce track reconstruction inefficiencies at high jet p_T from 8% to 4%.

These investigations indicate that despite the enhanced spatial granularity of the ITk compared to the current ID, cluster merging in dense environments deteriorates tracking performance. Given the significance of clustering and tracking in such settings for numerous physics analyses reliant on high-p_T jet reconstruction and flavour identification, these results show that the development or improvement of algorithms designed to mitigate the negative effects of cluster merging, such as dedicated algorithms for identifying merged clusters, remains necessary for the ITk.

CHAPTER 11

Conclusions

In this thesis, a search for heavy Higgs bosons decaying to a $t\bar{t}$ pair with the ATLAS Run-2 dataset is presented. This is the first search for a (pseudo)scalar particle decaying to $t\bar{t}$, including the interference effect with the SM $t\bar{t}$ production, with a full LHC Run-2 dataset. The most stringent constraints up to date are set on the parameter space of the hMSSM and related type-II 2HDM benchmarks. Additionally, the expected performance of clustering and tracking in dense hadronic environments with the ITk is presented. The studies shown in this thesis highlight the importance of investing in the development of new track-reconstruction algorithms for the ITk or in the improvement of the existing ones.

Highly efficient and accurate reconstruction of charged-particle tracks will be extremely important for the vast majority of physics analyses at the HL-LHC. The reconstruction and measurement of charged-particle tracks is particularly challenging in dense hadronic environments, such as the cores of high-p_T hadronic jets, where a high local density of charged particles is present. In dense hadronic environments, the energy deposits left by nearby particles in the detector, have a high probability of overlapping, and merging into a single cluster. High-quality tracking in dense environments is important for the reconstruction of heavy flavour hadron decays within the jets. This is, in turn, important for the success of the HL-LHC physics programme, as the reconstruction of $H \rightarrow b\bar{b}$ and top-quark decays is crucial for the measurement of the Higgs self-coupling and for the search for new particles decaying to $t\bar{t}$, as well as precision measurements, such as tests of quantum entanglement in $t\bar{t}$ final states, respectively.
This thesis presents the baseline performance of ITk tracking in dense hadronic environments for a recent layout of the ITk, which will be installed as part of the Phase-II upgrade of the ATLAS detector. The results of these studies are published in Ref. [121].
Cluster merging is found to be relevant in the ITk, despite the increased granularity with respect to the current ID. Cluster merging affects the resolution of the track parameter estimation and reduces the tracking efficiency in the core of jets with increasing jet p_T. If no identification of merged clusters is applied, a reduction of up to 8% in tracking efficiency is observed in the core of jets with $p_T \sim 2500$ GeV, compared to 500 GeV. This is a significant improvement compared to the 20% reduction observed in ID tracking, and highlights the improvements in ITk tracking in dense environments with respect to ID tracking, thanks to the improved detector granularity. Despite the notable improvement with respect to ID tracking, it is a non-negligible loss, that should be mitigated to the greatest extent possible. Assuming that merged clusters can be identified with perfect efficiency, the reduction in

tracking efficiency at high p_T can be reduced to 4%. This highlights the potential gain from dedicated algorithms for merged-cluster classification for the mitigation of the negative effects of merging with the ITk.

The main focus of this thesis is a new search for heavy scalar H and pseudoscalar A particles decaying to a $t\bar{t}$ pair, based on the full Run-2 dataset of proton-proton collisions at the centre-of-mass energy $\sqrt{s} = 13$ TeV, collected with the ATLAS detector, and corresponding to an integrated luminosity of 140 fb^{-1}. The search targets the gg-initiated A/H production with decay to $t\bar{t}$, taking into account the non-negligible signal-background interference, which leads to non-trivial interference patterns in the $m_{t\bar{t}}$ spectrum.

The search is conducted in two orthogonal channels, targeting a one-lepton and a two-lepton final state. The results from the two channels are statistically combined. In the one-lepton channel, which is the channel driving the sensitivity of the search and the main focus of this thesis, two topologies are considered for the hadronic decay of one of the top quarks: in the Resolved topology, three small-R jets are used to reconstruct the top-quark decay, while in the Merged topology a single large-R jet is used. The introduction of the Merged topology is a new addition compared to the previous ATLAS iteration of the search [17] and to the CMS partial Run-2 result [18] targeting the same signal process. The Merged channel was introduced in the context of this thesis work, with the purpose of enhancing the sensitivity of the search to large (pseudo)scalar masses. An approach based on variable-radius reclustered jets is used in the Merged topology to define the top-candidate large-R jet, and is the result of a study to optimise the sensitivity of the search to the target process for values of the (pseudo)scalar mass up to about 1 TeV. Events are divided into signal regions based on b-tagging information and on their angular topology, to further improve the sensitivity of the search.

In the context of this thesis, dedicated statistical tools and methods were developed to correctly account for the presence of signal-background interference effects in the statistical data analysis. The method used in ATLAS for obtaining p-value variations was revised, to work with the complex likelihood parametrisations characteristic of interference problems, leading to a new standard for the majority of ATLAS searches. Great attention was placed on the choice of the test statistics for the search and exclusion stages of the analysis, in order to correctly account for the signal-background interference effects. From a technical point of view, a method for processing histograms with negative entries in common statistics tools has been introduced.

The results of the search have recently been published in Ref. [19]. Results are interpreted in terms of different benchmark models predicting the existence of an additional Higgs doublet (Type-II 2HDM, hMSSM, 2HDM+a), as well as in terms of a generic (pseudo)scalar Lagrangian term. Constraints on the parameter space of the considered benchmark models are derived. For the Type-II 2HDM and hMSSM hypotheses, 95% CL exclusion regions are derived in the $m_A - \tan\beta$ plane of the parameter space, in the alignment limit ($\cos(\beta - \alpha) = 0$) and under the mass degenerate assumption ($m_A = m_H$) for the Type-II 2HDM case. In the hMSSM scenario, pseudoscalar masses up to 950 GeV are observed to be excluded at 95% CL for $\tan\beta = 1$, offering the strongest constraints to date in the low-mass, low-$\tan\beta$ region. In the generic (pseudo)scalar hypothesis, 95% CL exclusion regions are derived in the $m_{A/H} - g_{A/Ht\bar{t}}$ plane. The results in the Type-II 2HDM, hMSSM, and generic (pseudo)scalar scenarios solidly exclude signal hypotheses with $m_A \approx 400$ GeV, for which the CMS partial Run-2 search [18] targeting the same signal process saw a moderate excess[1]. Constraints on the 2HDM+a

[1]This thesis was written before the publication of a search for scalar and pseudoscalar particles from the CMS collaboration using the whole Run-2 dataset [167].

benchmark are derived in the $m_a - \tan\beta$ plane and values of $\tan\beta$ up to almost 1.2 (1.0) are observed to be excluded for $\sin\theta = 0.35$ (0.70) and $m_A = m_H = m_{H^\pm} = 600$ GeV. While these are not the strongest observed constraints up to date, this search provides the strongest expected constraints, and the future iteration of this analysis is extremely promising for further constraining the parameter space of this benchmark model.

The search presented in this thesis offers the strongest constraints to date on the parameter space of the Type-II 2HDM, hMSSM and generic (pseudo)scalar benchmarks, in the high-mass, low-$\tan\beta$ (low-$g_{A/Ht\bar{t}}$) region. The introduction and optimisation of the Merged topology for the reconstruction of boosted and moderately boosted top-quark hadronic decays greatly improved the sensitivity of the search to signals in these benchmark models. The statistical approach developed in the context of this thesis, for hypothesis testing in the presence of signal-background interference, will form the baseline for future interference searches on the ATLAS Run-3 dataset and beyond.

Appendix

APPENDIX A

Local p-values for the search stage

In this appendix, local p-values under the background-only hypothesis as a function of the mass of the BSM (pseudo)scalar, for the search stage (Section 8.4) of the analysis presented in this thesis, are shown.

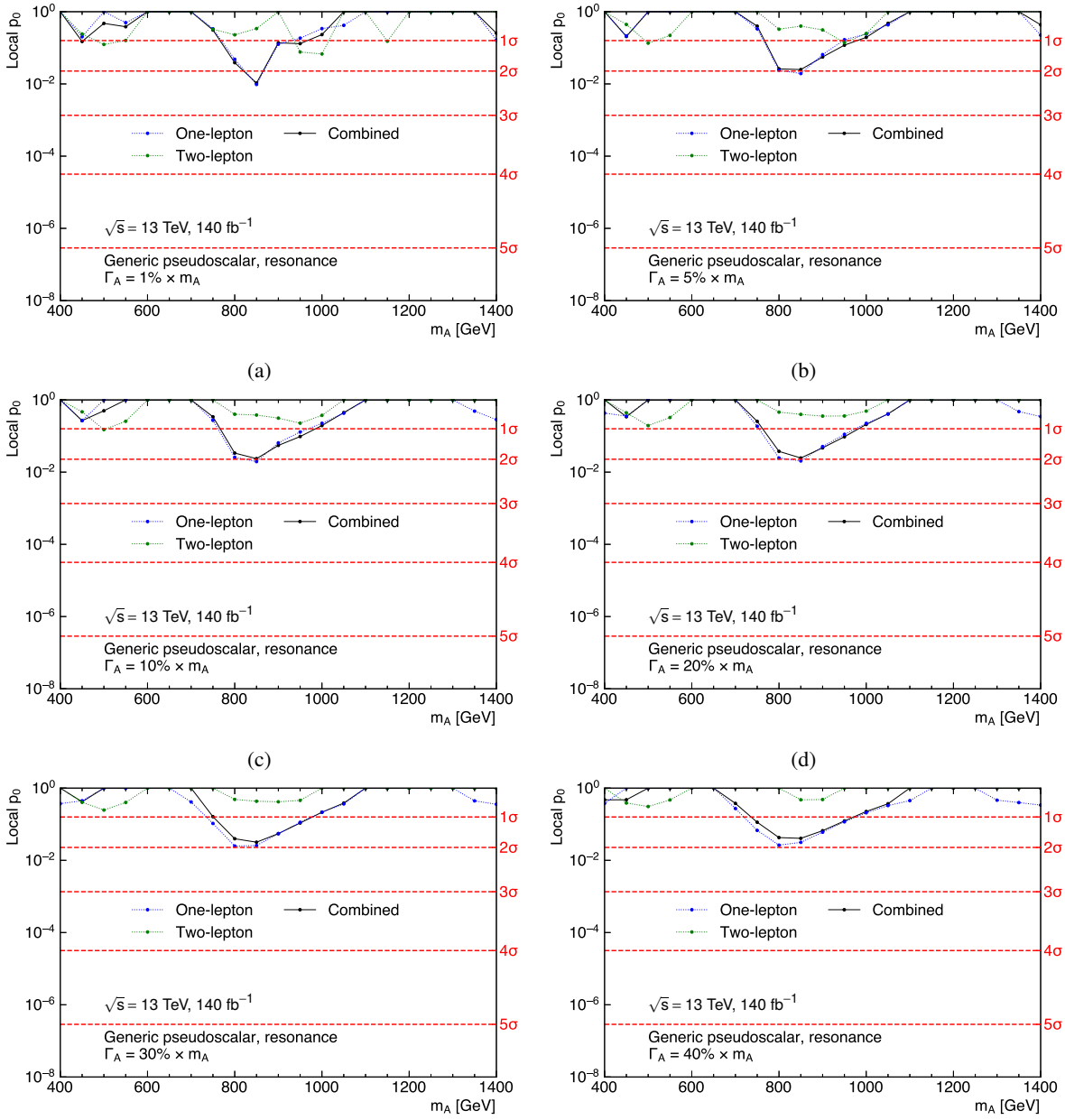

Figure A.1: Observed local p-values under the background-only hypothesis, against a pseudoscalar resonance hypothesis, as a function of m_A for different values of the relative width of the pseudoscalar A: (a) 1%, (b) 5%, (c) 10%, (d) 20%, (e) 30%, (f) 40%. The p-values are calculated separately in the one-lepton and two-lepton channels, and by combining both. On the right-hand y-axis, the Gaussian significances corresponding to the p-values on the left-hand y-axis are reported.

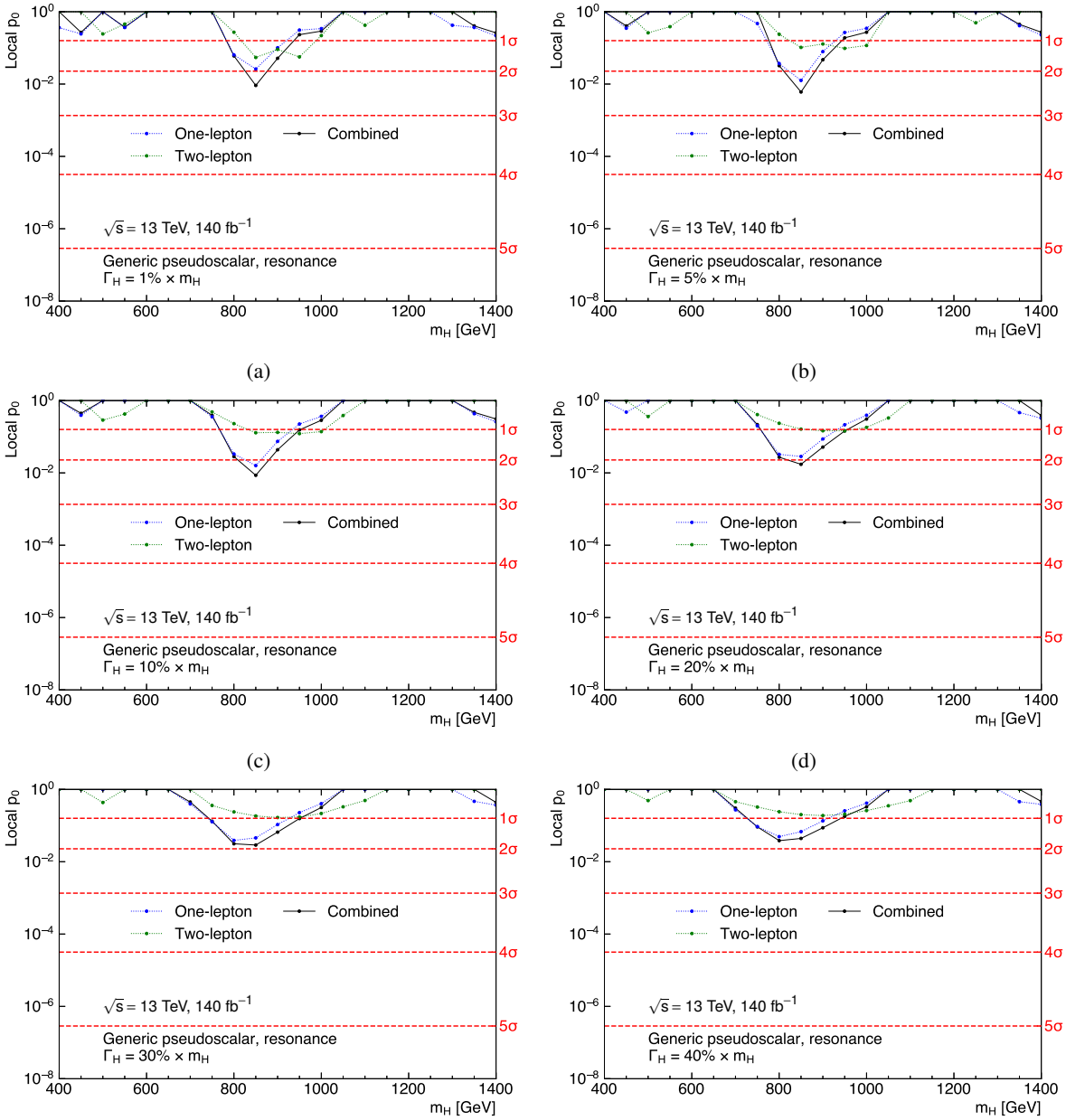

Figure A.2: Observed local p-values under the background-only hypothesis, against a scalar resonance hypothesis, as a function of m_H for different values of the relative width of the scalar H: (a) 1%, (b) 5%, (c) 10%, (d) 20%, (e) 30%, (f) 40%. The p-values are calculated separately in the one-lepton and two-lepton channels, and by combining both. On the right-hand y-axis, the Gaussian significances corresponding to the p-values on the left-hand y-axis are reported.

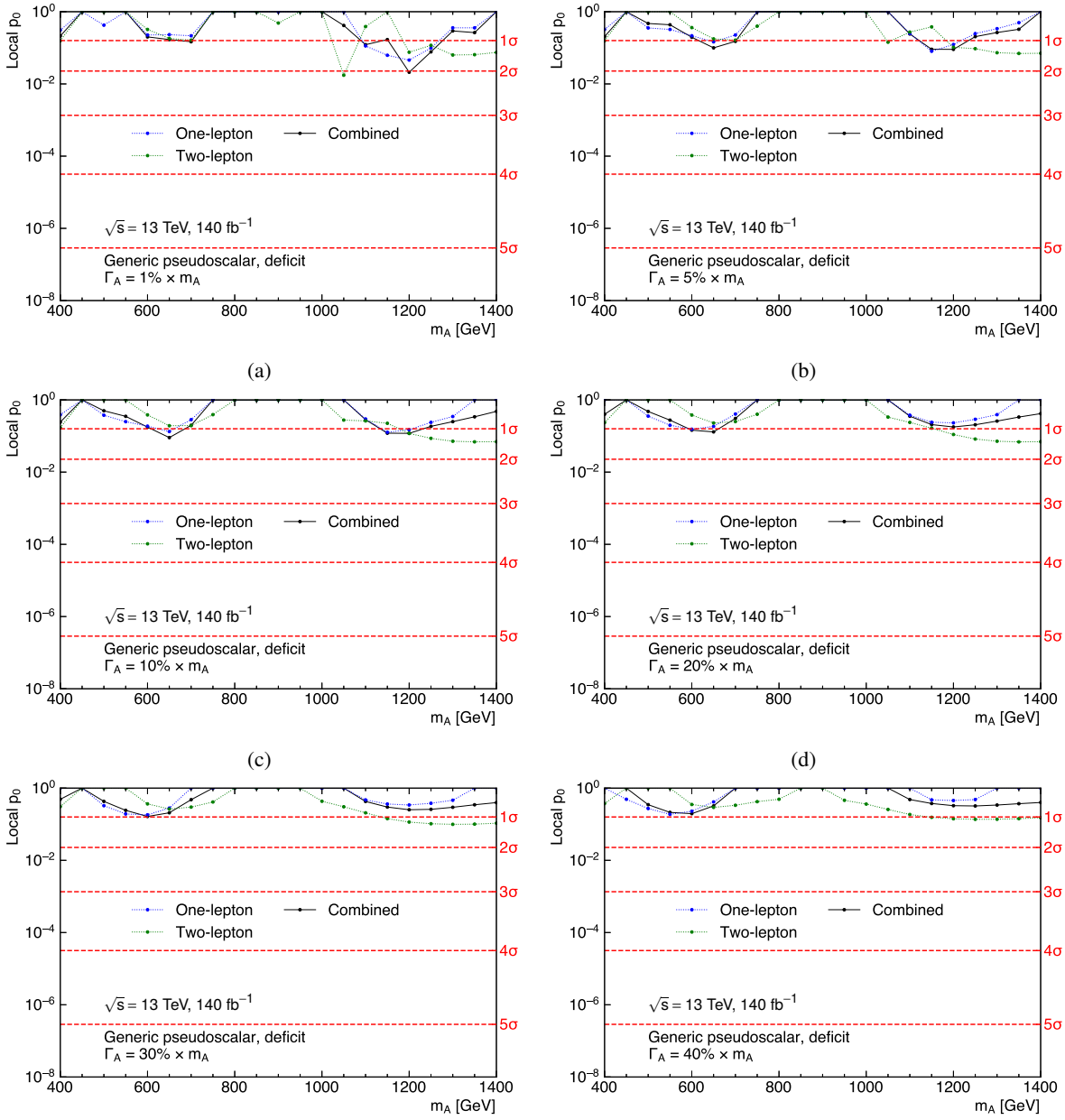

Figure A.3: Observed local p-values under the background-only hypothesis, against a pseudoscalar deficit hypothesis, as a function of m_A for different values of the relative width of the pseudoscalar A: (a) 1%, (b) 5%, (c) 10%, (d) 20%, (e) 30%, (f) 40%. The p-values are calculated separately in the one-lepton and two-lepton channels, and by combining both. On the right-hand y-axis, the Gaussian significances corresponding to the p-values on the left-hand y-axis are reported.

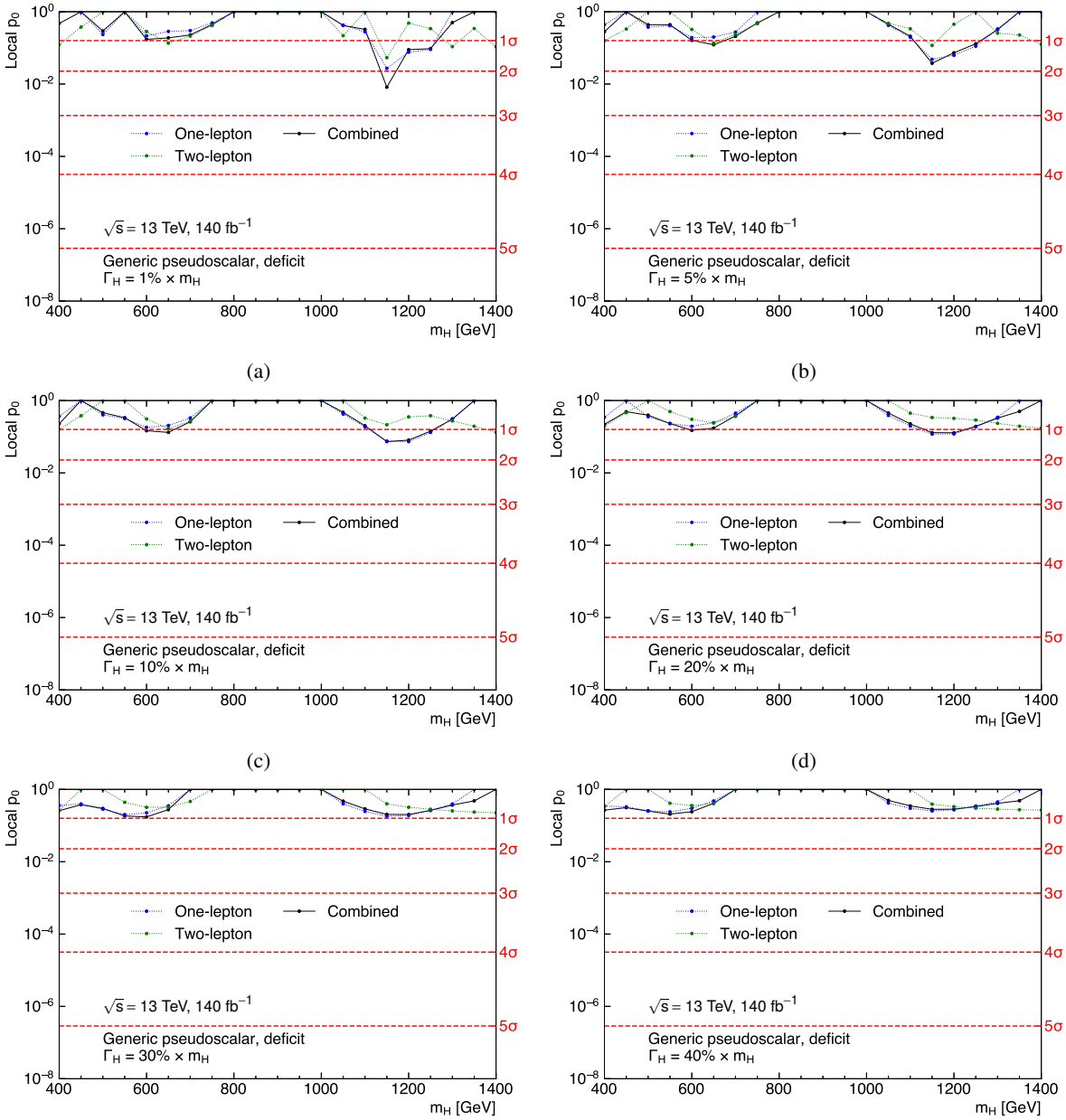

Figure A.4: Observed local p-values under the background-only hypothesis, against a scalar deficit hypothesis, as a function of m_H for different values of the relative width of the scalar H: (a) 1%, (b) 5%, (c) 10%, (d) 20%, (e) 30%, (f) 40%. The p-values are calculated separately in the one-lepton and two-lepton channels, and by combining both. On the right-hand y-axis, the Gaussian significances corresponding to the p-values on the left-hand y-axis are reported.

APPENDIX B

Constraints on the coupling strength modifier in the generic (pseudo)scalar interpretation

In the context of the search for heavy scalar and pseudoscalar particles decaying to a $t\bar{t}$ pair, normalisation factors were applied to the S and S+I samples of the 2HDM and hMSSM benchmark models to correct their LO cross-section to a partial NLO cross-section, as described in Section 4.2.6. The first results published by the ATLAS collaboration in April 2024 did not include correction factors to NLO precision for the signal samples of the generic (pseudo)scalar model. These are the results shown in this thesis, which was submitted to Universität Hamburg in May 2024, in Section 8.5.

The results published by the ATLAS collaboration in the Journal of High Energy Physics in August 2024 [19], also include correction factors to NLO precision for the signal samples of the generic (pseudo)scalar model and are shown in the following.

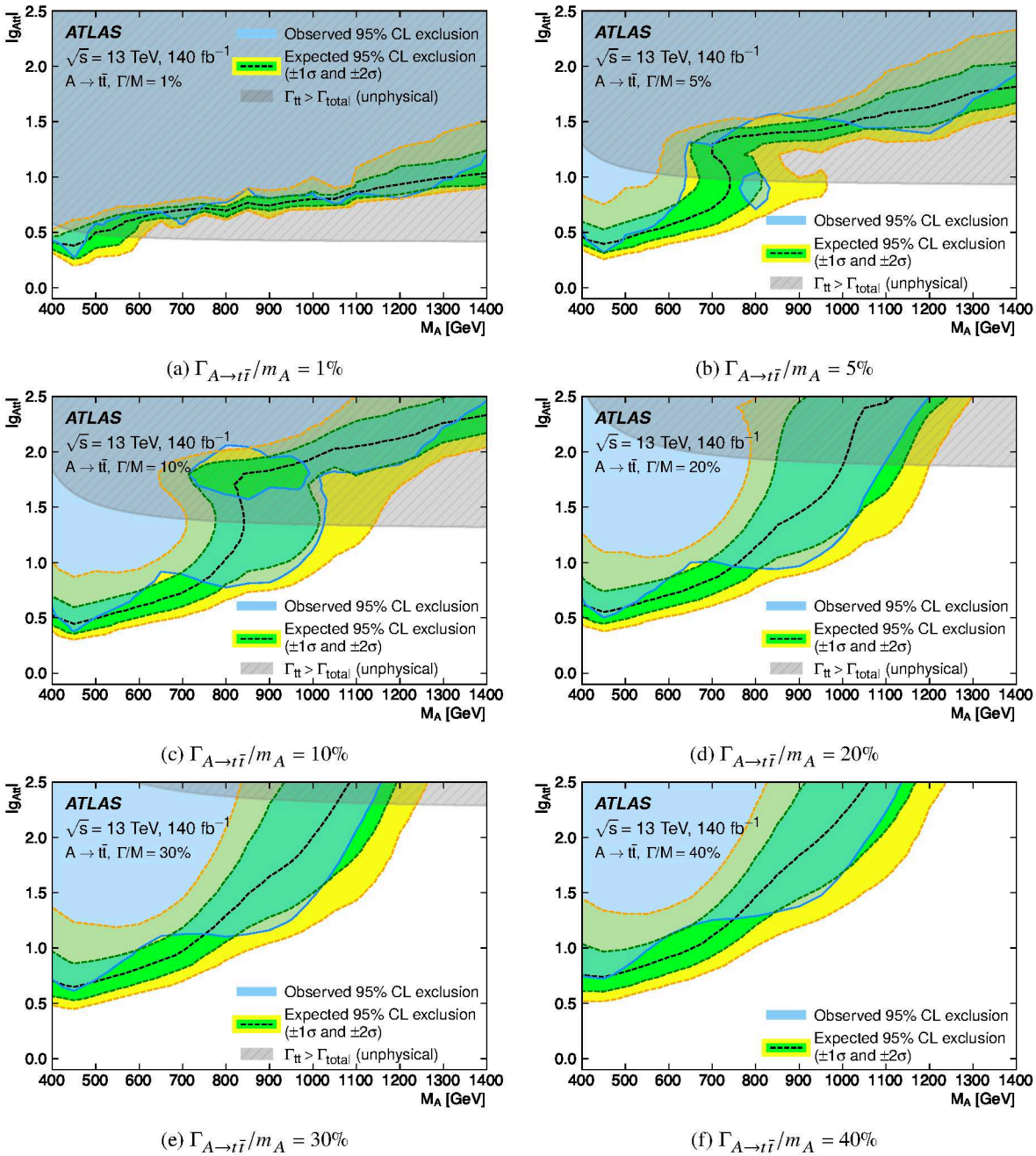

(a) $\Gamma_{A\to t\bar{t}}/m_A = 1\%$ (b) $\Gamma_{A\to t\bar{t}}/m_A = 5\%$

(c) $\Gamma_{A\to t\bar{t}}/m_A = 10\%$ (d) $\Gamma_{A\to t\bar{t}}/m_A = 20\%$

(e) $\Gamma_{A\to t\bar{t}}/m_A = 30\%$ (f) $\Gamma_{A\to t\bar{t}}/m_A = 40\%$

Figure B.1: Constraints on the coupling strength modifier $g_{At\bar{t}}$ as a function of m_A for different values of the relative width of the pseudoscalar A: (a) 1%, (b) 5%, (c) 10%, (d) 20%, (e) 30%, (f) 40%. Correction factors to NLO precision for the signal samples are applied. The hatched area marks the unphysical region of parameter space where the partial width $\Gamma(A \to t\bar{t})$ is larger than the total width of A. The observed exclusion regions are indicated by the shaded area. The boundary of the expected exclusion region under the background-only hypothesis is marked by the dashed line. The surrounding shaded bands correspond to the $\pm 1(2)\sigma$ variations of the expected excluded regions. Figure published in Ref. [19].

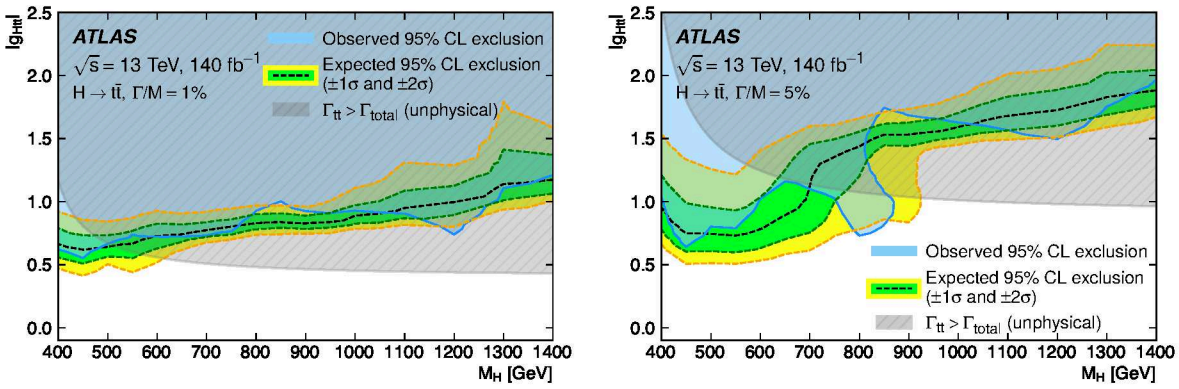

(a) $\Gamma_{H\to t\bar{t}}/m_H = 1\%$

(b) $\Gamma_{H\to t\bar{t}}/m_H = 5\%$

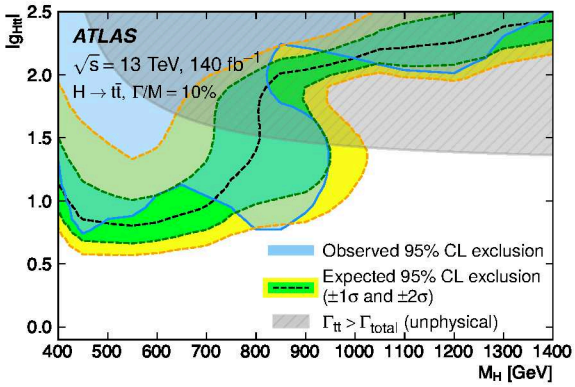

(c) $\Gamma_{H\to t\bar{t}}/m_H = 10\%$

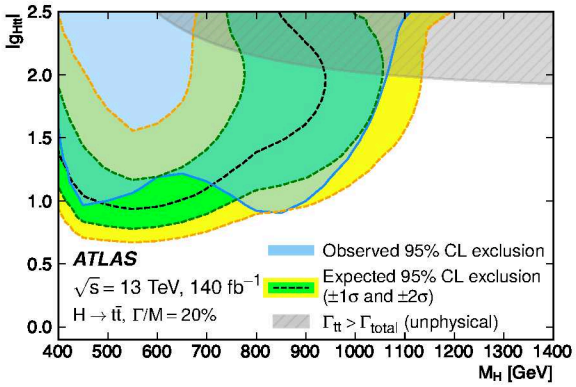

(d) $\Gamma_{H\to t\bar{t}}/m_H = 20\%$

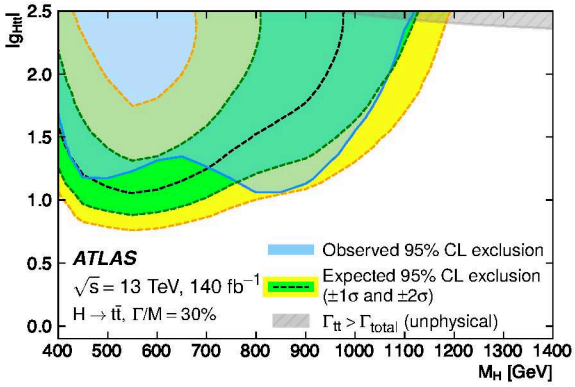

(e) $\Gamma_{H\to t\bar{t}}/m_H = 30\%$

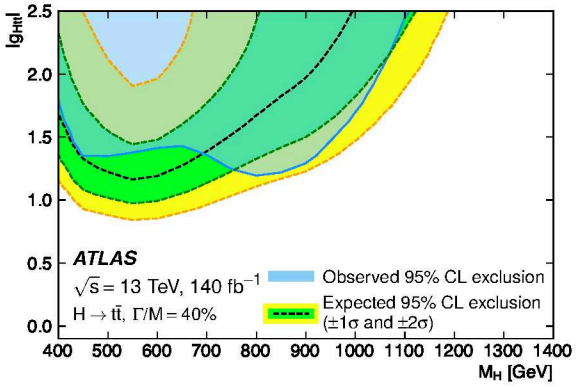

(f) $\Gamma_{H\to t\bar{t}}/m_H = 40\%$

Figure B.2: Constraints on the coupling strength modifier $g_{Ht\bar{t}}$ as a function of m_H for different values of the relative width of the scalar H: (a) 1%, (b) 5%, (c) 10%, (d) 20%, (e) 30%, (f) 40%. Correction factors to NLO precision for the signal samples are applied. The hatched area marks the unphysical region of parameter space where the partial width $\Gamma(H \to t\bar{t})$ is larger than the total width of H. The observed exclusion regions are indicated by the shaded area. The boundary of the expected exclusion region under the background-only hypothesis is marked by the dashed line. The surrounding shaded bands correspond to the $\pm 1(2)\sigma$ variations of the expected excluded regions. Figure published in Ref. [19].

Bibliography

[1] G. Arnison et al., *Experimental observation of isolated large transverse energy electrons with associated missing energy at s=540 GeV*, Physics Letters B **122** (1983) 103, ISSN: 0370-2693, URL: https://www.sciencedirect.com/science/article/pii/0370269383911772 (cit. on p. 1).

[2] M. Banner et al., *Observation of single isolated electrons of high transverse momentum in events with missing transverse energy at the CERN pp collider*, Physics Letters B **122** (1983) 476, ISSN: 0370-2693, URL: https://www.sciencedirect.com/science/article/pii/0370269383916052 (cit. on p. 1).

[3] F. Abe et al., *Observation of Top Quark Production in $p\bar{p}$ Collisions with the Collider Detector at Fermilab*, Physical Review Letters **74** (1995) 2626, ISSN: 1079-7114, URL: http://dx.doi.org/10.1103/PhysRevLett.74.2626 (cit. on p. 1).

[4] S. Abachi et al., *Observation of the Top Quark*, Phys. Rev. Lett. **74** (14 1995) 2632, URL: https://link.aps.org/doi/10.1103/PhysRevLett.74.2632 (cit. on p. 1).

[5] G. Altarelli and M. W. Grünewald, *Precision electroweak tests of the Standard Model*, Physics Reports **403–404** (2004) 189, ISSN: 0370-1573, URL: http://dx.doi.org/10.1016/j.physrep.2004.08.013 (cit. on p. 1).

[6] B. Mele, *Precision Tests of the Standard Model at LEP*, 1993, arXiv: hep-ph/9312285 [hep-ph] (cit. on p. 1).

[7] ATLAS Collaboration, *Observation of a new particle in the search for the Standard Model Higgs boson with the ATLAS detector at the LHC*, Phys. Lett. B **716** (2012) 1, arXiv: 1207.7214 [hep-ex] (cit. on p. 1).

[8] CMS Collaboration, *Observation of a new boson at a mass of 125 GeV with the CMS experiment at the LHC*, Phys. Lett. B **716** (2012) 30, arXiv: 1207.7235 [hep-ex] (cit. on p. 1).

[9] F. Zwicky, *On the Masses of Nebulae and of Clusters of Nebulae*, **86** (1937) 217 (cit. on pp. 1, 15).

[10] V. C. Rubin and J. Ford W. Kent, *Rotation of the Andromeda Nebula from a Spectroscopic Survey of Emission Regions*, **159** (1970) 379 (cit. on pp. 1, 15).

[11] P. A. R. Ade et al., *Planck2015 results: XIII. Cosmological parameters*, Astronomy amp; Astrophysics **594** (2016) A13, ISSN: 1432-0746, URL: http://dx.doi.org/10.1051/0004-6361/201525830 (cit. on pp. 1, 15).

[12] R. Massey, T. Kitching and J. Richard, *The dark matter of gravitational lensing*, Reports on Progress in Physics **73** (2010) 086901, ISSN: 1361-6633, URL: http://dx.doi.org/10.1088/0034-4885/73/8/086901 (cit. on pp. 1, 15).

[13] European Space Agency, *Planck - New Cosmic Recipe*, Accessed: April 11, 2024, 2018, URL: https://sci.esa.int/web/planck/-/51557-planck-new-cosmic-recipe (cit. on pp. 1, 15).

[14] J. F. Gunion and H. E. Haber, *CP-conserving two-Higgs-doublet model: The approach to the decoupling limit*, Physical Review D **67** (2003), ISSN: 1089-4918, URL: http://dx.doi.org/10.1103/PhysRevD.67.075019 (cit. on p. 2).

[15] A. Djouadi et al., *The post-Higgs MSSM scenario: habemus MSSM?*, The European Physical Journal C **73** (2013), ISSN: 1434-6052, URL: http://dx.doi.org/10.1140/epjc/s10052-013-2650-0 (cit. on pp. 2, 20).

[16] M. Bauer, U. Haisch and F. Kahlhoefer, *Simplified dark matter models with two Higgs doublets: I. Pseudoscalar mediators*, Journal of High Energy Physics **2017** (2017), ISSN: 1029-8479, URL: http://dx.doi.org/10.1007/JHEP05(2017)138 (cit. on pp. 2, 19, 20).

[17] ATLAS Collaboration, *Search for heavy Higgs bosons A/H decaying to a top quark pair in pp collisions at $\sqrt{s} = 8$ TeV with the ATLAS detector*, Phys. Rev. Lett. **119** (2017) 191803, arXiv: 1707.06025 [hep-ex] (cit. on pp. 2, 39, 73, 113, 114, 136).

[18] CMS Collaboration, *Search for heavy Higgs bosons decaying to a top quark pair in proton–proton collisions at $\sqrt{s} = 13$ TeV*, JHEP **04** (2020) 171, arXiv: 1908.01115 [hep-ex] (cit. on pp. 2, 114, 115, 136).

[19] ATLAS Collaboration, *Search for heavy neutral Higgs bosons decaying into a top quark pair in 140 fb1 of proton-proton collision data at $\sqrt{s} = 13$ TeV with the ATLAS detector*, Journal of High Energy Physics **2024** (2024), ISSN: 1029-8479, URL: http://dx.doi.org/10.1007/JHEP08(2024)013 (cit. on pp. 3, 62, 68, 101–103, 105, 109, 110, 136, 147–149).

[20] M. E. Peskin and D. V. Schroeder, *An Introduction to Quantum Field Theory, Student Economy Edition*, CRC Press, 2015, chap. 10 315, ISBN: 9780813350196 (cit. on p. 8).

[21] S. Weinberg, *The Quantum Theory of Fields, Volume 1: Foundations*, Cambridge University Press, 2013, ISBN: 9780521670531 (cit. on p. 8).

[22] S. Weinberg, *A Model of Leptons*, Physical Review Letters **19** (1967) 1264 (cit. on p. 9).

[23] R. L. Workman et al., *Review of Particle Physics*, PTEP **2022** (2022) 083C01 (cit. on pp. 12–14, 21, 37, 61).

[24] J. C. Collins, D. E. Soper and G. Sterman, *Factorization of Hard Processes in QCD*, 2004, arXiv: hep-ph/0409313 [hep-ph] (cit. on p. 12).

[25] J. M. Campbell, J. W. Huston and W. J. Stirling,
Hard interactions of quarks and gluons: a primer for LHC physics,
Reports on Progress in Physics **70** (2006) 89, ISSN: 1361-6633,
URL: http://dx.doi.org/10.1088/0034-4885/70/1/R02 (cit. on p. 12).

[26] G. Altarelli and G. Parisi, *Asymptotic freedom in parton language*,
Nuclear Physics B **126** (1977) 298 (cit. on p. 13).

[27] Y. L. Dokshitzer, *Calculation of the Structure Functions for Deep Inelastic Scattering and e+e- Annihilation by Perturbation Theory in Quantum Chromodynamics*,
Soviet Physics JETP **46** (1977) 641,
URL: http://www.jetp.ac.ru/cgi-bin/e/index/e/46/4/p641?a=list
(cit. on p. 13).

[28] V. N. Gribov and L. N. Lipatov, *Deep inelastic e p scattering in perturbation theory*,
Soviet Journal of Nuclear Physics **15** (1972) 438,
URL: http://www.jetp.ac.ru/cgi-bin/e/index/e/15/2/p438?a=list
(cit. on p. 13).

[29] A. D. Sakharov,
Violation of CP invariance, C asymmetry, and baryon asymmetry of the universe,
Soviet Physics Uspekhi **34** (1991) 392,
URL: https://dx.doi.org/10.1070/PU1991v034n05ABEH002497 (cit. on p. 15).

[30] R. D. Peccei and H. R. Quinn, *CP Conservation in the Presence of Pseudoparticles*,
Physical Review Letters **38** (1977) 1440 (cit. on p. 16).

[31] R. D. Peccei and H. R. Quinn,
Constraints Imposed by CP Conservation in the Presence of Instantons,
Physical Review D **16** (1977) 1791 (cit. on p. 16).

[32] Y. A. Golfand and E. P. Likhtman,
Extension of the Algebra of Poincare Group Generators and Violation of p Invariance,
JETP Lett. **13** (1971) 323 (cit. on p. 17).

[33] D. V. Volkov and V. P. Akulov, *Is the Neutrino a Goldstone Particle?*,
Phys. Lett. B **46** (1973) 109 (cit. on p. 17).

[34] J. Wess and B. Zumino, *Supergauge Transformations in Four-Dimensions*,
Nucl. Phys. B **70** (1974) 39, ed. by A. Salam and E. Sezgin (cit. on p. 17).

[35] J. Wess and B. Zumino, *Supergauge Invariant Extension of Quantum Electrodynamics*,
Nucl. Phys. B **78** (1974) 1 (cit. on p. 17).

[36] S. Ferrara and B. Zumino, *Supergauge Invariant Yang-Mills Theories*,
Nucl. Phys. B **79** (1974) 413 (cit. on p. 17).

[37] A. Salam and J. A. Strathdee, *Supersymmetry and Nonabelian Gauges*,
Phys. Lett. B **51** (1974) 353 (cit. on p. 17).

[38] J. E. Kim, *Light Pseudoscalars, Particle Physics and Cosmology*, Phys. Rept. **150** (1987) 1
(cit. on p. 17).

[39] ATLAS Collaboration,
Combined measurements of Higgs boson production and decay using up to 80 fb^{-1} *of proton-proton collision data at* $\sqrt{s}$ = 13 TeV *collected with the ATLAS experiment*,
Phys. Rev. D **101** (1 2020) 012002,
URL: https://link.aps.org/doi/10.1103/PhysRevD.101.012002 (cit. on p. 19).

[40] D. Abercrombie et al., *Dark Matter benchmark models for early LHC Run-2 Searches: Report of the ATLAS/CMS Dark Matter Forum*, Physics of the Dark Universe **27** (2020) 100371,
ISSN: 2212-6864, URL: http://dx.doi.org/10.1016/j.dark.2019.100371
(cit. on p. 19).

[41] A. Boveia et al., *Recommendations on presenting LHC searches for missing transverse energy signals using simplified s-channel models of dark matter*, 2016,
arXiv: 1603.04156 [hep-ex] (cit. on p. 19).

[42] A. Albert et al.,
Recommendations of the LHC Dark Matter Working Group: Comparing LHC searches for heavy mediators of dark matter production in visible and invisible decay channels, 2017,
arXiv: 1703.05703 [hep-ex] (cit. on p. 19).

[43] T. Abe et al., *LHC Dark Matter Working Group: Next-generation spin-0 dark matter models*, 2018, arXiv: 1810.09420 [hep-ex] (cit. on p. 20).

[44] ATLAS Collaboration,
Combination and summary of ATLAS dark matter searches interpreted in a 2HDM with a pseudo-scalar mediator using 139 fb^{-1} *of* $\sqrt{s}$ = 13 *TeV pp collision data*, 2023,
arXiv: 2306.00641 [hep-ex] (cit. on p. 20).

[45] T. Abe et al., *LHC Dark Matter Working Group: Next-generation spin-0 dark matter models*, 2018, arXiv: 1810.09420 [hep-ex] (cit. on p. 20).

[46] P. Fayet, *Supersymmetry and weak, electromagnetic and strong interactions*,
Physics Letters B **64** (1976) 159, ISSN: 0370-2693,
URL: https://www.sciencedirect.com/science/article/pii/0370269376903191
(cit. on p. 20).

[47] P. Fayet, *Spontaneously broken supersymmetric theories of weak, electromagnetic and strong interactions*, Physics Letters B **69** (1977) 489, ISSN: 0370-2693,
URL: https://www.sciencedirect.com/science/article/pii/0370269377908528
(cit. on p. 20).

[48] G. R. Farrar and P. Fayet, *Phenomenology of the production, decay, and detection of new hadronic states associated with supersymmetry*, Physics Letters B **76** (1978) 575,
ISSN: 0370-2693,
URL: https://www.sciencedirect.com/science/article/pii/0370269378908584
(cit. on p. 20).

[49] P. Fayet, *Relations between the masses of the superpartners of leptons and quarks, the goldstino coupling and the neutral currents*, Physics Letters B **84** (1979) 416,
ISSN: 0370-2693,
URL: https://www.sciencedirect.com/science/article/pii/0370269379912292
(cit. on p. 20).

[50] S. Dimopoulos and H. Georgi, *Softly broken supersymmetry and SU(5)*, Nuclear Physics B **193** (1981) 150, ISSN: 0550-3213, URL: https://www.sciencedirect.com/science/article/pii/0550321381905228 (cit. on p. 20).

[51] ATLAS Collaboration, *The ATLAS Experiment at the CERN Large Hadron Collider*, JINST **3** (2008) S08003, Also published by CERN Geneva in 2010, URL: https://cds.cern.ch/record/1129811 (cit. on p. 23).

[52] K. M. Potter, *The Large Hadron Collider (LHC) project of CERN*, (1996), URL: https://cds.cern.ch/record/308243 (cit. on p. 23).

[53] CERN, *CERN Home - Accelerator Complex*, Accessed 2024, URL: https://www.home.cern/science/accelerators/accelerator-complex (cit. on p. 24).

[54] CMS Collaboration, *The CMS experiment at the CERN LHC. The Compact Muon Solenoid experiment*, JINST **3** (2008) S08004, Also published by CERN Geneva in 2010, URL: https://cds.cern.ch/record/1129810 (cit. on p. 24).

[55] A. Collaboration, *The ALICE experiment at the CERN LHC*, JINST **3** (2008) S08002 (cit. on p. 24).

[56] LHCb Collaboration, *The LHCb Detector at the LHC*, JINST **3** (2008) S08005, Also published by CERN Geneva in 2010, URL: https://cds.cern.ch/record/1129809 (cit. on p. 24).

[57] ATLAS Collaboration, *Luminosity determination in pp collisions at $\sqrt{s} = 13$ TeV using the ATLAS detector at the LHC. Luminosity determination in pp collisions at $\sqrt{s} = 13$ TeV using the ATLAS detector at the LHC*, Eur. Phys. J. C **83** (2023) 982, arXiv: 2212.09379, URL: https://cds.cern.ch/record/2844887 (cit. on p. 24).

[58] ATLAS Collaboration, *LuminosityPublicResults*, URL: https://twiki.cern.ch/twiki/bin/view/AtlasPublic/LuminosityPublicResults (cit. on p. 25).

[59] A. Collaboration, *The ATLAS Experiment at the CERN Large Hadron Collider: A Description of the Detector Configuration for Run 3*, 2023, arXiv: 2305.16623 [physics.ins-det] (cit. on pp. 26, 28, 30–32).

[60] *ATLAS inner detector: Technical Design Report, 1*, Technical design report. ATLAS, Geneva: CERN, 1997, URL: https://cds.cern.ch/record/331063 (cit. on p. 27).

[61] ATLAS Collaboration, *ATLAS Insertable B-Layer: Technical Design Report*, ATLAS-TDR-19; CERN-LHCC-2010-013, 2010, URL: https://cds.cern.ch/record/1291633 (cit. on p. 28), Addendum: ATLAS-TDR-19-ADD-1; CERN-LHCC-2012-009, 2012, URL: https://cds.cern.ch/record/1451888.

[62] ATLAS Collaboration, *ATLAS Liquid Argon Calorimeter: Technical Design Report*, ATLAS-TDR-2; CERN-LHCC-96-041, 1996, URL: https://cds.cern.ch/record/331061 (cit. on p. 29).

[63] ATLAS Collaboration, *ATLAS Tile Calorimeter: Technical Design Report*, ATLAS-TDR-3; CERN-LHCC-96-042, 1996, URL: https://cds.cern.ch/record/331062 (cit. on p. 29).

[64] *ATLAS liquid argon calorimeter: Technical design report*, (1996) (cit. on p. 30).

[65] ATLAS Collaboration, *ATLAS Muon Spectrometer: Technical Design Report*, ATLAS-TDR-10; CERN-LHCC-97-022, CERN, 1997, URL: https://cds.cern.ch/record/331068 (cit. on p. 31).

[66] L. Evans and P. Bryant, *LHC Machine*, JINST **3** (2008) S08001 (cit. on p. 33).

[67] ATLAS Collaboration, *ATLAS Phase-II Upgrade Scoping Document*, CERN-LHCC-2015-020, LHCC-G-166, 2015, URL: https://cds.cern.ch/record/2055248 (cit. on p. 33).

[68] ATLAS Collaboration, *ATLAS Inner Tracker Pixel Detector: Technical Design Report*, ATLAS-TDR-030; CERN-LHCC-2017-021, 2017, URL: https://cds.cern.ch/record/2285585 (cit. on pp. 33, 120).

[69] ATLAS Collaboration, *ATLAS Inner Tracker Strip Detector: Technical Design Report*, ATLAS-TDR-025; CERN-LHCC-2017-005, 2017, URL: https://cds.cern.ch/record/2257755 (cit. on p. 33).

[70] ATLAS Collaboration, *ATLAS LAr Calorimeter Phase-II Upgrade: Technical Design Report*, ATLAS-TDR-027; CERN-LHCC-2017-018, 2017, URL: https://cds.cern.ch/record/2285582 (cit. on p. 33).

[71] ATLAS Collaboration, *ATLAS Tile Calorimeter Phase-II Upgrade: Technical Design Report*, ATLAS-TDR-028; CERN-LHCC-2017-019, 2017, URL: https://cds.cern.ch/record/2285583 (cit. on p. 33).

[72] ATLAS Collaboration, *ATLAS Muon Spectrometer Phase-II Upgrade: Technical Design Report*, ATLAS-TDR-026; CERN-LHCC-2017-017, 2017, URL: https://cds.cern.ch/record/2285580 (cit. on p. 33).

[73] ATLAS Collaboration, *A High-Granularity Timing Detector for the ATLAS Phase-II Upgrade: Technical Design Report*, ATLAS-TDR-031; CERN-LHCC-2020-007, 2020, URL: https://cds.cern.ch/record/2719855 (cit. on p. 33).

[74] ATLAS Collaboration, *ATLAS TDAQ Phase-II Upgrade: Technical Design Report*, ATLAS-TDR-029; CERN-LHCC-2017-020, 2017, URL: https://cds.cern.ch/record/2285584 (cit. on p. 33).

[75] ATLAS Collaboration, *Expected tracking and related performance with the updated ATLAS Inner Tracker layout at the High-Luminosity LHC*, ATL-PHYS-PUB-2021-024, 2021, URL: https://cds.cern.ch/record/2776651 (cit. on pp. 33, 34, 120, 121).

[76] ATLAS Collaboration, *Luminosity determination in pp collisions at*

$$\sqrt{s} = 13$$

TeV using the ATLAS detector at the LHC, The European Physical Journal C **83** (2023), ISSN: 1434-6052, URL: http://dx.doi.org/10.1140/epjc/s10052-023-11747-w (cit. on pp. 36, 78).

[77] A. Buckley et al., *General-purpose event generators for LHC physics*, Physics Reports **504** (2011) 145, ISSN: 0370-1573, URL: http://dx.doi.org/10.1016/j.physrep.2011.03.005 (cit. on p. 36).

[78] GEANT4 Collaboration, S. Agostinelli et al., *GEANT4 – a simulation toolkit*, Nucl. Instrum. Meth. A **506** (2003) 250 (cit. on pp. 36, 121).

[79] P. Nason, *A new method for combining NLO QCD with shower Monte Carlo algorithms*, JHEP **11** (2004) 040, arXiv: hep-ph/0409146 (cit. on p. 37).

[80] S. Frixione, G. Ridolfi and P. Nason, *A positive-weight next-to-leading-order Monte Carlo for heavy flavour hadroproduction*, JHEP **09** (2007) 126, arXiv: 0707.3088 [hep-ph] (cit. on p. 37).

[81] S. Frixione, P. Nason and C. Oleari, *Matching NLO QCD computations with parton shower simulations: the POWHEG method*, JHEP **11** (2007) 070, arXiv: 0709.2092 [hep-ph] (cit. on p. 37).

[82] S. Alioli, P. Nason, C. Oleari and E. Re, *A general framework for implementing NLO calculations in shower Monte Carlo programs: the POWHEG BOX*, JHEP **06** (2010) 043, arXiv: 1002.2581 [hep-ph] (cit. on p. 37).

[83] J. M. Campbell, R. K. Ellis, P. Nason and E. Re, *Top-Pair Production and Decay at NLO Matched with Parton Showers*, JHEP **04** (2015) 114, arXiv: 1412.1828 [hep-ph] (cit. on p. 37).

[84] R. D. Ball et al., *Parton distributions for the LHC run II*, JHEP **04** (2015) 040, arXiv: 1410.8849 [hep-ph] (cit. on p. 37).

[85] ATLAS Collaboration, *Studies on top-quark Monte Carlo modelling for Top2016*, ATL-PHYS-PUB-2016-020, 2016, URL: https://cds.cern.ch/record/2216168 (cit. on p. 37).

[86] ATLAS Collaboration, *ATLAS Pythia 8 tunes to 7 TeV data*, ATL-PHYS-PUB-2014-021, 2014, URL: https://cds.cern.ch/record/1966419 (cit. on p. 37).

[87] D. J. Lange, *The EvtGen particle decay simulation package*, Nucl. Instrum. Meth. A **462** (2001) 152 (cit. on pp. 37, 122).

[88] M. Czakon et al., *Top-pair production at the LHC through NNLO QCD and NLO EW*, JHEP **10** (2017) 186, arXiv: 1705.04105 [hep-ph] (cit. on pp. 37, 81).

[89] M. Beneke, P. Falgari, S. Klein and C. Schwinn, *Hadronic top-quark pair production with NNLL threshold resummation*, Nucl. Phys. B **855** (2012) 695, arXiv: 1109.1536 [hep-ph] (cit. on pp. 37, 80).

[90] M. Cacciari, M. Czakon, M. Mangano, A. Mitov and P. Nason, *Top-pair production at hadron colliders with next-to-next-to-leading logarithmic soft-gluon resummation*, Phys. Lett. B **710** (2012) 612, arXiv: 1111.5869 [hep-ph] (cit. on pp. 37, 80).

[91] P. Bärnreuther, M. Czakon and A. Mitov, *Percent-Level-Precision Physics at the Tevatron: Next-to-Next-to-Leading Order QCD Corrections to $q\bar{q} \to t\bar{t} + X$*, Phys. Rev. Lett. **109** (2012) 132001, arXiv: 1204.5201 [hep-ph] (cit. on pp. 37, 80).

[92] M. Czakon and A. Mitov, *NNLO corrections to top-pair production at hadron colliders: the all-fermionic scattering channels*, JHEP **12** (2012) 054, arXiv: 1207.0236 [hep-ph] (cit. on pp. 37, 80).

[93] M. Czakon and A. Mitov, *NNLO corrections to top pair production at hadron colliders: the quark-gluon reaction*, JHEP **01** (2013) 080, arXiv: 1210.6832 [hep-ph] (cit. on pp. 37, 80).

[94] M. Czakon, P. Fiedler and A. Mitov, *Total Top-Quark Pair-Production Cross Section at Hadron Colliders Through $O(\alpha_S^4)$*, Phys. Rev. Lett. **110** (2013) 252004, arXiv: 1303.6254 [hep-ph] (cit. on pp. 37, 80).

[95] M. Czakon and A. Mitov, *Top++: A program for the calculation of the top-pair cross-section at hadron colliders*, Comput. Phys. Commun. **185** (2014) 2930, arXiv: 1112.5675 [hep-ph] (cit. on pp. 37, 80).

[96] S. Alioli, P. Nason, C. Oleari and E. Re, *NLO single-top production matched with shower in POWHEG: s- and t-channel contributions*, JHEP **09** (2009) 111, arXiv: 0907.4076 [hep-ph] (cit. on p. 37), Erratum: JHEP **02** (2010) 011.

[97] E. Re, *Single-top Wt-channel production matched with parton showers using the POWHEG method*, Eur. Phys. J. C **71** (2011) 1547, arXiv: 1009.2450 [hep-ph] (cit. on p. 37).

[98] S. Frixione, E. Laenen, P. Motylinski, C. White and B. R. Webber, *Single-top hadroproduction in association with a W boson*, JHEP **07** (2008) 029, arXiv: 0805.3067 [hep-ph] (cit. on p. 38).

[99] R. Frederix, E. Re and P. Torrielli, *Single-top t-channel hadroproduction in the four-flavour scheme with POWHEG and aMC@NLO*, JHEP **09** (2012) 130, arXiv: 1207.5391 [hep-ph] (cit. on p. 38).

[100] P. Artoisenet, R. Frederix, O. Mattelaer and R. Rietkerk, *Automatic spin-entangled decays of heavy resonances in Monte Carlo simulations*, JHEP **03** (2013) 015, arXiv: 1212.3460 [hep-ph] (cit. on p. 38).

[101] N. Kidonakis, *Two-loop soft anomalous dimensions for single top quark associated production with a W^- or H^-*, Phys. Rev. D **82** (2010) 054018, arXiv: 1005.4451 [hep-ph] (cit. on pp. 38, 82).

[102] N. Kidonakis, *NNLL resummation for s-channel single top quark production*, Phys. Rev. D **81** (2010) 054028, arXiv: 1001.5034 [hep-ph] (cit. on pp. 38, 82).

[103] N. Kidonakis, *Next-to-next-to-leading-order collinear and soft gluon corrections for t-channel single top quark production*, Phys. Rev. D **83** (2011) 091503, arXiv: 1103.2792 [hep-ph] (cit. on pp. 38, 82).

[104] J. Alwall et al., *The automated computation of tree-level and next-to-leading order differential cross sections, and their matching to parton shower simulations*, JHEP **07** (2014) 079, arXiv: 1405.0301 [hep-ph] (cit. on pp. 38, 39).

[105] D. de Florian et al., *Handbook of LHC Higgs Cross Sections: 4. Deciphering the Nature of the Higgs Sector*, **2/2017** (2016), arXiv: 1610.07922 [hep-ph] (cit. on p. 38).

[106] S. Schumann and F. Krauss, *A parton shower algorithm based on Catani–Seymour dipole factorisation*, JHEP **03** (2008) 038, arXiv: 0709.1027 [hep-ph] (cit. on pp. 38, 39).

[107] S. Höche, F. Krauss, M. Schönherr and F. Siegert, *A critical appraisal of NLO+PS matching methods*, JHEP **09** (2012) 049, arXiv: 1111.1220 [hep-ph] (cit. on p. 38).

[108] S. Höche, F. Krauss, M. Schönherr and F. Siegert, *QCD matrix elements + parton showers. The NLO case*, JHEP **04** (2013) 027, arXiv: 1207.5030 [hep-ph] (cit. on p. 38).

[109] S. Catani, F. Krauss, B. R. Webber and R. Kuhn, *QCD Matrix Elements + Parton Showers*, JHEP **11** (2001) 063, arXiv: hep-ph/0109231 (cit. on p. 38).

[110] S. Höche, F. Krauss, S. Schumann and F. Siegert, *QCD matrix elements and truncated showers*, JHEP **05** (2009) 053, arXiv: 0903.1219 [hep-ph] (cit. on p. 38).

[111] S. Catani, L. Cieri, G. Ferrera, D. de Florian and M. Grazzini, *Vector boson production at hadron colliders: a fully exclusive QCD calculation at NNLO*, Phys. Rev. Lett. **103** (2009) 082001, arXiv: 0903.2120 [hep-ph] (cit. on p. 39).

[112] ATLAS Collaboration, *Multi-Boson Simulation for 13 TeV ATLAS Analyses*, ATL-PHYS-PUB-2017-005, 2017, URL: https://cds.cern.ch/record/2261933 (cit. on p. 39).

[113] T. Gleisberg and S. Höche, *Comix, a new matrix element generator*, JHEP **12** (2008) 039, arXiv: 0808.3674 [hep-ph] (cit. on p. 39).

[114] D. Eriksson, J. Rathsman and O. Stal, *2HDMC: Two-Higgs-Doublet Model Calculator Physics and Manual*, Comput. Phys. Commun. **181** (2010) 189, arXiv: 0902.0851 [hep-ph] (cit. on p. 39).

[115] R. V. Harlander, S. Liebler and H. Mantler, *SusHi: A program for the calculation of Higgs production in gluon fusion and bottom-quark annihilation in the Standard Model and the MSSM*, Comput. Phys. Commun. **184** (2013) 1605, arXiv: 1212.3249 [hep-ph] (cit. on p. 40).

[116] R. V. Harlander and W. B. Kilgore, *Next-to-next-to-leading order Higgs production at hadron colliders*, Phys. Rev. Lett. **88** (2002) 201801, arXiv: hep-ph/0201206 (cit. on p. 40).

[117] R. V. Harlander and W. B. Kilgore, *Higgs boson production in bottom quark fusion at next-to-next-to leading order*, Phys. Rev. D **68** (2003) 013001, arXiv: hep-ph/0304035 (cit. on p. 40).

[118] U. Aglietti, R. Bonciani, G. Degrassi and A. Vicini,
Two-loop light fermion contribution to Higgs production and decays,
Phys. Lett. B **595** (2004) 432, arXiv: hep-ph/0404071 (cit. on p. 40).

[119] R. Bonciani, G. Degrassi and A. Vicini,
On the Generalized Harmonic Polylogarithms of One Complex Variable,
Comput. Phys. Commun. **182** (2011) 1253, arXiv: 1007.1891 [hep-ph] (cit. on p. 40).

[120] R. Harlander and P. Kant,
Higgs production and decay: Analytic results at next-to-leading order QCD,
JHEP **12** (2005) 015, arXiv: hep-ph/0509189 (cit. on p. 40).

[121] *Clustering and Tracking in Dense Environments with the ATLAS Inner Tracker for the High-Luminosity LHC*, tech. rep., All figures including auxiliary figures are available at https://atlas.web.cern.ch/Atlas/GROUPS/PHYSICS/PUBNOTES/ATL-PHYS-PUB-2023-022: CERN, 2023, URL: https://cds.cern.ch/record/2867615
(cit. on pp. 41, 120, 135).

[122] R. Frühwirth, *Application of Kalman filtering to track and vertex fitting*,
Nuclear Instruments and Methods in Physics Research Section A: Accelerators, Spectrometers, Detectors and Associated Equipment **262** (1987) 444, ISSN: 0168-9002,
URL: https://www.sciencedirect.com/science/article/pii/0168900287908874
(cit. on p. 42).

[123] ATLAS Collaboration,
A neural network clustering algorithm for the ATLAS silicon pixel detector,
JINST **9** (2014) P09009, arXiv: 1406.7690 [hep-ex] (cit. on pp. 42, 119).

[124] ATLAS Collaboration, *Training and validation of the ATLAS pixel clustering neural networks*, ATL-PHYS-PUB-2018-002, 2018, URL: https://cds.cern.ch/record/2309474
(cit. on pp. 42, 119).

[125] ATLAS Collaboration, *Performance of the ATLAS track reconstruction algorithms in dense environments in LHC Run 2*, Eur. Phys. J. C **77** (2017) 673, arXiv: 1704.07983 [hep-ex]
(cit. on p. 42).

[126] ATLAS Collaboration, *Electron reconstruction and identification in the ATLAS experiment using the 2015 and 2016 LHC proton–proton collision data at* $\sqrt{s} = 13$ *TeV*,
The European Physical Journal C **79** (2019) 639, ISSN: 1434-6052,
URL: https://doi.org/10.1140/epjc/s10052-019-7140-6 (cit. on p. 43).

[127] W. Lampl et al., *Calorimeter Clustering Algorithms: Description and Performance*, tech. rep., All figures including auxiliary figures are available at https://atlas.web.cern.ch/Atlas/GROUPS/PHYSICS/PUBNOTES/ATL-LARG-PUB-2008-002: CERN, 2008, URL: https://cds.cern.ch/record/1099735 (cit. on p. 43).

[128] R. Frühwirth, *A Gaussian-mixture approximation of the Bethe–Heitler model of electron energy loss by bremsstrahlung*, Computer Physics Communications **154** (2003) 131,
ISSN: 0010-4655, URL:
https://www.sciencedirect.com/science/article/pii/S0010465503002923
(cit. on p. 43).

[129] ATLAS Collaboration, *Electron reconstruction and identification in the ATLAS experiment using the 2015 and 2016 LHC proton–proton collision data at* $\sqrt{s} = 13$ *TeV*, Eur. Phys. J. C **79** (2019) 639, arXiv: 1902.04655 [hep-ex] (cit. on p. 44).

[130] ATLAS Collaboration, *Electron and photon performance measurements with the ATLAS detector using the 2015–2017 LHC proton-proton collision data*, Journal of Instrumentation **14** (2019) P12006, URL: https://dx.doi.org/10.1088/1748-0221/14/12/P12006 (cit. on pp. 44, 45, 78).

[131] ATLAS Collaboration, *Muon reconstruction and identification efficiency in ATLAS using the full Run 2 pp collision data set at* $\sqrt{s} = 13$ *TeV*, Eur. Phys. J. C **81** (2021) 578, arXiv: 2012.00578 [hep-ex] (cit. on pp. 46, 47, 78).

[132] *Jet global sequential corrections with the ATLAS detector in proton-proton collisions at sqrt(s) = 8 TeV*, tech. rep., All figures including auxiliary figures are available at https://atlas.web.cern.ch/Atlas/GROUPS/PHYSICS/CONFNOTES/ATLAS-CONF-2015-002: CERN, 2015, URL: https://cds.cern.ch/record/2001682 (cit. on p. 48).

[133] ATLAS Collaboration, *Jet reconstruction and performance using particle flow with the ATLAS Detector*, Eur. Phys. J. C **77** (2017) 466, arXiv: 1703.10485 [hep-ex] (cit. on p. 48).

[134] ATLAS Collaboration, *New techniques for jet calibration with the ATLAS detector*, The European Physical Journal C **83** (2023), ISSN: 1434-6052, URL: http://dx.doi.org/10.1140/epjc/s10052-023-11837-9 (cit. on pp. 49, 64).

[135] ATLAS Collaboration et al., *Measurement of inclusive jet and dijet cross sections in proton-proton collisions at 7 tev centre-of-mass energy with the atlas detector*, arXiv preprint arXiv:1009.5908, 2010 (cit. on p. 50).

[136] *Close-by Jet Effects on Jet Energy Scale Calibration in pp Collisions at sqrt(s)=7 TeV with the ATLAS Detector*, tech. rep., All figures including auxiliary figures are available at https://atlas.web.cern.ch/Atlas/GROUPS/PHYSICS/CONFNOTES/ATLAS-CONF-2011-062: CERN, 2011, URL: https://cds.cern.ch/record/1345091 (cit. on p. 51).

[137] *Boosted Object Tagging with Variable-R Jets in the ATLAS Detector*, tech. rep., All figures including auxiliary figures are available at https://atlas.web.cern.ch/Atlas/GROUPS/PHYSICS/PUBNOTES/ATL-PHYS-PUB-2016-013: CERN, 2016, URL: https://cds.cern.ch/record/2199360 (cit. on p. 51).

[138] ATLAS Collaboration, *ATLAS flavour-tagging algorithms for the LHC Run 2 pp collision dataset*, The European Physical Journal C **83** (2023) 681, ISSN: 1434-6052, URL: https://doi.org/10.1140/epjc/s10052-023-11699-1 (cit. on p. 52).

[139] ATLAS Collaboration, *Monte Carlo to Monte Carlo scale factors for flavour tagging efficiency calibration*, ATL-PHYS-PUB-2020-009, 2020, URL: https://cds.cern.ch/record/2718610 (cit. on p. 52).

[140] *E_T^{miss} performance in the ATLAS detector using 2015-2016 LHC p-p collisions*, tech. rep., All figures including auxiliary figures are available at https://atlas.web.cern.ch/Atlas/GROUPS/PHYSICS/CONFNOTES/ATLAS-CONF-2018-023: CERN, 2018, URL: https://cds.cern.ch/record/2625233 (cit. on p. 53).

[141] ATLAS Collaboration, *Performance of jet substructure techniques for large-R jets in proton-proton collisions at $\sqrt{s}$ = 7TeV using the ATLAS detector*, Journal of High Energy Physics **2013** (2013) 76, URL: https://doi.org/10.1007/JHEP09(2013)076 (cit. on p. 54).

[142] ATLAS Collaboration, *Performance of pile-up mitigation techniques for jets in pp collisions at $\sqrt{s}$ = 8 TeV using the ATLAS detector*, The European Physical Journal C **76** (2016) 581, ISSN: 1434-6052, URL: https://doi.org/10.1140/epjc/s10052-016-4395-z (cit. on p. 55).

[143] *Constituent-Based Top-Quark Tagging with the ATLAS Detector*, tech. rep., All figures including auxiliary figures are available at https://atlas.web.cern.ch/Atlas/GROUPS/PHYSICS/PUBNOTES/ATL-PHYS-PUB-2022-039: CERN, 2022, URL: https://cds.cern.ch/record/2825328 (cit. on pp. 56, 118).

[144] ATLAS Collaboration, *Performance of electron and photon triggers in ATLAS during LHC Run 2*, Eur. Phys. J. C **80** (2020) 47, arXiv: 1909.00761 [hep-ex] (cit. on p. 59).

[145] ATLAS Collaboration, *Performance of the ATLAS muon triggers in Run 2*, JINST **15** (2020) P09015, arXiv: 2004.13447 [hep-ex] (cit. on p. 59).

[146] ATLAS Collaboration, *Measurement of the cross-section and charge asymmetry of W bosons produced in proton–proton collisions at $\sqrt{s}$ = 8 TeV with the ATLAS detector*, Eur. Phys. J. C **79** (2019) 760, arXiv: 1904.05631 [hep-ex] (cit. on p. 75).

[147] ATLAS Collaboration, *A search for $t\bar{t}$ resonances using lepton-plus-jets events in proton-proton collisions at $\sqrt{s}$ = 8 TeV with the ATLAS detector*, Journal of High Energy Physics **2015** (2015) 148, ISSN: 1029-8479, URL: https://doi.org/10.1007/JHEP08(2015)148 (cit. on p. 75).

[148] ATLAS Collaboration, *Search for heavy particles decaying into top-quark pairs using lepton-plus-jets events in proton–proton collisions at $\sqrt{s}$ = 13 TeV with the ATLAS detector*, The European Physical Journal C **78** (2018) 565, ISSN: 1434-6052, URL: https://doi.org/10.1140/epjc/s10052-018-5995-6 (cit. on p. 75).

[149] ATLAS Collaboration, *In situ calibration of large-radius jet energy and mass in* 13 *TeV proton–proton collisions with the ATLAS detector*, Eur. Phys. J. C **79** (2019) 135, arXiv: 1807.09477 [hep-ex] (cit. on p. 78).

[150] ATLAS Collaboration, *Jet reclustering and close-by effects in ATLAS Run 2*, ATLAS-CONF-2017-062, 2017, URL: https://cds.cern.ch/record/2275649 (cit. on p. 79).

[151] ATLAS Collaboration, *Measurements of b-jet tagging efficiency with the ATLAS detector using $t\bar{t}$ events at $\sqrt{s}$ = 13 TeV*, en, J. High Energy Phys. **2018** (2018) (cit. on p. 79).

[152] ATLAS Collaboration, *Studies on the improvement of the matching uncertainty definition in top-quark processes simulated with Powheg+Pythia8*, ATL-PHYS-PUB-2023-029, 2023, URL: https://cds.cern.ch/record/2872787 (cit. on p. 81).

[153] S. Höche, S. Mrenna, S. Payne, C. T. Preuss and P. Skands, *A Study of QCD Radiation in VBF Higgs Production with Vincia and Pythia*, SciPost Phys. **12** (2022) 010, URL: https://scipost.org/10.21468/SciPostPhys.12.1.010 (cit. on p. 81).

[154] ATLAS, CDF, CMS and DO Collaborations, *First combination of Tevatron and LHC measurements of the top-quark mass*, ATLAS-CONF-2014-008, 2014, URL: https://cds.cern.ch/record/1669819 (cit. on p. 81).

[155] A. Manohar, P. Nason, G. P. Salam and G. Zanderighi, *How Bright is the Proton? A Precise Determination of the Photon Parton Distribution Function*, Physical Review Letters **117** (2016), ISSN: 1079-7114, URL: http://dx.doi.org/10.1103/PhysRevLett.117.242002 (cit. on p. 81).

[156] R. D. Ball et al., *Parton distributions for the LHC run II*, Journal of High Energy Physics **2015** (2015), ISSN: 1029-8479, URL: http://dx.doi.org/10.1007/JHEP04(2015)040 (cit. on p. 82).

[157] C. D. White, S. Frixione, E. Laenen and F. Maltoni, *IsolatingWtproduction at the LHC*, Journal of High Energy Physics **2009** (2009) 074, ISSN: 1029-8479, URL: http://dx.doi.org/10.1088/1126-6708/2009/11/074 (cit. on p. 82).

[158] ATLAS Collaboration, *Search for heavy particles decaying into top-quark pairs using lepton-plus-jets events in proton–proton collisions at $\sqrt{s} = 13$ TeV with the ATLAS detector*, Eur. Phys. J. C **78** (2018) 565, arXiv: 1804.10823 [hep-ex] (cit. on p. 83).

[159] ATLAS Collaboration, *Search for the standard model Higgs boson produced in association with top quarks and decaying into a $b\bar{b}$ pair in pp collisions at $\sqrt{s} = 13$ TeV with the ATLAS detector*, Phys. Rev. D **97** (2018) 072016, arXiv: 1712.08895 [hep-ex] (cit. on p. 83).

[160] J. Alwall et al., *Comparative study of various algorithms for the merging of parton showers and matrix elements in hadronic collisions*, The European Physical Journal C **53** (2007) 473, ISSN: 1434-6052, URL: http://dx.doi.org/10.1140/epjc/s10052-007-0490-5 (cit. on p. 83).

[161] *TRExFitter Documentation*, URL: https://trexfitter-docs.web.cern.ch/trexfitter-docs/ (cit. on pp. 85, 100).

[162] W. Buttinger, *xroofit*, https://gitlab.cern.ch/will/xroofit, Accessed: May 5, 2024, 2024 (cit. on p. 85).

[163] L. Lista et al., *Statistical methods for data analysis in particle physics*, vol. 941, Springer, 2017 (cit. on p. 88).

[164] J. Neyman and E. S. Pearson,
On the Problem of the Most Efficient Tests of Statistical Hypotheses,
Phil. Trans. Roy. Soc. Lond. A **231** (1933) 289 (cit. on p. 91).

[165] G. Cowan, K. Cranmer, E. Gross and O. Vitells,
Asymptotic formulae for likelihood-based tests of new physics,
The European Physical Journal C **71** (2011), ISSN: 1434-6052,
URL: http://dx.doi.org/10.1140/epjc/s10052-011-1554-0 (cit. on pp. 92, 93).

[166] *Summary plots for beyond Standard Model Higgs boson benchmarks for direct and indirect searches*, tech. rep., All figures including auxiliary figures are available at https://atlas.web.cern.ch/Atlas/GROUPS/PHYSICS/PUBNOTES/ATL-PHYS-PUB-2024-008: CERN, 2024, URL: https://cds.cern.ch/record/2898861 (cit. on p. 115).

[167] *Search for heavy pseudoscalar and scalar bosons decaying to top quark pairs in proton-proton collisions at*, tech. rep., CERN, 2024,
URL: https://cds.cern.ch/record/2911775 (cit. on pp. 114, 136).

[168] *Search for top-quark-associated production of heavy scalar or pseudoscalar in pp collisions at 13 TeV*, tech. rep., CERN, 2024, URL: https://cds.cern.ch/record/2891814 (cit. on p. 116).

[169] A. Collaboration, *Combination and summary of ATLAS dark matter searches interpreted in a 2HDM with a pseudo-scalar mediator using 139 fb^{-1} of $\sqrt{s}$ = 13 TeV pp collision data*, 2023, arXiv: 2306.00641 [hep-ex] (cit. on p. 116).

[170] *Dark matter summary plots for s-channel, 2HDM+a, Higgs portal and Dark Higgs models*, tech. rep., All figures including auxiliary figures are available at https://atlas.web.cern.ch/Atlas/GROUPS/PHYSICS/PUBNOTES/ATL-PHYS-PUB-2024-010: CERN, 2024, URL: https://cds.cern.ch/record/2901527 (cit. on p. 117).

[171] ATLAS Collaboration, *Search for charged Higgs bosons decaying into a top quark and a bottom quark at $\sqrt{s}$ = 13 TeV with the ATLAS detector*, JHEP **06** (2021) 145,
arXiv: 2102.10076 [hep-ex] (cit. on p. 117).

[172] D. B. Franzosi, E. Vryonidou and C. Zhang, *Scalar production and decay to top quarks including interference effects at NLO in QCD in an EFT approach*, 2017,
arXiv: 1707.06760 [hep-ph] (cit. on p. 117).

[173] A. Shmakov et al., *SPANet: Generalized permutationless set assignment for particle physics using symmetry preserving attention*, SciPost Physics **12** (2022), ISSN: 2542-4653,
URL: http://dx.doi.org/10.21468/SciPostPhys.12.5.178 (cit. on p. 118).

[174] J. Zhou et al., *Graph neural networks: A review of methods and applications*,
AI Open **1** (2020) 57 (cit. on p. 118).

[175] ATLAS Collaboration, *ATLAS b-jet identification performance and efficiency measurement with $t\bar{t}$ events in pp collisions at $\sqrt{s}$ = 13 TeV*, Eur. Phys. J. C **79** (2019) 970,
arXiv: 1907.05120 [hep-ex] (cit. on p. 119).

[176] ATLAS Collaboration, *Graph Neural Network Jet Flavour Tagging with the ATLAS Detector*, ATL-PHYS-PUB-2022-027, 2022, URL: https://cds.cern.ch/record/2811135 (cit. on p. 119).

[177] E. E. Khoda, *ATLAS pixel cluster splitting using Mixture Density Networks*, 2019, URL: https://cds.cern.ch/record/2687968 (cit. on p. 119).

[178] ATLAS Collaboration, *Modelling of Track Reconstruction Inside Jets with the 2016 ATLAS $\sqrt{s}$ = 13 TeV pp Dataset*, ATL-PHYS-PUB-2017-016, 2017, URL: https://cds.cern.ch/record/2275639 (cit. on pp. 121, 132).

[179] T. Sjöstrand, S. Mrenna and P. Z. Skands, *PYTHIA 6.4 physics and manual*, JHEP **05** (2006) 026, arXiv: hep-ph/0603175 (cit. on p. 122).

[180] ATLAS Collaboration, *Summary of ATLAS Pythia 8 tunes*, ATL-PHYS-PUB-2012-003, 2012, URL: https://cds.cern.ch/record/1474107 (cit. on p. 122).

List of Figures

2.1 Fundamental vertices in QCD. . . . 8
2.2 Fundamental vertices for Higgs boson interactions, with $V = W^{\pm}, Z$ . . . 12
2.3 LO Feynman diagrams for SM $t\bar{t}$ production at hadron colliders. . . . 13
2.4 Radiative correction to the Higgs boson mass from a fermion loop. . . . 16
2.5 Regions of the $(\cos(\beta-\alpha), \tan\beta)$ plane excluded by fits to the measured Higgs boson production and decays. . . . 19
2.6 Feynman diagram at LO of the main production/decay chain of a heavy Higgs boson in a Type-II 2HDM . . . 21
2.7 Signal-plus-interference distributions in $m_{t\bar{t}}$ at parton level before final state radiation for (a) a single pseudoscalar A with mass $m_A = 500$ GeV and (b) a single scalar H with mass $m_H = 800$ GeV, for various values of $\tan\beta$ in a type-II 2HDM. . . . 22
2.8 Signal-plus-interference distributions in $m_{t\bar{t}}$ at parton level before final state radiation for (a) a single pseudoscalar A with mass $m_A = 800$ GeV and (b) a single scalar H with mass $m_H = 800$ GeV, for various values of $g_{A/Ht\bar{t}}$ in the generic (pseudo)scalar model. . . . 22

3.1 A schematic overview of the CERN accelerator complex along with the associated experiments [53]. . . . 24
3.2 Luminosity-weighted distribution of the number of interactions per bunch crossing in the ATLAS detector. Taken from Ref. [58]. . . . 25
3.3 A digital rendering of the ATLAS experiment, from Ref. [59]. This rendering refers to the detector configuration used in Run-3, which differs from the Run-2 configuration in the MS, particularly in the Small Wheels (Section 3.2.5). . . . 26
3.4 Transverse section of the ATLAS ID, from Ref. [59]. Going outward from the beamline the ID components are: the Pixel detector, including the insertable B-layer (IBL), the Semiconductor Tracker (SCT) and the Transition Radiation Tracker (TRT). 28
3.5 Digital rendering of the ATLAS calorimeter system, from Ref. [59]. Both the technology of each subsection and the function are specified in the labels. . . . 30
3.6 Schematic representation of the structure and segmentation of the central barrel section of the ATLAS EM LAr calorimeter [64]. . . . 30
3.7 Digital rendering of the ATLAS MS system in its Run-3 configuration, from Ref. [59]. The main muon detector components are visible. . . . 32
3.8 ITk geometry with the geometry version internally referred as 23-00-03. The details of this geometry are discussed in Ref. [75]. The red lines represent the Pixel Detector, while the blue lines mark the Strip Detector. . . . 34

4.1 Possible NNLO Feynman diagrams of single-top production in the Wt channel. Top and anti-top quarks are represented with double lines. 38

5.1 Typical path of a reconstructed electron in the ATLAS detector. The dashed line indicates a photon radiated by the electron. Figure taken from Ref. [126] 43
5.2 Electron reconstruction efficiency for the three working points of the likelihood-based electron identification. Figure taken from Ref. [130] 45

6.1 Schematic depiction of the three possible decay topologies in the one-lepton channel. t_h and b_h represent the hadronically-decaying top quark and the b-quark produced in this decay. Lines of the same colour are reconstructed as a single analysis object. Note that these are not Feynman diagrams, despite the similarity in style. 58
6.2 Selection efficiency times acceptance times $t\bar{t}$ branching ratio for the ℓ+jets ($\ell \in e, \mu$) final state (Eff x Acc x BR) as a function of the $t\bar{t}$ invariant mass at the parton level before the emission of FSR [19]. The distributions are obtained from all generated type-II 2HDM pure-signal pseudoscalar samples in the mass range 400 – 1400 GeV. The error bars correspond to the statistical uncertainty on the distributions. 62
6.3 Background composition in the merged, resolved 1b and resolved 2b signal regions. . 65
6.4 Definition of the angular variable θ^*. Momenta in different coordinates systems are shown with lines in different styles and colours 65
6.5 Ratio between the SM $t\bar{t}$ +2HDM (including the contribution of signal-background interference) and SM $t\bar{t}$ distribution of $|\cos\theta^*|$ for a few representative pseudoscalar signals, with a mass of 500 GeV in the Type-II 2HDM model, in the Resolved 1b and Resolved 2b regions. 66
6.6 Background composition in the ten resolved signal regions. The signal regions are defined based on the number of b-tagged jets in the event (one or two) and according to equidistant bins of the angular variable $|\cos\theta^*|$. 67
6.7 Distribution of the reconstructed $\Delta\phi_{\ell\ell}/\pi$ after the signal selection of the two-lepton channel for the SM backgrounds. The expected deviation from the SM in the presence of an interference pattern is also shown for two representative points in the ratio panel [19] 68
6.8 $m_{t\bar{t}}$ resolution as a function of the mass m_A of the pseudoscalar A in a type-II 2HDM with $\tan\beta = 0.4$, for all topologies with the different analysis strategies. Pure-signal samples are used for this study. Events containing an electron or a muon are considered separately. The resolved line is shared by both reclustering strategies. 70
6.9 Signal yield in different signal regions and for the two analysis strategies, for multiple pseudoscalar Type-II 2HDM pure-signal hypotheses with $\tan\beta = 0.4$. Each group of bars corresponds to a set of event categories for either the baseline VRC-based or the alternative RC-based categories in e+jets and μ+jets events, respectively. The first and third groups correspond to the RC-based categorisation, while the second and fourth groups correspond to the VRC-based baseline categorisation. 72
6.10 Comparison of upper limits on the signal strength for a selection of representative signal hypotheses involving a single pseudoscalar in a type-II 2HDM. In the ratio panel, the RC strategy is taken as a reference, and the relative improvement in the upper limits for the other tested strategies is calculated as $\frac{\Delta\mu}{\mu} = \frac{\mu^{up}_{\text{ref}} - \mu^{up}_{\text{test}}}{\mu^{up}_{\text{ref}}}$. 73

6.11 Comparison of upper limits on the signal strength for a selection of representative signal hypotheses involving a single scalar in a type-II 2HDM. In the ratio panel, the RC strategy is taken as a reference, and the relative improvement in the upper limits for the other tested strategies is calculated as $\frac{\Delta\mu}{\mu} = \frac{\mu^{up}_{\text{ref}} - \mu^{up}_{\text{test}}}{\mu^{up}_{\text{ref}}}$. 73

6.12 Upper limits on the signal strength for representative signal hypotheses involving both a scalar and a pseudoscalar with $m_A = m_H$ in a type-II 2HDM, comparing the simplified strategy with the more complex strategy based on $|\cos\theta^*|$ bins. In the ratio panel, the simplified strategy is taken as a reference, and the relative improvement in the upper limits for the other tested strategies is calculated as $\frac{\Delta\mu}{\mu} = \frac{\mu^{up}_{\text{ref}} - \mu^{up}_{\text{test}}}{\mu^{up}_{\text{ref}}}$. 74

7.1 Pulls on the NPs after the fits to the Asimov dataset for the experimental uncertainties, under a Type-II 2HDM scalar signal hypothesis, with $m_H = 500$ GeV and $\tan\beta = 1.0$, for the parametrisations without (a) and with (b) and offset term. 89

7.2 Pulls on the NPs after the fits to the Asimov dataset for the modelling uncertainties, under a Type-II 2HDM scalar signal hypothesis, with $m_H = 500$ GeV and $\tan\beta = 1.0$, for the parametrisations without (a) and with (b) and offset term. 90

7.3 Distribution of the exclusion test statistic for two selected 2HDM hypotheses, under the null (BSM) and alternative (SM-only) hypotheses, estimated using toy experiments (data points) and asymptotic formulas (solid lines). 94

7.4 Illustration of the application of the CL_s method in case of well-separated distributions of the test statistic under the null and alternative hypotheses (left) and in case of largely overlapping distributions (right), where the experiment has poor sensitivity to the signal. The shaded areas under the curves represent p-values. 95

7.5 Example of a p_{CL_s} scan as a function of $\sqrt{\mu}$ for the Type-II 2HDM signal hypothesis with $m_A = m_H = 700$ GeV and $\tan\beta = 1.4$. The expected and observed lines, as well as $\pm1\sigma$ and $\pm2\sigma$ lines do not exhibit a monotonic behaviour in terms of the POI $\sqrt{\mu}$. The red horizontal line corresponds to the p_{CL_s} value of 0.05 used as a threshold for the exclusion; values with $p_{\text{CL}_s} < 0.05$ are excluded at 95% CL. 97

8.1 Distributions of the reconstructed $m_{t\bar{t}}$ in (a-e) the five Resolved signal regions with 2 b-tags and (f) the Merged signal region of the one-lepton channel, after fit under the background-only hypothesis. In the top panel, the data points are overlaid on the SM prediction, while in the bottom panel, the ratio between the observed data and the post-fit SM expectation is shown. The ratio between the expected distributions under the BSM and the SM hypotheses is also shown in the bottom panel for two representative signal hypotheses. Figure published in Ref. [19]. 101

8.2 Distributions of the reconstructed $m_{t\bar{t}}$ in the five Resolved signal regions with 1 b-tag of the one-lepton channel, after fit under the background-only hypothesis. In the top panel, the data points are overlaid on the SM prediction, while in the bottom panel, the ratio between the observed data and the post-fit SM expectation is shown. The ratio between the expected distributions under the BSM and the SM hypotheses is also shown in the bottom panel for two representative signal hypotheses. Figure published in Ref. [19]. 102

8.3 Distributions of the reconstructed $m_{\ell\ell bb}$ in the five signal regions of the two-lepton channel, after fit under the background-only hypothesis. In the top panel, the data points are overlaid on the SM prediction, while in the bottom panel, the ratio between the observed data and the post-fit SM expectation is shown. The ratio between the expected distributions under the BSM and the SM hypotheses is also shown in the bottom panel for two representative signal hypotheses. Figure published in Ref. [19]. 103

8.4 Observed local p-values under the background-only hypothesis, against a pseudoscalar interference hypothesis, as a function of m_A for different values of the relative width of the pseudoscalar A: (a) 1%, (b) 5%, (c) 10%, (d) 20%, (e) 30%, (f) 40%. The p-values are calculated separately in the one-lepton and two-lepton channels, and by combining both. On the right-hand y-axis, the Gaussian significances corresponding to the p-values on the left-hand y-axis are reported. 107

8.5 Observed local p-values under the background-only hypothesis, against a scalar interference hypothesis, as a function of m_H for different values of the relative width of the scalar H: (a) 1%, (b) 5%, (c) 10%, (d) 20%, (e) 30%, (f) 40%. The p-values are calculated separately in the one-lepton and two-lepton channels, and by combining both. On the right-hand y-axis, the Gaussian significances corresponding to the p-values on the left-hand y-axis are reported. 108

8.6 Observed and expected exclusion regions in the $m_{A/H} - \tan\beta$ plane of a (a) Type-II 2HDM in the alignment limit ($\cos(\beta-\alpha) = 0$) with mass-degenerate pseudoscalar and scalar states, and the (b) hMSSM. The observed exclusion regions are indicated by the shaded area. The boundary of the expected exclusion region under the background-only hypothesis is marked by the dashed line. The surrounding shaded bands correspond to the $\pm 1(2)\sigma$ variations of the expected excluded regions. Figure published in Ref. [19]. 110

8.7 Observed and expected exclusion regions in the $m_a - \tan\beta$ plane for the 2HDM+a with $m_A = m_H = m_{H^\pm} = 600$ GeV and (a) $\sin\theta = 0.35$, (b) $\sin\theta = 0.70$. The observed exclusion regions are indicated by the shaded area. The boundary of the expected exclusion region under the background-only hypothesis is marked by the dashed line. The surrounding shaded bands correspond to the $\pm 1(2)\sigma$ variations of the expected excluded regions. Figure published in Ref. [19]. 110

8.8 Constraints on the coupling strength modifier $g_{At\bar{t}}$ as a function of m_A for different values of the relative width of the pseudoscalar A: (a) 1%, (b) 5%, (c) 10%, (d) 20%, (e) 30%, (f) 40%. The hatched area marks the unphysical region of parameter space where the partial width $\Gamma(A \to t\bar{t})$ is larger than the total width of A. The observed exclusion regions are indicated by the shaded area. The boundary of the expected exclusion region under the background-only hypothesis is marked by the dashed line. The surrounding shaded bands correspond to the $\pm 1(2)\sigma$ variations of the expected excluded regions. 111

8.9 Constraints on the coupling strength modifier $g_{Ht\bar{t}}$ as a function of m_H for different values of the relative width of the scalar H: (a) 1%, (b) 5%, (c) 10%, (d) 20%, (e) 30%, (f) 40%. the hatched area marks the unphysical region of parameter space where the partial width $\Gamma(H \to t\bar{t})$ is larger than the total width of H. The observed exclusion regions are indicated by the shaded area. The boundary of the expected exclusion region under the background-only hypothesis is marked by the dashed line. The surrounding shaded bands correspond to the $\pm 1(2)\sigma$ variations of the expected excluded regions. 112

9.1 Observed and expected exclusion regions in the $m_{A/H} - \tan\beta$ plane of a type-II 2HDM in the alignment limit ($\cos(\beta - \alpha) = 0$) with mass-degenerate pseudoscalar and scalar states, from (a) the previous search on 8 TeV data [17], and (b) the search presented in this thesis [17]. 114
9.2 Observed and expected constraints on the hMSSM benchmark in the $m_A - \tan\beta$ plane derived from a variety of different ATLAS searches using Run-2 data, from Ref. [166]. 115
9.3 Observed and expected exclusion regions in the $m_A - \tan\beta$ hMSSM plane from the CMS search in Ref. [18] 115
9.4 Feynman diagram for the production of a heavy (pseudo)scalar particle, H/A, produced in association with a pair of top quarks, with the (pseudo)scalar decaying into $t\bar{t}$, from Ref. [168]. 116
9.5 Observed (red solid line) and expected (black dashed line) 95% CL lower limits on $\tan\beta$ as a function of the $m_A = m_H$, assuming type-II 2HDM in the alignment limit [168]. The yellow bands illustrate the $\pm 1\sigma$ bands of the expected limits. The two red dashed lines correspond to the observed limits obtained with a variation of the theory cross sections by $\pm 1\sigma$. 116
9.6 Observed and expected exclusion regions in the $m_a - \tan\beta$ plane for the 2HDM+a with $m_A = m_H = m_{H^\pm} = 600$ GeV and (a) $\sin\theta = 0.35$, and (b) $\sin\theta = 0.70$, combining multiple results from searches on the full Run-2 ATLAS dataset, from Ref. [170] . . 117

10.1 Comparison of (a) the jet p_T and (b) the jet absolute pseudorapidity η^{jet} distributions for the $t\bar{t}$ PU0, $t\bar{t}$ PU200, and $Z' \to$ had samples. All distributions are normalised to unity. 122
10.2 Residuals (left) and pulls (right) on track θ (upper row), ϕ (middle row), q/p_T (bottom row) in $Z' \to$ had events. Two curves are shown separately for tracks containing and not containing a merged cluster. 124
10.3 Residuals (left) and pulls (right) on track d_0 in $t\bar{t}$ $\langle\mu\rangle = 0$, $t\bar{t}$ $\langle\mu\rangle = 200$, and $Z' \to$ had events. Two curves are shown separately for tracks containing and not containing a merged cluster. 125
10.4 Residuals (left) and pulls (right) on track z_0 in $t\bar{t}$ $\langle\mu\rangle = 0$, $t\bar{t}$ $\langle\mu\rangle = 200$, and $Z' \to$ had events. Two curves are shown separately for tracks containing and not containing a merged cluster. 126
10.5 Width of the d_0 residual distribution as a function of the number of merged pixel clusters per track in $Z' \to$ had events. 128
10.6 Average number of pixel hits per track as a function of (a) the ΔR between the track and the center of the jet and (b) the p_T of the jet, obtained in $Z' \to$ had events. 129

10.7 Average number of pixel hits per track in the innermost layer of the Pixel Detectoras a function of (a) the ΔR between the track and the center of the jet and (b) the p_T of the jet, obtained in $Z' \rightarrow$ had events. 130
10.8 Average number of all pixel hits per track in the next-to-innermost layer of the Pixel Detectoras a function of (a) the distance ΔR between the track and the center of the jet and (b) the p_T of the jet, obtained in $Z' \rightarrow$ had events. 130
10.9 Average number of strip hits per trackas a function of (a) the ΔR between the track and the center of the jet and (b) the p_T of the jet, obtained in $Z' \rightarrow$ had events. 131
10.10 Fraction of shared pixel hits per trackas a function of (a) the ΔR between the track and the center of the jet and (b) the p_T of the jet, obtained in $Z' \rightarrow$ had events. 131
10.11 Fraction of shared pixel hits per track in the innermost layer of the Pixel Detectoras a function of (a) the ΔR between the track and the center of the jet and (b) the p_T of the jet, obtained in $Z' \rightarrow$ had events. 132
10.12 Fraction of shared strip hits per trackas a function of (a) the ΔR between the track and the center of the jet and (b) the p_T of the jet, obtained in $Z' \rightarrow$ had events. 132
10.13 Track reconstruction efficiency for tracks inside jets as a function of jet p_T in $Z' \rightarrow$ had events. 133
10.14 Track reconstruction efficiency for tracks in the core of jets as a function of jet p_T in $Z' \rightarrow$ had events, comparing a reconstruction scenario with no classification of merged clusters with a scenario with perfect classification of merged clusters. 133

A.1 Observed local p-values under the background-only hypothesis, against a pseudoscalar resonance hypothesis, as a function of m_A for different values of the relative width of the pseudoscalar A: (a) 1%, (b) 5%, (c) 10%, (d) 20%, (e) 30%, (f) 40%. The p-values are calculated separately in the one-lepton and two-lepton channels, and by combining both. On the right-hand y-axis, the Gaussian significances corresponding to the p-values on the left-hand y-axis are reported. 142
A.2 Observed local p-values under the background-only hypothesis, against a scalar resonance hypothesis, as a function of m_H for different values of the relative width of the scalar H: (a) 1%, (b) 5%, (c) 10%, (d) 20%, (e) 30%, (f) 40%. The p-values are calculated separately in the one-lepton and two-lepton channels, and by combining both. On the right-hand y-axis, the Gaussian significances corresponding to the p-values on the left-hand y-axis are reported. 143
A.3 Observed local p-values under the background-only hypothesis, against a pseudoscalar deficit hypothesis, as a function of m_A for different values of the relative width of the pseudoscalar A: (a) 1%, (b) 5%, (c) 10%, (d) 20%, (e) 30%, (f) 40%. The p-values are calculated separately in the one-lepton and two-lepton channels, and by combining both. On the right-hand y-axis, the Gaussian significances corresponding to the p-values on the left-hand y-axis are reported. 144
A.4 Observed local p-values under the background-only hypothesis, against a scalar deficit hypothesis, as a function of m_H for different values of the relative width of the scalar H: (a) 1%, (b) 5%, (c) 10%, (d) 20%, (e) 30%, (f) 40%. The p-values are calculated separately in the one-lepton and two-lepton channels, and by combining both. On the right-hand y-axis, the Gaussian significances corresponding to the p-values on the left-hand y-axis are reported. 145

B.1 Constraints on the coupling strength modifier $g_{At\bar{t}}$ as a function of m_A for different values of the relative width of the pseudoscalar A: (a) 1%, (b) 5%, (c) 10%, (d) 20%, (e) 30%, (f) 40%. Correction factors to NLO precision for the signal samples are applied. The hatched area marks the unphysical region of parameter space where the partial width $\Gamma(A \to t\bar{t})$ is larger than the total width of A. The observed exclusion regions are indicated by the shaded area. The boundary of the expected exclusion region under the background-only hypothesis is marked by the dashed line. The surrounding shaded bands correspond to the $\pm 1(2)\sigma$ variations of the expected excluded regions. Figure published in Ref. [19]. 148

B.2 Constraints on the coupling strength modifier $g_{Ht\bar{t}}$ as a function of m_H for different values of the relative width of the scalar H: (a) 1%, (b) 5%, (c) 10%, (d) 20%, (e) 30%, (f) 40%. Correction factors to NLO precision for the signal samples are applied. The hatched area marks the unphysical region of parameter space where the partial width $\Gamma(H \to t\bar{t})$ is larger than the total width of H. The observed exclusion regions are indicated by the shaded area. The boundary of the expected exclusion region under the background-only hypothesis is marked by the dashed line. The surrounding shaded bands correspond to the $\pm 1(2)\sigma$ variations of the expected excluded regions. Figure published in Ref. [19]. 149

List of Tables

2.1 Branching fractions of $t\bar{t}$ decay modes, with their respective final states, as reported in [23]. In the modes including leptons, all flavours $l = e, \mu, \tau$ are included. 14

5.1 Reclustered jet reconstruction criteria. 52
5.2 Selection criteria for electrons. Those for looser control region electrons are shown in italics and square brackets. 55
5.3 Selection criteria for the muons. Those for looser control region muons are shown in italics and square brackets. 55
5.4 Small-R jet selection criteria 55
5.5 Reclustered jet selection criteria. 56

6.1 Summary of the used triggers and their requirements. 59
6.2 Summary of the event selection criteria used in the one-lepton channel. 61
6.3 Summary of normalisation uncertainties applied to different background components. 83

8.1 Post-fit fractional impacts [19] of different uncertainty groups, relative to the total uncertainty on the best-fit value $\hat{\sqrt{\mu}}$ of the POI, for two representative signal hypotheses in the Type-II 2HDM benchmark model: a single pseudoscalar with $m_A = 800$ GeV and $\tan\beta = 0.4$ and a scenario with both a scalar and a pseudoscalar, with $\tan\beta = 2.0$ and $m_A = m_H = 500$ GeV. The statistical uncertainty is obtained by subtracting in quadrature the total systematic uncertainty from the total uncertainty on $\hat{\sqrt{\mu}}$. The observed best-fit value of the POI is $\hat{\sqrt{\mu}} = -0.147 \pm 0.104$ for the hypothesis with $m_A = 800$ GeV and $\hat{\sqrt{\mu}} = +0.071 \pm 0.224$ for $m_A = m_H = 500$ GeV. Note that the total sum in quadrature of all impacts does not precisely reach 100% because of the rounding precision of the numbers provided within this table. 105

10.1 Width of the residual distributions for the track parameters θ, ϕ, q/p_T in $Z' \rightarrow$ had events. 127
10.2 Width of the pull distributions for the track parameters θ, ϕ, q/p_T in $Z' \rightarrow$ had events. 127
10.3 Width of the residual distributions for the track parameter d_0 in $t\bar{t}$ $\langle\mu\rangle = 0$, $t\bar{t}$ $\langle\mu\rangle = 200$, and $Z' \rightarrow$ had events. 127
10.4 Width of the pull distributions for the track parameter d_0 in $t\bar{t}$ $\langle\mu\rangle = 0$, $t\bar{t}$ $\langle\mu\rangle = 200$, and $Z' \rightarrow$ had events. 127
10.5 Width of the residual distributions for the track parameter z_0 in $t\bar{t}$ $\langle\mu\rangle = 0$, $t\bar{t}$ $\langle\mu\rangle = 200$, and $Z' \rightarrow$ had events. 127

10.6 Width of the pull distributions for the track parameter z_0 in $t\bar{t}$ $\langle\mu\rangle = 0$, $t\bar{t}$ $\langle\mu\rangle = 200$, and $Z' \rightarrow$ had events. 128